Image-based methods for the identification of in-plane composite moduli at high strain rates

Mr. Samuel Parry

A thesis presented for the degree of
doctor of philosophy

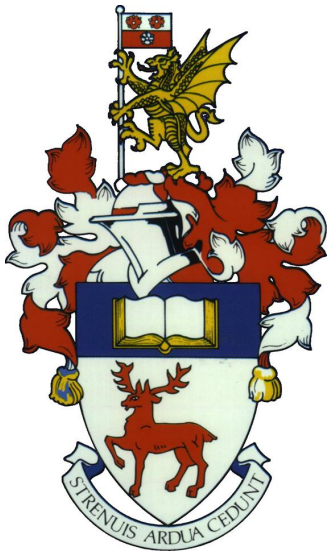

University of Southampton
Faculty of Engineering and Physical Sciences
Engineering Materials Research Group

2021

Abstract

This thesis describes the development of new image-based methods to characterise in-plane moduli for off-axis composites at high strain rates. It is difficult to accurately identify these properties with current experimental methods such as the split-Hopkinson bar, because the assumptions that the technique is based on can be violated at strain rates above a few hundred s^{-1}. With this new approach, transverse and shear moduli of Carbon Fibre Reinforced Polymer (CFRP) composite samples have been identified at strain rates in the 500 to 2000 s^{-1} domain.

The off-axis composite modulus identification methods were developed within the Image-Based Inertial Impact (IBII) test technique. Using the Virtual Fields Method (VFM), full-field measurements and rigid body virtual fields were included in the principle of virtual work to derive stress averages on a test sample. Transverse and shear moduli were then identified from linear fits to the average stress-strain response. This thesis details the numerical implementation of the VFM theory used to derive these moduli for unidirectional (UD) and multi-directional (MD) composite samples with configurations of UD90°, UD45° and MD45°.

An image deformation study was undertaken to verify the identification methods and to assess smoothing parameters for processing experimental images. Two full-field measurement techniques for calculating the displacement fields were evaluated in the image deformation simulations: the Grid Method and Digital Image Correlation (DIC). The first major goal of the study was to verify that DIC displacements could be used within the IBII test methodology. This was achieved by comparing the moduli identified from unsmoothed strain and acceleration fields with no simulated camera noise overlayed on the images. Here, the moduli identified with DIC were similar the Grid Method values. The second goal of the study was to obtain optimised smoothing parameters that gave the best trade-off between systematic and random errors on the identified moduli. This analysis showed that different optimised smoothing parameters were obtained for the UD45° samples, because of their more-complex kinematic fields compared to the UD90° samples. Optimised smoothing parameters that resulted in systematic and random errors of less than 1% were obtained for both grid and DIC images.

IBII tests were performed at the University of Southampton's high speed impact laboratory, where a 50 mm bore gas gun was used to launch aluminium projectiles at composite samples with impact speeds around 40 $m.s^{-1}$. A Shimadzu HPV-X ultra-high speed video camera operating at 2 MHz recorded images of the impacted samples and moduli were obtained from the deformed image sets. Validation of the modulus identification methods was achieved by comparing the moduli from different sample configurations. The transverse modulus E_{22} obtained from the UD45° samples was within one standard deviation (SD) of the UD90° sample result. Shear strain waves were detected in the UD90° sample strain maps, which were generated by a slight pitch-angle misalignment between the impacting components in the test. As a result, shear moduli were also obtained from the UD90° samples, with G_{12} values within on SD of the UD45° results. Shear moduli obtained from MD45° samples were around 6% lower than the UD values, which was consistent with the reduced laminate density of the MD samples. Comparison of the high strain rate moduli obtained in this study suggests that values reported in literature could be over-estimated, including both a material and a testing system response.

Comparison of the identified moduli from the two full-field measurement techniques showed that the E_{22} and G_{12} values were lower for DIC compared to the Grid Method. Voids were detected in the composite plates that the UD DIC samples were cut from, which provided an explanation for the lower DIC values. Shear moduli identified from MD45° samples using DIC and the Grid Method were within 1%, which was expected given that both samples were cut from the same plate. Results from this study suggest that both the Grid Method and DIC are suitable for high strain rate moduli identification within the IBII test methodology.

List of Acronyms

BMI	Bismaleimide
BPA	Bisphenol A
CFRP	Carbon Fibre Reinforced Polymer
CLT	Classical Lamination Theory
COV	Coefficient Of Variation
DIC	Digital Image Correlation
FE	Finite Element
FEMU	Finite Element Model Updating
FOV	Field Of View
FRP	Fibre Reinforced Polymer
GFRP	Glass Fibre Reinforced Polymer
IBII	Image-Based Inertial Impact
LSG	Linear Stress Gauge
MD	Multi-Directional
PPI	Pixels Per Inch
PVDF	Polyvinylidene difluoride
ONERA	Office National d'Etudes et de Recherches Aérospatiales (The French Aerospace Laboratory)
QS	Quasi-Static
ROI	Region Of Interest
SD	Standard Deviation
SiC	Silicon Carbide
SHPB	Split-Hopkinson Pressure Bar
SHTB	Split-Hopkinson Tension Bar
SSD	Sum of Squared Differences
UD	Uni-Directional
UHMWPE	Ultra-High Molecular Weight Polyethylene
UHSV	Ultra-High Speed Video
VFM	Virtual Fields Method
WWFE	World Wide Failure Exercise
ZNSSD	Zero-Normalised Sum of Squared Differences

Contents

Declaration of authorship

I declare that this thesis and the work presented in it is my own and has been generated by me as the result of my own original research.

I confirm that:

1. This work was done wholly or mainly while in candidature for a research degree at this University;
2. Where any part of this thesis has previously been submitted for a degree, or any other qualification at this University or any other institution, this has been clearly stated;
3. Where I have consulted the published work of others, this is always clearly attributed;
4. Where I have quoted from the work of others, the source is always given. With the exception of such quotations, this thesis is entirely my own work;
5. I have acknowledged all main sources of help;
6. Where the thesis is based on work done by myself jointly with others, I have made clear exactly what was done by others and what I have contributed myself;
7. Parts of this work have been published as:

   S. Parry, L. Fletcher and F. Pierron. "The off-axis IBII test for composites". *Journal of Dynamic Behavior of Materials* 7(1), 2021, pp. 127-155.

Signature: Mr Samuel L. Parry
Date: 23/03/2021

Acknowledgements

I am sincerely grateful for the help and guidance that my project supervisors Prof. Fabrice Pierron and Dr. Lloyd Fletcher gave me throughout this challenging research project. Our valuable discussions were inspiring and helped shape the content of my thesis. This unique learning opportunity was a gift that I will value for the rest of my career.

Over the past three years it was great to have reviews from Prof. Ian Sinclair, which were often from a micro-mechanical point of view. Thank you and Prof. Genevieve Langdon from the University of Sheffield for the challenging questions and interesting discussion during my *viva voce*. A number of scientists and engineers not directly connected to this work also assisted me over the duration of the project, including Neil Bourne, Anatoly Resnyansky, Jeremy Anderson and Sam Weckert. Previous work that I had undertaken with these people inspired me to undertake this PhD. In addition, I must give thanks to Rade Vignjevic for his criticism of my split-Hopkinson bar analysis.

It is quite important that I give thanks to all of the engineering materials group students, Jack Callaghan, Geir Ólafsson, Irene Jiménez Fortunato and Tobias Laux for their help in the early stages of my project. In times like these, it really makes me appreciate your help and companionship. Long periods in front of the computer screen were broken up by lab testing sessions with Jared Van Blitterswyk. Thanks for your help with learning some of the intricacies of full-field measurements. I also appreciated working with Xavier Régal and Aleksander Marek.

I am especially grateful to Simon Beever at the Engineering Design and Manufacturing Centre (EDMC), for his help cutting the test samples 'as you wait'. Thank you to Andrew Robinson at the Testing and Structures Research Laboratory (TSRL) for promptly signing-off my testing plans and help with test machine setup. Geoffrey Howell at the materials laboratory was also extremely knowledgeable and helpful with optical inspection. Lastly, I need to say thank you to Antonio De Grazia, Sebastian Rosini and the *Doughnuts* group for their technical help, support and friendship. It will be interesting to watch these researchers make their way in the world of science.

Thanks for the support from my mother Susan and my father Martyn, and the spiritual guidance from my deceased sister Alexandra. Each of you are inspiring in your own unique way, and helped me carry-on during tough times. This project would not have been completed without the love and support of my wife Francheska Lee. At times she was able to grasp some of the concepts in this project better than I did. This was somewhat concerning as she had not undertaken any tertiary mathematics, physics or materials training. I like to think that this resulted from my ability to explain complicated concepts in a straightforward way, but perhaps this also came from her parents Raymond and Rita. I must also give thanks to my godmother Catherine McKinnon, who sent me copies of *American Prometheous* and *The old man and the sea*. Although these texts were at opposite ends of the scale with regard to page limits, their common themes often provided inspiration for writing a PhD thesis. Last but by no means least, thanks to my best friend Ben Dalwood. See you soon mate.

After some time had passed I came to the realisation that elements within this project were similar to an Adam Jones riff. At first they appear quite difficult, but once you know what is going on, it's quite simple in nature.

Chapter 1

Introduction

1.1 Motivation

There are many industrial applications where components manufactured from composite materials are subjected to high strain-rate loads. The high specific stiffness and failure stress properties of composites have motivated their integration in automotive component design, in an effort to reduce weight, fuel consumption and greenhouse gas emissions [1]. Strain rates on the order of 3×10^2 s^{-1} have been reported in car engine rails in [2] and 1×10^3 s^{-1} at impact speeds of around 55 $km.hr^{-1}$ (≈ 15 $m.s^{-1}$) in [3]. Composite aircraft components such as the nose, wings and stabilisers are particularly vulnerable to impact from foreign objects including runway debris, hail and birds. It has been reported that bird strikes are one of the most significant problems for aviation worldwide, with annual costs exceeding 1 billion U.S. dollars per year [4, 5]. Bird strikes and foreign debris impact on aircraft panels can induce strain rates around 3×10^2 s^{-1} at impact speeds of 180 $km.hr^{-1}$ [6], noting that local strain rates extend to the thousand s^{-1} domain [7]. Fibre composites are also utilised in many military applications, including personnel body armour [8], missiles [9, 10] and vehicle armour, *e.g.* appliqué armour [11] and spall liners. Strain rates in composite armour systems subjected to projectile impact have been reported between 3×10^3 - 4×10^3 s^{-1} in [12]. Although, projectile impact scenarios can generate a broad range of strain rates over the duration of the engagement, with upper limits around the multiple thousands of s^{-1} mark [13]. Therefore, there are numerous industrial applications where composite materials and components are subjected to strain rates in the thousand s^{-1} regime.

Finite Element (FE) simulations are often used to predict the response of components under service loads. The ability of a simulation to predict realistic results often requires that material models specified for the components comprise of accurate experimental data *e.g.* in [14, 15]. It is therefore critical that constitutive models for strain-rate sensitive materials are constructed with reliable experimentally derived properties, obtained at the high strain-rates experienced in-service. A review of published literature on the in-plane high strain rate properties of composites shows inconsistency in the data trends. For example, considering the transverse modulus of Carbon Fibre Reinforced Polymer (CFRP) composites, some references reported increases [16–18] and others reported decreases [19, 20] with increasing strain rate. Inconsistency was also found with dynamic shear properties, with one example reporting an increasing shear modulus with increasing strain rate [20] and another reporting practically no strain rate sensitivity [18]. Therefore, when the same testing method is used to test similar materials, sample geometries and strain rates, different experimental campaigns yield conflicting results [18, 20]. Similar trends exist for Glass Fibre Reinforced Polymer (GFRP) composites, with some authors reporting increasing and others reporting decreasing moduli with increasing strain rate [21]. On the whole, there is a significant lack of consistent data at strain rates higher than a few hundred s^{-1}.

1.2 Background

Current experimental techniques used to evaluate high strain rate material properties rely on a number of assumptions, which must be satisfied in order to produce accurate results. The most common methods use split-Hopkinson bars, high-speed hydraulic test machines or drop towers. One of the limitations of the split-Hopkinson bar technique is the requirement to assume quasi-static equilibrium in the specimen, so that material parameters can be inferred from remotely mounted strain gauges. In mechanical tests, quasi-static equilibrium results when the inertial response of the analysed system is negligible. The split-Hopkinson bar technique uses long bars to mitigate inertial effects and small sample dimensions to reduce inertial effects in the specimen. However, inertial effects can become significant under dynamic loads that induce strain rates above 10^2 s^{-1} and it is doubtful that quasi-static equilibrium could be reached in composites evaluated in split-Hopkinson bar tests [22, 23]. Quasi-static equilibrium is particularly difficult to achieve when using the tension split-Hopkinson bar, because it usually requires specimen geometries with varying gauge widths and longer lengths that prolong the time for equilibrium to be established. Furthermore, quasi-brittle low-wave speed materials such as unidirectional (UD) composites are difficult to characterise in transverse tension or shear using the split-Hopkinson bar technique because they tend to fail at relatively low strains, resulting in failure stresses that occur prior to quasi-static equilibrium conditions. Therefore, when using the split-Hopkinson bar technique to derive composite material properties, the requirement of quasi-static equilibrium in the specimen restricts testing at strain rates around a few hundred s^{-1}.

Other regularly used test methods have limitations on the achievable strain rates from which accurate data can be obtained. High-speed hydraulic test machines are generally equipped with grips that allow the cross-head to reach the specified speed before gripping and engaging the specimen. Quasi-static equilibrium in the specimen is also assumed when deriving accurate data from high-speed hydraulic test machine experiments, because the force measurement is made remotely by a load cell mounted at one end of the specimen. Obtaining data from these devices is further complicated by the frequency response of the load cell, which can manifest as 'ringing' superimposed on the recorded material response [24]. For reliable results, the test duration must usually exceed the time for load cell ringing to dampen. Testing quasi-brittle composites is additionally difficult because failure may occur before the load cell ringing subsides. As a consequence of these two limitations, high-speed hydraulic test machines are usually restricted to testing composite specimens at strain rates $\leq 10^2$ s^{-1} [20]. Dynamic material properties are also derived from drop tower experiments, which can achieve similar strain rates to high-speed hydraulic load frames. However, strain-rate limitations are also imposed on drop tower tests because the force measurement methods are susceptible to inertial effects [25]. In summary, there is a common problem with current high strain-rate experimental techniques, in that they can only be used to obtain accurate material properties at strain rates on the order of a few hundred s^{-1}. Considering this limitation, the previously discussed scatter in the high strain rate properties of composites reported in literature is expected.

With the ongoing requirement to obtain material properties at strain rates on the order of a few thousand s^{-1}, it is important that techniques with fewer restrictions are developed. Recently, new experimental techniques based on the use of full-field measurements have emerged [26, 27]. An example of this is the Image Based Inertial Impact (IBII) test described in [28, 29]. The IBII test uses ultra-high speed imaging, full-field measurements and the Virtual Fields Method (VFM) to obtain material properties under dynamic loads by using the inertial response of the material as a kind of embedded load-cell. Because the technique does not need to assume quasi-static equilibrium in the specimen, it is ideal for testing the high strain rate properties of materials, including composites. In fact, because the test is purely inertial, quasi-static equilibrium is never reached. In recent times, material properties such as the transverse modulus and failure stress of a UD CFRP composite in [29] and stiffness components from a quasi-isotropic composite in [27] were identified from IBII tests. The technique has also been utilised to obtain the stiffness properties of a UD45° composite under a combined compression/shear stress state [30]. However, in [30] only a single sample was tested and as

with [29], the smoothing parameters selected to process the experimental data were based on previous evaluations. Therefore, there is scope to extend the IBII test method to evaluate the high strain-rate, in-plane modulus and failure stress properties of composites, with smoothing parameters that minimise the systematic and random errors in the particular material property being identified.

Until recently, the Grid Method [31] was selected for displacement field calculations in IBII tests. This has resulted in relatively-fine spatial resolutions to be achieved, compared to other full-field techniques such as Digital Image Correlation (DIC). However, there are several reasons why DIC could be the preferred full-field measurement technique. For example, in certain industrial settings it may not be possible to prepare samples with a regular grid on the imaged surface, which is a primary requirement of using the Grid Method. Some organisations may also be more familiar with speckle application processes and have access to DIC processing software. However, differences in the high-strain rate material properties for off-axis composites identified from IBII tests using DIC and Grid Method displacements are currently unknown. If these differences were quantified and of an acceptable amount, material testing laboratories would have more flexibility in the full-field measurement techniques they could apply in IBII tests. At a more general level, this analysis would also increase the universal nature of the IBII test methodology.

1.3 Aims and objectives

The primary aim of this PhD project was to develop a new procedure to identify in-plane material properties from off-axis composite samples at high strain rates. This was achieved using the IBII test methodology, combining full-field measurement techniques in the VFM without strain rate limiting assumptions. Two specific objectives were derived from the primary project aim. The first objective has addressed the previously discussed gaps in high strain-rate material properties reported in literature. The second objective has expanded the universal nature of the IBII test. These project objectives were:

1) Obtain an accurate in-plane material property dataset.

In-plane transverse and shear moduli of CFRP off-axis composites were obtained from IBII tests at strain rates on the order of 500 to 2000 s^{-1}. Optimised smoothing parameters, which minimised errors in the experimentally derived modulus values were determined in an image deformation study. Numerical methods for the off-axis modulus identification were validated across a range of samples including UD90°, UD45° and multi-directional (MD) MD45° configurations. Note that in this thesis, MD45° refers to a $[\text{MD}\pm45°]_{6S}$ stacking sequence. Strain-rate sensitivities of the identified moduli were then calculated relative to quasi-static values. Lower strain-rate sensitivities obtained in this study suggest that previous data reported in literature may contain both a testing apparatus and a material property response. Failure stress values were also identified from UD90° samples where again, lower strain rate sensitivities were obtained compared to in-literature figures.

2) Comparison of material properties derived from DIC and the Grid Method.

The second aim of this project was to identify dynamic material properties from off-axis composites with the IBII test and DIC derived displacements. Suitable subset sizing was confirmed with image deformation simulations, from which error-minimising smoothing parameters were obtained. This analysis revealed different optimised smoothing parameters for the DIC images, due to the reduced spatial resolution of DIC compared to the Grid Method. Transverse and shear moduli were then obtained from IBII tests on UD90° and UD45° samples. The DIC derived moduli were found to be lower than their Grid Method equivalents, which was consistent with the lower density of the DIC samples. However, when the different laminate densities were accounted for, the off-axis moduli derived with DIC and Grid Method displacements were similar.

1.4 Novelty

The methodology for obtaining high strain rate in-plane stiffness properties for a CFRP composite using the VFM and full-field measurements has been established in [27, 29]. The first novel result from this project is the generation of transverse and shear moduli data for a high grade aerospace CFRP composite, obtained in a single test at strain rates on the order of a few thousand s^{-1}. This data has been used for comparison to a viscoelastic material model for the composite, developed by one of the University of Southampton's collaborators: The French Aerospace Laboratory (ONERA) [20].

The second novel contribution was the development of a method to determine the elastic limit of the shear response of composites. A similar process had been conducted in [32] at in the lower strain rate regime around 50 s^{-1}. IBII Tests on UD45° and MD45° samples revealed a non-linear shear strain response, of which the elastic limit varied in space and time. Identification of the shear modulus to the maximum shear loading included the non-linear response, reducing the calculated value. In the new approach, progressive chord modulus fits were made to the shear stress-strain curves and the elastic limit was located when the chord modulus fell below the average (excluding noisy data at the initial loading). This method improved the accuracy of the shear modulus values identified from IBII tests on off-axis composites.

Similar to the previous off-axis composite evaluation in [29], a linear elastic constitutive law was selected for the transverse modulus identification. However, the high fibre stiffness of CFRP composites can influence the transverse response in the material. In this evaluation, the identified transverse modulus values were corrected to account for the fibre strains. However, the high stiffness of the fibres led to the experimentally derived fibre strains being corrupted by noise. In order to overcome this low signal-to-noise problem, fibre strains derived from finite element simulations were used in the transverse modulus correction. The outcome of this activity was a more accurate high strain rate transverse modulus dataset.

The fourth novel contribution was the development of a new process to validate high strain rate moduli from IBII tests on off-axis composites. Previous IBII tests used UD45° samples to identify in-plane shear moduli at high strain rates. However, there were no comparable datasets to assess the results against, so it was unknown how accurate the results were. In this new validation process, IBII tests were also conducted on samples with different laminate configurations and their modulus values were compared. This analysis showed that the transverse modulus obtained from UD45° samples was close to one standard deviation from the UD90° sample results. Tests on UD90° samples showed that a slight pitch angle misalignment between the impacting components can lead to an additional shear loading, from which the shear modulus can be identified. The shear modulus identified from UD90° samples was within one standard deviation of the UD45° specimen value. These results were useful because both the transverse and shear moduli could be obtained from a single test on either sample geometry. In addition, the similar results obtained from the different sample configurations validated the methods used to identify the off-axis moduli. Additional tests on MD45° specimens were performed and the derived dynamic shear moduli were compared with the UD specimen values. Here, the MD shear modulus was slightly lower than the UD sample results, in accordance with the lower measured density of the MD laminate. Because the MD45° specimen shear moduli were derived from a different composite layup to the UD45° samples, this additional validation increased the confidence in the shear moduli identification methods.

The last novel contribution in this thesis was an assessment of the differences in the high strain rate off-axis composite moduli identified from Grid Method and DIC displacements. Prior to this investigation, DIC had never been used in conjunction with the IBII test. Image deformation studies were used to select error-minimising smoothing parameters for processing experimental grid and DIC speckle images. In this process, displacement fields obtained from a finite element simulation of an IBII test were

imposed on a set of synthetic grid or speckle images. Transverse and shear moduli were then identified from the synthetic images using a range of spatial and temporal smoothing kernel sizes. Optimised smoothing parameters were identified as the smoothing kernel combination that gave the lowest error, relative to reference moduli. The image deformation study showed that the lower spatial resolution resulting from DIC led to different optimised smoothing parameters being obtained from the synthetic speckle images compared to the grids. However, systematic errors on the identified moduli of less than 1% were predicted from both image types, which verified the use of DIC. The optimised smoothing parameters were then applied in the experimental identification of the transverse and shear moduli from grid and DIC test samples. When the different sample densities were accounted for, the results were within 1% and therefore, the DIC approach was validated. This finding has broadened the options available for full-field measurement techniques that can be used within the IBII test methodology.

1.5 Thesis outline

Subsequent chapters in this report are divided into the major themes from the project aim of deriving high strain rate properties of off-axis composites. Chapter 2: Literature review gives a critical review of current high strain rate experimental testing techniques and their limitations. It then focuses on results published in literature, identifying trends in the data and inconsistencies resulting from test conditions that cannot satisfy the assumptions required by their respective techniques. Chapter 3: Theory derives the VFM equations and lists the assumptions required within the IBII test methodology for the identification of off-axis composite in-plane modulus and failure stress properties. A description of the composite samples, the gas-gun setup and the imaging system is first given in Chapter 4: Experimental methods. This chapter then explains how the theory in Chapter 3 is applied to the experimental data to derive off-axis composite properties. Results from a numerical study that was used to select optimised smoothing parameters for processing Grid Method and DIC samples are detailed in Chapter 5: Image deformation. Kinematic fields, stress-strain curves and material properties obtained from IBII tests using Grid Method displacements are presented in Chapter 6: Experimental results 1: Grid Method. Here, the focus is on the high strain rate moduli from off-axis samples and the failure stress of transverse composite samples. DIC derived kinematic fields are compared to the Grid Method fields in Chapter 7: Experimental results 2: DIC, which then lists the material properties obtained using DIC displacements. A discussion of the experimentally-validated high strain rate material properties and a comparison to values reported in literature is given in Chapter 8: Discussion. This Chapter also quantifies differences in the material properties identified from both full-field measurement techniques. Chapter 9: Future work outlines research topics that could build upon the results obtained in this work and finally, the project conclusions are given in Chapter 10: Conclusions.

Chapter 2

Literature review

The overall aim of this project was to develop new experimental methods to obtain in-plane, high strain-rate properties of off-axis composites. Therefore this chapter will cover the following topics associated with the project aim:

1. Current high strain rate experimental techniques and their limitations.
2. Full-field imaging techniques regularly used for material property identification and their application to high strain-rate testing.
3. Commonly used inverse methods for material property identification.
4. The IBII test and why it is very well adapted for characterising material properties of quasi-brittle composites at high strain rates.
5. A description of the composite material analysed in this project and a brief introduction to composite failure criteria.
6. A review of the in-plane, high strain-rate modulus and failure stress properties of composites reported in literature.

The final section of this chapter gives a summary of the major research gaps identified and how this project aims to fill these gaps.

2.1 Current high strain rate testing techniques

This section gives a review of the most regularly used experimental techniques for determining high strain rate properties of solid materials at the macroscopic length scale. In this project, 'high strain rate' refers to strain rates between $1\times10^2-1\times10^4$ s^{-1} induced in materials under transient or 'one-off' loads *i.e.* not fatigue.

2.1.1 The split-Hopkinson bar

The split-Hopkinson bar is one of the most commonly used devices for testing materials under dynamic loading conditions. Figure 2.1 (a) shows a schematic of the main components of the Split-Hopkinson Pressure Bar (SHPB) apparatus used for compression tests. Before the test is conducted, a specimen is positioned between the input and output bars. During the test, a striker rod impacts a long slender input bar where a compression wave develops, travels along the input bar and eventually loads the specimen. Strain gauges positioned on the input and output bars are used to measure the waves before and after interaction with the specimen, where ϵ_i and ϵ_r are the incident and reflected strains in the input bar, respectively and ϵ_t is the transmitted strain in the output bar. Figure 2.1 (a) also includes a free-body diagram of a SHPB specimen, showing the forces on either side of the specimen that are present during a test.

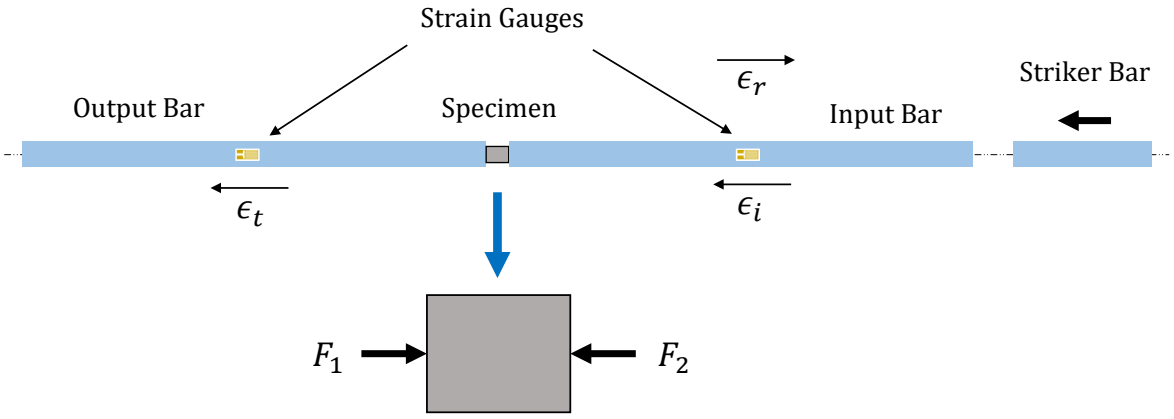

(a) SHPB and free body diagram of a loaded specimen.

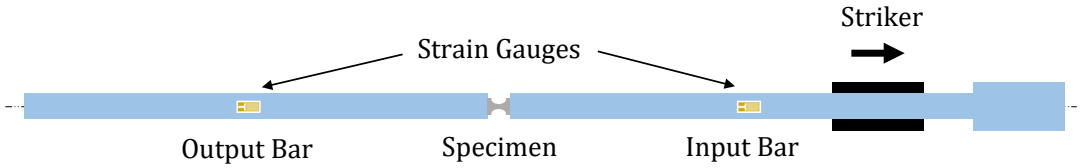

(b) SHTB.

Figure 2.1: Schematic showing the main components of the (a) Split-Hopkinson Pressure Bar (SHPB) and the resulting free body diagram of the loaded specimen, along with the (b) main components of the Split-Hopkinson Tension Bar (SHTB) apparatus.

Assuming 1D wave mechanics, linear elastic material behaviour in the bars and that the specimen is under a state of quasi-static equilibrium *i.e.* that the forces on either side of the specimen F_1 and F_2 are equal, the stress, strain rate and strain in the specimen can be derived from the input and output bar strain histories from the equations:

$$\sigma_s(t) = \frac{A_b}{A_s} E_b \, \epsilon_t(t)$$

$$\dot{\epsilon_s}(t) = \frac{2C_b}{L_s} \, \epsilon_r(t) \tag{2.1}$$

$$\epsilon_s(t) = \frac{2C_b}{L_s} \int_0^t \epsilon_r(t) \, dt$$

where $\sigma_s(t)$ is the stress, $\dot{\epsilon_s}(t)$ is the strain rate and $\epsilon_s(t)$ is the strain in the specimen, as a function of time [33]. Here, A_b, E_b and C_b are the bar cross-sectional area, Young's modulus and sound speed, respectively, assuming both bars are made from the same material and have the same diameter. Additionally, A_s is the specimen cross-sectional area and L_s is the length of the specimen.

The accuracy of results obtained from split-Hopkinson bar tests is highly dependent on the fulfilment of assumptions upon which the technique is based. One of these assumptions is that the specimen is loaded under uniaxial stress conditions. In split-Hopkinson bar tests, uniaxial or 1D stress loading of

the specimen is achieved in two ways, 1) with the use of long slender bars that transmit a predominantly 1D wave onto the specimen and 2) with well machined specimen and bar faces. However, the test is of course dynamic and in the early stages of loading, stresses on either side of the specimen are not equal. Time is required to establish quasi-static equilibrium so that the specimen stress can be inferred from the bar strains. In the Hopkinson bar test, it is assumed that $3-4$ stress wave passes over the specimen length are required to allow the specimen to 'ring-up' to a state of quasi-static equilibrium [34, 35]. Tests are often conducted with short specimens, so that the time to establish quasi-static equilibrium conditions can be minimised [22]. Given the large input and output bar mass, using small specimens also assists the requirement that the specimen remains in contact with the bars for the entire duration of the loading [36]. However, inertial effects can become significant under dynamic loads at strain rates above 1×10^2 s^{-1} [22], making quasi-static equilibrium difficult to achieve in split-Hopkinson bar tests under these conditions.

Quasi-static equilibrium can be even more challenging to achieve when testing low wave-speed materials such as composites [37]. In [38], quasi-static equilibrium in a split-Hopkinson bar test on a quasi-isotropic carbon fibre composite sample was assessed by comparing the stresses on either side of sample. Here, the stress on the left-hand side of the sample was inferred from the transmitted stress σ_t, calculated from the Young's modulus of the bars multiplied by the transmitted strain ϵ_t. In addition, the stress on the right-hand side of the sample was given by the sum of the incident and reflected stresses $\sigma_i + \sigma_r$, which were computed from the incident and reflected strains $\epsilon_i + \epsilon_r$, respectively, which were shown in Figure 2.1 (a). In this analysis, quasi-static equilibrium was determined to have occurred when the ratio of the left and right hand bar stresses $\sigma_t/(\sigma_i + \sigma_r)$ reached unity, which occurred in approximately $9-10$ μs for the sample with a length of 4 mm. This result was similar to the quasi-static equilibrium assessment performed on the S-2 glass woven fibre composite in [39], which plotted the difference in the left and right-hand stresses over the average stress as seen in Figure 2.2 (a). This analysis showed that quasi-static equilibrium was achieved in around $20-25$ μs however, like the analysis in [38], the sample size was relatively small. The problem with testing samples with small lengths is that they may not provide a sufficient representation of the laminate from which the material properties are sought, *e.g.* off-axis composites with low fibres angles. In addition, small sample sizes may also lead to material properties dominated by interfacial friction effects [40]. Lastly, this evaluation did not include on-sample measurements, which usually differ from the traditional stress-inference methods [19].

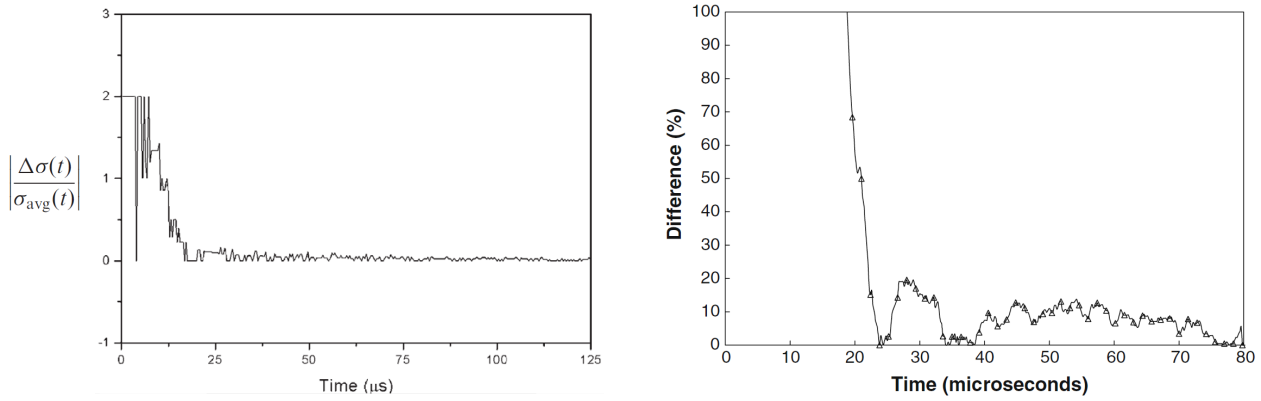

(a) SHPB tests on a $0°/90°$ woven S-2 glass composite sample of dimensions ϕ12.7 mm×6.35 mm [39].

(b) SHTB tests on a woven glass-filled epoxy composite with a sample length of 11 mm [41].

Figure 2.2: Quasi-static equilibrium assessments comparing the (a) difference in the stresses on either side of the sample to the mean sample stress and the (b) % difference between the two.

Similar results were obtained from [41], who claimed to have reached quasi-static equilibrium in a test on a glass-infused epoxy composite with a sample length of 11 mm after 20 μs. As seen in

Figure 2.2 (b), inertial effects were present late in the loading history, indicating that quasi-static equilibrium may not have been achieved throughout the loading duration of the test. In fact, when testing quasi-brittle materials at high strain rates, quasi-static equilibrium may never evolve regardless of its size [23]. If quasi-static equilibrium does evolve in the specimen, the time taken to reach this condition usually surpasses the elastic material response and consequently, elastic properties of materials cannot be obtained accurately in split-Hopkinson bar tests [42].

Achieving quasi-static equilibrium and uniform stress in the specimen is even more difficult in tensile split-Hopkinson bar tests. The split-Hopkinson Tension Bar (SHTB) system is essentially the same as the SHPB, however a tensile pulse is applied to a specimen positioned between the input and output bars as shown in Figure 2.1 (b). Traditionally, SHTB specimens are adhered to threaded inserts at the ends of the input and output bars and usually have a 'dumb-bell' profile to induce failure in the specimen gauge section, rather than at the adhesive/threaded insert interface. Tension specimens are also (typically) longer than compression specimens because they need to accommodate stress relieving transition radii on their profile. Transverse stress-strain curves obtained from a UD90° CFRP composite at quasi-static, intermediate and high strain rates are shown in Figure 2.3. When tested at the quasi-static strain rate of 1×10^{-5} s^{-1} and the intermediate strain rate of 1×10^{0} s^{-1} using a standard test machine, the stress-strain response was linear up to fracture, as expected for such a configuration. However, when the material was tested using the SHTB at 4×10^{2} s^{-1}, the response was non-linear and inertial effects can be seen throughout the loading history. Therefore, it was unlikely that quasi-static equilibrium in the specimen evolved during the test duration and consequently it is difficult to accurately determine the apparent modulus. Additionally, it is possible that the material failed when inertial effects were present and it is therefore unclear what the true failure stress for this test was. Thus, for quasi-brittle, low wave-speed materials such as composites, it is difficult to reliably obtain high strain rate stiffness and failure stress properties with the SHPB or the SHTB.

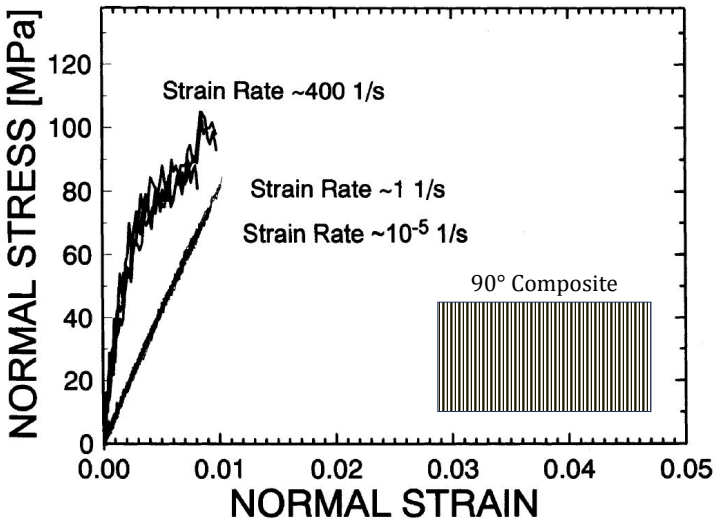

Figure 2.3: Stress-strain response from SHTB testing of a transverse CFRP composite in [16].

In more recent times, full-field imaging techniques have been integrated in Hopkinson bar tests. The use of full-field measurements to measure displacements and derive strains in the specimen has advanced the split-Hopkinson bar technique, as a number of works have shown that inferring the specimen strain from the bar strain histories results in an underestimate of the local specimen strain [17, 19, 43]. While the addition of full-field measurements has improved the strain measurement accuracy, it does (of course) not mitigate inertial effects and the need to assume quasi-static equilibrium in the specimen to infer the stress.

Another key assumption of the split-Hopkinson bar technique is that of 1D wave mechanics. During a test, the striker bar impact on the input bar generates an initially 3D incident wave. One of the reasons why long, slender input and output bars are used in Hopkinson bar tests is to allow enough time for the 3D pulse to evolve to a state where it may be considered predominantly 1D or uniaxial. However, the incident wave is formed of a range of frequencies, and the high frequency components can disperse from the low frequency components in the main pulse as the wave travels the length of the long input bar [44]. The dispersion in the incident wave can induce multi-dimensional loading in the specimen and thus violate the 1D wave mechanics assumption [27]. Correction techniques [45] can be used to account for wave dispersion, however these techniques are still evolving [44]. Pulse shaping techniques that produce a ramped rather than a sharp rise in the incident pulse have also been developed [33]. However, pulse shaping methods limit the achievable strain rates in Hopkinson bar tests.

2.1.2 High-speed hydraulic test machine

The operational principle of a high-speed hydraulic test machine is similar to a standard test machine, with a few exceptions. Firstly, pressure stored in the accumulators is released to the impact cylinder over a short duration. This permits faster loading of the sample compared to a standard electro-mechanical test machine. Depending on the sample configuration, tests can be performed over tens of milliseconds *e.g.* 20 ms in [46]. However, there is no feedback loop to control the actuator during a test, so the system has a 'fire and forget' quality. They are also equipped with special grips that allow the cross-head to accumulate speed before engaging and loading the specimen. The purpose of the special grips or the 'slack-adaptor' is to reduce the inertial effects from the lower grip and the actuator during the loading stage [47]. High speed hydraulic test machines can operate between $\approx$ 1 mm.s^{-1} $-$ 25 m.s^{-1} and can therefore induce a range of strain rates, usually to a maximum of 1×10^2 s^{-1} [18, 48, 49]. Strain measurement in high speed hydraulic test machine experiments is relatively straightforward, with on-specimen strain gauges or full-field measurements [2].

The main problem with high-speed hydraulic test machines is that it is difficult to accurately measure the load. The first problem with the load measurement arises from inertial effects in the specimen. Because the force is measured with a load cell located at one end of the specimen, the assumption of quasi-static equilibrium is required to infer the specimen stress [24]. This is essentially the same assumption required in the split-Hopkinson bar technique. In addition, the bulky design of the specimen grips and requirements for strain measurement methods mean that relatively large specimen gauge lengths are required, which further prolongs the establishment of quasi-static equilibrium in the sample. The second problem comes from the inertial response of the load cell itself, which generates 'ringing' superimposed on the recorded material response. Because the recorded signal consists of both the material and the load cell responses, it is difficult to accurately determine material properties such as stiffness or failure stress. Finite element simulations can be used to predict the extent of load cell ringing, as reported in [50]. Figure 2.4 (a) shows the finite element geometry used in simulations of a CFRP composite loaded in a high-speed hydraulic test machine. The resulting force-strain histories are shown alongside in Figure 2.4 (b), where the extent of load cell ringing was evident at relatively low impact speeds between 5$-$15 m.s^{-1}. In order to mitigate the effects of load cell ringing, test durations are often required to outlast the time for the ringing to dissipate. However, this presents a problem for testing low strain to failure materials such as composites, because if the failure occurs before the load cell ringing has subsided, the failure stress identification will include the load cell effects. In [51], a damping material was positioned between the contact faces of the slack adaptor to reduce oscillations recorded from load cell. These oscillations were thought to be caused by the metal-on-metal contact in the slack adaptor during the test however, the exact source or sources of the oscillations are unknown. As a result of the inertial effects in the specimen and the load cell, high-speed hydraulic test machines are limited to testing materials to *c.* 1×10^2 s^{-1}.

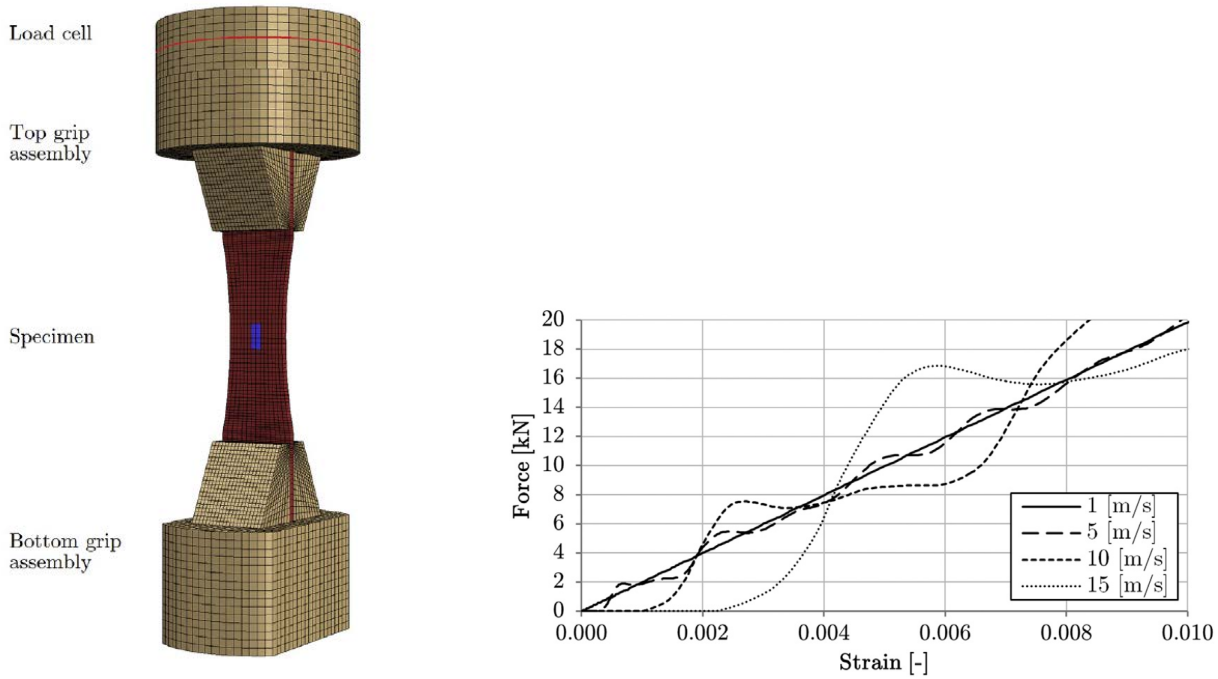

(a) Finite element mesh geometry for the specimen, load cell, top and bottom grips.

(b) Force *vs.* strain curves show significant inertial effects at test speeds of 10 and 15 m.s^{-1}.

Figure 2.4: Images from [50] showing the (a) mesh and the (b) force *vs.* displacement curves from the finite element simulation of a high-speed hydraulic test machine loading of a CFRP composite.

2.1.3 Drop-weight tower

Drop-weight towers can be used to test basic specimen geometries in compression and special fixtures can be used to test in tension [52] and combined compression/shear states of stress, at strain rates up to several hundred s^{-1} [53]. A load cell positioned underneath the specimen and velocity instrumentation can be used to establish a relationship between the system impulse and the output voltage of the load cell [25]. The stress in the specimen is then obtained by differentiation of the impulse-time history and the specimen cross-sectional area. Additionally, an accelerometer positioned on the drop weight can be used to obtain the force from the mass and acceleration of the drop weight [54].

Similar to the SHPB and high-speed hydraulic test machine methods, the drop-weight tower force measurement technique assumes quasi-static equilibrium in the specimen. Again, in dynamics it is unlikely that this condition is maintained over the duration that material properties are derived from and therefore, interpretation of the results becomes troublesome. Measurements can be made both above and below the specimen however, the results are susceptible to superimposition of the system vibration response on the material response. Therefore, this is similar to the high-speed test machine load cell ringing problem [21, 25]. In summary, drop-weight towers have similar limitations to high-speed hydraulic test machines and are therefore, restricted to accurate dynamic material property identification at strain rates up to a few hundred s^{-1}.

2.1.4 Limitations of current high strain rate test methods

This review of current high strain rate experimental techniques has shown that commonly used methods rely on the assumption of quasi-static equilibrium in the specimen. Therefore, current techniques

are limited to testing materials at strain rates on the order of 1×10^2 s^{-1}, so that inertial effects are minimised and results accuracy is improved. This is a major limitation given that many engineering components are subjected to strain rates on the order of 1×10^3 s^{-1}. Single point measurements have been traditionally used to infer or measure the specimen strains, however some users have integrated full-field measurement techniques to measure strains on the specimen surface. Some of the most commonly used full-field techniques are discussed in the next section.

2.2 Full-field imaging techniques

2.2.1 Digital Image Correlation (DIC)

In the application of macro-scale material characterisation, DIC is a widely used non-interferometric full-field imaging technique. DIC uses naturally-occurring surface variations or a random speckle pattern applied to the specimen surface to track the deformations as a sample or item is loaded. Images obtained from a DIC test are first divided into pixel subsets and each subset pixel grey level histogram is quantified [55]. Displacements are calculated by matching the location of the subsets between successive images in a least-squares sense. The resulting displacement vectors are obtained and the strains are calculated from the spatial gradient of the smoothed displacements [56]. Interpolation functions are used to predict grey level values at non-integer positions, leading to sub-pixel accuracy [57].

DIC has been used to obtain the displacements under dynamic loads in a wide variety of materials and test configurations, including three-point bend tests on aluminium [58], Brazilian disk tests on ceramics and polymers [34] and compression [59], tension [18] and shear [60] tests on composites. One of the advantages of the DIC technique is that it can measure 3D surface displacements when used in the stereo configuration. However, when considering the in-plane properties of composites, the out-of-plane response is expected to be relatively small and therefore 2D measurements can be used. One of the main limitations of the DIC technique is that it has a relatively low spatial resolution. This limitation comes from the fact that each subset must be unique in order for the correlation procedure to accurately measure displacements. The size of the speckles on the specimen surface is influenced by the application technique, however the size of the speckles recorded on the camera pixel array should usually be on the order of 3−5 pixels [61]. Given that 2−3 speckles in each direction are required for unique subset identification in DIC, the minimum subset size is approximately 13×13 pixels per independent measurement point. So the spatial resolution of DIC is driven by the pixel array size of the camera and the subset size requirement. However, it has been shown that an alternative full-field measurement technique, the Grid Method, has an improved compromise between spatial and measurement resolution when compared to DIC [31]. This is particularly beneficial when using standard high speed and Ultra-High Speed Video (UHSV) cameras, which typically have small pixel array sizes. This technique is discussed in the following section.

2.2.2 The Grid Method

The Grid Method is an optical technique that uses the spatial phase shift of a regular grid to calculate full-field surface displacements. The basic operational concept of the Grid Method is illustrated in Figure 2.5. First, a series of deformed sample images are recorded with a camera. For simplicity, only two specimen images at times t_1 and t_2 are shown in Figure 2.5 (a). A region of the specimen outlined in red is magnified and shown underneath the specimen in Figure 2.5 (b), revealing the digitised grey levels for each pixel of the grid recorded by the camera. Phase values are calculated from the spatial frequency of the grid pitch, using a windowed discrete Fourier transform that moves horizontally and vertically over the specimen surface. Displacements are then determined from the change in phase ϕ_2 - ϕ_1 occurring between successive images and the strains are given by the spatial gradient of the

displacement fields. A simplified representation of the phase change with respect to a specimen deformation from time t_1 to t_2 is shown in Figure 2.5 (c). As explained in [27], spatial and temporal unwrapping procedures are required when using the Grid Method in dynamics, in order to account for phase jumps larger than one grid pitch. A comprehensive explanation and review of the method can be found in [31].

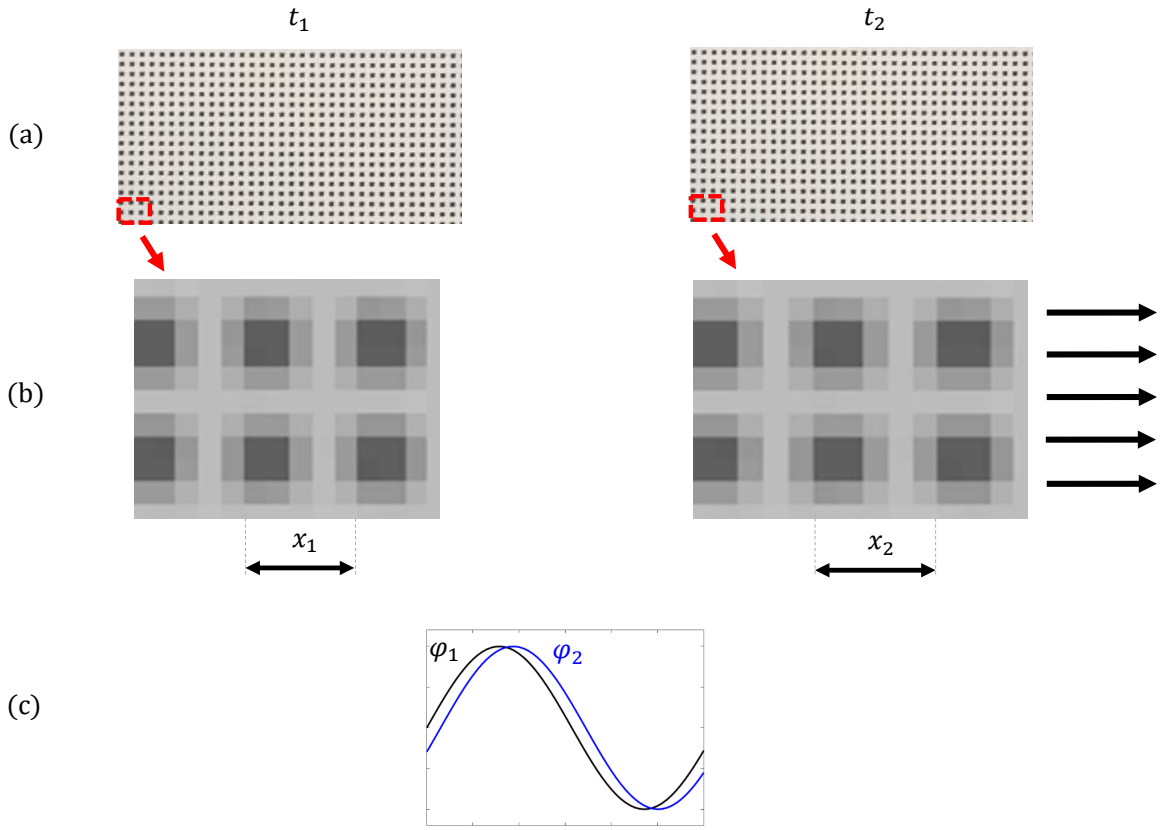

Figure 2.5: Simplified representation of the phase change between two deformed specimen images at t_1 and t_2, where (a) shows the specimen grid images, (b) shows a magnified region of the grid and (c) gives a representation of the phase change.

One of the limitations of the Grid Method is that a regular grid must be placed on the specimen [62]. However, grids can be easily printed onto composite samples with access to a flat-bed ink-jet printer, providing their surface is relatively smooth [63–65]. The main advantage of using the Grid Method is that a minimum sampling of five pixels per period can be assessed, which results in an improved spatial resolution compared to DIC [31]. This is important for impact testing of off-axis composites because previous investigations have revealed highly heterogeneous strain fields, leading to stress concentrations on the specimen surface [29]. It is therefore advantageous to use a technique with a 'finer' spatial resolution, so that the strain concentrations are not smeared by larger sampling sizes. A concern for both techniques is that one pitch or subset of data on the borders of the specimen is lost due to strain discontinuity. This lost data needs to be reconstructed by extrapolation and for the Grid Method, this reconstruction area can be smaller than for a DIC subset (depending on the subset size), making the overall systematic error smaller. In summary, the Grid Method provides a better compromise between spatial and displacement resolution than DIC and is therefore, well suited for high strain rate testing of composite materials, which often generate heterogeneous strain gradients. This advantage is additionally important considering the relatively sparse pixel array sizes available in high-speed cameras.

2.3 Inverse material property identification

Full-field measurements were initially used as an alternative to single point measurements from strain gauges and extensometers, providing additional information in material tests. However, full-field measurements were later used with inverse methods to identify material properties. As outlined in [66], there are several approaches to identifying material properties using inverse methods and full-field measurements, with the most natural approach being Finite Element Model Updating (FEMU). Fields obtained from a finite element simulation are usually idealised. One reason for this is that the boundary conditions used in their calculation exclude experimental occurrences such as slip in the specimen/grips interface and localised plasticity [67]. FEMU aims at including these experimental occurrences in the finite element simulation during material parameter identification. In this process, an experiment is conducted and single-point or full-field measurements are obtained at the boundary conditions, *e.g.* force or displacement histories. A finite element simulation of the experimental configuration is then conducted, where an initial guess is made for the material parameters, *e.g.* Young's modulus or Poisson ratio. A cost function is then used to assess material parameter values (within a range close to the reference) that generate boundary conditions with the lowest error compared to the experimental measurements.

One of the major limitations of the FEMU process is that it is sensitive to boundary conditions [68]. The experimental measurements need to be very precise, so that the finite element model includes physically meaningful data used for the material property identification. Collecting accurate experimental data at the boundaries of a test specimen can be challenging, regardless of the technique used to take the measurements. Another limitation of FEMU is that it is computationally expensive because of the iterative calculation procedure [69, 70] requires that many finite element simulations must be performed to converge on a result that minimises the cost function. Given that the aim of this project is to determine the high strain rate properties of composites, the time cost of executing many explicit dynamic simulations would be significant. An alternative to FEMU that can be insensitive to boundary conditions and computationally efficient is the VFM, which is discussed in the next section.

2.3.1 The Virtual Fields Method (VFM)

The VFM uses the principle of virtual work to establish equilibrium equations relating the internal and external forces on a solid deformable body under load. The principle of virtual work can be used to describe equilibrium in a solid body in the absence of body forces as:

$$-\int_V \boldsymbol{\sigma} : \boldsymbol{\epsilon}^* \, dV + \int_{\delta V} \boldsymbol{T} \cdot \boldsymbol{u}^* \, dS = \int_V \rho \, \boldsymbol{a} \cdot \boldsymbol{u}^* \, dV \tag{2.2}$$

where $\boldsymbol{\sigma}$ is the stress tensor, $\boldsymbol{T}$ is the traction vector and $\boldsymbol{a}$ is the acceleration vector [71]. The virtual displacement vector is $\boldsymbol{u}^*$ and is related to the virtual strain tensor $\boldsymbol{\epsilon}^*$ through:

$$\epsilon^*_{ij} = \frac{1}{2}(u^*_{i,j} + u^*_{j,i}) \ , \ i,j = 1,2 \tag{2.3}$$

The first term in Equation 2.2 is the internal virtual work over the solid volume V, the second term is the external virtual work on the volume surface δV and the third term is the acceleration virtual work over V. In quasi-static applications, the acceleration virtual work term in Equation 2.2 is zero and virtual fields can be selected to relate the internal virtual work to the external virtual work, which contains external load information [68]. Full-field displacement data can then be used together with a constitutive model for the material to relate the internal stresses to the applied loads.

The selection of virtual fields for material property identification using the VFM is influenced by the constitutive behaviour of the material. For linear elastic and some non-linear elastic material models, manually defined and noise-optimised virtual fields have been shown to be appropriate [68]. Virtual fields for other material behaviours are further described in [68, 71]. The VFM has been used extensively to investigate the quasi-static response of a variety of materials [71, 72]. As this project is focused on high strain rate applications, the application of the VFM in dynamics is further discussed in the next section.

2.3.2 The VFM in dynamics

For dynamic applications, the acceleration virtual work term in Equation 2.2 is non-zero. The VFM in dynamics involves the selection of virtual fields that cancel the internal or external virtual work terms in Equation 2.2. This results in an expression that relates the stress to the acceleration over the specimen surface. At this point the main advantage of the VFM for deriving dynamic material properties is clear: the material's inertial response is used to derive material parameters. Full-field measurements and an appropriate constitutive model are then included in the principle of virtual work to identify the material behaviour. The equations used to derive the modulus and failure stress for the material specimens analysed in this project (UD90° and off-axis composites) are given in Chapter 3: Theory.

The VFM has been used to identify material properties under high strain rates in several applications. In [73] the VFM and full-field measurements were used to identify different dynamic Young's Moduli in compression and tension for concrete. The VFM was also used to characterise failure in a concrete specimen in [73, 74] without relying on the interpretation of 1D signals from the rear surface of the specimen, as in [75]. Other applications of the VFM in dynamics have been performed on composites [26, 27] tungsten carbide ceramic-metallics (cermets) [28], rubber [76] and metals [77]. A VFM-inspired approach was also used for foams in [78] and rubber in [79].

One limitation of using full-field measurements within the VFM is that if specimen strains are low, noise levels can significantly influence the quality of the derived material parameters [72]. However, a well designed test that generates sufficient signal to noise ratios can yield accurate dynamic material properties [26]. An emerging experimental test methodology that uses full-field measurements and the VFM in dynamic applications is described in the next section.

2.4 The Image-Based Inertial Impact (IBII) test

The IBII test uses full-field measurements and the VFM to obtain material properties at high strain rates. The test utilises a gas gun to launch a projectile at a specimen/wave guide assembly as shown in Figure 2.6. When the projectile hits the wave guide, a compressive pulse travels through the wave guide and into the specimen. The specimen deformations are recorded with an UHSV camera, typically at 1 MHz or more. Advances in camera and computing technology have resulted in commercially available UHSV cameras with framing rates above 1 MHz and pixel array sizes usable for resolving the material response under high strain rate loads [80]. For example, the Shimadzu HPV-X UHSV camera can record 400 × 250 pixel images at up to 5 MHz (0.2 μs inter-frame time). Figure 2.6 also shows the free-body diagram of the specimen in the IBII test, where there is only one impact force F_1 acting on the body. Using Newton's second law, $F = -ma$, the impact force is:

$$F_1 = -\int_V \rho \boldsymbol{a}\, dV \tag{2.4}$$

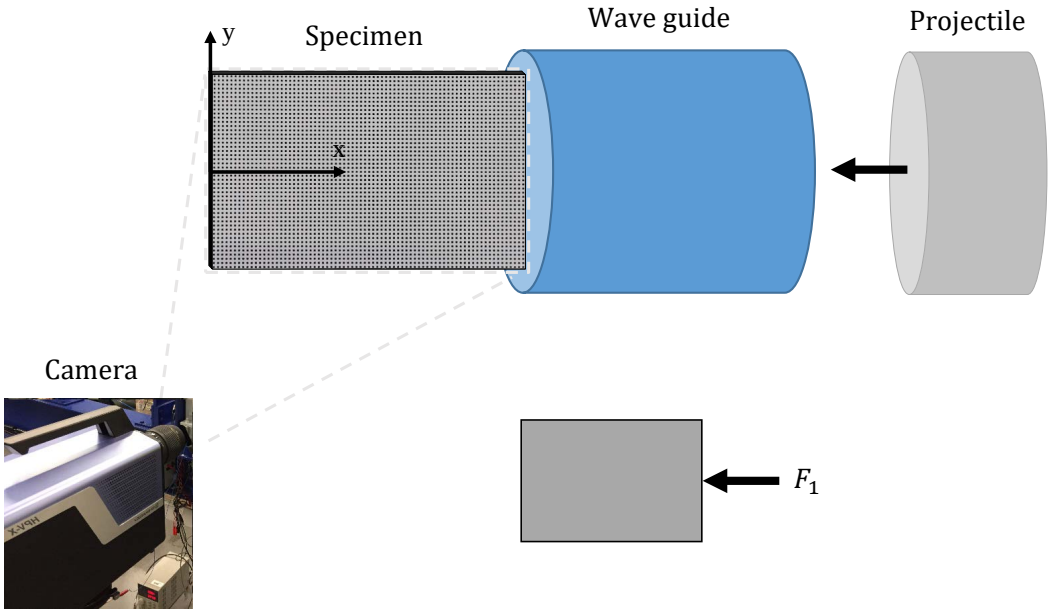

Figure 2.6: Schematic of the IBII test and the specimen free body diagram.

Because the inertial response *i.e.* the acceleration of the specimen is measured, there is no need to assume quasi-static equilibrium in the specimen, as required in current experimental techniques such as the split-Hopkinson bar test. A full-field imaging technique such as that in Section 2.2.2 is used to derive the surface displacements. Strains are then obtained by the spatial differentiation of the displacements and the acceleration vector $\boldsymbol{a}$ in Equation 2.4 is obtained by twice differentiating the displacements with respect to time. The strain and acceleration fields, together with selected virtual fields are then combined in Equation 2.2 to relate the stresses to the surface accelerations on the specimen under a dynamic load.

Recent high strain-rate applications of the IBII test used the Grid Method for calculating the displacement fields because of the improved spatial resolution compared to other techniques. However, there may be instances where other full-field measurement methods are called-for *e.g.*, a company or research group may be more familiar with DIC. Differences between VFM derived material parameters for concrete using DIC and the Grid Method were recently reported in [81]. However, differences in composite material properties identified with the IBII test using DIC and Grid Method derived displacements have not yet been evaluated. This topic should be investigated to increase its compatibility with different full-field measurement techniques.

The IBII test has been used to obtain the inter-laminar tensile properties of composites at high strain rates in [65]. Furthermore, it has been employed to characterise the in-plane properties of UD90° composites [29]. Recently, the IBII test method was extended to evaluate the transverse and shear stiffness in UD45° off-axis composite specimens in [30] however, only a single test was conducted in that work. Additionally, the failure stress identification procedures in [29] were not extended to the application of off-axis composites. Therefore, there is potential to extend the IBII test method to characterise the stiffness and failure stress of off-axis composite specimens subjected to a wider range of combined stress states. In the next section, orthotropic Fibre Reinforced Polymer (FRP) composites and their resulting failure response under combined states of stress are discussed.

2.5 Fibre composites

This project will consider test methods applied to FRP composites and the specific type of composite system that will be analysed is a CFRP composite. CFRP composites are used extensively in aerospace and automotive applications, where they are subjected to impact loads making their high strain rate properties of particular interest. Typical fibre composites are formed by embedding long continuous fibres in a polymer matrix. The resulting properties of the composite material give high specific strength and stiffness compared to standard engineering metals. This makes these materials useful for applications in transport where weight reductions can lead to decreased fuel costs.

Several reinforcing fibre materials can be used in composites including: carbon, glass, Aramid (Kevlar) and Ultra-High Molecular Weight Polyethylene (UHMWPE), with the most common fibres being carbon and glass. Carbon and glass fibres have relatively high stiffness and strength properties compared to the polymer matrix. The polymer matrix material is generally an epoxy based thermosetting polymer, but recently there has been considerable interest in thermoplastic resins due to the ability to melt the resin and recycle the composite. Nonetheless, thermosetting epoxy resins offer relatively good toughness and durability properties, making them an ideal matrix material in composite components specified in industrial applications.

Another advantage of composite materials is that they can be formed into thin sheets called laminae, which consist of a single layer of fibres embedded in the matrix material. The laminae exhibit a higher strength and stiffness when loaded in the direction of the fibres however, these laminae can be stacked in a variety of configurations to produce a laminate with a desired structural response. The work in this thesis will generally focus on characterising the properties of UD laminates that consist of laminae stacked with the same fibre direction. Figure 2.7 gives a schematic showing how a UD laminate comprises of multiple laminae with the fibres orientated in the same direction. In this thesis the standard coordinate system convention for composite laminae will be adopted. Specifically, the 1-axis refers to the fibre direction, the 2-axis refers to the axis transverse to the fibres, in-plane as shown in Figure 2.7. The 3-axis refers to the through-thickness direction of the laminate. The experiments presented in this thesis will concentrate on the in-plane properties of composites so the focus will be on the 1-2 plane. Reference to the global coordinate system is conventional, with the x-axis being horizontal, the y-axis vertical and the z-axis out-of-plane. This project will mostly consider rectangular specimens where the long axis of the rectangle is aligned with the x-axis, which is the direction of impact as previously shown in the IBII schematic in Figure 2.6.

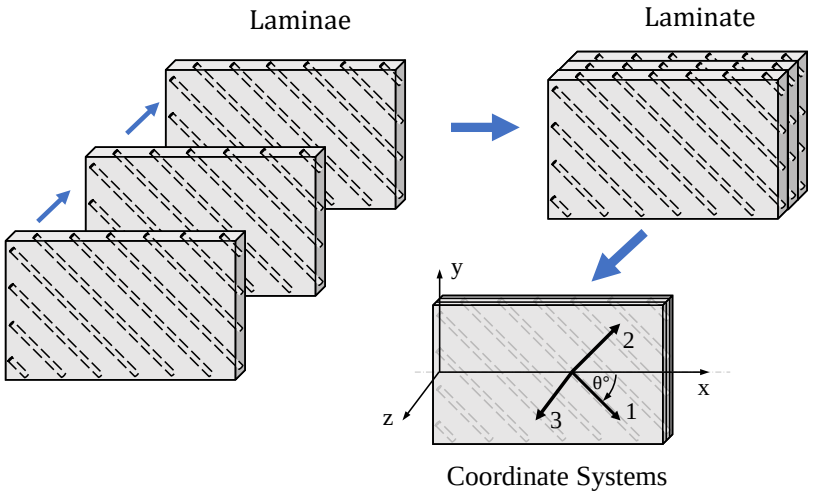

Figure 2.7: Composition of a UD composite laminate made from multiple laminae, together with the applicable global and material coordinate systems.

2.5.1 Failure envelopes

Tests on off-axis composite specimens can be used to obtain the in-plane transverse and shear failure stresses in material coordinates. The combination of normal/shear failure stresses can be plotted in the transverse *vs.* shear stress space as shown in the failure envelope in Figure 2.8. Representations of the different loading and specimen configurations used to derive in-plane data for the different regions of the failure envelope are also given in Figure 2.8. Observing the experimental failure stress values on the envelope, the tension/shear side of graph shows how increasing tensile stress lowers the ability of the material to support shear stress. In contrast, the compression/shear side of graph shows how increasing compressive stress strengthens the shear stress material response due to the Mohr-Coulomb strengthening effect [82].

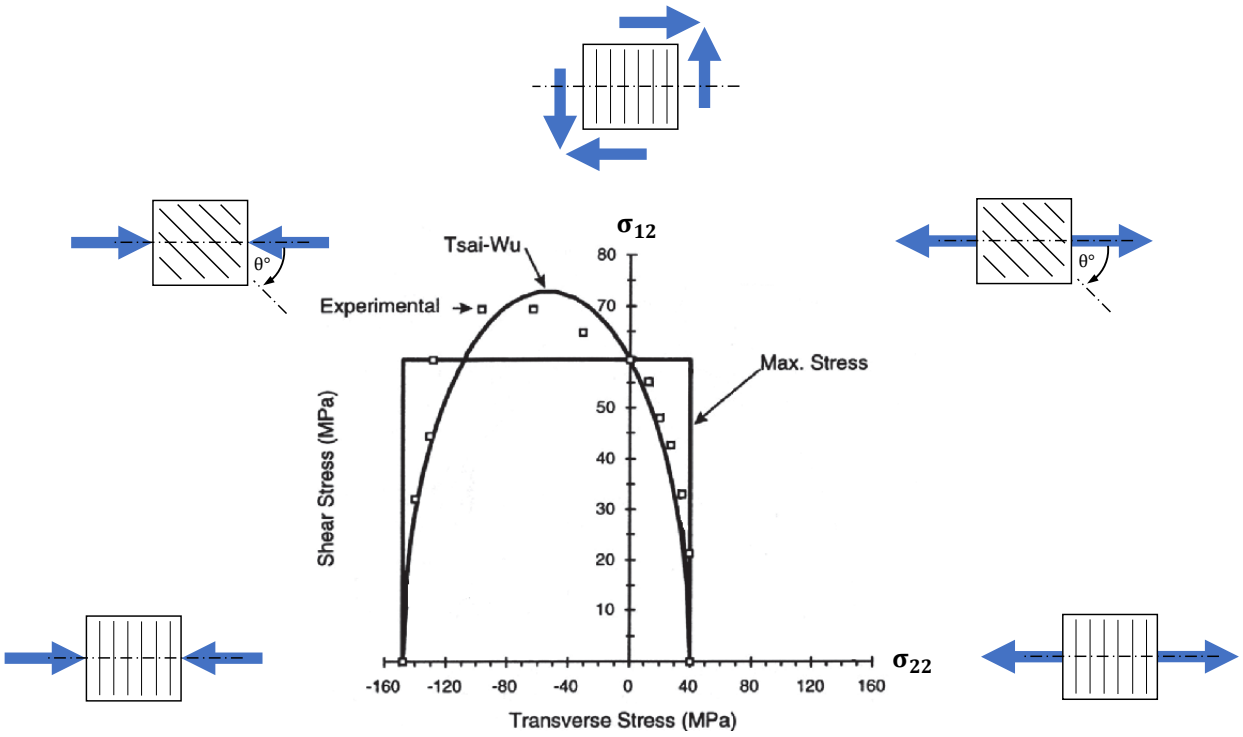

Figure 2.8: In-plane failure envelope for an example composite material at quasi-static strain rates showing experimentally derived failure stresses, together with maximum stress and Tsai-Wu failure criteria fits to the data [83]. Also shown are representations of the loading configurations for off-axis composites used to obtain data for the different regions of the failure envelope.

There are a number of existing composite failure theories, with the most basic being the maximum stress criterion. In the maximum stress criterion, failure occurs when the stress in the principal or shear directions reaches a critical value. However, the maximum stress criterion is limited because there is no interaction between the principal and shear stresses [84]. One theory that accounts for the interaction between the principal and shear stresses is called the Tsai-Wu failure criterion [85]. An example of the Tsai-Wu failure model applied to a composite material is also shown in Figure 2.8. It is clear from this plot that use of the maximum stress criterion at the extreme left and right sides of the graph is problematic because it predicts the material will not fail, when in reality it has failed due to the combination of normal/shear stresses. It also predicts that the material will fail at the top region of the graph although in the experiments failure had not occurred in this region. As shown in Figure 2.8, the Tsai-Wu criterion gives an improved prediction of the failure response of the material. There are many other composite failure theories that attempt to capture the shear/tension

and shear/compression coupling effect on the failure envelope for composite materials. However, one of the main limiting factors on accurately calibrating these failure criterion at high strain rates is the lack of accurate experimental data. The majority of data in literature on composite failure envelopes was obtained at quasi-static strain rates. As discussed in the next section, composite materials are strain rate sensitive and therefore high strain rate failure envelopes should be developed in order to accurately predict the response of composite under dynamic loads.

2.6 Strain rate sensitivity of composite materials

This section provides a review of published literature regarding the in-plane composite material properties obtained from high strain rate experiments, focusing on modulus and failure stress. Before considering the rate dependence of composite materials as a whole, it is useful to consider the rate dependence of the individual constituents because the composite system properties are influenced by the type of fibres and matrix used to construct the laminate. Therefore, the rate sensitivity of composite fibres and matrix materials is first reviewed. It is also important to consider the strain rate sensitivity of composites loaded in different orientations with respect to their fibre axis. This section therefore provides a review of the axial, transverse and shear moduli and failure stress strain rate sensitivities for carbon and glass fibre composites tested in tension and compression. Finally, high strain rate failure envelope data reported in the literature is discussed.

2.6.1 Strain rate sensitivity of the fibres

Two of the most common fibres used in automotive and aerospace industry composites are carbon and glass fibres. Bundles of pure carbon fibres were tested between $\dot{\epsilon} \approx 1.0 \times 10^{-3}$ to 1.3×10^{3} s^{-1} using a SHTB apparatus in [86], where it was found that both the modulus and failure stress were strain rate insensitive. The tensile strength strain rate sensitivity of the carbon fibres was compared to that of Kevlar-49, Silicon Carbide (SiC) and E-glass fibres as shown in Figure 2.9, where significant rate dependence for the glass fibres was observed. The tensile strength rate sensitivity of glass fibre bundles was also evaluated in [87], where an increase from 800 MPa at a quasi-static strain rate to 2100 MPa at 1.6×10^{2} s^{-1} was recorded. No tests were conducted at intermediate strain rates and it is therefore, unclear if the exponential relationship between tensile strength and strain rate shown in Figure 2.9 was realistic. In general, there is limited data on carbon and glass fibres at high strain rates, potentially because the materials are rarely used on their own in engineering applications. Next, the strain rate sensitivity of commonly used matrix materials is reviewed.

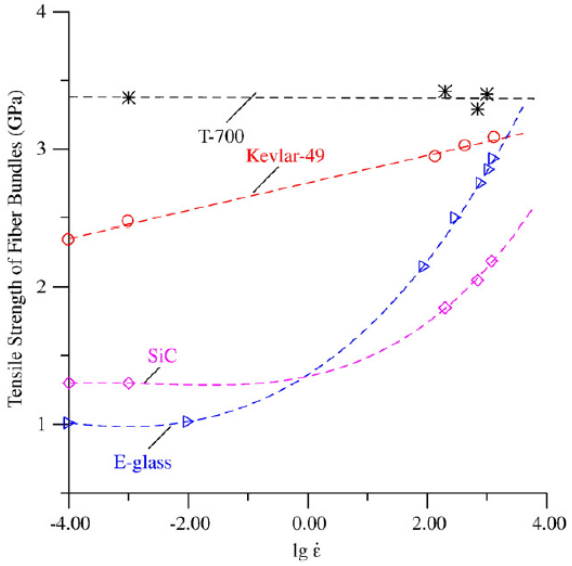

Figure 2.9: Tensile strength *vs.* strain rate for carbon, Kevlar-49, SiC and E-glass fibre bundles [86].

2.6.2 Strain rate sensitivity of matrix materials

Several examples of experimentally derived high strain rate properties of epoxy resins exist in literature, with most tests being conducted using the SHPB or SHTB apparatus [88]. In general, epoxy resins show increasing modulus and failure stress with increasing strain rate. For example, Figure 2.10 shows a plot of peak tensile stress against strain rate obtained from tests on an Epon 826 epoxy resin [89], where a clear strain rate sensitivity can be seen. The linear strain rate sensitivity changes slope at approximately 1×10^2 s^{-1}, which interestingly corresponds to the change from testing with a high speed hydraulic test machine to a Hopkinson bar apparatus [88].

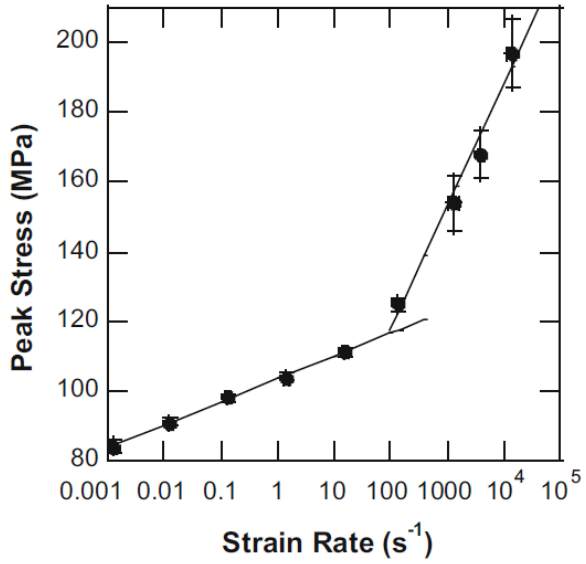

Figure 2.10: Tensile failure stress *vs.* strain rate for Epon 826 epoxy resin from [88].

The stiffness and tensile failure stress of an epoxy resin used in a CFRP material was evaluated using a SHTB at $\dot{\epsilon} = 3.6 \times 10^2$ s^{-1} in [16]. The failure stress appeared to reduce at high strain rate however, it was reported that this may have been induced by stress concentrations at the strain gauge bonding area. This finding highlights one of the obvious benefits of non-contact full-field measurements. There was also significant inertial effects seen on the stress-strain response, so interpretation of the true failure stress would have been troublesome. The stiffness was found to be strain rate sensitive, but no modulus values were identified from the stress-strain curves. Considering the high strain rates, the low wave speed in the material and the relatively-long tensile specimen length, it is unlikely that quasi-static equilibrium was established during the elastic portion of the material response.

High strain rate compression and tension tests on three different epoxy resins were conducted using the SHPB and SHTB apparatus in [90]. Increases in the compressive failure stress were reported as 79% for a Bisphenol A (BPA) resin, 72% for a modified Bisphenol A (mBPA) resin and 50% for a Bismaleimide (BMI) resin in SHPB tests conducted at $\dot{\epsilon} = 4.5 \times 10^3$ s^{-1}. However, increases on the order of 10% in the tensile failure stress were reported for all three polymers in the SHTB tests. There was a significant difference in the reported increases in the stiffness for the three materials, with 64% for the BPA, 75% for the mBPA and a large increase of 290% for the BMI resin at $\dot{\epsilon} = 2.0 \times 10^3$ s^{-1}. Difficulties were reported for some of the tensile tests, in that misalignment between the specimen and bar ends would result in bending stresses and premature specimen failure. For this reason, only the results obtained from tests where the specimen fractured in the gauge section were reported. Nevertheless, it is unknown whether a 1D state of stress was present in the tension tests and it is therefore, difficult to assess the accuracy of the complete dataset. Unfortunately the stress-strain curves were not published, so it was not possible to assess the inertial response of the SHTB system. Shear testing of epoxy resin materials using the Torsion SHB has also been conducted, with increases in modulus and failure stress with increasing strain rate reported in [91, 92].

In summary, most sources report an increase in modulus and failure stress with increasing strain rate for matrix materials. However, the magnitude of this effect is unclear given the variability in the reported data for similar epoxy resins. The extent of the strain rate sensitivity is also limited, given the strain rate restrictions imposed on the test techniques that the data was acquired from. It can be suggested that the resin dominant *i.e.* the transverse and shear properties of a composite system are rate dependent, but the net result of this effect is unclear. In the next section, the strain rate sensitivity of composite systems is reviewed.

2.6.3 Axial strain rate sensitivity of composites

The axial tensile stiffness of UD CFRP composites is mostly considered strain rate insensitive [17, 18, 93] and this is also the case for the axial compressive stiffness [54, 94, 95]. This stiffness strain-rate insensitivity is most likely due to the dominance of the carbon fibre response, which shows negligible strain rate dependence between $\dot{\epsilon} = 1 \times 10^{-3}$ and 1.3×10^{3} s^{-1}, as previously shown in Figure 2.9. However, the compressive failure stress of CFRP composites does show strain rate sensitivity. In one example, the axial compressive failure stress of a CFRP composite was evaluated between $\dot{\epsilon} = 1.0 \times 10^{-2}$ and 1.0×10^{2} s^{-1} in [54]. Figure 2.11 shows the stress-strain response, where only marginal stiffness strain rate dependence was seen, however significant failure stress strain rate dependence resulted. The strain rate sensitivity in the compressive axial failure stress is explained by the structural nature of the test. As the specimen is loaded, matrix cracks develop and permit buckling of the relatively strong carbon fibres. The response of the composite system is then matrix dominated and therefore some strain rate sensitivity is expected. In [54], different test methods were used to generate the data: a servo-hydraulic test machine was used for $\dot{\epsilon} < 1.0 \times 10^{1}$ s^{-1} and a drop tower for $\dot{\epsilon} > 1.0 \times 10^{1}$ s^{-1}. In contrast, the axial tensile failure stress of CFRP composites is generally strain rate insensitive because the dominant failure mode is tensile fibre failure [17, 18, 93].

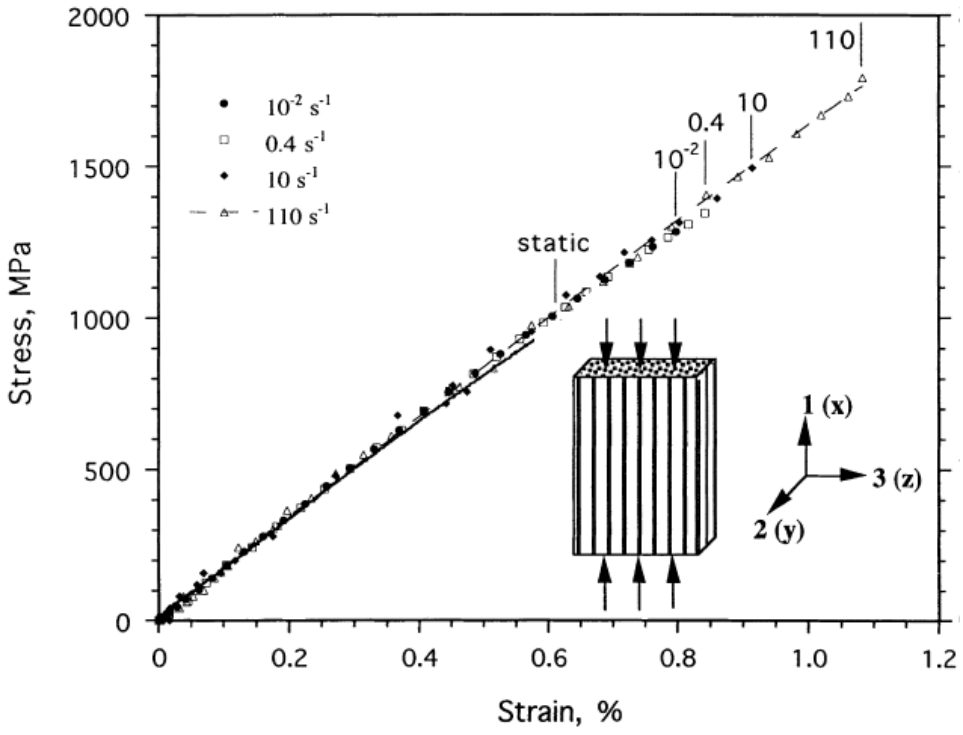

Figure 2.11: Axial compressive stress *vs.* strain response for a UD0° CFRP composite tested at different strain rates from [54].

The material considered in this report is a CFRP composite and therefore, only a general review of dynamic modulus and failure stress properties for GFRP composites is given. There is limited data available in literature on high strain rate testing of the axial properties of UD GFRP composites. Several examples assessed the strain rate sensitivity of GFRP composites with woven fibres, for example in [21, 93, 96]. These composite systems can develop 3D stresses due to the woven configuration of the fibres and therefore, will generally not be considered in this project. Most of the available high strain rate data on UD GFRP composites comes from tension tests however, there are some inconsistencies in the results. For example, an increase of 13.5% in the axial tensile stiffness was obtained from high-speed hydraulic test machine tests on a UD0° GFRP composite, where the strain rate was on the order of $\dot{\epsilon} = 8.5 \times 10^1$ s^{-1} as reported in [48]. However, tests on a similar material at a strain rate around $\dot{\epsilon} = 4.1 \times 10^1$ s^{-1} reported in [97] showed no strain rate sensitivity of the tensile axial stiffness. Some authors reported increases [48, 98] and others no change [97, 99] and therefore, there is no clear trend for the axial tensile modulus of GFRP composites reported in the literature.

With the exception of tests conducted at a low strain rate of $\dot{\epsilon} = 2.0 \times 10^1$ s^{-1} in [99], most examples in literature report an increasing axial tensile failure stress strain rate sensitivity for GFRP composites [48, 97, 98, 100]. This may be due to the fibre dominant response in axial tests, with the individual glass fibres being more strain rate dependent than carbon fibres. However the extent of the increase is again unclear. For example, Figure 2.12 shows the axial failure stress against strain rate from [100], where a step-change in the failure stress can be seen from the results generated with a pneumatic test machine at $\dot{\epsilon} = 1.0 \times 10^1$ s^{-1} to that generated with a SHTB at $\dot{\epsilon} = 7.0 \times 10^2$ s^{-1}. Therefore, it is not clear whether the increasing rate sensitivity is a true material effect, or a result of the quasi-static equilibrium assumption being violated in the split-Hopkinson bar tests. In summary, results presented in literature provide no clear indication of the magnitude of the axial tensile stiffness or failure stress rate sensitivity of GFRP composites.

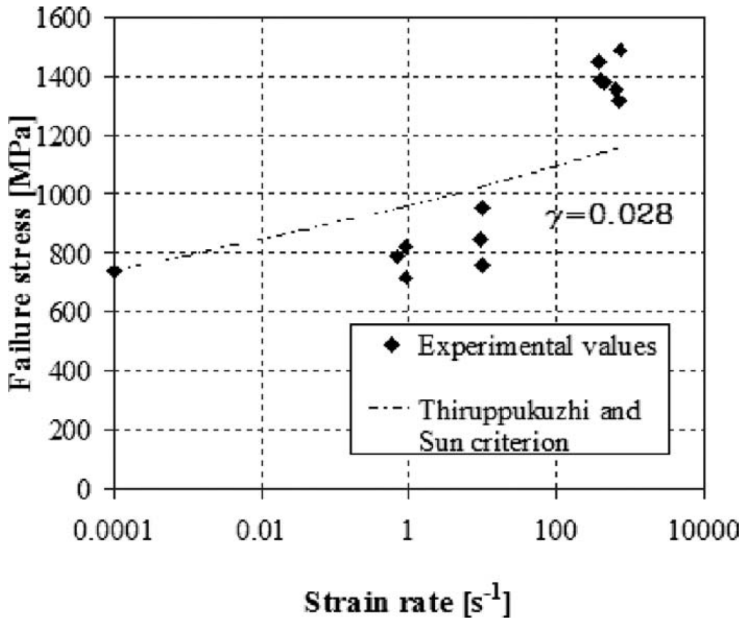

Figure 2.12: Axial tensile failure stress *vs.* strain rate for a UD0° GFRP composite in [100].

2.6.4 Transverse strain rate sensitivity of composites

Figures 2.13 (a) and (b) provide a summary of the in-plane transverse tensile and compressive modulus and failure stress rate sensitivities, respectively, for CFRP composites reported in literature. For both figures, the vertical axis is the percentage change in the dynamic to quasi-static material property (modulus or failure stress), where no change is equal to zero. Circular and square markers give results

for tension and compression tests, respectively, while error bars show the extent of measurement variation if reported. Figure 2.13 (a) shows the percentage change in dynamic transverse modulus relative to quasi-static values, where the range of variation in the reported data, or 'scatter' on the order of 30% can be seen between $\dot{\epsilon} \approx 1 \times 10^{-3}$ and 1×10^{2} s^{-1}. Above $\dot{\epsilon} = 1 \times 10^{2}$ s^{-1}, the scatter increases to around 60% (-20% to +40%) due to the decreasing transverse stiffness rate sensitivity reported in [19].

(a) Transverse modulus.

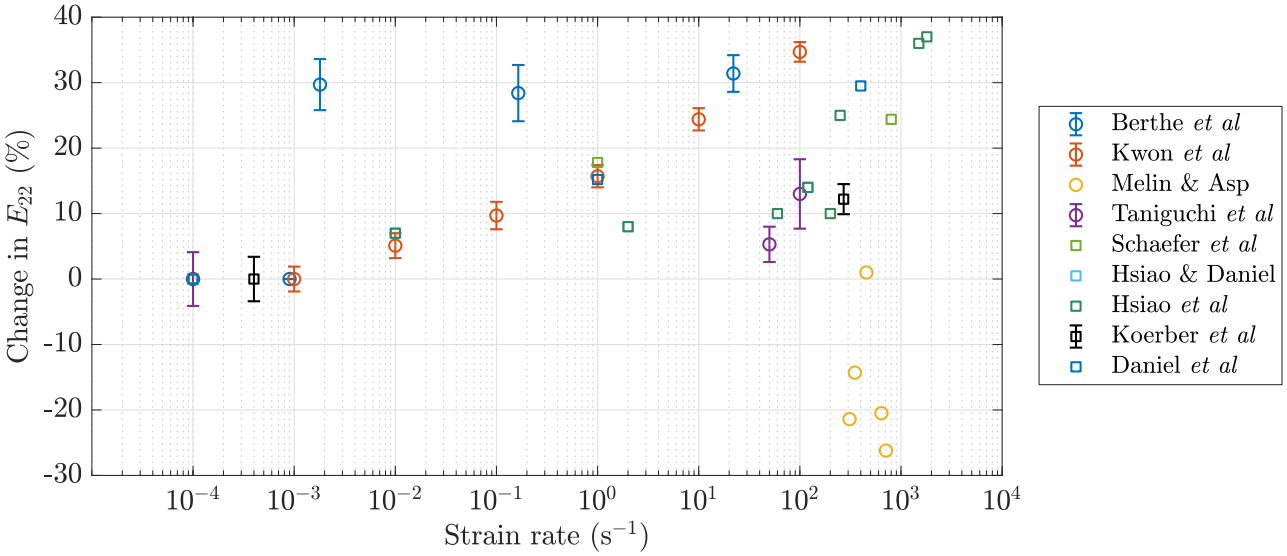

(b) Transverse failure stress.

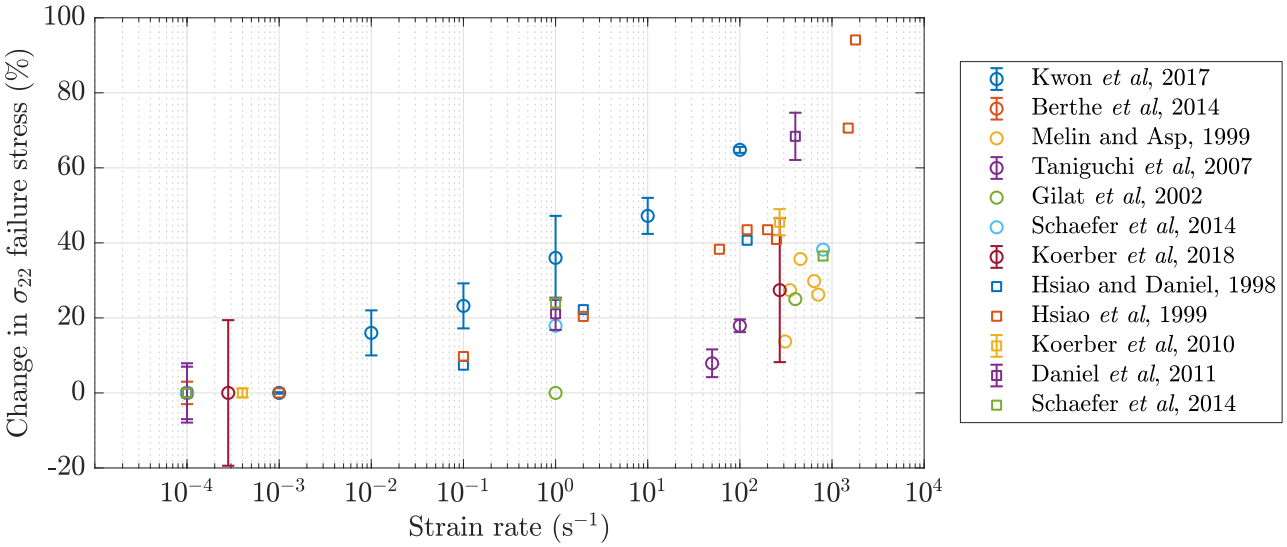

Figure 2.13: Percentage change in the dynamic to quasi-static in-plane transverse (a) modulus and (b) failure stress *vs.* strain rate for UD90° CFRP composites. Circular markers show tension test results and square markers show compression results from [16–20, 53, 54, 59, 95, 101, 102].

In some investigations, the transverse tensile modulus increased with increasing strain rate [17, 18] and in others it was unchanged [20] or decreasing [19]. Some of the possible reasons for the inconsistency in the reported transverse modulus values include testing at different strain rates, testing different materials and specimen geometries. However, there is still considerable scatter in the reported results for CFRP composites evaluated at similar strain rates. The main reason for the scatter is thought to be due to the requirement to assume quasi-static equilibrium in the specimen, in order to infer the stress from remote strain gauges in the Hopkinson bar, or the load cell in high speed hydraulic test machines. This assumption is further complicated when testing long slender tensile specimens

under dynamic loads. With some tests coming from the SHTB apparatus and some from high speed hydraulic test machines, significant variation in the results is therefore expected. Results in literature regarding the transverse compressive modulus are somewhat more consistent, with many examples reporting increasing strain rate sensitivity [53, 54, 59, 101]. However, there is significant variation in the reported strain rate sensitivity magnitude and this is again probably caused by the quasi-static equilibrium assumption being violated at higher strain rates. Therefore, it is not surprising that the majority of dynamic transverse modulus data for CFRP composites reported in literature is limited to strain rates under 1×10^3 s^{-1}. In consideration of the scatter in the data, it is difficult to quantitatively assess the strain rate dependence of the transverse modulus for CFRP composites.

The strain rate sensitivity of the transverse tensile and compressive failure stress of CFRP composites reported in literature is shown in Figure 2.13 (b). Here, an increasing trend in the transverse failure stress with respect to increasing strain rates can be seen, which was presumably due to the dominance of the strain-rate sensitive matrix. There was approximately 30% scatter in the reported values at $\dot{\epsilon} \approx 1 \times 10^2$ s^{-1}, which may be a result of inertial effects present in the high-speed hydraulic test machine experiments. Above $\dot{\epsilon} \approx 1 \times 10^2$ s^{-1}, the scatter diverges to approximately 60%. This increased scatter is presumably caused by quasi-static equilibrium in the specimen not developing and consequently reducing results accuracy in the split-Hopkinson bar tests. Therefore, it is again not clear whether the reported rate sensitivities are true material properties. Overall, there was considerable scatter in the reported transverse modulus and failure stress values, which was likely caused by violation of the quasi-static equilibrium assumption required in the split-Hopkinson bar and high-speed hydraulic test machine experiments. Uncertainty in the results accuracy coming from the current test methods means that the extent of the transverse modulus and failure stress strain-rate sensitivity for FRP composites is ambiguous. In the next section, the shear modulus and failure stress strain-rate sensitivity of FRP composites is reviewed.

2.6.5 Shear strain rate sensitivity of composites

High strain rate in-plane shear modulus and failure stress properties of composites are typically obtained using UD45° or MD±45° specimens. The high strain rate shear stress-strain behaviour for composites is initially linear until the composite begins to form damage, at which point the response becomes non-linear. For example in [32], the onset of non-linearity was characterised for a MD±45° CFRP composite at $\dot{\epsilon} = 5 \times 10^1$ s^{-1}. Generally speaking, shear failure stress magnitudes are higher for MD±45° samples compared to a UD45° configuration because of the additional structural support of the -45° laminae. Shear modulus and failure stress strain-rate dependencies for MD±45° composites can be different to that for UD45° composites, for example in [18]. A review of the shear modulus and failure stress data for CFRP and GFRP composites is given in [103], showing a generally increasing trend with increasing strain rate coming from the different test methods (split-Hopkinson bar, high-speed hydraulic test machine, drop-weight tower) in tension and compression. Torsion split-Hopkinson bars can be used to evaluate the shear properties of composites [104] and offer the advantage of no wave dispersion when testing thin cylindrical specimens [22]. However, manufacturing the cylindrical specimens for torsion Hopkinson bar tests is complex and such specimens are likely to be unrepresentative of the same material in plate form, especially for FRP composites.

Figure 2.14 (a) shows the percentage change in dynamic to quasi-static shear modulus for UD45° CFRP composites as reported in literature. Most of the data comes from compression tests using a SHPB [53, 101, 105] with one source using a drop tower apparatus [54]. Only one reference reported values from tension tests using a high speed hydraulic test machine [18]. The strain rate sensitivity appears to increase linearly from $\dot{\epsilon} = 1 \times 10^{-2}$ s^{-1}, where scatter of approximately 30% is present in the results at $\dot{\epsilon} \approx 1 \times 10^2$ s^{-1}. One of the complications of testing off-axis specimens in compression is that the friction at the specimen/bar interface prevents specimen end rotation because

of the compression/shear coupling during loading. In [105] this was assessed by checking that the y-axis displacements were the same at each end of the specimen. However, specimen rotation was not reported in [53, 101] and may have contributed to the increased values because friction can have a stiffening effect. In general, there is more available data for the in-plane shear failure stress of UD45° CFRP composites, as shown in Figure 2.14 (b). An increasing trend in the failure stress strain-rate sensitivity can be seen, but a divergence of approximately 30% occurs at $\dot{\epsilon} \approx 1 \times 10^1$ s^{-1}. The increased scatter is thought to be caused by inertial effects, which prevent quasi-static equilibrium evolving in the specimen and limit results accuracy in current experimental techniques.

(a) Shear modulus.

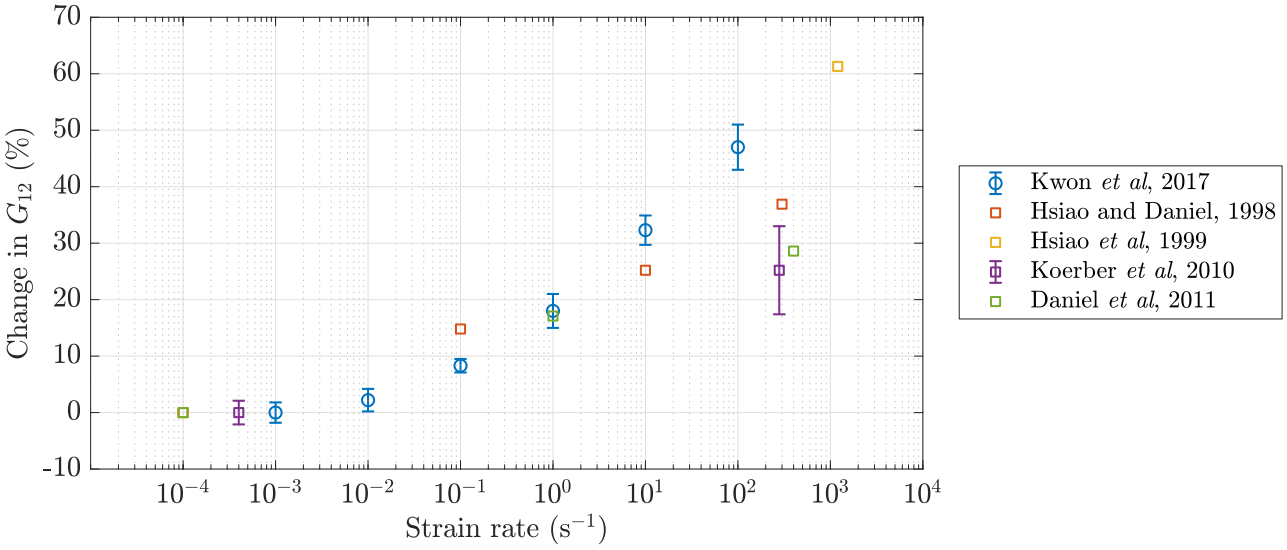

(b) Shear failure stress.

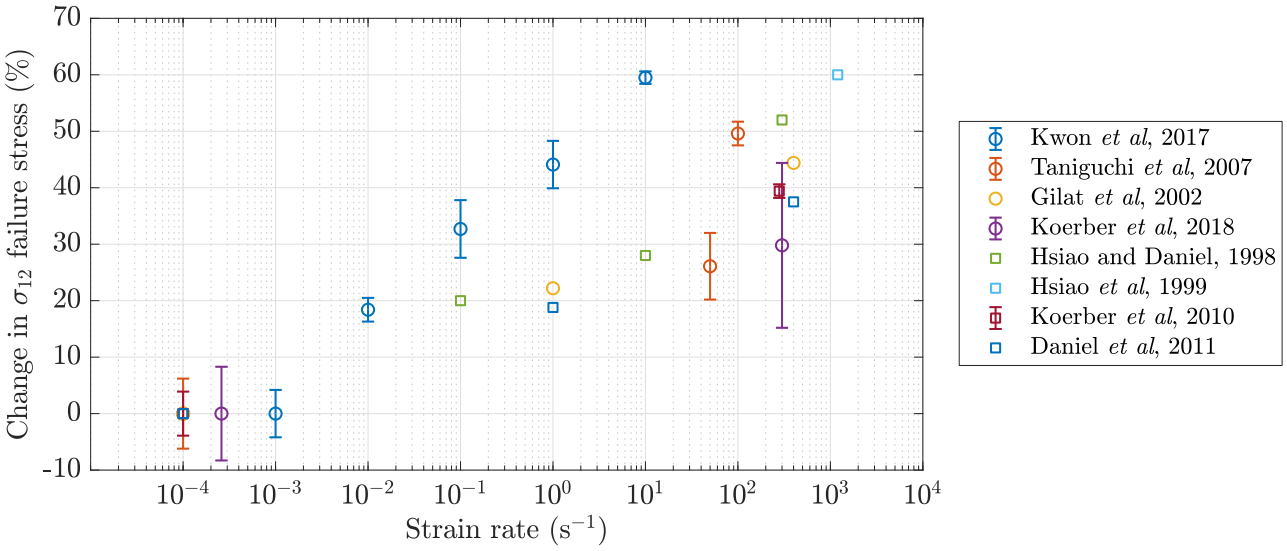

Figure 2.14: Percentage change in the dynamic to quasi-static in-plane shear (a) modulus and (b) failure stress *vs.* strain rate for UD45° CFRP composites. Circular and square markers show tension and compression results, respectively, from [16–18, 20, 53, 54, 59, 95, 101, 102].

The percentage change in dynamic to quasi-static shear modulus for MD±45° CFRP composites reported in literature is shown in Figure 2.15 (a). A significant discrepancy in the results presented in Figure 2.15 (a) is seen, with [18] reporting insignificant variation and [20] showing a 30% increase in the shear modulus strain-rate sensitivity for a similar material, test machine and strain rate. One of the differences between the tests was that the specimen gauge lengths were different, which could

have increased the time for quasi-static equilibrium to evolve in the specimen. From the available data, there was an increasing trend in the strain rate sensitivity however, scatter in the results at $\dot{\epsilon} = 1 \times 10^2$ s^{-1} was on the order of 80%. Therefore, the exact magnitude of the shear modulus strain-rate sensitivity is not clear. The shear failure stress stain-rate sensitivity for MD±45° CFRP composites is given in Figure 2.15 (b) and shows an increasing trend, with a maximum scatter around 70% at $\dot{\epsilon} = 1 \times 10^2$ s^{-1}. No clarity in the exact magnitude of the increase in shear failure stress with increasing strain rate is obvious. However, the shear failure strength of MD±45° composites involves inter-laminar effects dependent on the architecture of the laminate. Therefore, the failure stress can only be considered an apparent failure stress. In summary, significant scatter in the reported shear modulus and failure stress values for CFRP composites was seen at $\dot{\epsilon} \approx 1 \times 10^2$ s^{-1}. Some of the causes for the scatter have been identified as increased friction in compression tests and increased time for quasi-static equilibrium to evolve in longer tension specimens. However, increased scatter is present in both compression and tension tests and therefore, quasi-static equilibrium not evolving in the specimen is likely to be the main cause for the discrepancy.

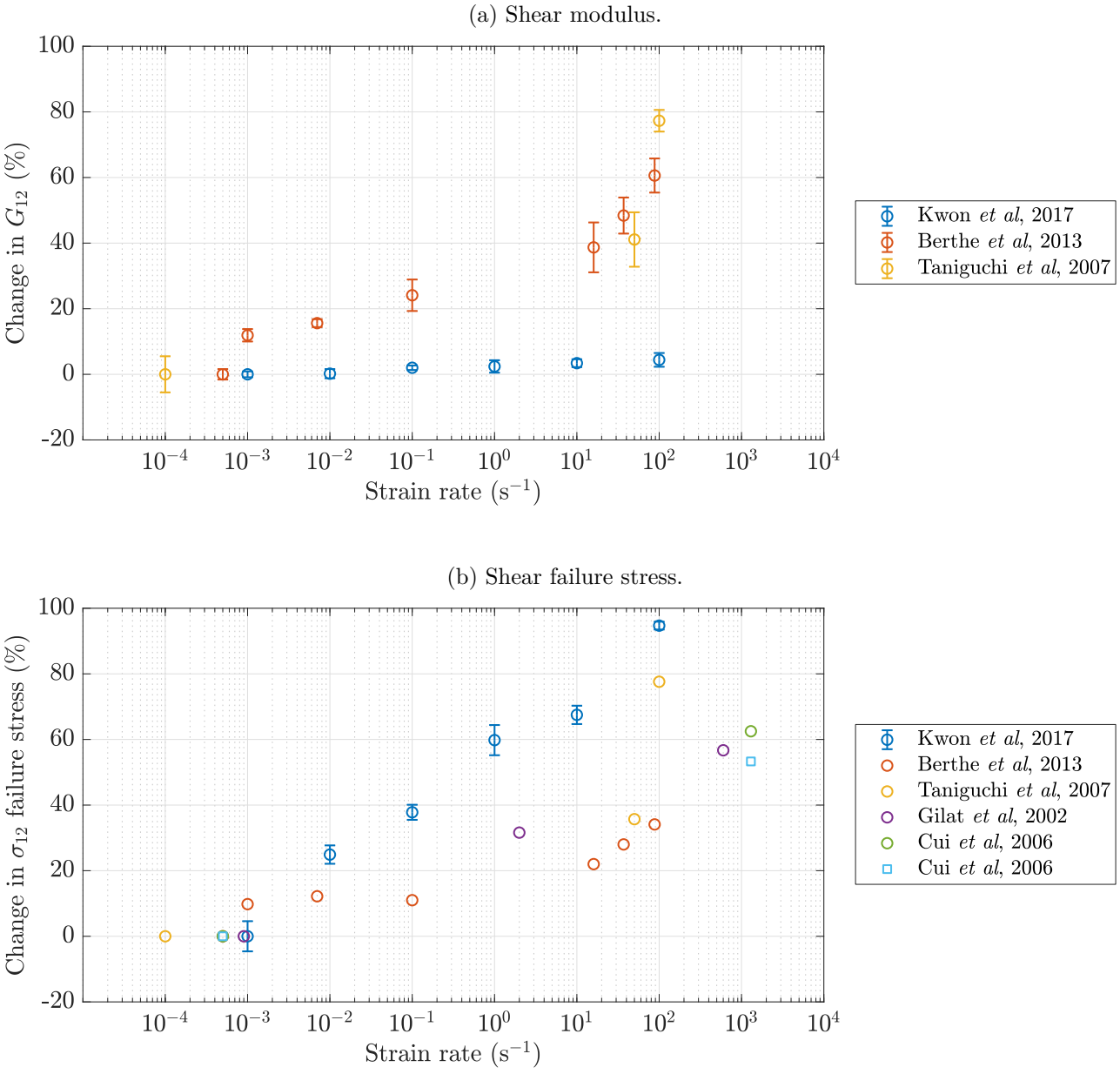

Figure 2.15: Percentage change in the dynamic to quasi-static shear (a) modulus and (b) failure stress *vs.* strain rate for MD±45° CFRP composites. Data collated from [16–18, 20, 106].

The shear failure stress for GFRP composites is mostly considered strain rate dependent, as summarised in [103] and shown in Figure 2.16. High strain-rate shear modulus data for UD45° or MD±45° GFRP composites with UD fibres (not woven or plain weave) is limited because usually, only the failure stress values are reported, *e.g.* in [107–109]. In [110], a negative shear stiffness strain rate sensitivity for a MD±45° GFRP composite was reported. However, positive shear stiffness strain rate sensitivities were reported in [21, 93] although these composites used woven glass fibres. Given the differences between UD and woven fibre composites, it is difficult to decipher trends in the shear stiffness strain rate sensitivity for GFRP composites.

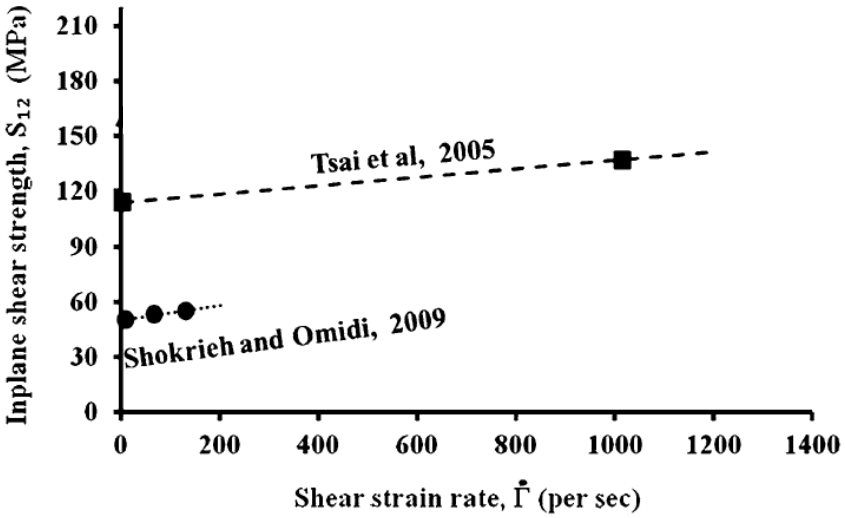

Figure 2.16: Shear failure stress *vs.* strain rate results for GFRP composites from different authors reported in [103].

On the whole, there is a reasonable amount of data on the high strain rate shear properties of composites that suggests an increase in stiffness and failure stress with loading rate. However, the data shows considerable scatter even when differences in material systems are taken into account. Furthermore, there is a lack of high strain rate data that can be used to accurately populate the in-plane failure stress envelope for composites at strain rates greater than 1×10^3 s^{-1}. Literature on tests aimed at populating FRP composite failure envelopes is discussed in the next section.

2.6.6 High strain rate failure envelopes

In literature, there is a reasonable amount of high strain rate in-plane failure envelope data for FRP composites, as compiled in [111]. Usually UD90° specimens are used to populate the normal stress locations and off-axis 15°, 30°, 45°, 60° and 75° specimens can be used to populate the combined stress regions of the failure envelope. Results reported in literature show a generally increasing trend in the strain rate sensitivity of CFRP [59, 95, 101] and GFRP [107–109] composite failure envelopes. Most of the high strain rate failure envelope data comes from compression tests made with the SHPB. Only one example was found to have reported dynamic tension failure envelope data [102], however restrictions on SHTB test conditions were the possible cause for reporting data at relatively low strain rates around $\dot{\epsilon} \approx 3.0 \times 10^2$ s^{-1}.

There are a number of concerns with populating failure envelopes using Hopkinson bar data. Firstly, the tensile portion of the curve is usually not characterised, but rather extrapolated from quasi-static data that is not experimentally validated. This is shown in the failure envelope in Figure 2.17, where

no high strain rate data points are given on the tension/shear side of the graph. A follow-on problem from the lack of tensile data is that extrapolation, rather than interpolation methods have been used to predict the pure shear response on the failure envelope, as in [59, 108]. Another assumption used when generating failure envelope data with axial measurements is that Poisson's ratio and the shear coupling coefficients used in strain transformations are not significantly affected by strain rate, as mentioned in [101]. However, the main problem with using current high strain rate techniques to populate failure envelopes is that only axial stress values are considered. Rotation equations transform the axial data into the material coordinates for population of the failure envelope, however there is currently no way to experimentally validate these results.

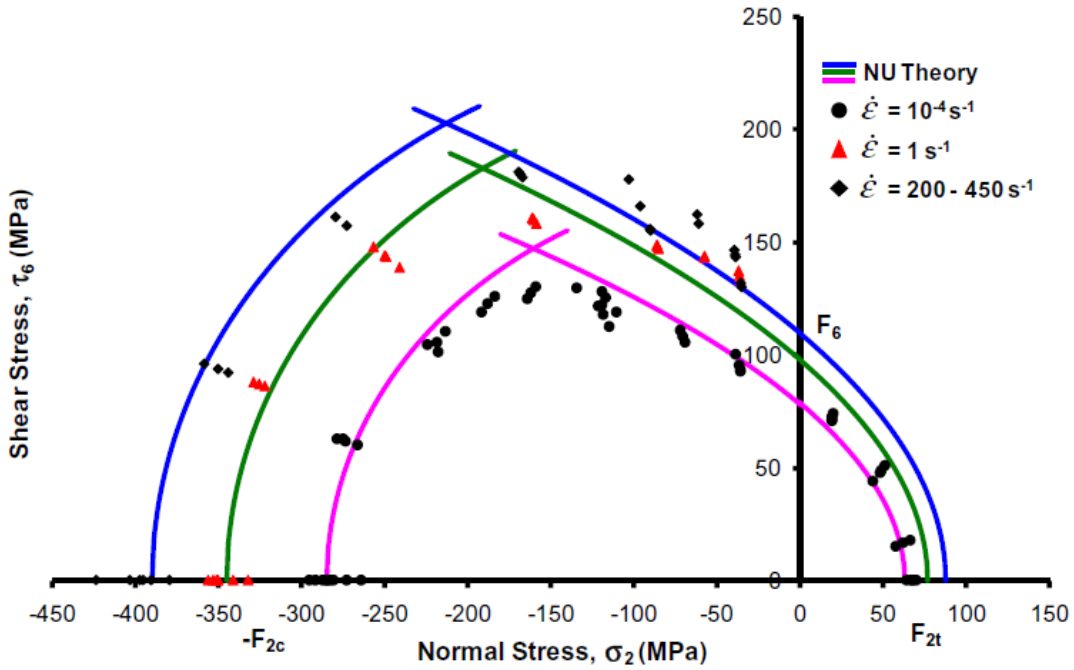

Figure 2.17: Failure envelope constructed from UD15°, UD30°, UD45°, UD60°, UD75° and UD90° composite specimens at quasi-static and dynamic strain rates in [101].

The overarching aim of the World Wide Failure Exercise (WWFE) was to benchmark failure theories in their ability to predict failure in composites. In the first WWFE, five theories were assessed against experimental test cases involving 2D in-plane bi-axial load cases. One of the results of the exercise was that none of the theories could predict final failure to within ±50% of the experimentally measured values, in more than 75% of the test cases [112]. Failure models identified during the WWFE have been extended to predict composite failure under dynamics loads, such as the Northwestern failure theory (abbreviated as NU Theory in Figure 2.17) [101]. A failure theory's ability to accurately predict failure hinges largely on the accuracy of the experimentally derived data used for the model parameters. Considering the previously discussed scatter in the dynamic properties of composites, it is unknown whether current theories will be able to accurately predict dynamic damage in composites. One of the primary goals of the second WWFE was to accurately predict the response of composites subjected to extreme loads such as blast and penetration [113]. Given that the strain rates in these scenarios are on the order of several thousand s^{-1} and that current data is limited to under 1×10^3 s^{-1}, there is an urgent need to utilise test methods without strain rate limitations to derive high strain failure envelope data for use in failure models.

In general, most of the high strain rate failure envelope data has been generated with the SHPB technique. This means the tension/shear portion of the failure envelope is not validated experimentally and the strain rates are limited to a few hundred s^{-1}. Having considered the material response of orthotropic composites and the strain rates applicable in their engineering applications, there is a clear need to generate accurate composite failure envelope data at strain rates around 1×10^3 s^{-1}.

2.7 Summary

This literature review has assessed a number of themes relevant to the high strain rate properties of FRP composites. A summary of the key findings in the literature and how they relate to the overall aim of this project are listed below:

1. Significant scatter in the high strain rate transverse and shear modulus properties of FRP composites exists in literature. This scatter is thought to be caused by the violation of assumptions required for accurate results with the use of current experimental techniques. This problem will be addressed by developing different IBII test specimen configurations for transverse and shear modulus identification. Methods used to identify the modulus values will be validated across a range of laminate configurations so that an accurate dataset can be obtained. This accurate dataset will then be compared to the in-literature values to confirm some of the suspected causes of scatter.

2. Current experimental techniques are not suitable to generate reliable high strain rate failure stress data for FRP composites. In this project, full-field measurements obtained from IBII tests will be used in the VFM to derive accurate transverse failure stress data for a UD90° CFRP composite material, at strain rates on the order of 1×10^3 s^{-1}. Similar to the modulus investigation, the failure stress results from this experimental campaign will then be compared to in-literature values and reasons for the scatter will be discussed.

3. To date, the Grid Method has been used for calculating displacement fields in the IBII test, mainly because of its improved spatial resolution compared to other full-field techniques such as DIC. However, in certain industrial settings DIC may be the preferred full-field measurement technique selected for a material identification campaign. Therefore, in this project the differences between modulus properties identified from off-axis composites evaluated in IBII tests with DIC and Grid Method derived displacements will be quantified. Results from this investigation will add to the versatility of the IBII technique.

Chapter 3

Theory

This chapter derives equations used in the VFM to obtain in-plane modulus and failure stress properties of off-axis composites. It begins with a discussion of the principle of virtual work applicable to the geometry of an IBII test specimen. Next, the constitutive model selected for the composite material analysed in this project is derived. Equations that include virtual fields and full-field measurements in the principle of virtual work are then given. This process results in equations describing stress averages over vertical and angled slices on the specimen's surface. Finally, the modulus and failure stress identification procedures are described.

3.1 The VFM

There are a number of assumptions made in this application of the VFM, which are listed below:

1. The specimen is in a state of 2D plane stress.
2. The kinematic fields are constant through-the-thickness of the specimen.
3. The specimen thickness is constant.
4. The specimen density is constant in both space and time.

Assumption 1 can be applied because the test sample's thickness is small relative to its length and height, as shown in Figure 2.6 of Chapter 2. Assumptions $2-3$ are presumed to occur under assumption 1 [114] however, variations in the through-thickness kinematics that may occur are assumed to be negligible. In this project, this requirement must be made because the full-field measurement techniques only measure surface displacements on one side of the sample. When the kinematic fields vary more significantly through the thickness of the sample (*e.g.* under misaligned impact conditions), back-to-back imaging can be applied [115]. The question of whether assumption 3 can be applied is easily assessed by measuring the sample thickness at a number of locations over its length and ensuring that the thickness variation is low. For all samples evaluated in this project, the variation in thickness was under 1.6%. The assumption of constant density is not completely necessary, but is employed as significant density variations or shock conditions are not expected. If necessary, the density can be updated based on the measured strains, *e.g.* in [116]. If we apply the aforementioned assumptions and neglect body forces, then the principle of virtual work given in Equation 2.2 of Chapter 2 can be written in 2D as follows:

$$-\int_S \boldsymbol{\sigma} : \boldsymbol{\epsilon}^* \, dS + \int_l \boldsymbol{T} \cdot \boldsymbol{u}^* \, dl = \rho \int_S \boldsymbol{a} \cdot \boldsymbol{u}^* \, dS \tag{3.1}$$

where all the terms are the same as described in Section 2.3.1, but in this instance the integrals are applied over the specimen surface area S and the specimen perimeter l. Lastly, the tensorial and vectorial fields are functions of both space and time, but the function notation has been omitted here for ease of writing the equations.

Two types of virtual fields can be used for stiffness identification. The first approach is to select virtual fields that cancel the external virtual work term at the impact edge and relate the internal virtual work to the acceleration virtual work in the specimen. With an appropriate constitutive model, generic virtual fields can be applied to identify the stiffness tensor over the specimen surface for each time step. The second approach is to use rigid body virtual fields (with zero virtual strains) that cancel the internal virtual work and relate the external virtual work to the acceleration virtual work. This results in equations that relate stress averages for each position on the specimen length to accelerations over the specimen surface. A constitutive model is assumed and the stiffness is identified by plotting the average stress against the average strain. The second approach therefore gives the stiffness as a function of the specimen length, for each time step. With the second approach, the non-linear response in the shear stress-strain curves can be observed without assuming a constitutive law for the material (for uniform field distributions on slices) and will therefore be the focus of this report.

The VFM for failure stress identification is more involved. Heterogeneous strain fields resulting from dynamic loads on impact specimens can lead to stress states that initiate fracture locally. Rigid body virtual fields generate stress values that are averaged over the height of the specimen and are therefore not suitable for deriving the failure stress. For this reason, a linear approximation of the stress distribution in the specimen is required to identify the failure stress. Before discussing how Equation 3.1 can be used with rigid body virtual fields for stiffness and failure stress identification, we will briefly consider the constitutive models that are relevant for the UD composites considered in this work.

3.2 Constitutive model

Transverse composite specimens

Consider the transverse composite specimen shown in Figure 3.1 (a), subjected to the axial force $F_x(t)$ in the global (x−y) coordinate system. Here, we will assume a linear elastic orthotropic constitutive model, which is generally suitable for UD fibre composites. For this material, the only component that is expected to include any non-linearity is the shear term. As described in [54], this non-linearity is reduced with strain rate, so there should be an appreciable portion of the shear loading that is linear elastic. The derivation of the constitutive law for a transverse composite is described in [29], however the derivation is recalled here in material coordinates because it leads into the derivation for the off-axis composite. Under 2D plane stress conditions, the constitutive relationship is:

$$\begin{bmatrix} \sigma_{22} \\ \sigma_{11} \\ \sigma_{12} \end{bmatrix} = \begin{bmatrix} Q_{22} & Q_{12} & 0 \\ Q_{12} & Q_{11} & 0 \\ 0 & 0 & Q_{66} \end{bmatrix} \begin{bmatrix} \epsilon_{22} \\ \epsilon_{11} \\ \gamma_{12} \end{bmatrix} \tag{3.2}$$

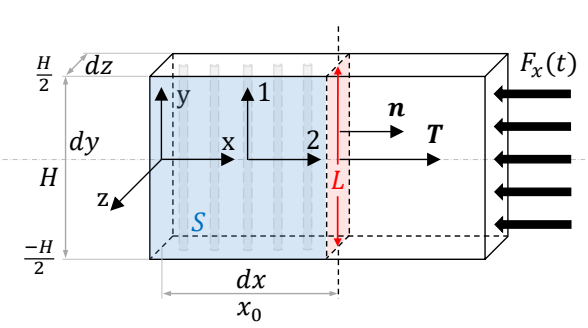

(a) Traction vector $\boldsymbol{T}$ and and normal vector $\boldsymbol{n}$ acting on a vertical slice L made at the distance x_0 from $x = 0$ on the specimen of height H.

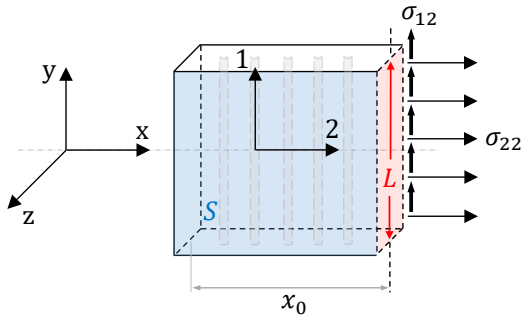

(b) Transverse stress σ_{22} and shear stress σ_{12} components acting on the vertical slice.

Figure 3.1: Schematic representing the transverse specimen impacted with the force $F_x(t)$, showing the global (x−y) and material (2−1) coordinate systems.

As the impact loading is aligned with the 2−axis, the transverse stress component will be most significant and therefore, the 2−axis stresses are analysed. Matrix multiplication of the stiffness tensor and the strain vector in Equation 3.2 gives the stress-strain relationship for the σ_{22} component:

$$\sigma_{22} = Q_{22}\epsilon_{22} + Q_{12}\epsilon_{11} \tag{3.3}$$

where Q_{22} is the transverse stiffness and Q_{12} is the stiffness due to the Poisson effect. The elastic stiffnesses Q_{22} and Q_{12} are related to Poisson's constants through:

$$Q_{12} = \nu_{12}Q_{22} \;;\; Q_{22} = \frac{E_{22}}{1 - \nu_{12}\nu_{21}} \tag{3.4}$$

where ν_{12} and ν_{21} are the major and minor Poisson's ratios, respectively. Equation 3.3 can then be written as:

$$\sigma_{22} = Q_{22}(\epsilon_{22} + \nu_{12}\epsilon_{11}) \tag{3.5}$$

Axial impact of the transverse composite results in low 1−axis (*i.e.* fibre) strains. Nevertheless, the fibre axis strain ϵ_{11} can be proportioned into the strain induced by the Poisson effect and the strain due to σ_{11} as in:

$$\sigma_{22} = Q_{22}(\epsilon_{22} + \nu_{12}({\epsilon_{11}}^{(P)} + {\epsilon_{11}}^{(\sigma_{11})})) \tag{3.6}$$

The elastic constant relationships in Equation 3.4 can then be used to approximate the fibre strains due to the Poisson effect through ${\epsilon_{11}}^{(P)} = -\nu_{21}\epsilon_{22}$. Thereafter, ϵ_{22} is factorised and the relationships for Q_{22} are again included as:

$$\begin{aligned} \sigma_{22} &= Q_{22}(\epsilon_{22} + \nu_{12}(-\nu_{21}\epsilon_{11} + {\epsilon_{11}}^{(\sigma_{11})})) \\ &= E_{22}\epsilon_{22} + Q_{12}{\epsilon_{11}}^{(\sigma_{11})} \end{aligned} \tag{3.7}$$

Because of the high stiffness of the carbon fibres, the contribution of ${\epsilon_{11}}^{(\sigma_{11})}$ is expected to be small and can therefore be neglected for the 2−axis stress in transverse specimens:

$$\sigma_{22} = E_{22}\epsilon_{22} \tag{3.8}$$

Validation of the constitutive law was performed in [29], where the elastic moduli obtained with Equation 3.8 were less than 1% of the reference values.

Characterisation of the shear modulus can be obtained from IBII tests on transverse composite samples that generate a relatively strong shear response. The strength of the shear response can depend on the how the load is introduced to the sample (see Chapter 4). Matrix multiplication of the shear response in Equation 3.2 gives the constitutive relationship for the shear component:

$$\sigma_{12} = Q_{66}\gamma_{12} \tag{3.9}$$

where Q_{66} is the in-plane shear modulus G_{12} and γ_{12} is the engineering shear strain in material coordinates equal to $2\epsilon_{12}$. Next, the derivation for the constitutive relationship for an off-axis composite specimen is described.

Off-axis composite specimens

Consider the impact of an off-axis specimen as shown in Figure 3.2 (a) with the 1-axis aligned with the fibres at an angle θ to the x-axis, and the 2-axis perpendicular to the 1-axis. In the material coordinate system, the constitutive relationship for an off-axis composite is:

$$\begin{bmatrix} \sigma_{11} \\ \sigma_{22} \\ \sigma_{12} \end{bmatrix} = \begin{bmatrix} Q_{11} & Q_{12} & 0 \\ Q_{12} & Q_{22} & 0 \\ 0 & 0 & Q_{66} \end{bmatrix} \begin{bmatrix} \epsilon_{11} \\ \epsilon_{22} \\ \gamma_{12} \end{bmatrix} \tag{3.10}$$

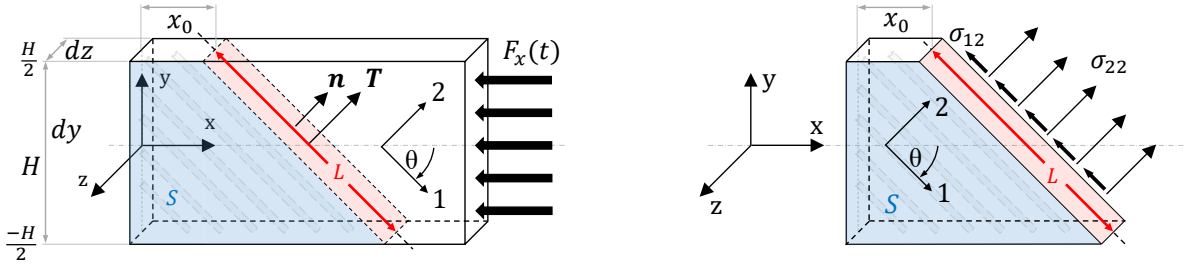

(a) Traction vector $\boldsymbol{T}$ and and normal vector $\boldsymbol{n}$ acting on L made at the distance x_0 from $x = 0$ on the specimen of height H.

(b) Normal stress σ_{22} and shear stress σ_{12} components acting on L.

Figure 3.2: Schematic representation of the off-axis specimen impacted with the force $F_x(t)$ with the material 1−axis rotated clockwise from the global x−axis. Here, S is the surface area on the specimen from the free edge to the angled slice L.

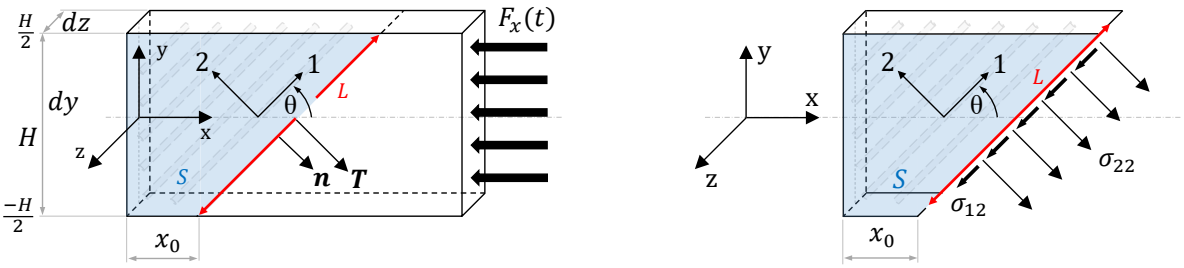

(a) Traction vector $\boldsymbol{T}$ and and normal vector $\boldsymbol{n}$ acting on L made at the distance x_0 from $x = 0$ on the specimen of height H.

(b) Normal stress σ_{22} and shear stress σ_{12} components acting on L.

Figure 3.3: Schematic representing the off-axis specimen impacted with the force $F_x(t)$ with the material 1−axis rotated counter-clockwise from the global x−axis. Again, S is the surface area on the specimen from the free edge to the angled slice L.

Both the transverse and shear response of off-axis composites will be considered here. The transverse stress relationship is obtained by matrix multiplication in Equation 3.10 as:

$$\sigma_{22} = Q_{12}\epsilon_{11} + Q_{22}\epsilon_{22} \tag{3.11}$$

A similar approach to derive the constitutive relationship for the transverse composite is then used, assuming that the stiffness in the fibre direction Q_{11} is high and the strains due to stresses in the fibre direction are negligible. The constitutive relationship for the transverse response of the off-axis composite is:

$$\sigma_{22} = E_{22}\epsilon_{22} \tag{3.12}$$

Similar to the transverse samples, matrix multiplication of the shear response in Equation 3.10 gives the constitutive relationship for the shear component in off-axis samples:

$$\sigma_{12} = Q_{66}\gamma_{12} \tag{3.13}$$

where again, Q_{66} is the in-plane shear modulus G_{12} and γ_{12} is the engineering shear strain in material coordinates equal to $2\epsilon_{12}$. In this section, the transverse and shear constitutive relationships for the off-axis composite were derived. In the next section, these constitutive laws will be used with the VFM for modulus identification.

3.3 Virtual fields for modulus identification

Previous implementations of the IBII test used rigid body virtual fields for stiffness and failure stress identification of composite materials [27, 29]. In this section, rigid body virtual fields are applied in the VFM to identify both the transverse and shear moduli from transverse and off-axis composite samples in material coordinates.

3.3.1 UD90° samples: transverse component

Consider the UD90° composite specimen in Figure 3.1 (a). Here we apply the rigid body virtual field describing a rigid translation along the material 2−axis:

$$\begin{cases} u_2^* &= 1 \\ u_1^* &= 0 \end{cases} \quad \begin{cases} \epsilon_{22}^* &= 0 \\ \epsilon_{11}^* &= 0 \\ \epsilon_{12}^* &= 0 \end{cases} \tag{3.14}$$

For this rigid body virtual field the virtual strain field is null, cancelling the contribution of the internal virtual work term. This virtual field can now be substituted into the principle of virtual work in Equation 3.1 as follows:

$$\int_L \boldsymbol{T} \cdot \begin{bmatrix} 1 \\ 0 \end{bmatrix} \, dL = \rho \int_S \boldsymbol{a} \cdot \begin{bmatrix} 1 \\ 0 \end{bmatrix} \, dS \tag{3.15}$$

with the only non-zero tractions on the specimen perimeter l acting on the slice L. Now consider the free body diagram showing a vertical slice on the impacted specimen in Figure 3.1 (a). This gives the traction vector $\boldsymbol{T}$ and the normal vector $\boldsymbol{n}$, acting in the 2−axis in a direction opposing $F_x(t)$. Here, $\boldsymbol{T}$ is equal to the dot product of $\boldsymbol{\sigma}$ and $\boldsymbol{n}$ as:

$$\boldsymbol{T} = \boldsymbol{\sigma} \cdot \boldsymbol{n} = \begin{bmatrix} \sigma_{22} & \sigma_{12} \\ \sigma_{12} & \sigma_{11} \end{bmatrix} \cdot \begin{bmatrix} 1 \\ 0 \end{bmatrix} = \begin{bmatrix} \sigma_{22} \\ \sigma_{12} \end{bmatrix} \tag{3.16}$$

This relationship is then included in Equation 3.15 along with the acceleration vector components in material coordinates a_2 and a_1 as:

$$\begin{gathered} \int_L \begin{bmatrix} \sigma_{22} \\ \sigma_{12} \end{bmatrix} \cdot \begin{bmatrix} 1 \\ 0 \end{bmatrix} \, dL = \rho \int_S \begin{bmatrix} a_2 \\ a_1 \end{bmatrix} \cdot \begin{bmatrix} 1 \\ 0 \end{bmatrix} \, dS \\ \int_L \sigma_{22} \, dL = \rho \int_S a_2 \, dS \end{gathered} \tag{3.17}$$

The integrals in Equation 3.17 are then applied to the IBII test specimen over the region of interest shown in Figure 3.1 (b) as follows:

$$\int_{-H/2}^{H/2} \sigma_{22} \, dy = \rho \int_{-H/2}^{H/2} \int_0^{x_0} a_2 \, dx dy \tag{3.18}$$

During the IBII test, images of the specimen deformation are obtained with a UHSV camera and a full-field imaging technique is used to derive the kinematic fields. When using a camera to obtain full-field kinematics, a discrete number of measurement points are obtained over the specimen's surface. Therefore, the surface area of the specimen S can be discretised into smaller surface areas s^i where i is a measurement point for $i = 1 : n$, with n being the number of measurement points on S as shown in Figure 3.4. Here, the accelerations at each measurement point a^i act at the centre of each s^i. Given this discrete set of measurement points, the acceleration integral on the right hand side of Equation 3.18 can be approximated as a discrete sum (using the rectangle method) as follows:

$$
\begin{aligned}
\rho \int_{-H/2}^{H/2} \int_{0}^{x_0} a_2 \, dxdy &\simeq \rho \sum_{i=1}^{n} a_2^{(i)} \, s^{(i)} \\
&\simeq \rho \, s^{(i)} \sum_{i=1}^{n} a_2^{(i)} \\
&\simeq \rho \frac{S}{n} \sum_{i=1}^{n} a_2^{(i)} \\
&\simeq \rho \frac{H x_0}{n} \sum_{i=1}^{n} a_2^{(i)} \\
&\simeq \rho \, H x_0 \, \overline{a_2}^{S}
\end{aligned}
\tag{3.19}
$$

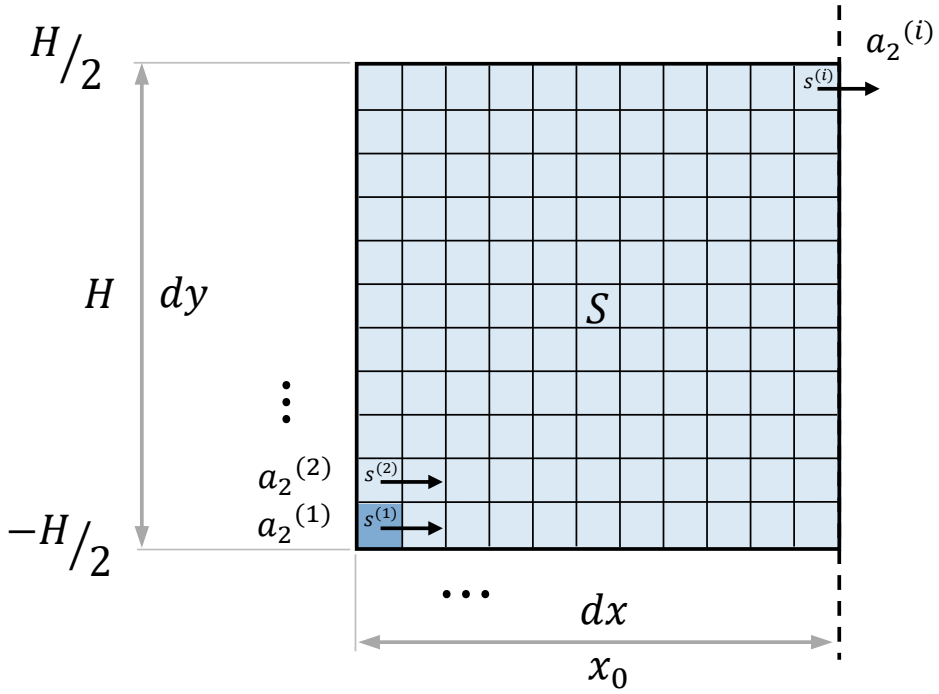

Figure 3.4: Discretised acceleration components $a_2{}^{(i)}$ acting at the centroid of each discretised surface $s^{(i)}$ over the specimen surface S.

In Equation 3.19, $\overline{a_2}^{S}$ is the average 2−axis acceleration over the area S. Note that in the rest of this document, the overline notation combined with a superscript S indicates spatial averaging over the surface of interest. In a similar way, the left-hand side of Equation 3.18 can be approximated as a discrete sum:

$$
\int_{-H/2}^{H/2} \sigma_{22} \, dy \simeq H \, \overline{\sigma_{22}}^{L} \tag{3.20}
$$

where $\overline{\sigma_{22}}^{L}$ is the 2−axis or normal stress averaged over a vertical slice on the specimen. For the transverse case samples, the overline notation combined with a superscript 'L' is used to indicate

averaging over a vertical slice. Equations 3.19 and 3.20 are then substituted back into Equation 3.18 to give the transverse 'stress gauge' equation:

$$\overline{\sigma_{22}}^{L} = \rho\, x_0\, \overline{a_2}^{S} \tag{3.21}$$

Identification of the transverse modulus E_{22} is then undertaken using the constitutive law derived previously in Equation 3.8: $\sigma_{22} = E_{22}\epsilon_{22}$, by plotting $\overline{\sigma_{22}}^{L}$ against $\overline{\epsilon_{22}}^{L}$ and linearly fitting the linear elastic part of the response.

3.3.2 UD90° samples: shear component

The shear modulus can also be identified from tests on UD90° samples where the shear response is strong. Here we utilise a rigid body virtual field describing a 1−axis translation:

$$\begin{cases} u_2^* = 0 \\ u_1^* = 1 \end{cases} \quad \begin{cases} \epsilon_{22}^* = 0 \\ \epsilon_{11}^* = 0 \\ \epsilon_{12}^* = 0 \end{cases} \tag{3.22}$$

Similar to the transverse case, the traction vector is obtained through Equation 3.16 and is applied in the principle of virtual work together with the virtual fields from Equation 3.22, giving the relationship:

$$\int_L \sigma_{12}\, dL = \rho \int_S a_1\, dS \tag{3.23}$$

Thereafter, the discretisation procedures in Equations 3.18 to 3.20 are applied to give the shear stress gauge equation for transverse composite samples:

$$\overline{\sigma_{12}}^{L} = \rho\, x_0\, \overline{a_1}^{S} \tag{3.24}$$

The shear modulus is then identified by applying the constitutive model in Equation 3.9 and fitting the linear portion of the $\overline{\sigma_{12}}^{L}$ against $\overline{\gamma_{12}}^{L}$ response. Equations 3.21 and 3.24 are valid for any transverse section of interest, so stress-strain curves can be plotted for any 'x_0' position of interest. This gives the transverse and shear elastic moduli as a function of position along the specimen length. Our goal in the next section is to derive 'stress-gauge' equations in the material coordinate system, which can be used for modulus identification from off-axis samples. This requires that all kinematic fields are first rotated from global x−y to material 1−2 coordinates, as described in the following section.

3.3.3 Off-axis case: coordinate system rotation

The global coordinate system acceleration fields can be rotated into the material coordinate system using the vector rotation matrix, as follows:

$$\begin{bmatrix} a_1 \\ a_2 \end{bmatrix} = \begin{bmatrix} cos\theta & sin\theta \\ -sin\theta & cos\theta \end{bmatrix} \begin{bmatrix} a_x \\ a_y \end{bmatrix} \tag{3.25}$$

The strain tensor can be rotated into material coordinates using:

$$\begin{bmatrix} \epsilon_{11} \\ \epsilon_{22} \\ \gamma_{12} \end{bmatrix} = \begin{bmatrix} cos^2\theta & sin^2\theta & sin\theta cos\theta \\ sin^2\theta & cos^2\theta & -sin\theta cos\theta \\ -2sin\theta cos\theta & 2sin\theta cos\theta & (cos^2\theta - sin^2\theta) \end{bmatrix} \begin{bmatrix} \epsilon_{xx} \\ \epsilon_{yy} \\ \gamma_{xy} \end{bmatrix} \tag{3.26}$$

For samples that are configured with the fibres rotated counter-clockwise to the x-axis such as that shown in Figure 3.3 (a), the angle θ used in Equations 3.25 and 3.26 is positive. Whereas, -θ is used for samples that are orientated with its fibres rotated clockwise from the x-axis, such as that shown in Figure 3.2 (a). Now that the kinematic fields are in the material coordinate system, we will combine them with the principle of virtual work using rigid body virtual fields.

3.3.4 Off-axis case: transverse component

Given the off-axis specimen configuration shown in Figure 3.2 (a), we now consider a virtual field in material coordinates describing a translation along the $2-$axis. This virtual field is similar to the previously considered rigid body virtual field applied to the transverse case, so the analysis here will be alike. The virtual field is:

$$\begin{cases} {u_1}^* = 0 \\ {u_2}^* = 1 \end{cases} \quad \begin{cases} {\epsilon_{11}}^* = 0 \\ {\epsilon_{22}}^* = 0 \\ {\epsilon_{12}}^* = 0 \end{cases} \tag{3.27}$$

In Figure 3.2 (a), the traction vector $\boldsymbol{T}$ opposes $F_x(t)$, pointing in the positive direction of the $2-$axis. Therefore, both normal vector components are positive and $\boldsymbol{T}$ is obtained by:

$$\boldsymbol{T} = \boldsymbol{\sigma} \cdot \boldsymbol{n} = \begin{bmatrix} \sigma_{11} & \sigma_{12} \\ \sigma_{12} & \sigma_{22} \end{bmatrix} \cdot \begin{bmatrix} 0 \\ 1 \end{bmatrix} = \begin{bmatrix} \sigma_{12} \\ \sigma_{22} \end{bmatrix} \tag{3.28}$$

Similar to the process applied in the transverse case, the resolved traction vector and acceleration vector components are incorporated in the principle of virtual work leading to the relationship:

$$\int_L \sigma_{22}\, dL = \rho \int_S a_2\, dS \tag{3.29}$$

The discretisation procedures in Equations 3.19 and Equation 3.20 are followed to give the transverse stress gauge equation for an off-axis composite:

$$\overline{\sigma_{22}}^L = \frac{\rho S \overline{a_2}^S}{L} \tag{3.30}$$

where $\overline{\sigma_{22}}^L$ is the average normal stress in the $2-$axis acting over an angled slice of length L, and S is the trapezoidal surface area shown in Figure 3.2 (b). Note that hereafter the overline notation combined with a superscript L will be used to indicate averaging over an angled slice in the material coordinate system.

For off-axis samples that are impacted with the the fibres rotated counter-clockwise to the x−axis as shown in Figure 3.3 (a), the normal vector 2−component points in the opposite direction of the material 2−axis and $\boldsymbol{T}$ is obtained as:

$$\boldsymbol{T} = \boldsymbol{\sigma} \cdot \boldsymbol{n} = \begin{bmatrix} \sigma_{11} & \sigma_{12} \\ \sigma_{12} & \sigma_{22} \end{bmatrix} \cdot \begin{bmatrix} 0 \\ -1 \end{bmatrix} = \begin{bmatrix} -\sigma_{12} \\ -\sigma_{22} \end{bmatrix} \tag{3.31}$$

As with the previous case, the traction and acceleration vectors are applied in the principle of virtual work to establish the relationship:

$$-\int_L \sigma_{22}\, dL = \rho \int_S a_2\, dS \tag{3.32}$$

Again, the discretisation procedures in Equations 3.19 and Equation 3.20 are followed to give the transverse stress gauge equation for an off-axis composite with its fibres rotated counter-clockwise to the x-axis:

$$\overline{\sigma_{22}}^{L} = -\frac{\rho S \overline{a_2}^{S}}{L} \tag{3.33}$$

Note that Equations 3.30 and 3.33 are the same, but the later case includes a minus sign accounting for the different direction of the material coordinate system 1−axis. The transverse modulus E_{22} is then identified from off-axis composites using the constitutive law in Equation 3.12 by plotting a line of best fit to $\overline{\sigma_{22}}^{L}$ *vs.* $\overline{\epsilon_{22}}^{L}$ and linearly fitting the elastic response.

3.3.5 Off-axis case: shear component

For the shear component we consider a rigid body virtual field in the material coordinate system describing a translation along the slice shown in the free body diagram in Figure 3.2 (a). This virtual field takes the following form:

$$\begin{cases} {u_1}^* = 1 \\ {u_2}^* = 0 \end{cases} \quad \begin{cases} {\epsilon_{11}}^* = 0 \\ {\epsilon_{22}}^* = 0 \\ {\epsilon_{12}}^* = 0 \end{cases} \tag{3.34}$$

The processes used in Equations 3.15 to Equation 3.17 are followed to give the relationship:

$$\int_L \sigma_{12}\, dL = \rho \int_S a_1\, dS \tag{3.35}$$

where σ_{12} acts on the slice L and a_1 acts over the surface area S defined by the blue coloured trapezoid in Figure 3.2 (b). Similar to the transverse case, the integrals in Equation 3.35 can again be approximated as discrete sums of the quantities obtained from full-field measurements, giving the shear stress gauge equation for an off-axis composite:

$$\overline{\sigma_{12}}^{L} = \frac{\rho S \overline{a_1}^{S}}{L} \tag{3.36}$$

where $\overline{\sigma_{12}}^L$ is the average shear stress acting over L on the specimen shown in Figure 3.2 (b). For samples in the configuration shown in Figure 3.3 (a), the stress gauge equation is:

$$\overline{\sigma_{12}}^L = -\frac{\rho S \overline{a_1}^S}{L} \tag{3.37}$$

Average shear stresses can also be obtained over slices transverse to the fibres shown in Figures 3.2 (a) and 3.3 (a). Here, the $\overline{a_1}^S$ term in Equations 3.36 and 3.37 is replaced by $\overline{a_2}^S$. For the average shear stress reconstruction from slices transverse to fibres orientated CCW as in Figure 3.3 (a), the minus sign is removed from Equation 3.37 because the normal vector is aligned with the positive 1-axis. Equations 3.36 and 3.37 are combined with the average shear strain $\overline{\gamma_{12}}^L$ derived from full-field measurements to establish stress-strain curves for the duration of the loading recorded in the experiments. The shear modulus G_{12} is then obtained by plotting a line of best fit to the linear portion of the $\overline{\sigma_{12}}^L$ *vs.* $\overline{\gamma_{12}}^L$ curves. Plotting stress averages are sufficient for stiffness identification however, for localised material properties such as the failure stress, alternative procedures are required. This is briefly discussed in the next section.

3.4 Virtual fields for failure stress identification

The VFM equations used to reconstruct the failure stress in an impacted transverse composite were derived in [29], so only the main result and the essence of the derivation is given here. In brief, three rigid body virtual fields are selected to give stress and stress moment averages, which are combined with a linear approximation of the stress distribution over the specimen height. The three rigid body virtual fields are 1) a translation in the x-axis that gives the average transverse stress, *i.e.* the transverse stress gauge given in Equation 3.21, 2) a translation in the y-axis that gives the average shear stress and 3) a rotation that resolves the average of the first moment of the axial stress. These stress and moment field averages are combined with a linear approximation of the normal stress over the specimen height, in what is termed the Linear Stress Gauge (LSG) equation:

$$\sigma_{xx}(LSG) = \rho x_0 \overline{a}_x^S + \frac{12\rho x_0 y}{H^2}\left(\overline{a_x y}^S - \overline{a_y x}^S + x_0 \overline{a_y}^S\right) \tag{3.38}$$

where $\overline{a_x y}^S$ and $\overline{a_y x}^S$ are the first moments of the acceleration averages. This gives an improved representation of the x-axis normal stress in the specimen over the standard stress gauge 'average' over the specimen height.

3.5 Summary

This chapter has shown how the combination of the VFM with full-field measurement techniques can be used to obtain elastic moduli for both UD90° and off-axis composites with orthotropic linear elastic material behaviour. This has been performed without the need for remote stress measurements or the requirement for quasi-static equilibrium in the specimen. In the next chapter, the experimental method for testing off-axis composite samples will be described.

Chapter 4

Experimental methods

This chapter describes the materials, instrumentation and processing methods used to obtain dynamic material properties from the impact experiments. Quasi-static tests on the same material system were conducted to establish the strain-rate sensitivity of the transverse and shear moduli and therefore, the materials and methods for these experiments are presented first. Thereafter, the dynamic test sample composition and layup are given, along with a brief description of the gas gun used to impart the dynamic loads. Prior to each batch of IBII tests, a procedure to align the target was performed so that the specimen was axially loaded. This alignment procedure is discussed in detail and reference images obtained during the process are provided. Imaging system specifications are listed together with a description of the full-field measurement techniques used to calculate the displacement maps. Methods for the kinematic field calculations and material property identification are then outlined.

4.1 Quasi-static tests

4.1.1 Quasi-static specimens

Quasi-static tests were conducted on UD45° tensile test samples in order to establish the strain rate sensitivity of the transverse and shear modulus for the CFRP material evaluated in this project. The quasi-static tensile test specimens were manufactured from Hexply M21/35%/268/T700GC UD pre-preg from Hexcel, France. This pre-preg system consists of M21 themosetting epoxy resin and T700GC carbon fibres. Laminates were made from 12 hand-layed plies, cured in an autoclave at the French aerospace laboratory (ONERA) in Lille, France. Appendix A gives the method and measurements used to calculate the laminate density of 1514 ± 20 kg.m^{-3}. UD45° tensile test specimens were cut from the UD0° laminates by orientating the laminate fibres at 45° to the specimen edges. ImageJ was used to measure the fibre angles from images of the sample faces, which were found to be 45° ± 1°. Rectangles with nominal dimensions of 250×25×3 mm were first cut from the laminates with a water-jet cutting machine. The sample ends were then cut with a water-cooled tile saw to final dimensions of 230×25×3 mm. Front and back surfaces of the specimens were then lightly sanded using 500 grit sand paper, smoothing the peel-ply imprint so that the nominal specimen thickness was 3.14 mm. Standard strain gauge application procedures were followed in the application of TML FRA-3-11 0°/45°/90° rosette strain gauges to the front and back surfaces, as shown in Figure 4.1.

4.1.2 Quasi-static testing method

Tests were conducted on an Instron 5569 testing machine at 1 mm.min^{-1}, loading the specimens within the elastic range to 4000 N and then unloading them at the same rate. In these tests the goal was to obtain moduli, so the specimens were not loaded to failure. Strain signal conditioning was achieved with a Strainsmart 8000 series transducer with a quarter-bridge configuration and 2 volts excitation for each individual gauge. In order to maximise the signal to noise ratio for each gauge, the

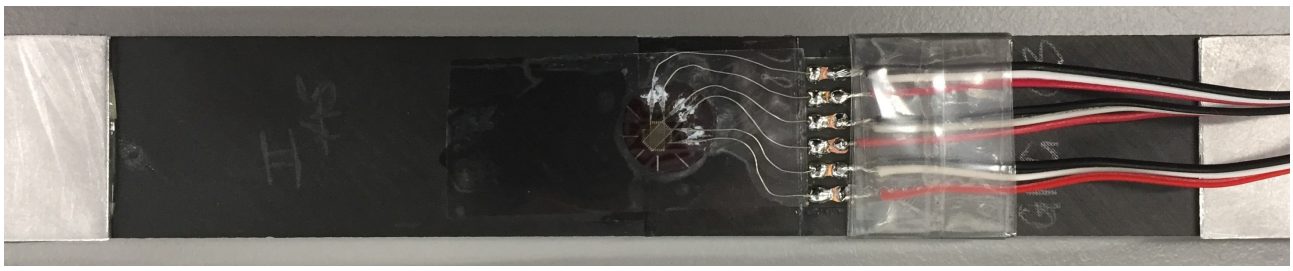

Figure 4.1: Quasi-static tensile test specimen.

0°/45°/90° rosette strain gauges were positioned with the first gauge aligned at 45° to the material coordinate system as shown in Figure 4.2 (a). This configuration was determined by first assuming some material properties (Young's moduli and Poisson's ratios), and then estimating the strain output of each strain gauge as a function of angular position with respect to the material coordinate system. Figure 4.2 (b) shows the results of this analysis, where the strain output of each gauge was estimated through the equation:

$$\begin{bmatrix} \epsilon_{SG1} \\ \epsilon_{SG2} \\ \epsilon_{SG3} \end{bmatrix} = \begin{bmatrix} cos^2\alpha_1 & sin^2\alpha_1 & sin\alpha_1 cos\alpha_1 \\ cos^2\alpha_2 & sin^2\alpha_2 & sin\alpha_2 cos\alpha_2 \\ cos^2\alpha_3 & sin^2\alpha_3 & sin\alpha_3 cos\alpha_3 \end{bmatrix} \begin{bmatrix} \epsilon_{11} \\ \epsilon_{22} \\ \gamma_{12} \end{bmatrix} \tag{4.1}$$

where ϵ_{SGi} is the strain from each gauge on the rosette, positioned at angle α_i for $i = 1, 2, 3$ with respect to the material coordinate system shown in Figure 4.2 (a). Note that for the strain gauge rosette applied here, $\alpha_2 = \alpha_1 + 45°$ and $\alpha_3 = \alpha_1 + 90°$. The material coordinate strain $\boldsymbol{\epsilon}$ was obtained from the relationship $\boldsymbol{\epsilon} = \boldsymbol{Q^{-1}\sigma}$ under the assumption of 2D plane stress, where Young's Moduli and the Poisson's ratios ($\boldsymbol{E_{11}}$, $\boldsymbol{E_{22}}$, $\boldsymbol{\nu_{12}}$ and $\boldsymbol{\nu_{21}}$) given in Chapter 3 were used to form the material coordinate stiffness tensor $\boldsymbol{Q}$. Here, the material coordinate stress $\boldsymbol{\sigma}$ was attained by rotating the global stress components (assuming uni-axial stress in the global coordinates) with the relationship:

$$\begin{bmatrix} \sigma_{11} \\ \sigma_{22} \\ \sigma_{12} \end{bmatrix} = \begin{bmatrix} cos^2\theta & sin^2\theta & 2sin\theta cos\theta \\ sin^2\theta & cos^2\theta & -2sin\theta cos\theta \\ -sin\theta cos\theta & sin\theta cos\theta & (cos^2\theta - sin^2\theta) \end{bmatrix} \begin{bmatrix} \sigma_{xx} \\ \sigma_{yy} \\ \sigma_{xy} \end{bmatrix} \tag{4.2}$$

After the strain gauge orientation was determined, the tests were conducted and the transverse and shear moduli were obtained in the following steps. First, the rosette strains were converted to material coordinate strain components using Equation 4.1. Next, the global stress tensor was constructed from the load cell force and the specimen cross-sectional area, then transformed into material coordinates using Equation 4.2. The constitutive models defined in Chapter 3 were then used to obtain the transverse and shear moduli *via* linear fits to the stress-strain curves, with the component strains taken as the average of the front and back measurements. Three samples were tested six times (total of 18 tests), each time removing and re-gripping the sample between tests. After the first three tests on each sample, the sample was rotated 180° *i.e.* turned upside-down. These operations were performed to ensure that bias due to gripping boundary conditions was minimised.

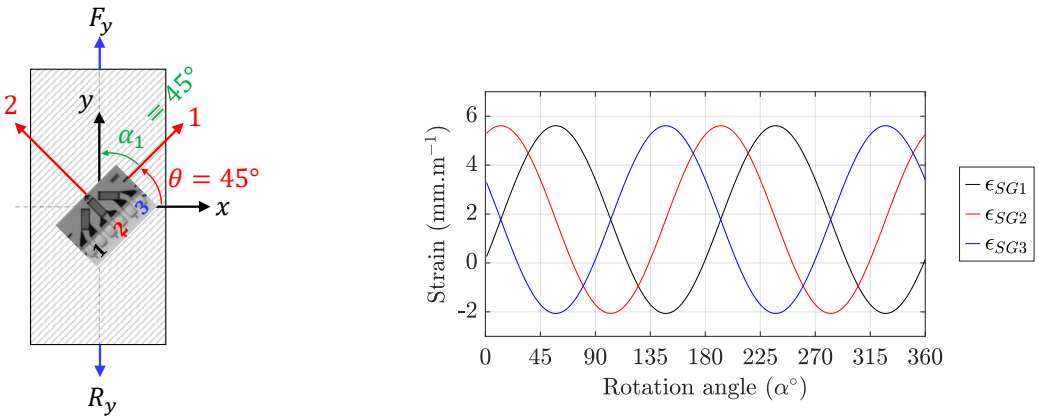

(a) Free-body diagram of the UD45° quasi-static tensile test sample.

(b) Strain output from each strain gauge *vs.* angular position, with respect to the material coordinate system.

Figure 4.2: Free-body diagram of the quasi-static test in (a) and the predicted strain outputs from the rosette strain gauge in (b).

4.2 Dynamic tests

4.2.1 IBII specimens

The IBII test specimens were also made from laminates manufactured by ONERA. UD90° and UD45° samples were obtained by cutting rectangles from the laminates, with the long edge at 90° and 45° to the laminate fibres, respectively. As described later in Sections 4.2.7 and 4.2.8, two full-field measurement techniques (the Grid Method and DIC) were used to calculate displacements from the IBII test images. The UD IBII specimens evaluated with the Grid Method were cut from a plate with a calculated density of 1575 ± 17 kg.m^{-3} (UD0° Plate 1 in Appendix A). This plate had the same specification, but a different calculated density to the plate used for the UD IBII specimens evaluated with DIC and the quasi-static samples, which had a density of 1514 ± 20 kg.m^{-3} (UD0° Plate 2 in Appendix A). Both the Grid Method and DIC MD±45° samples were manufactured from 12 ply 0°/90° laminates with a density of 1530 ± 41 kg.m^{-3}. In this work, the MD±45° samples had the stacking sequence of $[\text{MD}\pm45°]_{6S}$. All of the IBII samples were cut from the laminates in two stages. First, 5 mm oversized rectangles were cut from the laminates with a water-jet cutting machine. The sample edges were then cut using a water-cooled precision cutting machine fitted with a diamond coated disc, to finished nominal dimensions of 70×43 mm. The peel-ply imprint on the top and bottom specimen faces was abraded with 500 grit silicon carbide (SiC) sand paper used on a rotary sanding machine. Care was taken to ensure only the peel-ply imprint was removed and water coolant minimised heat conduction into the specimen. Each specimen was then cleaned with demineralised water and left to dry at room temperature. Images of the finished UD90° and UD45° specimens prior to grid or speckle pattern application are given in Figures 4.3 (a) and 4.3 (b), respectively. Note that an MD±45° sample image is not provided as it appeared identical to the UD45° specimen. One face of the sample (the imaged surface) was then painted with three thin coats of white acrylic spray paint and left to dry for 30 minutes in an oven set at 50° after each coat.

For the Grid Method samples, a regular grid of black squares was printed on the specimen's painted surface with a flat-bed printer. Figure 4.3 (c) shows the printed grid, where the distance between the black squares or the grid pitch was 0.9 mm. More information on the grid printing procedure can be found in [117]. For the DIC samples, a black speckle pattern with a speckle size of 0.72 mm was first printed onto a 'dry-rub' vinyl transfer sheet. A section that was 10 mm oversized from the sample dimensions was cut from the transfer sheet and positioned face-down on the sample's painted surface. Pressure was then applied to the transfer backing sheet using a cloth and moderate thumb-pressure.

After checking that all speckles were adhered to the sample's surface, the sample was placed in an oven set at 50° for 30 minutes, with a 5 kg weight placed on top of the transfer pattern. Figure 4.3 (d) shows an image of the applied speckle pattern. More information on the grid and speckle pattern specifications is given in Sections 4.2.7 and 4.2.8.

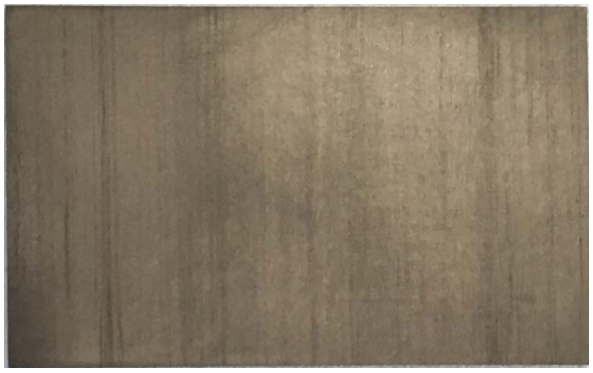

(a) UD90° specimen.

(b) UD45° specimen.

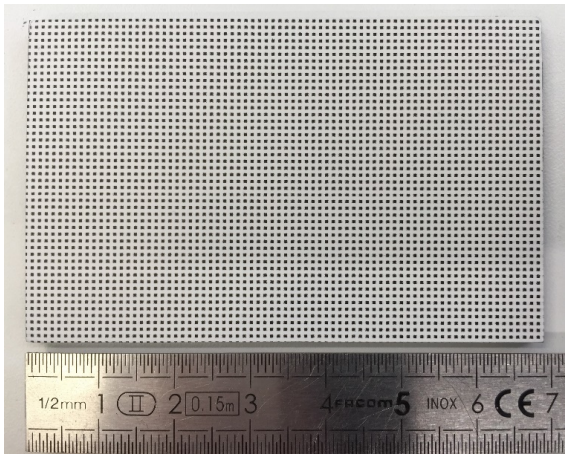

(c) Grid printed on the specimen surface.

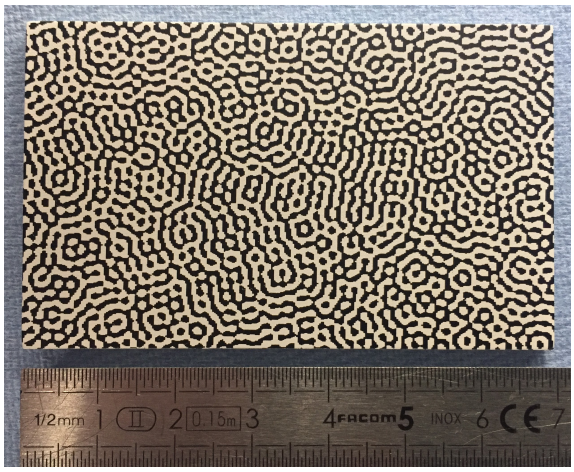

(d) DIC speckle pattern.

Figure 4.3: Unpainted IBII test specimens in the (a) UD90° and (b) UD45° configurations, together with finished examples of the (c) grid and (d) DIC specimens.

4.2.2 Gas gun

A gas gun was used to generate the dynamic loading required for the IBII tests. The major components of the gas gun system are the barrel, pressure vessel and target trap shown in Figure 4.4 (a). Before a test is conducted, a projectile/sabot assembly is loaded into the gas gun barrel and the pressure vessel is pressurised to the desired firing pressure. Previous test campaigns established that a firing pressure of 1.1 bar was required to launch 45 mm diameter by 25 mm long aluminium projectiles at a nominal velocity of 40 m.s^{-1} [29]. This firing pressure was selected for all tests conducted in this thesis. When the system is fired, a solenoid valve opens and the pressurised gas accelerates the projectile/sabot assembly down the gas gun barrel toward the target assembly. For these tests, the target assembly consisted of a specimen bonded to a 45 mm diameter, 50 mm long right-angled aluminium cylinder called a 'wave guide'. The purpose of the wave guide is to 1) hold the specimen and 2) provide good contact with the projectile, allowing the input pulse to load the specimen. The specimen and wave guide rest on a 'v-shaped' foam stand as shown in Figure 4.4 (b). The foam stand was positioned on an aluminium plate secured to a five-axis mechanical stage (discussed in the next section), which can be adjusted to align the axis of the wave guide with the gas gun barrel. The target assembly is encased by a steel target trap shown in Figure 4.4 (c), which protects users and instrumentation

from impact debris and facilitates the recovery of the impacted specimen. One side of the target trap contains a Polycarbonate window through which the imaging system can record the specimen surface deformations. Further information on the gas gun apparatus is given in [117]. Positioning of the camera and the flash light is also shown in Figure 4.4 (c).

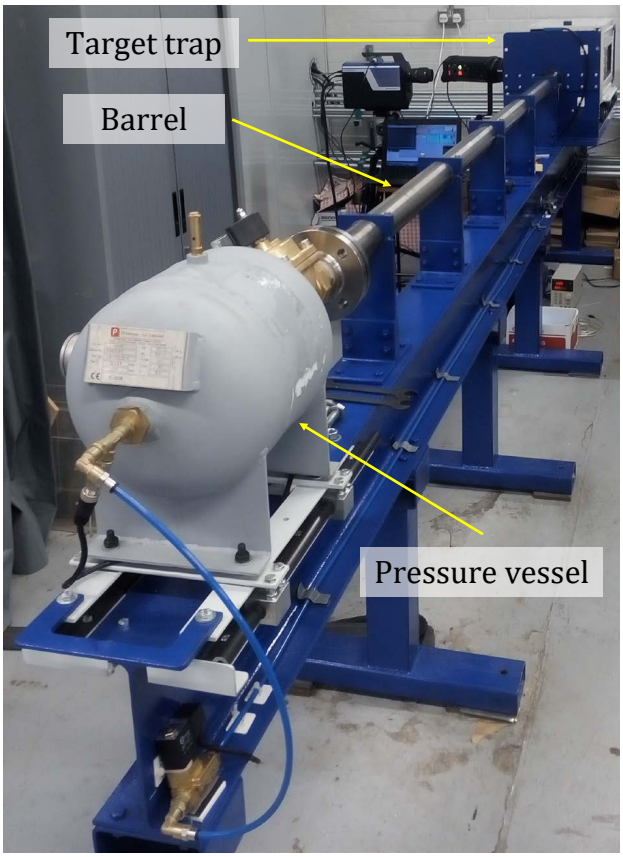

(a) Major components of the gas gun system.

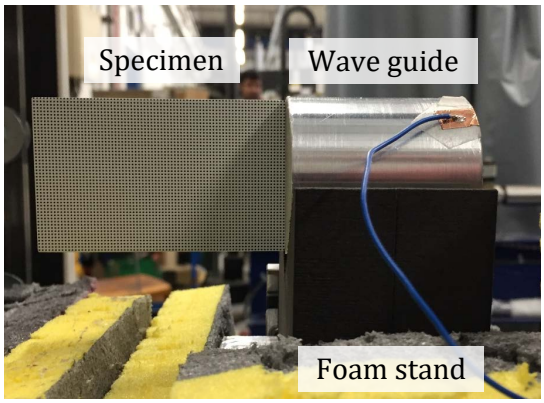

(b) Specimen and wave guide on foam stand.

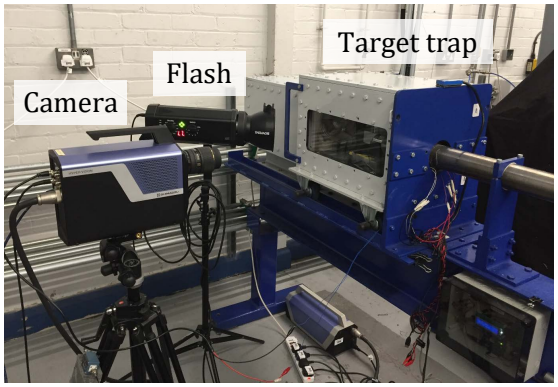

(c) Target trap, camera and flash light.

Figure 4.4: Gas gun components, specimen assembly and imaging system arrangement used in the IBII tests.

4.2.3 Imaging system

Deformations on the surface of each sample were recorded with a Shimadzu HPV-X UHSV camera with a framing rate of 2 MHz. The camera records 128 images, which gives a total recording time of 64 μs. Benefits of using this camera for dynamic full-field measurements have been previously discussed in [118]. The camera was fitted with a Sigma 105 mm lens and positioned approximately 700 mm from the specimen. Figure 4.5 shows the field of view, in which the camera's pixel array size of 400 $\times$ 250 pixels was occupied by the specimen, plus a small region of free space surrounding the specimen's top, bottom and free edges. This free space allowed for a few grid pitches of rigid body translation and a small amount of rigid body rotation in the specimen, which can occur during a test. With the given imaging set-up and specimen grid pitch of 0.9 mm, the resulting spatial frequency (sampling) of the grid images recorded by the camera was 5 pixels per pitch, as shown in the magnified view of a horizontal portion of the grid in Figure 4.5. Table 4.1 provides a summary of the main imaging system specifications.

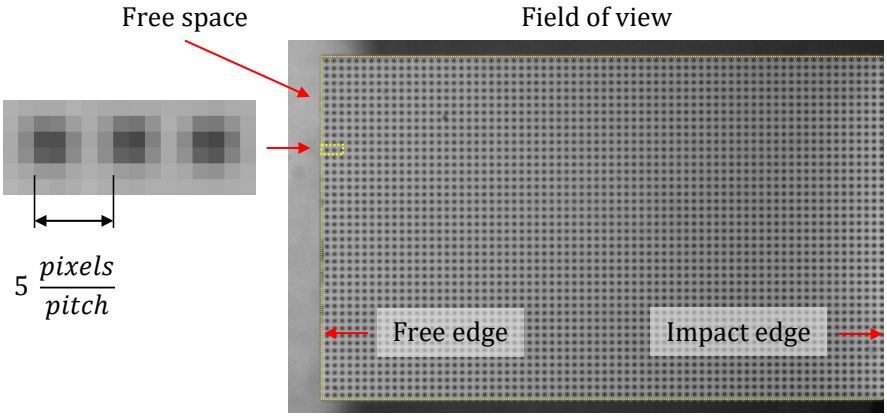

Figure 4.5: Image recorded during the IBII tests showing the field of view, together with a magnified view of the grid showing its spatial frequency.

Table 4.1: Imaging system specifications.

Camera	Shimadzu HPV-X
Pixel array size	400 × 250
Sensor bit depth	10 bits
Total frames	128
Inter-frame time	0.5 μs
Integration (shutter) time	0.2 μs
Imaging distance	700 mm (approx.)
Lens	Sigma 105 mm 1:2.8 DG Macro
Flash Light	Bowens Gemini 1000 Pro
Field of view	72 × 45 mm
Magnification	0.18 mm/pixel

The camera was triggered by a contact circuit consisting of two thin copper tabs adhered to the front face of the wave guide, which were connected to the camera trigger port with electrical wires. When the contacts were impacted by the metallic projectile, an electrical circuit was completed and the camera triggering circuitry registered a voltage. The camera started recording after a short programmed delay, which accounts for the time for the input pulse to travel the length of the wave guide, arriving at the impact edge of the specimen. It is often advantageous to record a few frames ($\approx 6-8$) prior to the wave impacting the specimen, so that temporal smoothing effects are minimised at the start of the test. For this reason, a delay slightly less than the time for an acoustic wave to travel the length of the wave guide is used for the UHSV camera recording time. Adequate lighting of the specimen surface was provided with a Bowens Gemini 1000 Pro flash light, positioned to the left of the camera as shown in Figure 4.4 (c). It is important to have the appropriate light intensity and duration over the time that full-field measurements are made during the test. The flash light intensity-time curve includes a rise time, a near-constant or 'useable' portion and a fall time as indicated in Figure 4.6. Therefore, a flash light triggering set-up is required to ensure that the usable portion of the light is present for the duration of the test recording. Figure 4.6 gives a schematic of the triggering system used for the flash light, showing the projectile and sabot, gas gun barrel, light gates and the wave guide/specimen assembly. Light gates positioned at the end of the barrel are used in combination with an Arduino system to calculate the projectile velocity V. The Arduino system then calculates the required flash light delay time from the distance between the second light gate, the length of the

sabot/projectile assembly, the projectile velocity and the flash rise time as shown in Figure 4.6. The distance from the second light gate to the front face of the wave guide must be programmed into the Arduino software prior to the test, so that the correct flash delay time can be calculated. After the flash and camera have triggered, a series of surface deformation images are recorded and soon after, processed with an appropriate full-field measurement technique to derive displacement fields.

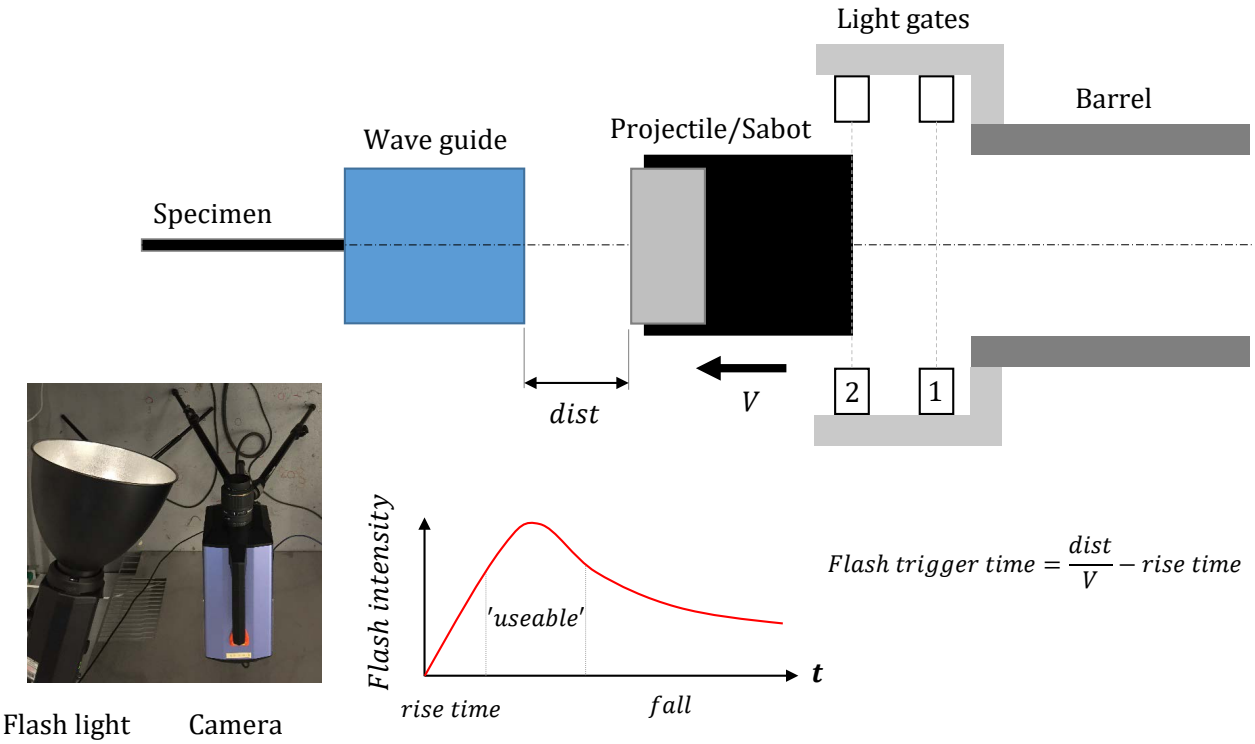

Figure 4.6: Schematic showing the camera and flash triggering arrangements.

4.2.4 Pre-test projectile and wave guide alignment

It is important that all of the components involved in the impact event are axially-aligned, so that the stress wave progression through the wave guide into the specimen is predominantly 2D, *i.e.* out-of-plane effects such as bending are minimised [115]. For the IBII tests conducted in this work, the alignment of two interfaces in the target assembly were considered, which were that between 1) the projectile and the wave guide and 2) the wave guide and the sample. Procedures developed to measure the alignment of these interfaces during testing are now discussed.

Measuring the impact angles of projectiles and targets using high-speed imaging is regularly undertaken in terminal ballistics studies. After tests are conducted, images recorded with a high-speed video camera are viewed in imaging software such as ImageJ, and the pixel locations of the components are measured to determine their impact angles. Usually the camera is positioned horizontally to the shot line, so the 'pitch' angle of the projectile is obtained. If a mirror is placed above the vertical centreline of the projectile and positioned at approximately 45° to the camera lens, a top-down view of the incoming projectile can be obtained and the 'yaw' angle can also be measured, as performed in [119]. This general concept was adapted to the IBII tests to measure the pitch and yaw impact angles between the projectile and the wave guide. Here, the pitch and yaw angle measurements were made independently in 'side-on' and 'top-down' tests, respectively. Both of these angles were measured by recording images of a projectile impacting a wave guide at the intended test impact speed. Before

the alignment tests were conducted, a polymer alignment rod was placed in the end of the barrel to approximately align the wave guide to the barrel axis, as shown in Figure 4.7 (a). The front face of the projectile was made approximately planar to the polymer alignment rod 'by-eye', using the adjustment dials on the five-axis stage. Verniers on the Goniometer and the rotary stage were then read to determine the 'pitch' and 'yaw' angle setting, as shown in Figure 4.7 (b). The stage rotation dials were then locked and the alignment rod was removed before conducting the first side-on alignment test.

Figure 4.7 (c) shows the configuration used for the pitch or 'side-on' alignment tests, where the camera was positioned horizontally. Here, a camera pre-trigger was set to record a number of images before the projectile impacted the wave guide. In the first side-on alignment test, the relative angle between the front face of the projectile and the wave guide was measured from an image like that shown in Figure 4.7 (d). When the gun is fired, air in front of the projectile is compressed as the projectile accelerates down the barrel. For high projectile speeds, the compressed air in front of the projectile can load the front face of the wave guide, causing it to pitch upwards because the bottom of the wave guide is secured to the foam stand. This causes non-planar contact between the projectile and the wave guide and at the same time, can cause the specimen grid to tilt, affecting the displacement field calculations in the Grid Method. However, the rotary stage can be adjusted so that the wave guide is pitched slightly 'nose-down', compensating for the projectile air-loading and any pitch angle misalignment. Following the adjustment, a second validation test was undertaken and the angle was again measured from the recorded images to ensure the pitch alignment was planar.

After the side-on alignment tests, the camera was repositioned at an angle approximately 45° to the horizontal. This gave a top-down view of the wave guide, reflected from a mirror positioning above the wave guide as shown in Figure 4.7 (e). An image from a 'top-down' alignment test is shown in Figure 4.7 (f), where a similar procedure to the 'side-on' offset angle calculation was followed to calculate the 'top-down' alignment angle from the recorded image.

For both the side-on and top-down alignment tests, two hand-picked points are required to measure the projectile and wave guide impact angles. If the camera is positioned such that the two points used to measure the front face of the projectile and the wave guide are within one pixel, the method can measure impact angles to a resolution of 0.23°. This angular measurement resolution is specific to these tests and calculated from the trigonometric relationship between the magnification of 0.18 mm.pixel^{-1} and the wave guide diameter of 45 mm *i.e.* $\theta = \sin^{-1}(0.18/45)$. One limitation of the pre-test alignment procedure is that both side-on and top-down alignments are not obtained simultaneously. Another limitation is that the pitch and yaw angles are not measured during a test, meaning that their effect on the identified material properties is unknown. During a test campaign, the pitch and yaw angles on the five-axis stage are checked after each test on the pitch and yaw verniers shown in Figure 4.7 (b), which have measurement resolutions of 0.08° and 0.16°, respectively. If the readings on the verniers have not changed between tests, it is assumed that the projectile/wave guide alignment has not changed because the angular measurement resolutions on the verniers are within the bounds of the errors calculated from the recorded images (*i.e.* within 0.23°).

Influences on the identified material properties from tests where this alignment procedure was and was not followed were assessed in [115] using a back-to-back imaging setup. This analysis showed that only minor effects in the identified modulus of around a few percent were induced by misaligned tests. However, in that investigation the alignment angles were calculated before a series of tests were conducted and therefore, small changes in the alignment angles resulting from the assembly of the impacted components were not measured. Although these small deviations would likely have a minor effect on the identified modulus, more significant effects could be expected in localised properties, *e.g.* failure stress [115]. Alignment-induced effects can be detected from a deviation in the expected stress-strain response however, this approach could be complicated when assessing the non-linear shear response of composites.

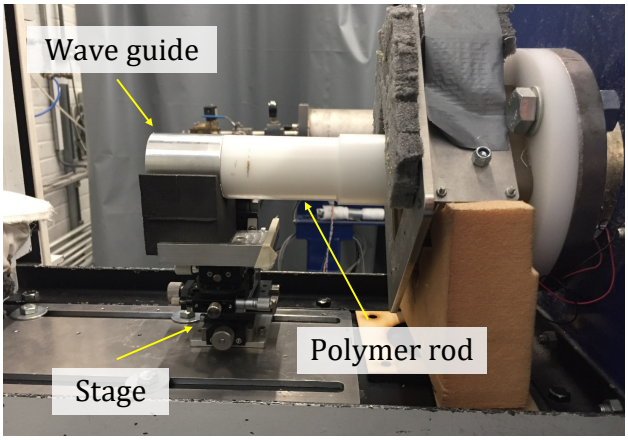

(a) Polymer rod used for the initial alignment of the wave guide.

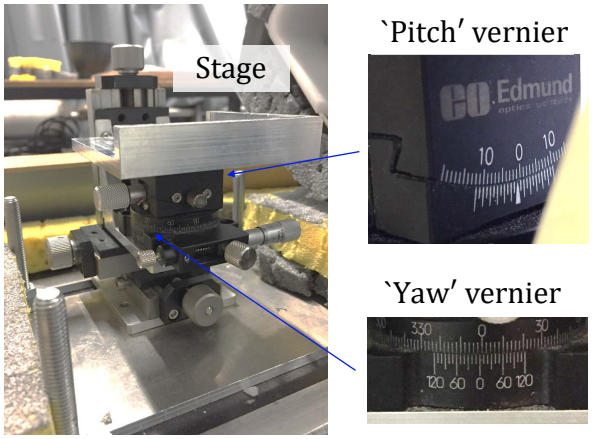

(b) Five-axis stage showing the verniers used for the pitch and yaw angle readings.

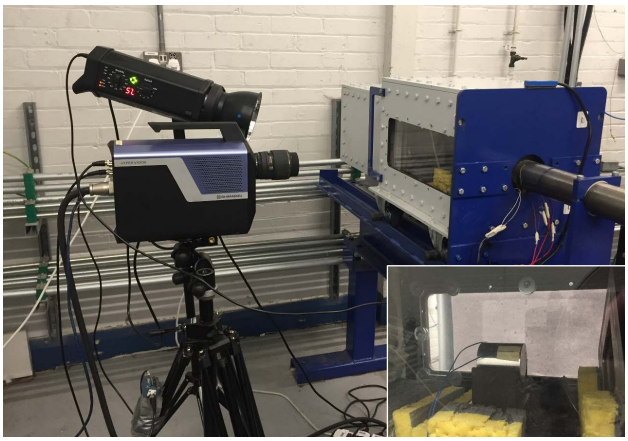

(c) Side-on alignment test configuration with a view of the wave guide on the foam stand.

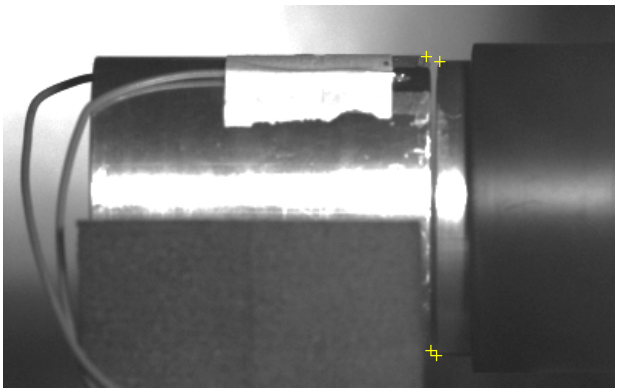

(d) Image recorded during a side-on alignment test. Markers in yellow show the locations used to measure the relative angle between the wave guide and the projectile.

(e) Top-down alignment test configuration with a view of the mirror stand manufactured for the tests.

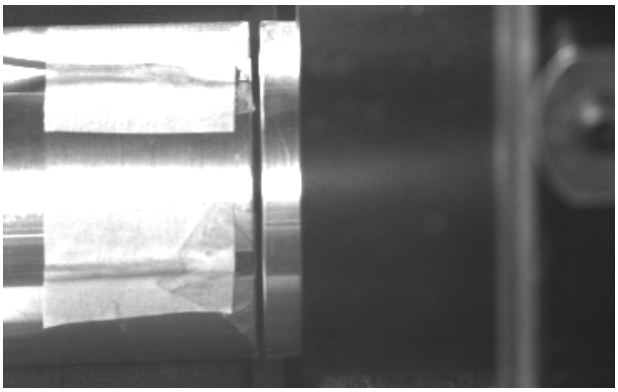

(f) Image recorded during a top-down alignment test.

Figure 4.7: Experimental set-up and images recorded during the projectile/wave guide alignment tests.

4.2.5 In-test projectile and wave guide alignment

For the IBII tests on DIC samples, a new method was used to measure the alignment between the projectile and the wave guide during an experiment. This was achieved by positioning two contacts at four locations on the wave guide as shown in Figure 4.8 (a). These contacts were part of an electrical circuit that generated a voltage spike when shorted by the incoming projectile, as shown in Figure 4.8 (b). Together with the speed of the projectile, the pitch and yaw angles were calculated from the difference in time between the top and bottom, and left and right rise-times, respectively. In principle, this was a low-cost version of the method used to measure tilt angles in plate impact experiments [120]. Figure 4.8 (c) gives a schematic showing the parameters used to calculate the pitch angle, which was obtained from the relationship $\theta = \sin^{-1} \frac{s}{l}$, where $s = v \times (t_T - t_B)$, v is the projectile velocity and l is the diameter of the wave guide. Here, t_T and t_B are the rise times for the top and bottom locations on the wave guide, determined from the time that the trace started to rise above zero. The voltage rise times can be seen in Figure 4.8 (b), which plots the results obtained from one of the tests. Note that the trace from the top contact had a different profile to the remaining contacts because a different circuit was used to produce the voltage spike (see Appendix C). A similar procedure was used to calculate the yaw angle from the rise times t_L and t_R, from the left and right locations on the wave guide, respectively, as shown in Figure 4.8 (d). The procedure for constructing the contacts and aligning the sample on the wave guide is given in Appendix C.

One advantage of this technique is that the overall resolution of the angle calculation (0.05°) was finer than the pre-test alignment method (0.23°). This was a result of the high temporal resolution of the oscilloscope (50 ns) used to record the difference in the impact times and the relatively-high spatial resolution of the image (0.02 mm/px) used to measure the distance between the contacts positioned on the wave guide. However, this resolution would have been finer than 0.05° if printed contacts were used rather than the hand-cut copper tabs, which decreased the accuracy of the value of l measured from the wave guide image shown in Figure 4.8 (a). Nevertheless, the main advantage of this technique is that the alignment measurements can be made during each test that material properties are identified from. Effects on the in-plane modulus identification from the degree of misalignment were obtained experimentally and are presented later in Chapter 7. In this investigation, in-test alignment measurements confirmed that when the pre-test alignment procedure was followed (*i.e.* the pitch and yaw angles were within 1 pixel or 0.23°), there was insignificant effect on the identified in-plane transverse and shear moduli. This was likely a result of Saint-Venant's principle in dynamics [57], as alignment-induced effects diminish at a certain distance from where the load is applied.

4.2.6 Wave guide and sample alignment

The second target assembly interface where alignment was considered was that between the wave guide and the sample. In IBII tests, it is important that the specimen has a flat impact edge, with a surface that is perpendicular to its long edge. This will ensure that the long edge of the sample is perpendicular to the back face of the wave guide, when viewed from the top-down perspective in Figure 4.9 (a). Assuming that the wave guide faces were perpendicular to its axis within general engineering tolerances, a flat specimen impact edge will allow the loading pulse to transition from the wave guide to the specimen with minimal out-of-plane effects. Before the IBII tests were conducted, macroscopic 'top-down' images of the impact edges from a representative group of six UD45° specimens were taken. ImageJ was then used to measure the impact edge angles as shown in Figure 4.9 (b). A diagram showing the measurement locations and their values is given in Appendix B, where the mean angle was measured as 90.13° ± 0.37°. Here the '±' value was taken as the SD of all measurements taken. However, it is noted that the macroscopic images only provided a 2D view of the top surface of the specimen and consequently, did not reveal the angular variance along the specimen height. Therefore, in this work it was assumed that the manufacturing tolerances resulting from the standard material specimen cutting operation were sufficient to provide a flat impact edge on the specimen, and did not contribute to any 3D loading of the specimen.

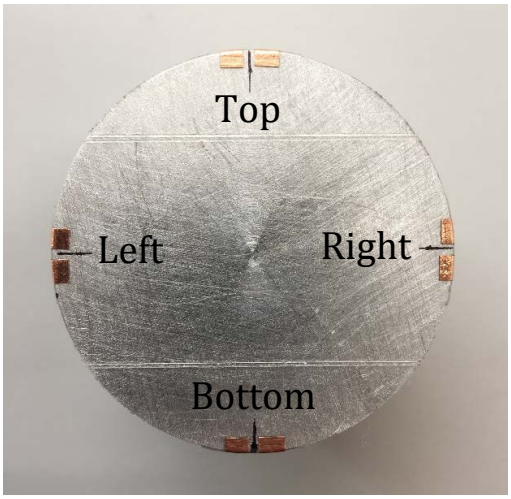

(a) Wave guide with four contacts.

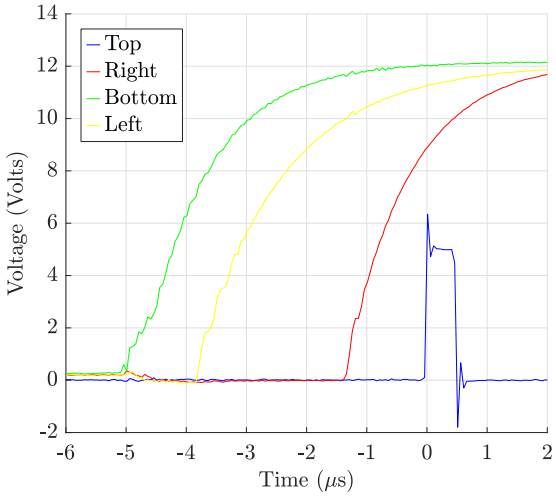

(b) Voltage-time history from the contacts.

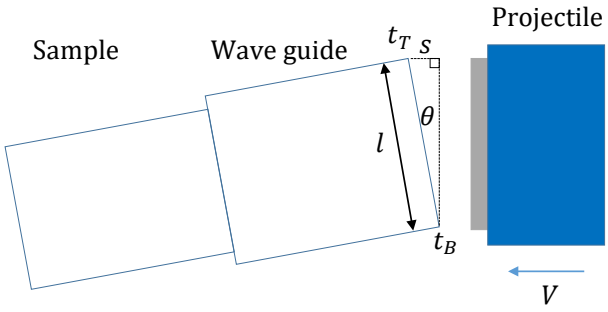

(c) Schematic for the in-test pitch angle calculation.

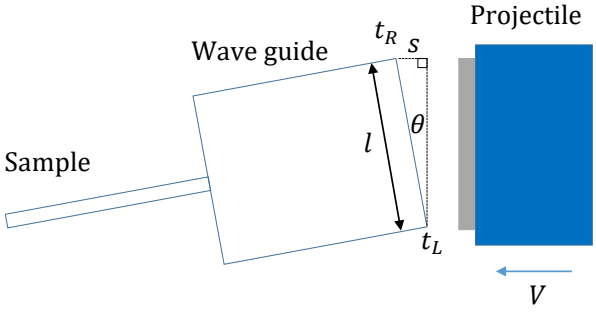

(d) Schematic for the in-test yaw angle calculation.

Figure 4.8: Four contact pairs positioned at the 'Top', 'Bottom', 'Left' and 'Right' positions on the wave guide in (a) and the voltage−time history from each location recorded during a test in (b). Schematics showing the variables used for the calculation of the pitch and yaw angles between the projectile and the wave guide are shown in (c) and (d), respectively. Note that the angle of the wave guide has been exaggerated to highlight the angles.

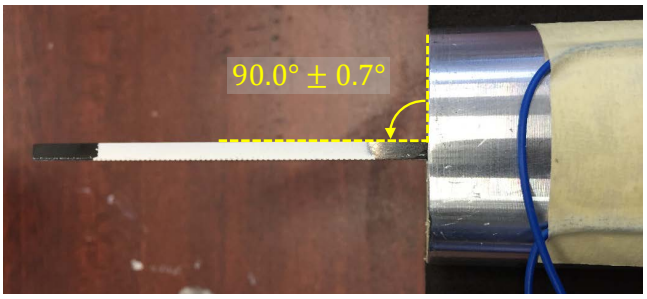

(a) Sample adhered to a wave guide.

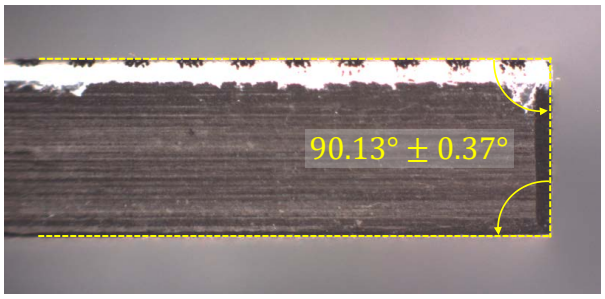

(b) Macrograph of a sample edge.

Figure 4.9: (a) Top-down image of the sample and wave guide and (b) macrograph of the sample edge.

The procedure outlined in Appendix C was undertaken to maintain consistency in the positioning of the samples on the wave guides for each test. After each sample was positioned and adhered to a wave guide, a top-down image of the assembly was taken like that shown in Figure 4.9 (a). ImageJ was

then used to measure the angle of the sample relative to the back face of the wave guide. If the angle was measured outside the range of 90° ± 0.7°, the sample was removed, cleaned and re-positioned on the wave guide, ensuring that the measured angle was within this range. Table C1 in Appendix C provides the measurements obtained from the IBII tests on DIC samples.

4.2.7 Displacement calculations: the Grid Method

Full-field displacement maps were obtained from the deformed grid images using the Grid Method. A thorough explanation and review of the Grid Method can be found in [31] and therefore, only a summary of the main steps in this application is given here. For this work, an open source Matlab code containing the Grid Method procedure in [31] was used to calculate the displacement fields. The main steps in the Grid Method can be summarised as follows:

1. **Phase maps**. A windowed discrete Fourier transform is used to calculate phase maps from the specimen grid deformation images recorded by the camera.

2. **Spatial unwrapping**. For deformations that are more than one grid pitch, the calculated phase can extend beyond a single wavelength *i.e.* lie outside the domain (-π, π). When this occurs, integers of 2π radians are added to the phase maps. To illustrate why this is done, consider the schematic in Figure 4.10 (a), showing a specimen with a simplified grid before and after impact from a projectile at times $t1$ and $t2$, respectively. At $t2$ the grid has deformed from the incoming compressive wave. Figure 4.10 (b) gives a representation of the spatial frequency of the first four squares in the grid before impact at $t1$, indicated by the blue line on the amplitude against phase plot. The red line is the phase representation of the deformed grid at $t2$, considering only the first three squares for brevity. For illustrative purposes, the phase calculated at the square closest to the impact edge (square #1 at $t2$) is greater than 2π however, the windowed discrete Fourier transform interprets this phase as $\pi/4$. In reality, the phase has extended beyond the (-π, π) domain by $\pi/4$, so the actual phase should be $9\pi/4$. If the calculated phase at ϕ_{t2} was $\pi/4$, a discontinuous jump in the phase would occur in this region, as values within the (-π, π) domain suddenly drop (incorrectly) to $\pi/4$. As described in [117] the Matlab code used to calculate the phase maps in this work incorporates a phase unwrapping algorithm described in [121].

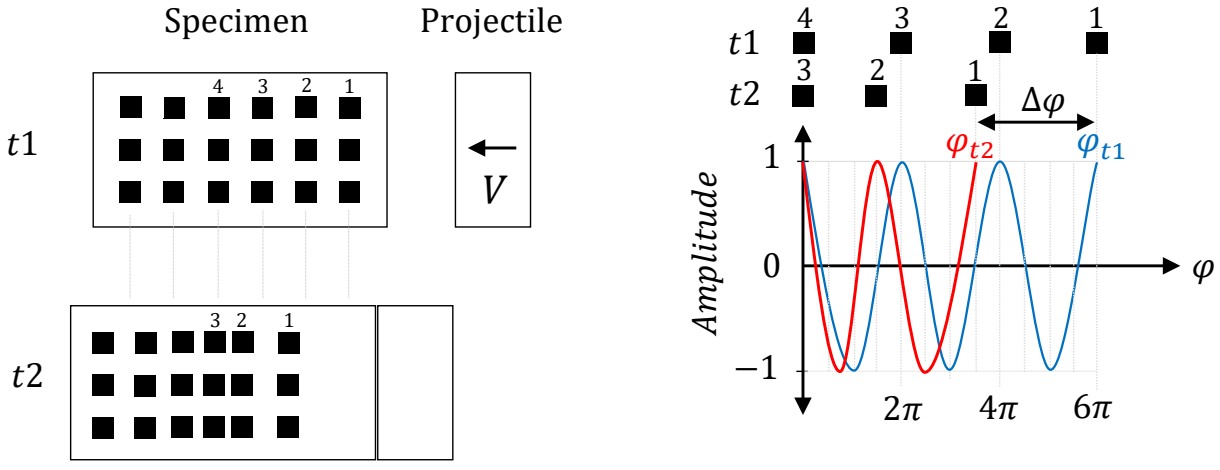

(a) Representation of a simplified grid before and after deformation.

(b) Representation of the phase change between two simplified grids.

Figure 4.10: Illustration of the spatial unwrapping requirement for a phase calculated from a deformation greater than one grid pitch.

3. **Temporal unwrapping**. Integers of 2π radians are added to the phase maps where the calculated phase extends beyond the domain (-π, π) between frames (*i.e.* in time).

4. **Phase difference maps**. Phase difference maps are calculated by subtracting the phase map of a reference un-deformed grid (reference phase) from each phase map in the loading history.

5. **Displacement calculation**. The displacement fields are calculated from the phase difference between the reference and deformed images and the grid pitch p using the equation:

$$u_i = \frac{p}{2\pi}\Delta\phi_i \ , \ i = x, y \tag{4.3}$$

   Equation 4.3 provides the initial guess for the displacement calculation. However, the iterative procedure outlined in [31] is used to obtain the corrected displacement value, accounting for grid defects and the relative movement between frames.

Table 4.2 provides a summary of the Grid Method processing parameters, where phase calculations were made at every pixel using a bi-triangular window with a width of nine pixels. This domain was selected for phase calculations considering results from the analysis in [122]. Note that sizing of the spatial and temporal smoothing kernels is discussed in Chapter 5.

Table 4.2: Grid Method specifications.

Grid pitch	0.9 mm
Grid sampling	5 pixels.pitch^{-1}
Grid configuration	Black squares on white background
Analysis window	Bi-triangular
Window width	9 pixels
Phase calc. step	1 pixel
Disp. calc. method	Iterative [31]

One difficulty of using the Grid Method in this application results from the low pixel fill factor of the Shimadzu HPV-X camera used in the IBII tests [29, 123]. The low fill factor produces image distortions amplified by the presence of sharp edges (high spatial frequencies in the image) [124]. This problem is reduced by slightly blurring the recorded image by changing the lens focus. An optimal level of blurring is determined prior to each IBII test with an out-of-plane movement test. In this test, a reference image is recorded with the camera and loaded into grid image processing software that calculates the grid phase. The stand-off distance between the camera and the specimen is then changed by a known amount using a horizontal translation stage to which the camera is secured. This simulates a hydrostatic strain over the specimen surface. The software calculates the phase change between the two images and the resulting displacement using the Grid Method. Strain is then derived by spatial differentiation of the displacements. The resulting strains should be uniform however, fill factor effects lead to the presence of oscillations in the strain maps. Therefore, the amount of blurring is adjusted and the process is repeated until the strain oscillations disappear. An adverse consequence of blurring the image is that its dynamic range is reduced and therefore the light intensity on the flash light may have to be increased or alternatively, the lens aperture can be opened.

4.2.8 Displacement calculations: Digital Image Correlation

In addition to the Grid Method, Digital Image Correlation (DIC) was used to derive displacement fields from images recorded during IBII tests. For this application, the focus was on traditional subset-based or local DIC rather than global DIC methods. DIC theory has been extensively described in many texts (*e.g.* in [55]) and is not covered here. Rather, a summary of the main steps involved in this DIC application is given. After a set of deformed speckle images are obtained, subsets are first defined within the region of interest (ROI) on a reference image, as shown in Figure 4.11. The overall aim is to obtain the displacement vector **u** between the centre of each subset on the reference and deformed images. A summary of the main actions in this process are listed below:

1. **Correlation criterion**. As the reference subset (centre) position is known, the position of the subset on the deformed image needs to be located. This is commonly obtained as the subset with the minimum Sum of the Squared Differences (SSD) in the subset pixel grey levels on the displaced image using the equation:

$$\min_{i \in i^n} \chi^2 = \sum_i [G_i - F_i]^2 \tag{4.4}$$

   where F and G are the reference and deformed images, respectively, and χ^2 is the function to be minimised for $i = 1{:}n$ pixels in each subset [55]. Variations in contrast between the recorded images (which can result from *e.g.* non-constant illumination) can be accounted for by subtracting the mean contrast from each subset through the expression:

$$\min_{i \in i^n} \chi^2 = \sum_i \left[(G_i - \overline{G_i}) - (F_i - \overline{F_i}) \right]^2 \tag{4.5}$$

   where $\overline{G_i} = \frac{1}{n} \sum G_i$ and $\overline{F_i} = \frac{1}{n} \sum F_i$. In this work, a Zero-Normalised Sum of Squared Differences (ZNSSD) criterion was applied. This criterion provides additional compensation for contrast contraction and expansion (or the contrast scale), by normalising the pixel grey levels in the deformed image in the equation:

$$\min_{i \in i^n} \chi^2 = \sum_i \left[\frac{(G_i - \overline{G_i})}{\sqrt{\sum (G_i - \overline{G_i})^2}} - \frac{(F_i - \overline{F_i})}{\sqrt{\sum (F_i - \overline{F_i})^2}} \right]^2 \tag{4.6}$$

   Equation 4.6 gives the 'initial guess' of the displaced coordinates with integer pixel accuracy.

2. **Interpolation function**. Pixel grey levels at non-integer pixel locations were determined by fitting cubic splines to the surrounding pixel grey levels. Values between four pixel centres were interpolated from the corner and adjacent pixels, in both the x and y-axis. Therefore, bi-cubic spline interpolation was applied in this work.

3. **Shape function**. In Equation 4.6 the subset is permitted to move to a new position in its original 'square' shape. For this DIC application, the subset deformation was constrained using an affine shape function, allowing for rigid body translation, rotation and shear deformation. Therefore, the shape of the subset was permitted to deform like that shown in Figure 4.11.

4. **Displacement calculation**. The displacement vector **u** is obtained by subtracting the centre positions of a deformed subset $P(x_2, y_2)$ from the reference subset $P(x_1, y_1)$, from all subsets on each deformed image.

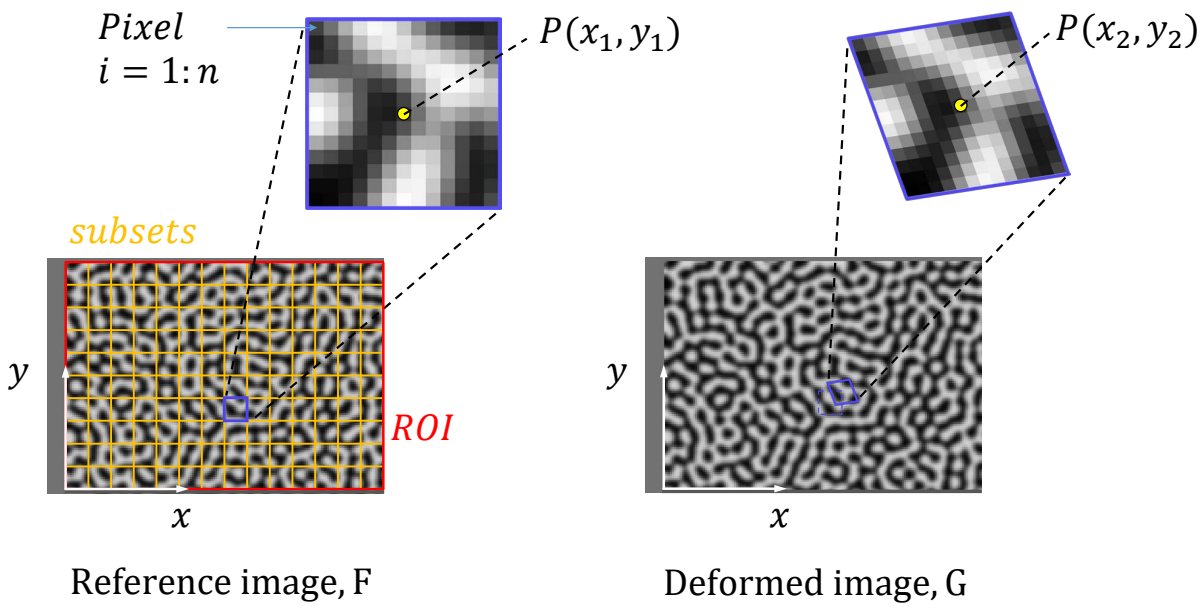

Figure 4.11: Schematic showing a reference speckle image with a region of interest (ROI) and subsets.

Deformed speckle image sets obtained from the IBII tests were processed in MatchID using the parameters listed in Table 4.3. Here, the speckle pattern had an average speckle size of approximately 4× the 0.18 mm.pixel^{-1} magnification of the imaging setup (giving an average speckle size of approximately 0.72 mm). This ensured that the average speckle size was between the 3 to 5 pixel range and therefore, aliasing effects would be minimised during image digitisation [125]. Next, a subset size of 13 pixels was selected so that the spatial resolution was close to the sampling used for the grids (5 pixels.pitch^{-1}). Using 4 pixel speckles and 13-pixel subsets would provide 'uniqueness' in the subset grey level distributions, leading to higher correlation coefficients. Displacement values at each pixel were obtained with a step size of one, so that field sampling was similar to the Grid Method values. Using the local DIC approach causes a loss in displacement field data equal to half a subset size around the specimen edges. Therefore, MatchID's missing data compensation option was employed to reconstruct this data using the subset's affine shape function. Note that in this work, DIC was only used to derive displacement fields and not strains.

Table 4.3: DIC processing parameters.

Software	MatchID
Subset size	13 pixels
Step size	1 pixel
Correlation criterion	ZNSSD
Shape function	Affine
Interpolation method	Bi-cubic spline
Image pre-filter	None
Image size	400×250 pixels

4.2.9 Strain and acceleration calculations

As explained in [29], when calculating displacements with the Grid Method, one grid pitch worth of data is erroneous at the specimen edges. For this work, a 'padding' technique was used to first crop the 'corrupted' data and replace it with extrapolated values. This technique has shown to improve the material property identification when using the VFM and DIC in [126]. For test results processed in this report, the edge data extrapolation method developed in [65] was selected. Here, one grid pitch worth of horizontal u_x displacement data was first removed. A linear fit to the displacement values over one grid pitch within the cropped edges was then extrapolated over the cropped region. This procedure was also performed on the vertical u_y displacements.

Following the edge padding procedure, spatial smoothing was applied to the displacement fields to reduce the effects of camera noise on the strain calculations. Without spatial smoothing, camera noise is amplified by the spatial differentiation used to determine the strains. Therefore, Gaussian spatial smoothing was applied to the displacement fields prior to the strain field calculations. Sizing of the Gaussian smoothing kernel was determined from an image deformation study, which is described in Chapter 5. After spatial smoothing, the strain fields were obtained by differentiating the displacements once, with respect to space. Temporal smoothing was also required to mitigate the effects of camera noise on the acceleration fields. Third-order polynomial smoothing was applied to the (un-smoothed) displacement fields prior to the acceleration field calculations. The number of frames used for temporal smoothing was also determined in the image deformation study. Following temporal smoothing, the acceleration fields were calculated by twice differentiating the displacements with respect to time. Differentiation of the displacement fields was performed with an in-house developed Matlab code using the *gradient* function [29]. Here, a centred finite difference approach was used so that gradients were calculated from one data point forward and backward from the calculated value.

4.2.10 Strain rate calculations

IBII test strain rates are inherently heterogeneous in space and time. Peak average strain rates give the upper limit of the strain rate range experienced by the material, reported here as the maximum value from all specimen slices over the loading duration of the test. In order to give an indication of an 'effective' strain rate, we define a second strain rate quantity, which is the strain-weighted strain rate:

$$\hat{\dot{\epsilon}}_{22} = \frac{\sum_{f=1}^{f_t} \sum_{i=1}^{n} |\dot{\epsilon}_{22}\epsilon_{22}|}{\sum_{f=1}^{f_t} \sum_{i=1}^{n} |\epsilon_{22}|} \tag{4.7}$$

$$\hat{\dot{\gamma}}_{12} = \frac{\sum_{f=1}^{f_t} \sum_{i=1}^{n} |\dot{\gamma}_{12}\gamma_{12}|}{\sum_{f=1}^{f_t} \sum_{i=1}^{n} |\gamma_{12}|} \tag{4.8}$$

where f is the frame, f_t is the total number of frames recorded during the test (128) and n is the number of spatial sampling points. Smoothing kernel edge effects were removed from the calculation by cropping the strain and strain rate fields by $S_k/2$ + one grid pitch from all edges, where S_k is the spatial smoothing kernel size in pixels. Given the nominal sample dimensions of 70×43 mm, 0.18 mm.pixel^{-1} sampling and $S_k = 25$ pixels, the total number of pixels or spatial calculation points n was 71,104. However, n varied for each sample because of the different sample dimensions and smoothing kernel size selected to process the laminate configuration (see Chapter 5).

4.2.11 Modulus and failure stress identification for the UD90° case

Experimental data processing procedures for the UD90° case modulus and failure stress identification are thoroughly explained in [29, 117]. Therefore, only a brief description of the procedure is given here, as the focus of this report is on the UD45° case. Displacement fields obtained using the grid method or DIC are generated in the global coordinate system. For the UD90° case, the material coordinate system is aligned with global coordinate system and therefore, the global acceleration and strain fields can be used directly to establish average stress-strain relationships along vertical slices on the specimen surface (see Section 3.3.1 of Chapter 3). Transverse modulus values for each slice are then obtained from linear fits to the linear part of the stress-strain response. Here, the spatial variation of transverse moduli along the specimen surface is revealed. Averaging these values over the specimen length, or a portion of the specimen length then gives an overall average identified modulus value. For the UD90° samples, moduli were obtained over the middle 50% of slices so that spatial smoothing effects at the vertical edges, and low signal-to-noise data at the free-edge were not included in the identification. Transverse stress-strain curves and the transverse modulus spatial variation over a UD90° IBII test sample are given in Chapter 6.

For the UD90° specimens that formed a crack during the IBII tests, the crack location, time of failure and failure stress value were obtained by realising that a crack can be detected as a spuriously high 'strain' concentration in the strain fields, which is in fact not a strain but a crack opening. The failure location was determined by scanning through the unsmoothed strain fields and finding regions of concentrated strain. Additionally, the specimen deformation images recorded by the UHSV camera will often show the crack location. In order to determine the time of failure in the specimen, the stress calculated using a constitutive law and the strain fields $\overline{\sigma_{xx}}^{A}(\epsilon)$ was plotted against the stress calculated with the LSG equation $\overline{\sigma_{xx}}^{A}(LSG)$ (see Section 3.4 of Chapter 3) over a 'virtual gauge area' surrounding the crack, as shown in Figure 4.12. The point at which the two stresses diverge gives the onset of the spuriously high 'strain' value *i.e.* the onset of crack formation. At this time, the LSG stress reaches a maximum, which gives the time of failure and the failure stress. In this work, a virtual gauge size of 20 × 30 pixels was used to track the average stress values in the vicinity of the crack over the loading history. The crack location, time of failure, failure stress value and the location of the virtual gauge is shown for an example specimen in Chapter 6.

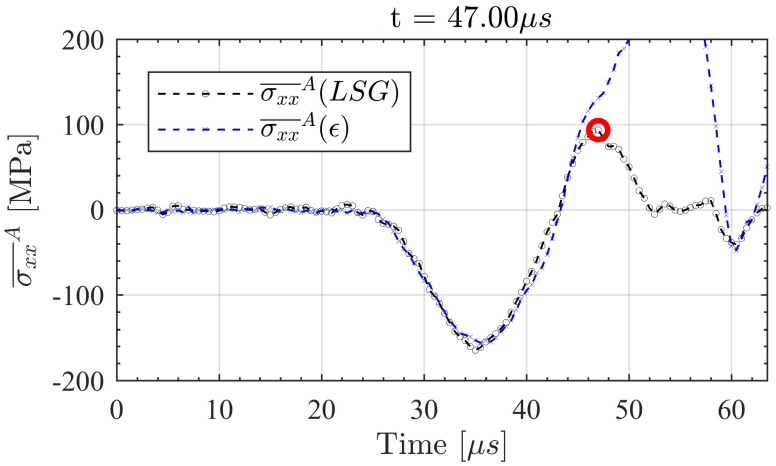

Figure 4.12: Stress calculated using a constitutive law and the strain fields $\overline{\sigma_{xx}}^{A}(\epsilon)$ and the stress calculated from the LSG equation $\overline{\sigma_{xx}}^{A}(LSG)$ over a 'virtual gauge area' surrounding the crack, against time.

4.2.12 Modulus identification for the UD45° case

For off-axis composites, material properties are obtained from angled slices aligned with the principal axis of the material coordinate system. Recall that in this work, the material coordinate system for off-axis composites is aligned with the fibres. Therefore, it was first necessary to rotate the global acceleration and strain fields into material coordinates by the off-axis fibre angle, using standard rotation matrices. Angled slices are considered over the specimen surface and the stress component averages over the slices are calculated using the stress gauge equations. Here, samples orientated with the fibres at -45° use Equations 3.30 and 3.36, whereas samples orientated with the fibres at +45° use Equations 3.33 and 3.37 of Chapter 3 (Note CCW+ convention). One of the processes in calculating the stress averages on an angled slice is to determine $\overline{a_1}^S$ and $\overline{a_2}^S$. Here, it is recalled that Equations 3.30 and 3.36 take the form:

$$\overline{\sigma_{ij}}^L = \frac{\rho S \overline{a_j}^S}{L} \ , \ i = 1, 2 \ \& \ j = 2 \tag{4.9}$$

This was achieved in four steps, as indicated in the flow chart in Figure 4.13 (a). Firstly, the acceleration and strain fields were rotated into the material coordinate system using Equations 3.25 and 3.26 in Chapter 3. Example a_1 acceleration fields in global and material coordinates are given in Figure 4.13 (b) to help illustrate the $\overline{a_i}^S$ calculation procedure. Next, an angled slice is applied to the specimen. In this example, the slice is at -45° to the global x-axis as shown in Figure 4.13 (c), where the number of measurement points on the diagram has been reduced for clarity. The coordinates of the angled slice were determined by calculating the linear equation describing the slice in the global (x, y) system, where the slope of this equation was determined from the fibre angle. In this work, the x-coordinate of the slice was calculated from the y-coordinate of the specimen height. Therefore, the number of x-coordinates considered was equal to the number of y-coordinate divisions in the global coordinate system. The next step was to create a logical mask to be applied to the rotated acceleration fields. This mask was generated by starting at the y-axis pixel location and scanning horizontally along each x-axis pixel to determine whether it was less than the slice x-coordinate. The process was repeated for each y-axis pixel location on the specimen surface, leading to a logical mask consisting of 1's to the left of the slice and 'Not a Number' (NaN) values to the right, as shown in Figure 4.13 (d). The logical mask was then applied to the rotated acceleration fields as in Figure 4.13 (e) and $\overline{a_1}^S$ was calculated from the mean of each masked acceleration field. This process was repeated for each frame and each slice on the specimen for both $\overline{a_1}^S$ and $\overline{a_2}^S$. Here, the range of specimen slices started at the top left-hand corner of the specimen and progressed rightward, until the lower slice coordinate intersected the impact edge, as shown in the schematic in Figure 4.13 (c). Note that the slices did not intersect the impact edge, so that unknown forces were not included in the average stress calculation. Slices can intersect the free-edge of the specimen, however in this report the slices did not intersect the free-edge, so that the number of data points on each slice was consistent.

One of the drawbacks of this method is that it results in a 'staircase' approximation of $\overline{a_1}^S$ over the angled slice, as shown in Figure 4.13 (c). A more accurate method could include a weighted average of the pixel area to the left of the slice equations. However, the error resulting from the staircase approximation to the acceleration surface average was validated with FE simulations in [127], where the error between the calculated and FE modulus values was 0.3%. After the acceleration surface averages were calculated, the surface area S was determined for each specimen slice using the equation $S = H(x_0 + 0.5L\cos\theta)$, recalling that H is the specimen height, x_0 is the distance from the free-edge to the top corner of the slice, L is the slice length and θ is the off-axis angle of the specimen. Lastly, the slice length L was calculated from the specimen geometry and the angle of the fibres using the trigonometric relationship $L = H\sin\theta$. After all terms in Equation 4.9 were calculated numerically, average transverse and shear stresses over each angled slice $\overline{\sigma_{22}}^L$ and $\overline{\sigma_{12}}^L$, respectively, were obtained. Average shear stresses were also calculated from slices orthogonal to the sample fibres, which are labelled slices 2 on Figure 4.13 (c).

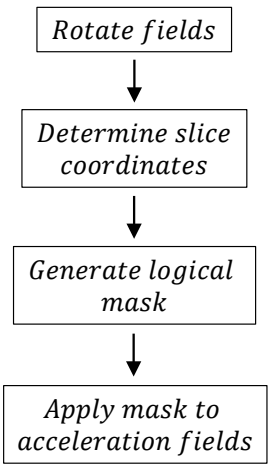

(a) Flowchart for calculating $\overline{a_1}^S$.

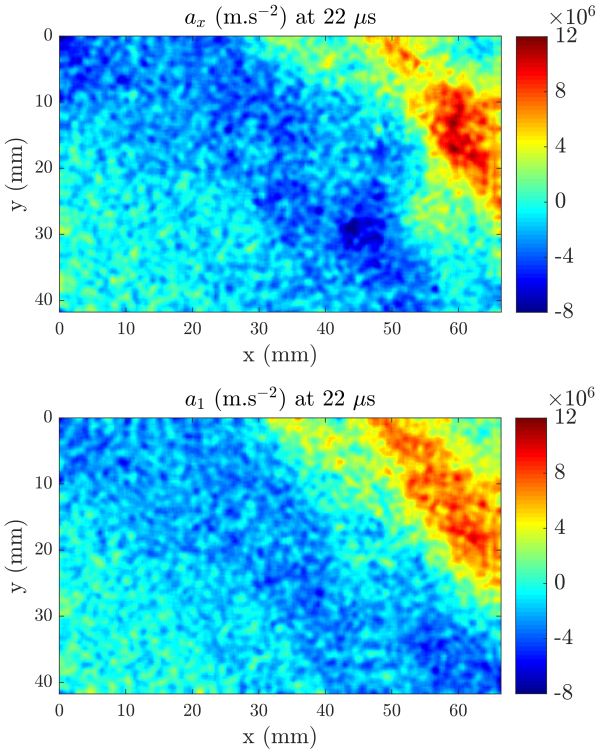

(b) Example a_x and a_1 acceleration fields.

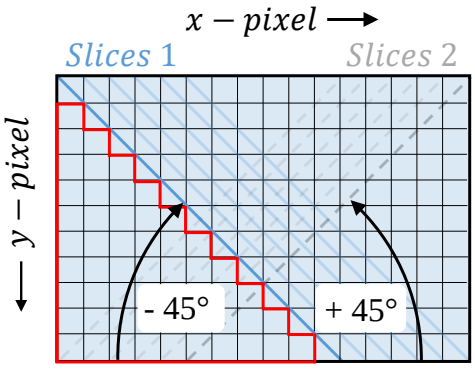

(c) 45° slices on an off-axis specimen.

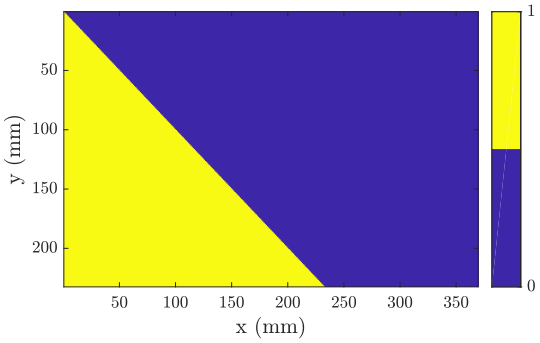

(d) Logical mask for the first slice.

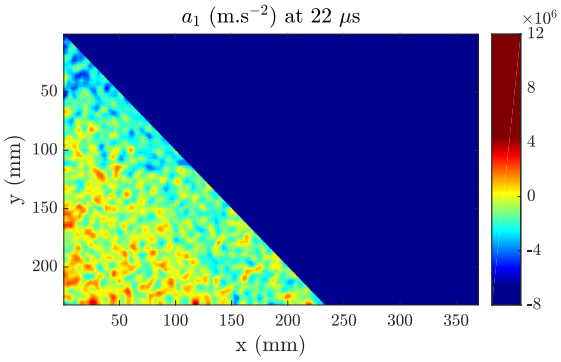

(e) Logical mask applied to a_1, slice 1. $\overline{a_1}^S$ is the average of these data.

Figure 4.13: Flowchart and process to obtain $\overline{a_1}^S$ for an off-axis specimen on slice 1.

Before the average stress-strain curves could be produced for the off-axis samples, average strain values along each angled slice were first determined. For 45° slices, slice strain values coincide with the measurement points (*i.e.* on a pixel centroid), as shown in Figure 4.14 (a). With the exception of a vertical slice, strain values on other slice angles do not coincide with the pixel strains and therefore, strain interpolation to the slice is required. Interpolation of the strain values onto the angled slices was performed in Matlab using the function *scatteredInterpolant*. First, the slice equation was overlaid on the strain field and then the strain value at the x-coordinate of the slice was interpolated from the adjacent data points. This process was repeated for each y-axis pixel location on the specimen surface, as shown in Figure 4.14 (b), for all slices and time steps.

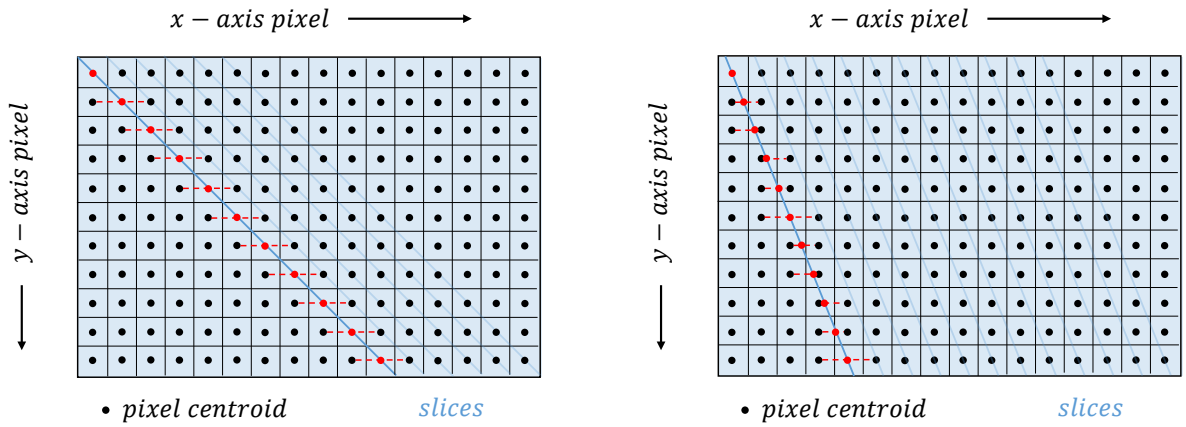

(a) Strains on 45° slices aligning with the pixel strains.

(b) Strains on 60° slices do not align with the pixel strains.

Figure 4.14: Schematic showing how the strains are interpolated along (a) 45° slices and (b) 60° slices.

Average transverse and shear strains were calculated at each slice and plotted against their respective average stress components. Elastic moduli were calculated at each slice from linear fits to the linear portion of the stress-strain curves, using Equation 3.12 and Equation 3.13 of Chapter 3, respectively. Finally, the transverse and shear moduli were identified as the average of all slice modulus values on the sample. Contrary to the UD90° case, all of the slice data was used to identify moduli from the off-axis samples. The reason for this was that data located on the angled slices was further away from the specimen impact and free-edges and was therefore, less sensitive to edge effects within one smoothing kernel size. Note that shear moduli were also identified from linear fits to average shear stress-strain curves obtained from slices orthogonal to the sample fibres. In this report, the shear moduli identified from slices 1 and 2 are $G_{12,\,Sl.1}$ and $G_{12,\,Sl.2}$, respectively. Stress-strain curves and the spatial variation of transverse and shear moduli obtained from a UD45° specimen are given in Chapter 6. In the next chapter, the procedure used to obtain optimised smoothing parameters for experimental results processing is explained.

Chapter 5

Image deformation simulations and numerical verification

During image deformation, displacement fields from a finite element simulation with 'known' inputs (loads, boundary conditions, mesh element size and material properties) are imposed on a synthetically generated image. This process is repeated for each time step of the loading duration, resulting in a set of deformed images from which material properties can be obtained. Because the simulation inputs are known, systematic errors resulting from an experiment can be 'incorporated' in the deformed image set. Therefore, the systematic and random errors resulting from a particular experimental setup can be assessed before an actual test is conducted. Image deformation has provided researchers with the opportunity to analyse the effects of changing various parameters on data obtained from full-field experiments *e.g.* in [28, 65, 124, 126, 128–133]. A key benefit of image deformation is that these effects can be studied prior to a test being performed, saving time and money in material property identification campaigns. Another advantage of incorporating image deformation is that one can obtain 'optimised' processing parameters, which minimise systematic and random errors in material properties identified from experiments. Some of these processing parameters include camera pixel array size and framing rate (particularly in dynamics), image pattern specifications, image contrast, noise and technique specifics *e.g.* speckle size for DIC.

This image deformation study assesses the systematic and random errors resulting from the IBII test setup, from which high strain-rate composite moduli were identified (see Chapter 4). It then shows how these errors change when different combinations of spatial and temporal smoothing were applied during the identification process. It is difficult to quantify the magnitude of the experimental systematic and random errors because the experimental (or actual) dynamic moduli are unknown. Therefore, 'reference' material properties were first specified in the finite element simulations of the IBII tests from which the deformed image sets were created. Prior to this work, the material's strain-rate sensitivity was unknown, so the quasi-static moduli were used for the reference value. Deformed image sets were then processed with a range of smoothing parameters in an image deformation sweep, where the systematic and random errors (relative to the reference) were obtained. The smoothing kernel combination that resulted in the best compromise between the systematic and random errors was then selected to process the experimental images. The specific aims of this chapter are to:

- Predict errors in the modulus values expected from the IBII experiments.
- Compare the resulting errors and processing parameters from grid and DIC speckle images.
- Obtain optimal smoothing parameters that give the best compromise between systematic and random errors on the identified moduli.

5.1 Image deformation procedure

5.1.1 Finite element simulation

The first step in the image deformation procedure was to produce finite element simulations of IBII tests on UD90° and UD45° samples. Each simulation was verified by identifying moduli from the stress and strain fields (FE calculated) with the methods explained in Chapter 4, ensuring that less than 1% difference from the reference values listed in Table 5.1 was obtained. During the verification process, an optimal mesh size was determined from an element size dependence study, where the calculated modulus values converged using a mesh element size of 0.25 mm. Figure 5.1 (a) shows the sample dimensions and the impact edge that was loaded with the pressure profile $\sigma_{xx}(t)$ illustrated in Figure 5.1 (b), which was reconstructed from an experimentally-obtained loading pulse. Numerical instabilities in the finite element calculations caused by high frequency oscillations [134] can be controlled with Rayleigh damping *via* the stiffness proportional damping coefficient β. However, damping and bulk viscosity were disabled because the 'smooth step' function in Abaqus produces a smoothly-varying pulse that does not excite any high-order frequencies. Average stress-strain curves were reconstructed from angled slices on the finite element stress and strain fields (directly). This ensured that edge effects generated from calculating acceleration and strain fields from displacements were removed from the model verification. Figures 5.1 (c) and 5.1 (d) give the UD45° simulation ϵ_{22} strain and σ_{22} stress fields at 20 μs, respectively. Here, the dashed black lines show the range of slices from which the stress-strain curves were reconstructed. Figure 5.1 (e) shows the σ_{22} *vs.* ϵ_{22} curve from the angled slice at the position $x_0 = 12.9$ mm, which is indicated as the red dashed line on Figures 5.1 (c) and 5.1 (d). Modulus values were identified by averaging the moduli over the range of x_0 positions on the sample (black dashed lines on Figures 5.1 (c) and 5.1 (d)), as shown in Figure 5.1 (f). Here, the E_{22} identification utilised the constitutive relationship given in Equation 3.12 of Chapter 3, which assumes that the fibre strains are small relative to the matrix strains.

Table 5.1: Finite element simulation parameters used for the image deformation procedure.

Solver	Abaqus/Explicit
Element type	CPS4R[1] with hourglass control
Specimen size	70×44×4 mm
Element size	0.25×0.25 mm
Material model	Lamina, Elastic
Density	1.57×10^3 kg.m^{-3}
E_{11}	135 GPa [20]
E_{22}	8.0 GPa [20]
G_{12}	4.0 GPa [20]
ν_{12}	0.32 [20]
ν_{21}	0.019
Load	Experimentally derived (see Figure 5.1 (b))
Time steps	128
Output step time	0.5 μs
Solver time step	$1/\sqrt{2}$: 1 × critical time step
Damping	Disabled

[1] 2D plane stress four-node reduced integration point

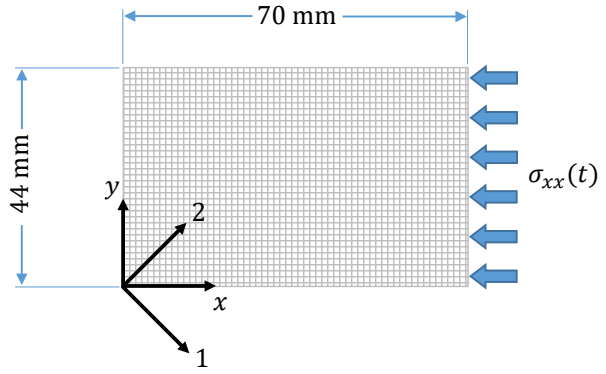

(a) Representation of the sample mesh, indicating the global and material coordinate systems and the edge where the load was applied. Note that the mesh element size is not to scale.

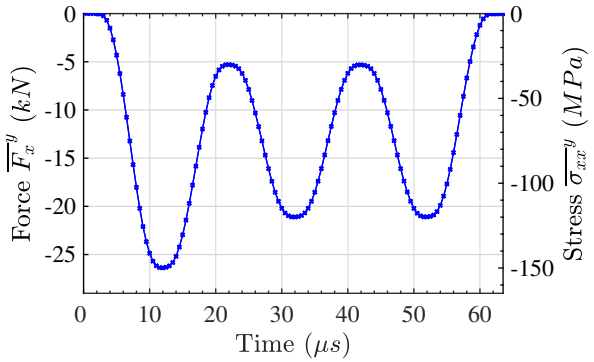

(b) Loading pulse applied to the finite element mesh.

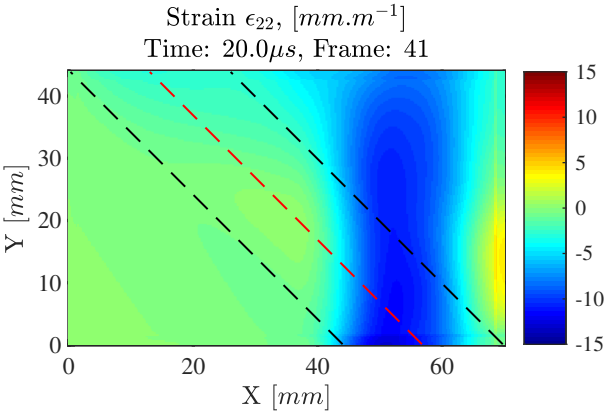

(c) Strain ϵ_{22} field at 20 μs.

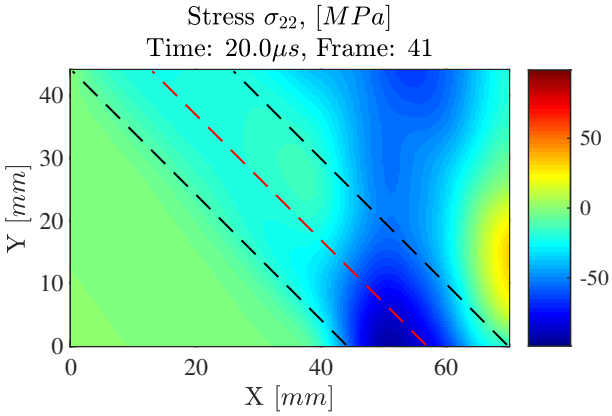

(d) Stress σ_{22} field at 20 μs.

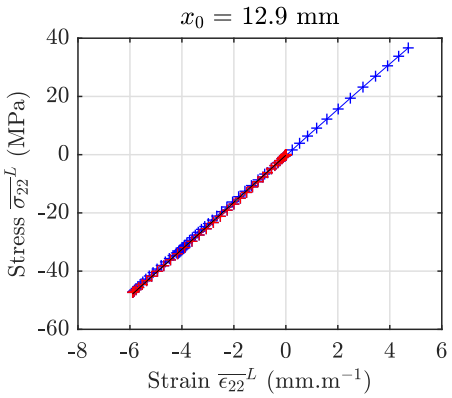

(e) Transverse stress-strain curve at $x_0 = 12.9$ mm with red markers indicating the E_{22} fitting region.

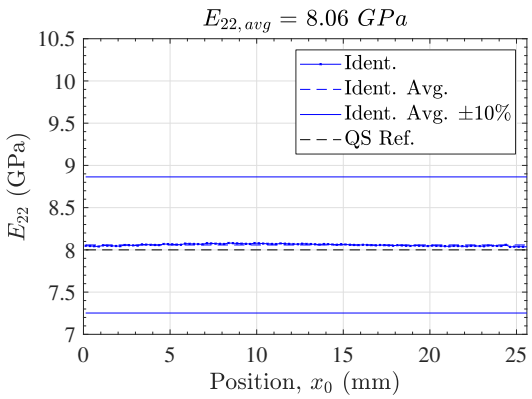

(f) E_{22} *vs.* x_0 position.

Figure 5.1: Setup and results from the finite element simulation of a UD45° IBII test sample. The sample mesh is shown in (a) and the applied load in (b). The ϵ_{22} strain and σ_{22} stress fields at 20 μs are given in (c) and (d), respectively, where the dashed red lines indicate the slice at position $x_0 = 12.9$ mm from which the σ_{22} *vs.* ϵ_{22} plot in (e) was constructed. The E_{22} modulus *vs.* x_0 position is given in (f), where the range of x_0 positions is shown overlayed on the fields in (c) and (d) as dashed black lines.

5.1.2 Synthetic image generation

The second step in the image deformation procedure was to generate a synthetic image that would be artificially deformed using the finite element displacement fields. In this project, two types of synthetic images were produced: a Grid Method 'grid' and a DIC speckle pattern. Details of how each image type was generated and subsequently deformed are now described.

Synthetic grid image

A synthetic grid image comprising of solid white squares and a black background was used for the grid image deformation simulations. Figure 5.2 (a) shows the grid image generated using the equation:

$$G(x,y) = 2^b \left[I_0 + \frac{\gamma}{4} \left(1 + \cos\left(\frac{2\pi x}{p} \right) \right) \left(1 + \cos\left(\frac{2\pi y}{p} \right) \right) \right] \tag{5.1}$$

where $G(x,y)$ is the grey level intensity of the sinusoidal grid, b is the bit depth of the image, I_0 is the average illumination expressed as a fraction of the dynamic range (between 0 and 1), γ is the contrast amplitude expressed as a fraction of the dynamic range (between 0 and 0.5) and p is the grid pitch [117]. Similar to an image generated with the Shimadzu HPV-X camera, the synthetic grid image was initially encoded with 10-bits of information. The size of the image was equal to the camera array size (400 × 250 pixels) and included 10 pixels of free space at the free-edge and 2 pixels of free space above and below the grid. Note that the pixel grey level of the free space was equal to the mean grey level of the grid. Therefore, the size of the actual 'grid' within the synthetic image occupied 390 × 246 pixels. Sizing and the location of the grid within the synthetic image was made to be similar to an experimentally obtained grid image, like that shown in Figure 4.5 of Chapter 4. Including free-space around the grid permitted deformation and rigid body translation of the grid within the bounds of the FOV, similar to an IBII test image. The synthetic grid image histogram given in Figure 5.2 (b) shows a relatively narrow grey level distribution within its dynamic range, due to its formulation from Equation 5.1. Note that the histogram shows the pixel counts and pixel grey levels for the pattern area only, *i.e.* it does not include the free-space surrounding the pattern.

Digital speckle image

Optimised smoothing parameters for processing the IBII test samples with DIC were also obtained using image deformation. For this work, a synthetic DIC speckle image with an average speckle size of 4 pixels was created using the computer generated pattern described in [135, 136]. With this design the position and size of the speckles is controlled with respect to the size of the sample. The speckle pattern is generated by first constructing a random distribution of white and black pixel grey levels over a domain defining the pattern edges. The average speckle size is then controlled by the threshold frequency of a low-pass filter applied to the image [137]. The pixel grey levels in the synthetic speckle pattern were multiplied by 2^{10}, so that the image was initially encoded with 10-bits (similar to the grid image). Because the original speckle pattern was produced from a binary image comprising of only black or white pixels, a Gaussian filter with a standard deviation of 1.25 was applied to increase the distribution of grey levels within the dynamic range. This minimised sharp transitions from black to white pixel grey levels in the image, which can induce displacement field distortions during processing. The image contrast was then matched to an experimentally obtained image. This was achieved by adjusting the minimum and maximum pixel grey levels in the speckle pattern shown in Figure 5.2 (c) until the resulting histogram, shown in Figure 5.2 (d), resembled that from a experimental static image. A link to the Matlab application *Optimised Speckle Generator* used to create the image is provided in the digital dataset located at the end of this thesis. Similar to the synthetic grid image, the size of the speckle pattern was 390 × 246 pixels and including the free-space around the pattern, the FOV was 400 × 250 pixels. As the 70 mm specimen occupied the full 390 pixels of the speckle pattern, the resulting magnification of the image was 0.1795 mm.pixel^{-1}. Table 5.2 provides the specifications for the synthetic DIC speckle images.

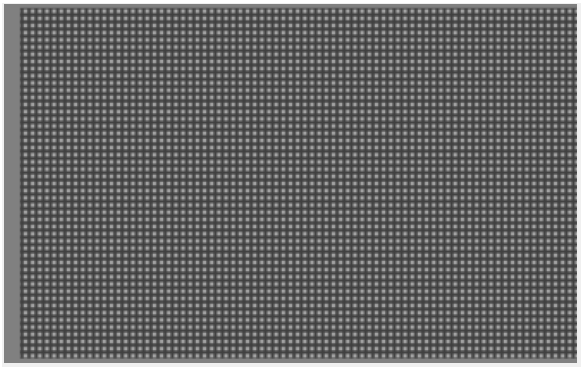

(a) Synthetic grid image.

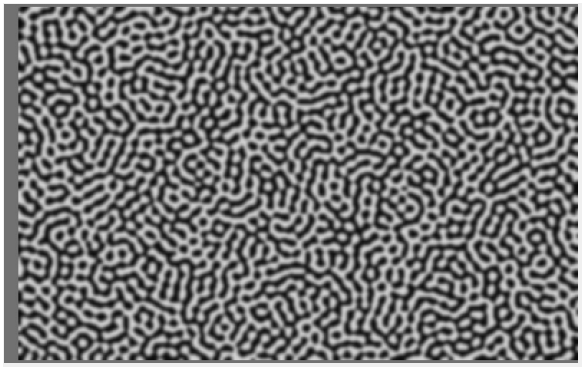

(c) Synthetic speckle pattern image.

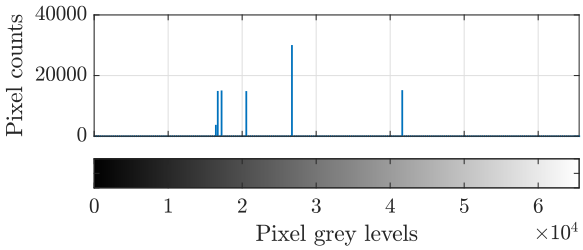

(b) Synthetic grid histogram.

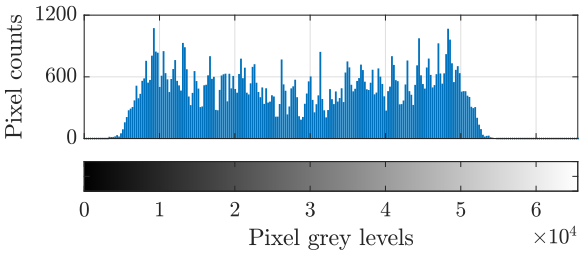

(d) Synthetic speckle pattern histogram.

Figure 5.2: Synthetic grid and speckle pattern images (16-bit) and their histograms.

Table 5.2: Synthetic DIC speckle pattern specifications.

Pattern	Optimised [135, 137]
Printer resolution	446×451 PPI
Average speckle size	4 pixels
Image filter	Gaussian, SD = 1.25
Image size	400 x 250 pixels
Bit depth	10-bit (deformed images scaled to 16-bit)

5.1.3 Deformed image sets

Displacement fields from each finite element simulation output step were imposed on the synthetically generated images, creating sets of deformed grid and speckle images as shown in process schematic shown in Figure 5.3. Deformed analytic grid images were produced by interpolating the undeformed synthetic grid image pixel centroids to the finite element simulation u_x and u_y nodal displacements, and then inserting them into Equation 5.1. However, a different process called sub-pixel interpolation was used to deform the 'random' DIC speckle patterns. Here, the resolution of the synthetic image was initially made finer by linearly interpolating the pixel grey levels by a factor of five, as described in [124, 126]. Nodal values in the finite element displacement fields were then interpolated to the up-sampled synthetic image coordinates. Finally, the displaced image was down-sampled by averaging over the original pixel area, returning the image to its original size. Without these up-sampling and down-sampling processes, the finite element displacements can be applied to pixels adjacent to the desired location. This can lead to errors in the calculated kinematic fields [126] and material properties during processing with full-field techniques. Each deformed image was then scaled to 16-bits, similar to an image that is generated with the Shimadzu HPV-X camera. The Matlab script used to create the deformed image sets can be accessed from the link to the digital dataset.

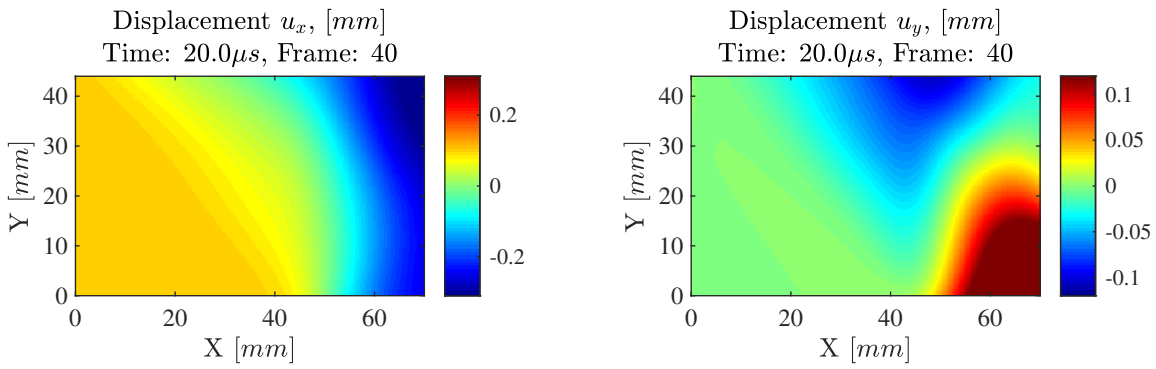

(a) Finite element simulation u_x and u_y displacement fields from the UD45° case at 20 μs.

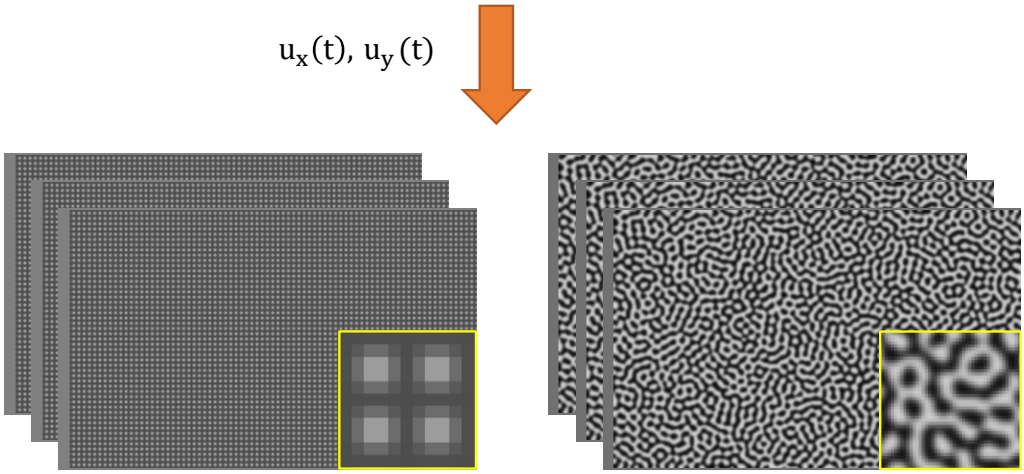

(b) Three of the 128 grid and speckle images from the deformed image sets.

Figure 5.3: Schematic giving an overview of the deformed image set creation where the finite element displacements in (a) are imposed on the synthetic images, creating a set of deformed images represented in (b) for each time step of the simulation (0.5 μs inter-frame time, 64 μs total time).

Despite the up-sampling and down-sampling processes, residual interpolation errors in the deformed speckle image sets were anticipated [126]. Therefore, equal comparison was made between the speckle and grid image deformation results by additionally analysing a grid image set deformed using sub-pixel interpolation. Therefore in this work, image deformation results from three different types of deformed image sets were compared:

- Grid images deformed using an analytical equation.
- Grid images deformed with sub-pixel interpolation.
- Speckle images deformed with sub-pixel interpolation.

5.1.4 Image deformation verification and sweep

In the last step of the image deformation process, material parameters were identified from the synthetically deformed images using the same methods for processing experimental images (see Chapter 4). Further interrogation of the deformed images was then undertaken to assess the following:

1) Systematic errors - no smoothing, no noise (verification)
2) Systematic errors - smoothing, no noise (combine with 3. to check noise-induced bias)
3) Systematic and random errors - smoothing and noise (obtain optimised smoothing parameters)

The purpose of 1) was to verify that the systematic errors on the moduli identified from each image type were reasonable (*i.e.* were within a few percent of the reference) without smoothing or added noise. In assessment 2) the deformed image sets were processed using a range of spatial and temporal smoothing kernel size combinations (without the addition of simulated noise). For this analysis, smoothing kernel sizes of $S_k = [0, 11, 21, 31, 41, 51, 61]$ and $T_k = [0, 5, 11, 15, 21, 25, 31]$ were assessed, where S_k and T_k are the spatial and temporal smoothing kernel sizes, respectively. For assessment 3) Gaussian white noise was added to the deformed image sets to simulate the noise generated from the Shimadzu HPV-X camera in IBII tests [117]. Here, the noise field amplitude was iteratively adjusted until the displacement field resolution obtained from a set of 128 static synthetic images matched that from a set of experimental statics. Following this process resulted in noise amplitudes of 0.4% and 0.32% of the dynamic range for the grid and speckle images, respectively. In total, thirty copies of images polluted with unique, random noise fields were assessed in the image deformation sweeps. Before the combined systematic and random error assessment, the results from 2) and 3) were compared to ensure that there was no noise-induced bias on the systematic errors. This was expected to be low due to the linear elastic material behaviour of the CFRP composite analysed here.

5.1.5 Definition of errors

Systematic, random and total errors on modulus values identified with the IBII test method were assessed in the image deformation study. In this application, systematic errors result from the camera pixel array size and selected framing rate, while random errors are generated from the amount of noise in the recorded images. Spatial and temporal smoothing is undertaken to reduce the effects of noise (*i.e.* random errors) on the identified modulus. However, there is a trade-off between systematic and random error reduction with smoothing, in that increased smoothing will reduce the random error, but can increase the systematic error (and vice-versa). In this image deformation study, the ideal compromise between systematic and random errors on the identified modulus values was determined. This was achieved by calculating the systematic, random and total errors on the identified moduli, for a range of smoothing kernel sizes and noise representative of that present in a real test. The smoothing parameter combination that minimised the total error on the identified modulus was then selected to process the experimental results. In this work the systematic error Err_{sys} is defined as:

$$Err_{sys} = \frac{(\overline{Q_{ii,ID}} - Q_{ii,FE})}{Q_{ii,FE}} \ , \ i = 2, 6 \tag{5.2}$$

where $\overline{Q_{ii,ID}}$ is the mean identified stiffness over 30 noise copies and $Q_{ii,FE}$ is the reference stiffness value specified in the finite element simulation material model. Here we recall that for this material the transverse modulus $E_{22} \approx Q_{22}$ and $G_{12} \approx Q_{66}$ (see Chapter 3). The random error is defined as the SD of the calculated stiffness values over 30 copies of noise, normalised by the reference stiffness:

$$Err_{rnd} = \frac{1}{Q_{ii,FE}} \sqrt{\frac{\sum_{k=1}^{N} (Q_{ii,ID}^{k} - Q_{ii,FE})^2}{N - 1}} \tag{5.3}$$

where $N = 30$ total iterations and $Q_{ii,ID}^{k}$ is the stiffness identified for the k^{th} iteration. The total error between the stiffness value calculated for each smoothing kernel size combination relative to the 'reference' stiffness specified in the finite element simulation is:

$$Err_{tot} = |Err_{sys}| + 2Err_{rand} \tag{5.4}$$

5.2 Image deformation results: no noise

5.2.1 Numerical verification of the identified moduli

Prior to the error assessments, the modulus values identified from the grid and speckle images (without smoothing) were compared to the finite element simulation results. UD45° case E_{22} *vs.* x_0 position plots from the three deformed image types are overlaid in Figure 5.4. Here, the identified moduli listed in the legend are the average of the modulus values obtained over the range of slices on the sample, as shown on Figure 5.1 (f). Figure 5.4 shows that the transverse modulus identified from the analytic grids of 8.11 GPa was within 0.63% of the finite element simulation value of $E_{22} = 8.06$ GPa. This result was expected, as low errors were anticipated from the analytically deformed images. Grid images deformed with sub-pixel interpolation were also within 1% of finite element value and therefore, the method of deforming grids with sub-pixel interpolation was verified. Figure 5.4 also shows the identified modulus value obtained from the speckle images, which was less stable over the specimen width but also within 1.1% of the finite element calculation. Similar results were obtained from the UD90° case E_{22} and the UD45° case G_{12} identifications, which are catalogued in Appendix A. Given that the moduli obtained from all three image types were within 1.1% of the finite element values, the methods used to deform the images were considered verified. Note that these numerical verifications of the identified modulus values were for the noiseless case, and that effects from noise were assessed in the image deformation sweeps in the next section.

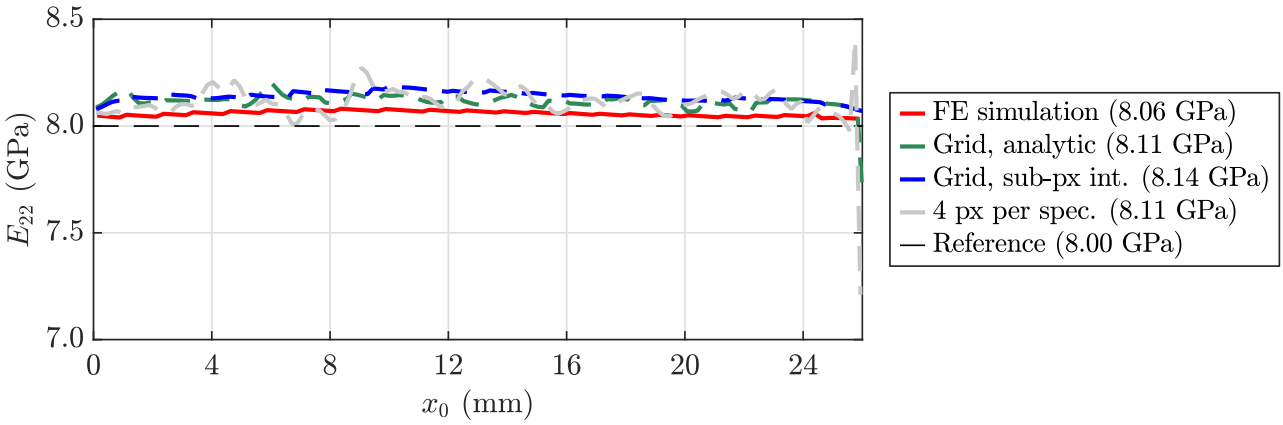

Figure 5.4: UD45° case E_{22} *vs.* x_0 position results from the finite element simulation and the three types of deformed image sets.

5.2.2 Systematic error analysis

Noise influences on the systematic errors obtained from each smoothing kernel combination were assessed by comparing the results from the noiseless and noise-polluted images. Systematic error maps from the noiseless and noisy images for the UD90° case Q_{22} identification from the analytic grids are shown in Figures 5.5 (a) and (b), respectively. In these heat maps, the colour bar indicates the error magnitude on the identified stiffness component resulting from each spatial and temporal smoothing kernel size combination. Captions above each heat map indicate the type of error on the identified stiffness component (in %). These maps show the effect of increasing the spatial kernel size on the systematic error. As the spatial kernel size increases the strains are 'smeared', which increases the calculated stiffness and makes the systematic error more positive. Effects on the systematic error from an increasing temporal smoothing kernel size are also visible. When the temporal smoothing kernel size increases, the accelerations (and calculated stresses) are 'smeared', so the calculated stiffness is reduced and the systematic error becomes more negative. Figure 5.5 (a) also shows a green coloured valley where the trade-off between the average stress and strain was in balance, giving an overall reduced systematic error on the stiffness. For some of the stiffness components, it was difficult to

assess the influence of noise on the systematic errors calculated from the noisy images 'by-eye'. This can be more explicitly seen in Figure 5.5 (c), which plots the noisy minus the noiseless systematic errors for the UD90° case Q_{22} identification. From this result it was clear that after a small amount of spatial smoothing was applied, effects from noise on the systematic errors were removed. Results for the sub-pixel interpolated grids and speckles were similar, as shown in Figures 5.5 (d), (e) and (f) and Figures 5.5 (g), (h) and (i), respectively. These trends extended to the UD45° case results, which for brevity are not shown here but can be found in Appendix B. Given the low error magnitudes obtained from the difference maps from all image types and sample configurations, influences from noise on the systematic errors were deemed minor. This result was expected given the linear elastic material model specified in the finite element simulation.

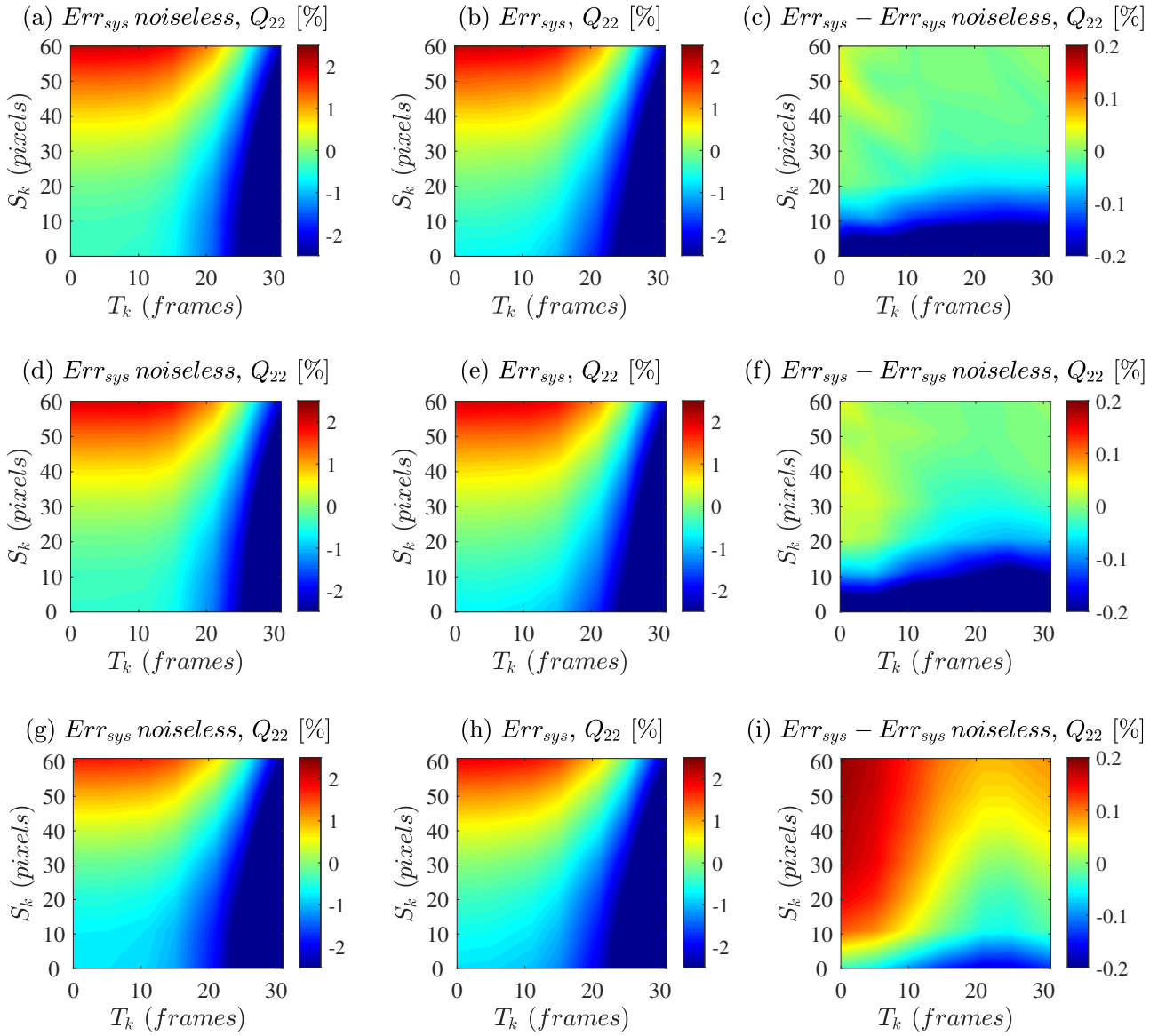

Figure 5.5: Systematic error maps from the noiseless sweep, the noise sweep and the difference between the noise and noiseless sweeps for the analytic grids (a)−(c), sub-pixel interpolation grids (d)−(f) and sub-pixel interpolation speckles (g)−(i) for the UD90° case Q_{22} identification.

5.3 Image deformation results: noise

Systematic, random and total errors from a range of smoothing parameter combinations were obtained from an image deformation sweep using the noise-polluted images. Here it is recalled that the range of spatial and temporal smoothing kernels assessed were S_k = [0, 11, 21, 31, 41, 51, 61] and T_k = [0, 5, 11, 15, 21, 25, 31]. Errors were obtained from each smoothing parameter combination [S_k, T_k] over 30 copies of noise, meaning that a total of $49 \times 30 = 1470$ calculations were performed in each sweep. In the following heat maps, the red cross gives the smoothing kernel size combination that results in the lowest error.

5.3.1 Sweep results: UD90° case

Systematic, random and total errors on Q_{22} for the UD90° case are shown in Figure 5.6. Note that the noisy systematic error map shown in Figure 5.6 (a) is the same as that shown in Figure 5.5 (a), from which trends in the systematic errors were previously discussed. Figure 5.6 (b) shows the random error, which was largely insensitive to spatial smoothing. The heat map also shows that only a small amount of temporal smoothing was required to drastically decrease the random error, as indicated by the large 'blue' area in Figure 5.6 (b). Observing the heat maps in Figures 5.6 (a) and (b), the trade-off between systematic and random errors in relation to the smoothing parameters is revealed. To demonstrate, in Figure 5.6 (a) there is a large 'green' area where systematic errors are low for spatial and temporal smoothing kernel sizes between 10−30 pixels and 0−15 frames, respectively. Over this range of smoothing parameters, one could select no temporal smoothing and obtain a low systematic error, however this would result in the maximum random error, as indicated by the 'red' region in Figure 5.6 (b). Conversely, if too much temporal smoothing is applied, the systematic error would become more negative, as indicated by the 'blue' region in Figure 5.6 (a). Although, it is noted that the random error magnitudes were relatively low compared to the systematic error magnitudes, meaning that the effects from the camera's pixel array size and framing rate were more significant than noise (over the range of smoothing kernels assessed). The dominance of the systematic error was evident in the total error map shown in Figure 5.6 (c), which essentially represents absolute values of the systematic errors. This heat map shows a large 'blue' valley of low total error, where effects from the spatial and temporal smoothing kernels are balanced. Because the valley of low total error spans a significant portion of the total error maps, there is some flexibility in the smoothing kernel combination that can be selected to minimise errors under 1%.

Comparing the error maps in Figures 5.6 (a)−(c) and Figures 5.6 (d)−(f), no significant differences were obtained from the grids deformed with the analytic equation and sub-pixel interpolation. Therefore, errors obtained from the DIC images are comparable to the grids irrespective of the method used to deform the images. Results from the DIC images are given in Figures 5.6 (g)−(i), which were generally similar to the results from the grid images. However, the systematic error map in Figure 5.6 (g) was slightly shifted upwards compared to the grid results in Figures 5.6 (a) and (d). This upward shift was likely due to the lower spatial resolution resulting from the 13-pixel subsets used to process the DIC images. With the lower spatial resolution, the acceleration (and calculated stress) fields are 'smeared' and the identified modulus value is reduced. As indicated in Figure 5.6 (g), additional spatial smoothing was required to smear the strains, increase the modulus and reduce the systematic error. Overall trends in the random error magnitudes from the DIC images were similar to the grids, with values spanning from 0.02−0.08% over the range of smoothing kernels evaluated here. The slight upward shift in the systematic error map translated to the total error map shown in Figure 5.6 (i). Here, the location of the 'red' cross gives the smoothing parameter combination resulting in the minimum error, which was slightly higher for the DIC images compared to the grids. Given the large 'blue' valley of low total error magnitudes, one could select similar smoothing parameters to process both grid and DIC images for the identification of E_{22} in the UD90° case.

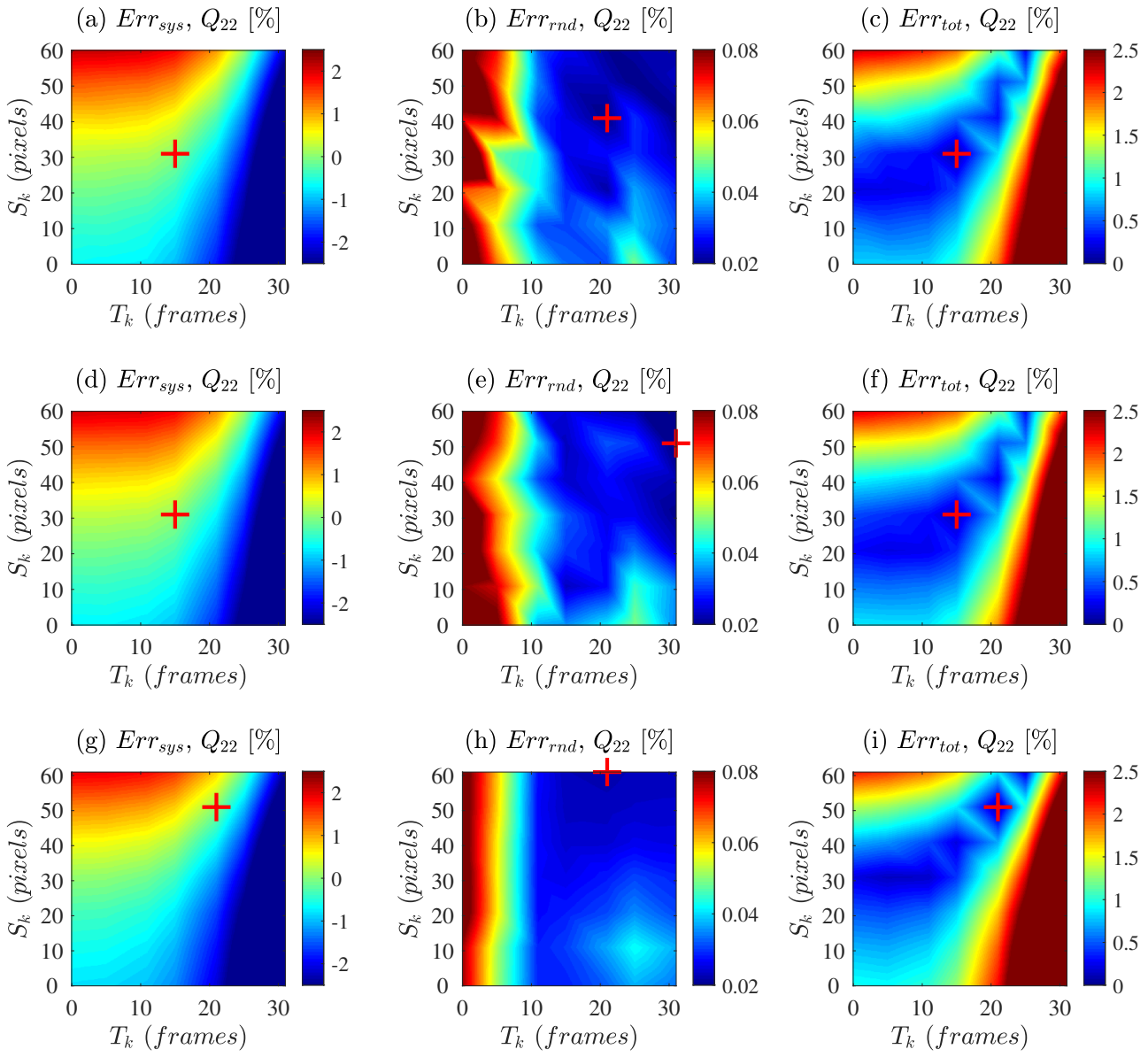

Figure 5.6: UD90° case systematic, random and total error maps for the identification of Q_{22} from the (a)−(c) analytic grids, (d)−(f) sub-pixel interpolation grids and the (g)−(i) speckle images.

5.3.2 Sweep results: UD45° case

Systematic, random and total error maps for the UD45° case Q_{22} identification from the three image types are given in Figure 5.7. The Q_{22} systematic error map from the analytic grids in Figure 5.7 (a) revealed a slightly unbalanced relationship between the spatial and temporal smoothing kernel sizes. This trade-off was more balanced for the UD90° case however, the angled fibres in the UD45° samples generated more complex kinematics, which resulted in a different relationship between spatial and temporal smoothing. Trends in the UD45° case Q_{22} random error maps were similar to the UD90° case, however the random error magnitudes were slightly higher at around 0.3%. This higher random error magnitude was expected because of the slightly lower signal-to-noise ratio obtained from the UD45° case ϵ_{22} strain fields. The unbalanced relationship between the spatial and temporal smoothing effects on the systematic error influenced the total error map shown in Figure 5.7 (c). Overall, the UD45° case Q_{22} error maps from the analytic and sub-pixel interpolation grids were similar, which can be seen comparing Figures 5.7 (a), (b) and (c) with Figures 5.7 (d), (e) and (f). However, the UD45° case Q_{22} systematic error map obtained from the DIC images was shifted downwards compared to the grids, as shown in Figure 5.7 (g). This can be more easily seen when comparing the

systematic errors for the no-smoothing condition, which were around 1% for DIC and -0.1% for the grids (compare the lower left-hand corner of Figures 5.7 (g) and (a)). The reason for the downwards shift in the DIC case systematic error heat maps was likely a result of the reduced spatial resolution of DIC. This leads to increased systematic errors in the spatial gradients of the displacements (strains) and the temporal gradients (accelerations), both of which contribute to the identified stiffness. The random and total error heat maps from the DIC images again followed the trends obtained from the grid images in terms of overall shape and magnitude, as seen in Figures 5.7 (h) and (i). For the UD45° case, less spatial smoothing was required to reduce the total errors on the Q_{22} identification (compare Figures 5.7 (i) and (c)). Considering that there was already some inherent spatial smoothing coming from the 13-pixel subsets, this result seemed logical. However, this was contrary to the UD90° result shown in Figure 5.6 (g), where more spatial and temporal smoothing was required compared to the grids in Figure 5.6 (c). These results implied that the strains and accelerations (and calculated stiffness) were affected differently by the lower spatial resolution in each sample configuration.

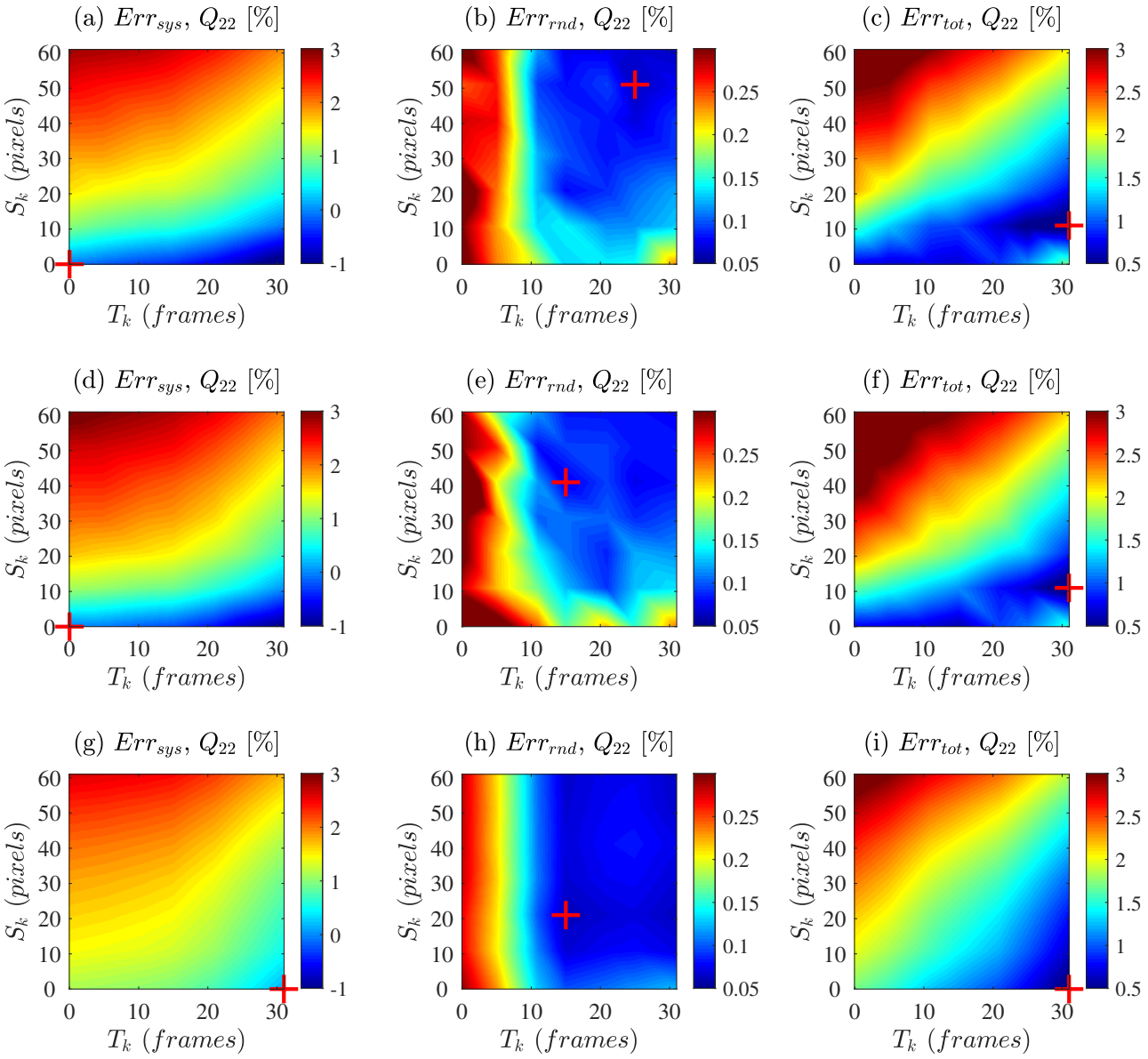

Figure 5.7: UD45° case systematic, random and total error maps for the identification of Q_{22} from the (a)−(c) analytic grids, (d)−(f) sub-pixel interpolation grids and the (g)−(i) speckle images.

Error maps for the UD45° case Q_{66} identification from slices 1 and 2 are given in Figures 5.8 and 5.9, respectively. One noticeable difference in the Q_{66} systematic and total error maps from the two slices is that the trends from slices 2 are almost a mirror image of slices 1. As seen in the systematic error plots from slices 1 in Figures 5.8 (a), (d) and (g), increasing temporal smoothing makes the systematic errors more negative. Conversely, increasing temporal kernel sizes leads to more positive systematic errors for the slice 2 results shown in Figures 5.9 (a), (d) and (g). Because the random error magnitudes were low, this trend was also clearly seen in the total error plots in Figures 5.8 (c), (f) and (i) and Figures 5.9 (c), (f) and (i). This observation can be attributed to the different average strain and acceleration histories from the two slices obtained over the duration that the stiffness values are calculated. To illustrate this point, representative slices parallel (slices 1) and transverse (slices 2) to the fibres are shown overlayed on the γ_{12} strain field at 20 μs in Figure 5.10 (a). Average shear strain histories from the two slices are shown alongside in Figure 5.10 (b). Here, the strains are plotted to their maximum absolute value, which defines the fitting region for the stiffness identification. As the slices see different average strains over the loading history, the systematic errors calculated from each smoothing kernel combination will also be different, resulting in unique heat maps for each slice.

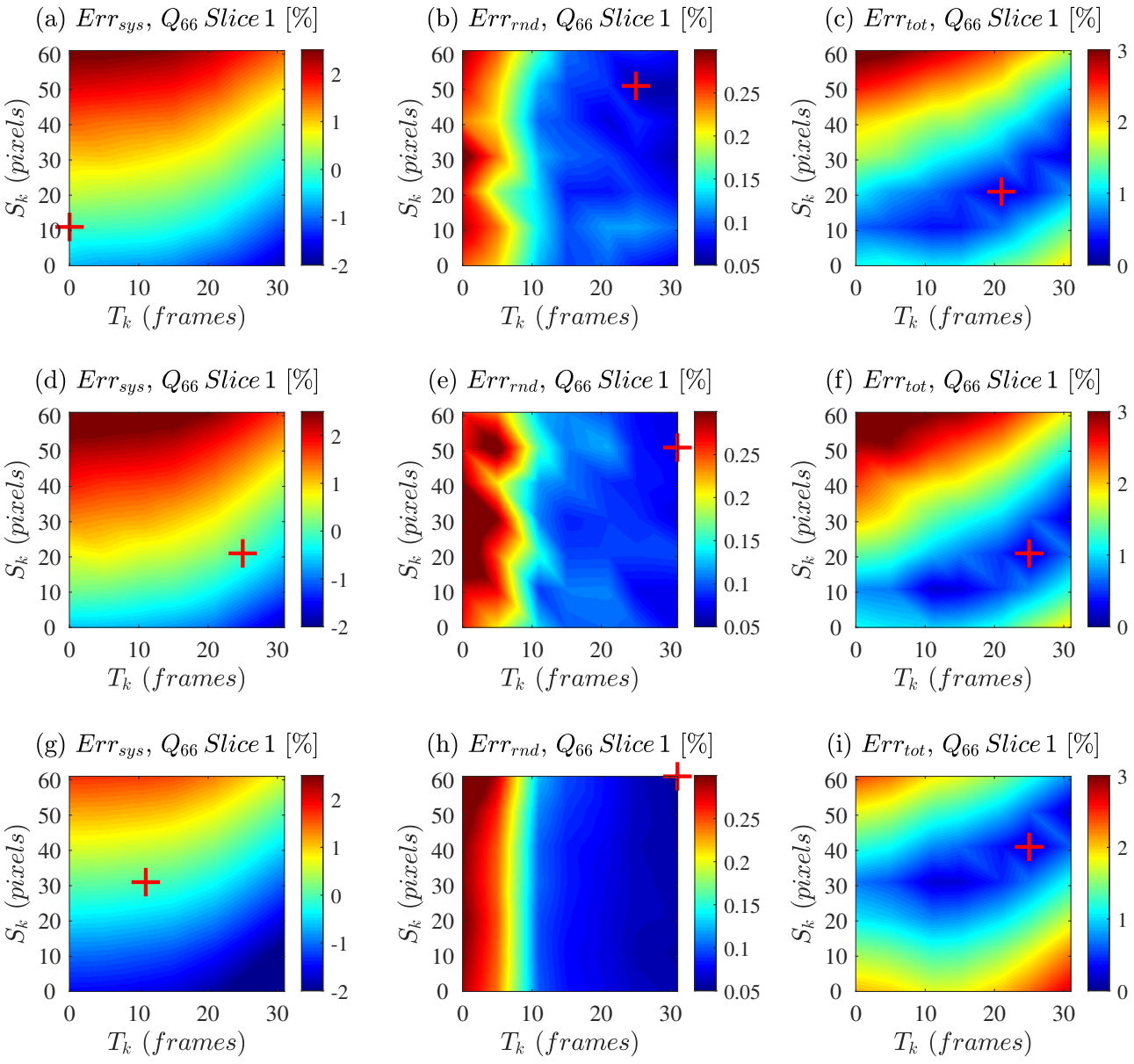

Figure 5.8: UD45° case systematic, random and total error maps for the identification of $Q_{66\,Sl.\,1}$ from the (a)−(c) analytic grids, (d)−(f) sub-pixel interpolation grids and the (g)−(i) speckle images.

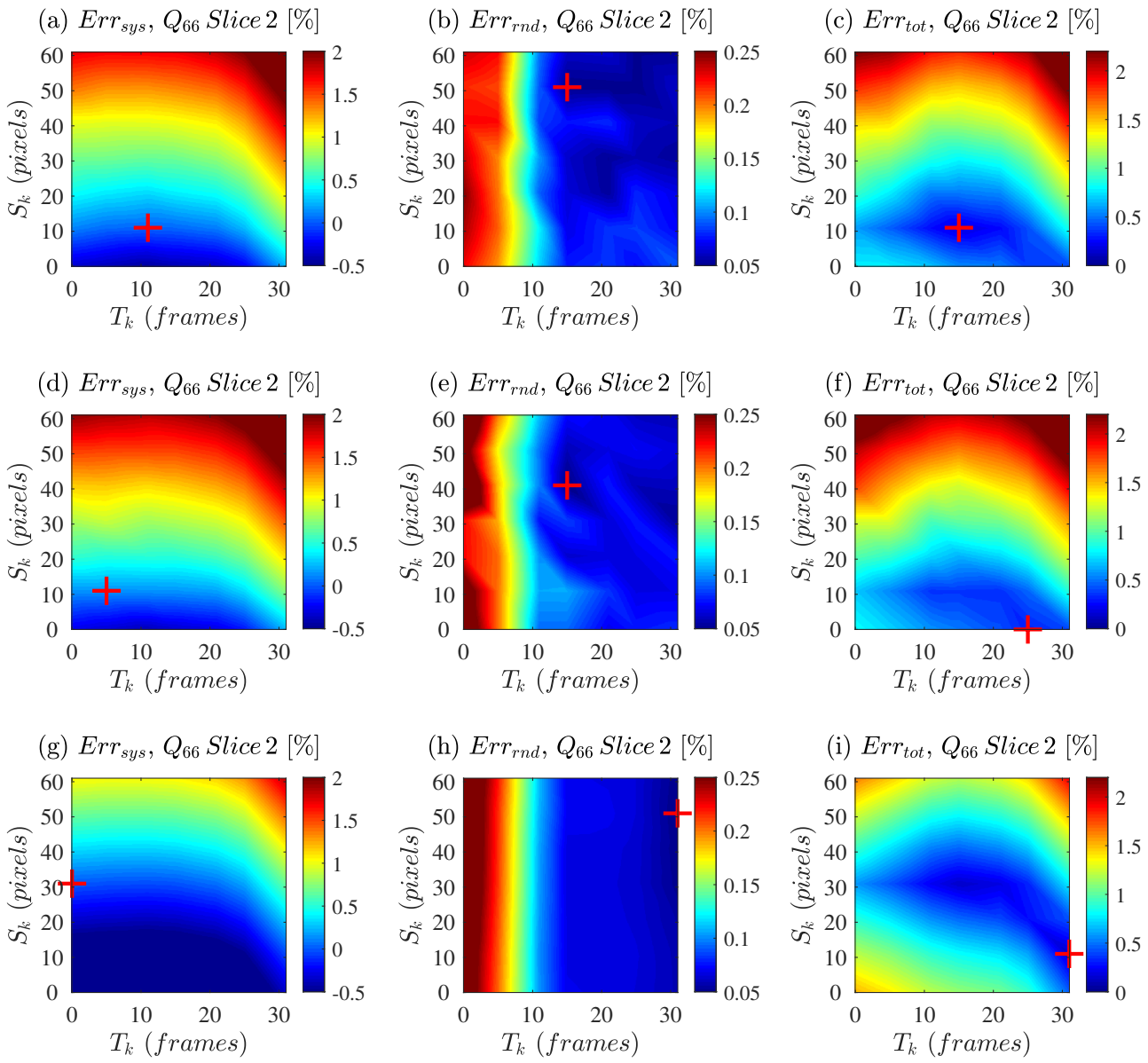

Figure 5.9: UD45° case systematic, random and total error maps for the identification of $Q_{66\,Sl.\,2}$ from the (a)−(c) analytic grids, (d)−(f) sub-pixel interpolation grids and the (g)−(i) speckle images.

5.3.3 Optimised smoothing parameters

Optimised smoothing parameters were determined from the spatial and temporal smoothing kernel combination that resulted in predicted total errors of less than 1% for both sample configurations. Table 5.3 summarises the optimal smoothing parameters and the predicted errors (systematic, random and total) on the identified moduli for the analytic grids and DIC images. For the UD90° case grids, the total error was minimised to 0.05% with spatial and temporal kernels of 31 pixels and 15 frames, respectively. With this smoothing kernel combination, the resulting systematic and random errors were 0.002% and 0.03%, respectively, as listed in Table 5.3. Therefore, this kernel combination (S_k=31 pixels, T_k=15 frames) was selected to process experimental results from the UD90° grid specimens. For the deformed UD90° case speckle images, the total error on the identified transverse modulus was minimised to 0.06% with a smoothing kernel combination of S_k=51 pixels, T_k=21 frames. However,

another blue region of low total error can be seen on the left-hand side of Figure 5.6 (i). In this region, a smoothing kernel combination with lower kernel values of S_k=31 pixels, T_k=5 frames resulted in a total error of 0.14%. As these smoothing parameters would also be used to process more localised failure stress properties, this smoothing parameter combination (S_k=31 pixels, T_k=5 frames) was selected to process the UD90° case speckle images. With this kernel combination the resulting systematic and random errors were 0.03% and 0.06%, respectively, as listed in Table 5.3.

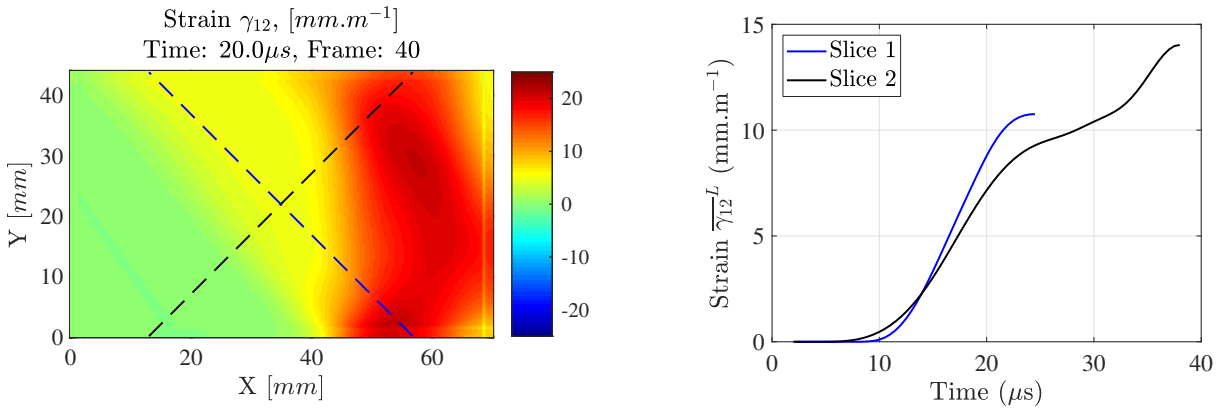

(a) γ_{12} field at 20 μs with representative slices parallel (slice 1) and transverse (slice 2) to the fibres at position x_0 = 12.9 mm.

(b) Average shear strain $\overline{\gamma_{12}}^{L}$ *vs.* time over the loading duration for slices 1 and 2 at position x_0 = 12.9 mm.

Figure 5.10: UD45° case finite element simulation (a) shear strain field and (b) average shear strain.

In consideration of the total error plots for the off-axis case, it is clear that different kernel combinations were required to optimise each of the modulus components. Different smoothing parameters could be used to identify each modulus component individually however, this would increase the time to process each test. Therefore, optimal smoothing was determined by selecting the temporal and spatial kernel combination that minimised the sum of the total errors from all identified modulus components using the Equation 5.5:

$$\min_{S_k,T_k\in(0:61,0:31)} \frac{(Err_{tot},\, Q_{22}) + (Err_{tot},\, Q_{66}\, Slice\, 1) + (Err_{tot},\, Q_{66}\, Slice\, 2)}{3} \tag{5.5}$$

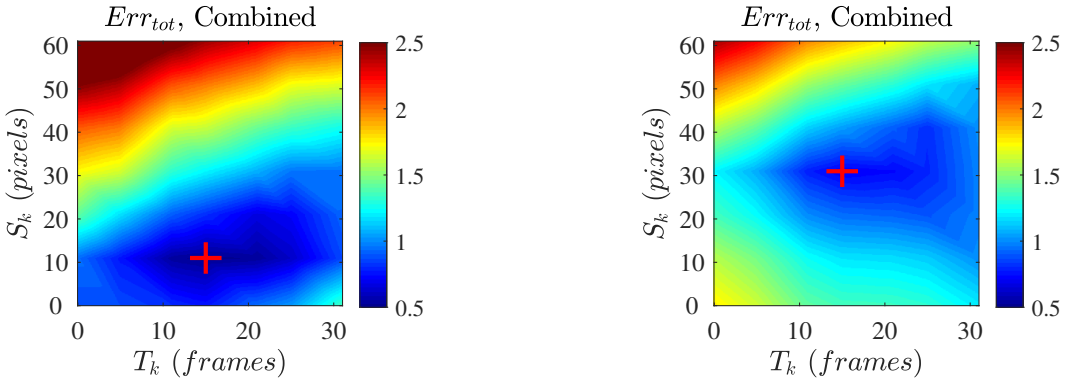

(a) Analytic grids.

(b) DIC speckle images.

Figure 5.11: Average of the total errors for all stiffness components for the UD45° case. The red cross gives the smoothing kernel combination that resulted in the lowest combined total error.

Table 5.3: Random Err_{rnd} and systematic Err_{sys} errors resulting from the smoothing parameter combination $[S_k, T_k]$ that minimised the total error Err_{tot} on the identified stiffness components, for the analytic grid and speckle images.

Case	Comp.	Analytic grid images				DIC speckle images			
		$[S_k, T_k]$ (Px, fr)	Err_{sys} (%)	Err_{rnd} (%)	Err_{tot} (%)	$[S_k, T_k]$ (Px, fr)	Err_{sys} (%)	Err_{rnd} (%)	Err_{tot} (%)
UD90°	Q_{22}	[31, 15]	0.002	0.03	0.05	[51, 21]	0.009	0.02	0.06
						[31, 5][1]	0.03	0.06	0.14
UD45°	Q_{22}	[11, 31]	-0.08	0.13	0.34	[0, 31]	0.15	0.13	0.40
UD45°	$Q_{66,\,Sl.\,1}$	[21, 21]	0.06	0.08	0.23	[41, 25]	-0.04	0.06	0.17
UD45°	$Q_{66,\,Sl.\,2}$	[11, 15]	0.04	0.07	0.18	[11, 31]	-0.03	0.06	0.14
UD45°	Eq. 5.4	[11, 15]	0.17	0.10	0.51	[31, 15]	0.52	0.07	0.72

[1] Did not minimise the total error

Figure 5.11 (a) shows the average of the total errors from each UD45° case modulus component for the analytic grids, where Equation 5.5 was minimised to 0.51% with spatial and temporal kernels of 11 pixels and 15 frames, respectively. The same process was applied to the speckle images, where Equation 5.5 was minimised to 0.72% with spatial and temporal kernels of 31 pixels and 15 frames, respectively. This region of minimum error for the combined modulus components can be seen from the red cross in Figure 5.11 (b)). Table 5.3 gives a summary of the optimised smoothing parameters used to process the experimental grid and DIC speckle images. It should be noted that for all cases, quite a large area in the heat maps produced low errors (dark blue zones). This was reassuring as it confirmed that the identification behaviour was rather stable over the range of smoothing kernel sizes assessed. However, without this study one could have ended up selecting harsher spatial smoothing leading to significantly larger systematic errors, or large random errors from not smoothing at all. Therefore, the results generated from image deformation studies are useful for an informed selection.

5.3.4 Verification of using the quasi-static reference

After the IBII tests were performed, a single image deformation study was performed using the experimentally obtained dynamic modulus values as the reference in the finite element simulation. Transverse and shear modulus values of $E_{22} = 10.0$ GPa and $G_{12} = 5.5$ GPa obtained from IBII tests were specified for both the UD90° and UD45° cases. Deformed analytic grid image sets were created and processed with the optimised smoothing parameter combinations listed in Table 5.3, recalling that these parameters were obtained from the image deformation sweep that used the quasi-static modulus values as the reference. Similar to the previous analysis, 30 copies of noise were assessed in each sweep. For the UD90° case, the total error on the identified Q_{22} modulus was 0.24%. Total errors on the UD45° case Q_{22}, $Q_{66,\,Sl.\,1}$ and $Q_{66,\,Sl.\,2}$ moduli were 0.82%, 0.35% and 0.67%, respectively. Because the resulting errors on all modulus components for both cases were less than 1%, the approach of using the quasi-static value as the reference in the image deformation simulations was reasonable.

5.4 Summary

In this chapter, results from an image deformation study provided the ability to make informed choices when selecting smoothing parameters to processing full-field displacement data. Smoothing parameters were selected to minimise errors in the high strain-rate modulus properties for off-axis composites identified from IBII tests. A summary of the main findings of this chapter is given below:

- For both the UD90° and UD45° cases, the systematic, random and total errors in the stiffness components identified from the synthetic grid images deformed through the analytic equation and sub-pixel interpolation were similar.
- Generally speaking, for the imaging setup used in this project (Shimadzu HPV-X camera with a pixel array size of 400×250 pixels and a frame rate of 2 MHz), a DIC speckle pattern with a speckle size of 4 pixels could be used to identify stiffness values with predicted errors of ±2.5% and -1 to +3% for the UD90° and UD45° cases, respectively. Analysis of the systematic and random error maps generated during the image deformation study was used to obtain optimised smoothing parameters, which reduce these errors to less than 1%.
- More complex kinematics in the UD45° sample shifted the relationship between the spatial and temporal smoothing on the systematic error, which was present for the UD90° case. This highlights the importance of incorporating an image deformation analysis for material property identification with off-axis samples, *i.e.* the UD90° case optimised smoothing parameters are not transferable to the UD45° case.
- Additional spatial smoothing was required to offset the reduced UD90° case Q_{22} stiffness obtained from the DIC images, resulting from the lower spatial resolution of the 13-pixel subsets compared to the 5 pixel grid pitch. However, the more complex kinematic fields in the UD45° sample required less spatial smoothing to minimise errors on the Q_{22} stiffness identification from the DIC images.
- The lower signal-to-noise ratio of the strains for the UD45° configuration led to an increased random error magnitude compared to the UD90° case. Although the random error magnitudes were low, noise-optimised virtual fields could be included in future image deformation analysis [77].
- Slightly more spatial smoothing was required to reduce the combination of errors in the UD45° case Q_{22}, $Q_{66,\,Sl.\,1}$ and $Q_{66,\,Sl.\,2}$ stiffness values obtained from the DIC images compared to the grids. This result was expected because the reduced spatial resolution from DIC affected each stiffness component differently.

Chapter 6

Experimental results 1: Grid Method

6.1 Quasi-static tests

Figure 6.1 (a) shows the transverse stress *vs.* strain response from the quasi-static tensile test on UD45° Specimen 1. Transverse modulus E_{22} values were obtained from linear fits over the predominantly linear region of the curve, to a transverse strain value of 2.0 mm.m^{-1}. Figure 6.1 (b) shows the shear stress-strain curve, which transitioned from a linear to a non-linear response at approximately 3.0 mm.m^{-1}. This non-linear onset strain was similar to that reported in [32], who obtained a value of 2.5 mm.m^{-1} in similar tests on an MD±45° configuration of the same material. Table 6.1 gives the mean transverse and shear moduli obtained from six tests on each specimen. Transverse modulus values were corrected to account for fibre strains by fitting the $\sigma_{22} - Q_{12}\epsilon_{11}$ *vs.* ϵ_{22} response to obtain Q_{22} Corr, which is represented as the yellow line in Figure 6.1 (a). Note that Q_{12} was obtained from the relationship $Q_{12} = \nu_{12}E_{22}/(1 - \nu_{12}\nu_{21})$, with $\nu_{12} = 0.32$ and $\nu_{21} = 0.019$. Here, the uncorrected E_{22} value was obtained by linearly fitting the σ_{22} *vs.* ϵ_{22} curve, shown as the blue line in Figure 6.1 (a). The corrected transverse modulus E_{22} was then calculated using the relationship: $E_{22} = Q_{22}$ Corr$(1 - \nu_{12}\nu_{21})$. From the total of 18 tests (3 samples tested 6 times each) the mean E_{22} value was 8.30 GPa, which was obtained at a transverse strain rate of 6.86×10^{-5} s^{-1} as listed in Table 6.1. In addition, the mean G_{12} value was 4.73 GPa and the average shear strain rate was 1.1×10^{-4} s^{-1}. This quasi-static G_{12} result was consistent with that in [20], where MD±45° specimens made from the same material were evaluated.

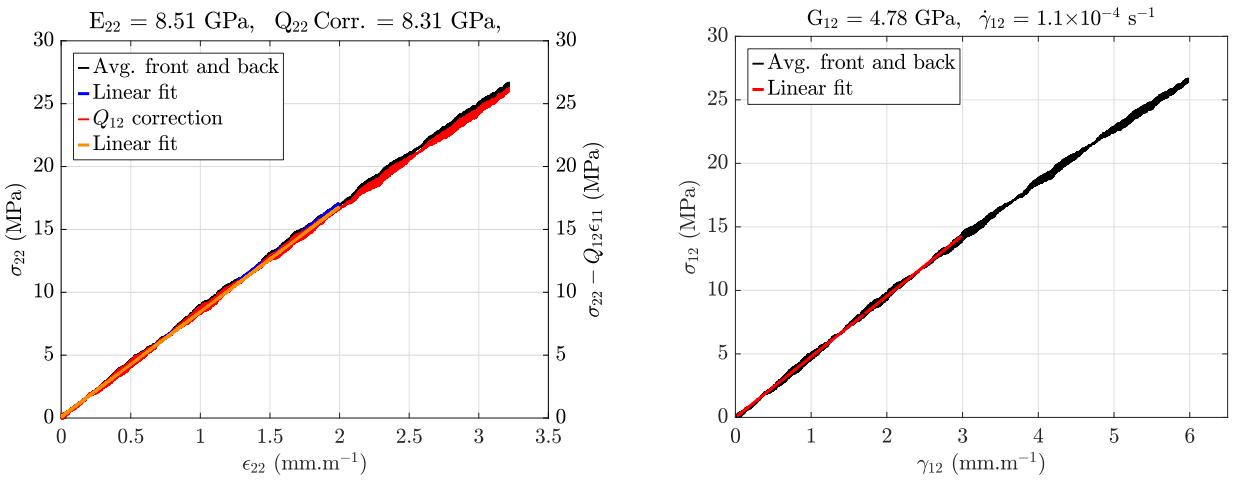

Figure 6.1: (a) Transverse and (b) shear stress *vs.* strain obtained from the UD45° quasi-static tensile test Specimen 1. The strain rate and modulus obtained from linear fits to the curves are also given.

Table 6.1: The transverse modulus E_{22}, shear modulus G_{12}, transverse strain rate $\dot{\epsilon_{22}}$ and shear strain rate $\dot{\gamma_{12}}$ identified from quasi-static tensile tests on three UD45° specimens. The mean, SD and coefficient of variation (COV) from six tests on each specimen are listed at the bottom of the table.

Specimen (#)	$\boldsymbol{E_{22}}$ (GPa)	$\boldsymbol{G_{12}}$ (GPa)	$\boldsymbol{\dot{\epsilon_{22}}}$ ($\times 10^{-5}$ s^{-1})	$\boldsymbol{\dot{\gamma_{12}}}$ ($\times 10^{-4}$ s^{-1})
Sample 1−Test 1	8.31	4.78	6.85	1.11
Sample 1−Test 2	8.31	4.78	6.82	1.12
Sample 1−Test 3	8.30	4.76	6.57	1.12
Sample 1−Test 4	8.27	4.76	6.68	1.08
Sample 1−Test 5	8.27	4.80	6.81	1.12
Sample 1−Test 6	8.29	4.76	6.90	1.13
Sample 2−Test 1	8.34	4.83	6.79	1.10
Sample 2−Test 2	8.29	4.79	6.74	1.13
Sample 2−Test 3	8.30	4.75	6.82	1.05
Sample 2−Test 4	8.33	4.76	6.66	1.09
Sample 2−Test 5	8.34	4.77	6.80	1.08
Sample 2−Test 6	8.32	4.74	6.62	1.13
Sample 3−Test 1	8.32	4.70	7.35	1.16
Sample 3−Test 2	8.26	4.64	6.17	0.99
Sample 3−Test 3	8.32	4.62	7.36	1.14
Sample 3−Test 4	8.31	4.63	7.12	1.14
Sample 3−Test 5	8.31	4.61	7.25	1.14
Sample 3−Test 6	8.33	4.62	7.24	1.14
Mean	**8.30**	**4.73**	**6.86**	**1.11**
SD	**0.0236**	**0.0698**	**3.05**	**3.96**
COV (%)	**0.284**	**1.48**	**4.44**	**3.57**

6.2 Kinematic field resolutions

Kinematic field resolutions were obtained by processing sets of 128 static images from each IBII test sample, taking the SD of all field values. Table 6.2 lists the mean displacement resolutions for each batch of samples, together with the means from all sample types. Considering the mean from all sample configurations, the displacement component resolutions were similar, with values of $u_x = 2.49$ μm and $u_y = 2.23$ μm. Strain and acceleration resolutions were also calculated as the SD of all 128 field values. Here, it is noted that the displacement fields were smoothed with the optimised smoothing parameters obtained in Chapter 5 prior to the strain and acceleration calculations. These smoothing parameters are recalled here: $[S_k, T_k] = [31, 15]$ for the UD90° samples and [11, 15] for the UD45° and MD45° samples, with S_k, T_k being the spatial and temporal smoothing kernel sizes in pixels and frames, respectively. The mean strain component resolutions from all sample configurations were balanced, with values of $\epsilon_{xx} = 565$ μm.m^{-1}, $\epsilon_{yy} = 516$ μm.m^{-1} and $\gamma_{xy} = 708$ μm.m^{-1}. Finally, the mean acceleration component resolutions were also balanced, with values of 8.66×10^5 m.s^{-2} and 7.74×10^5 m.s^{-2} for a_x and a_y, respectively.

Table 6.2: Displacement, strain and acceleration resolutions obtained by processing 128 static experimental grid images.

	Displacement		Strain			Acceleration	
	$\boldsymbol{u_x}$	$\boldsymbol{u_y}$	$\boldsymbol{\epsilon_{xx}}$	$\boldsymbol{\epsilon_{yy}}$	$\boldsymbol{\gamma_{xy}}$	$\boldsymbol{a_x}$	$\boldsymbol{a_y}$
	(μm) [pixels]		(μm.m^{-1})			($\times 10^5$ m.s^{-2})	
UD90° (6 tests)	2.36 [0.013]	2.09 [0.012]	545	487	600	8.13	7.21
UD45° (7 tests)	2.61 [0.014]	2.32 [0.013]	597	534	776	9.09	8.08
MD±45° (4 tests)	2.50 [0.014]	2.28 [0.013]	552	525	750	8.75	7.94
Mean	2.49	2.23	565	516	708	8.66	7.74

6.3 Kinematic fields

This section provides the kinematic fields obtained from IBII tests on the UD90° and UD45° samples, where the displacement fields were calculated with the Grid Method. Fields obtained from the UD90° specimens are first presented because it is easier to follow the kinematic field wave paths in specimens with material coordinates orthogonal to the loading pulse. Full-field kinematics from the UD45° samples are then presented in both global and material coordinates. Differences in the field evolutions are described and compared to the transverse specimen fields. In this chapter, a naming convention will be used for the results from a particular specimen, *e.g.* UD90-S3 is UD90° sample three, UD45-S7 is UD45° sample seven and MD45-S1 is MD45° specimen one.

6.3.1 UD90° specimen

Figure 6.2 shows the x-axis displacement u_x and y-axis displacement u_y fields at two time steps in the recorded loading history during the IBII test on UD90-S3. Here, the global coordinate system origin is at the lower left-hand corner of the field, with positive x to the right, and positive y upwards. In Figure 6.2 (a), the u_x wave front had progressed approximately to the centre of the specimen at 20 μs. Figure 6.2 (b) shows the u_x field at 47 μs, well after the loading pulse had reflected off the specimen free-edge. For the remainder of this section, the kinematic fields for the test specimens will be shown at the same time intervals of 20 μs and 47 μs. Figure 6.2 (c) and (d) show how the u_y fields were lower in magnitude than the u_x fields, because u_y was at 90° to the loading pulse $F_x(t)$. At 20 μs in Figure 6.2 (c), the u_y wave profile was slightly angled in comparison to the vertical u_x wave front shown in Figure 6.2 (d). During the test, a slight pitch angle misalignment between the projectile and the wave guide introduced a non-planar loading on the sample's impact edge, resulting in the angled field seen in Figure 6.2 (c).

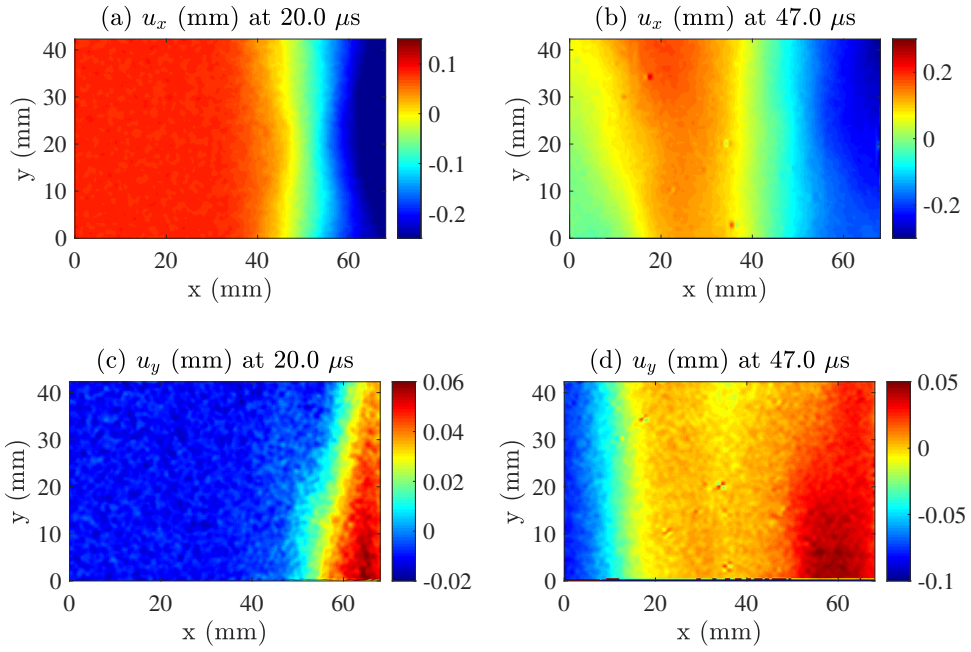

Figure 6.2: Global coordinate system displacement fields for UD90-S3: u_x at (a) 20 μs & (b) 47 μs and u_y at (c) 20 μs & (d) 47 μs.

Global coordinate strain maps obtained from the IBII test on UD90-S3 are presented in Figure 6.3. At 20 μs the ϵ_{xx} wave front had reached the approximate specimen centre, as shown in Figure 6.3 (a). Given that a delay time of 4 μs was chosen for this test, the time for the u_x wave front to travel 35 mm (to the middle of the specimen) was approximately 16 μs. Therefore, the speed of the u_x wave front was on the order of 2.2 mm.μs^{-1}, which is similar for epoxy resins [138] and expected, given that the loading was in-line with the resin dominated direction of the composite (*i.e.* transverse to the fibres). However, it must be noted that this kinematic relationship is approximate only, given here to provide a general understanding of the longitudinal wave motion in the specimen during the compressive loading. Later in the test at 47 μs, a tensile strain region had developed in the ϵ_{xx} field, as the compressive loading pulse reflected off the free-edge of the sample. This tensile region can be seen as the red zone on the left side of the specimen in Figure 6.3 (b). Relatively-high peak ϵ_{xx} values around 20 mm.m^{-1} were obtained at 20 μs as seen in Figure 6.3 (a), which was primarily due to the axial loading and the low stiffness of the epoxy matrix. However, the high stiffness of the carbon fibres and resulting low minor Poisson's ratio, caused the ϵ_{yy} strains to be an order of magnitude lower, at approximately 2 mm.m^{-1} as shown in Figures 6.3 (c) and (d). Compared to the transverse and shear strains, more noise can be seen in the y-axis strain maps because of the lower signal-to-noise ratio of the fibre strains. Shear strain γ_{xy} fields at the two time steps are given in Figures 6.3 (e) and (f) and had peak values ranging from around 5$-$10 mm.m^{-1}. In Figure 6.3 (e), a γ_{xy} wave front had developed due to y-axis strains evolving from the projectile/wave guide pitch misalignment during the IBII test. The development of a shear strain wave in the UD90° samples was unexpected, but also pleasing because it gave the possibility of identifying the shear modulus from the same test.

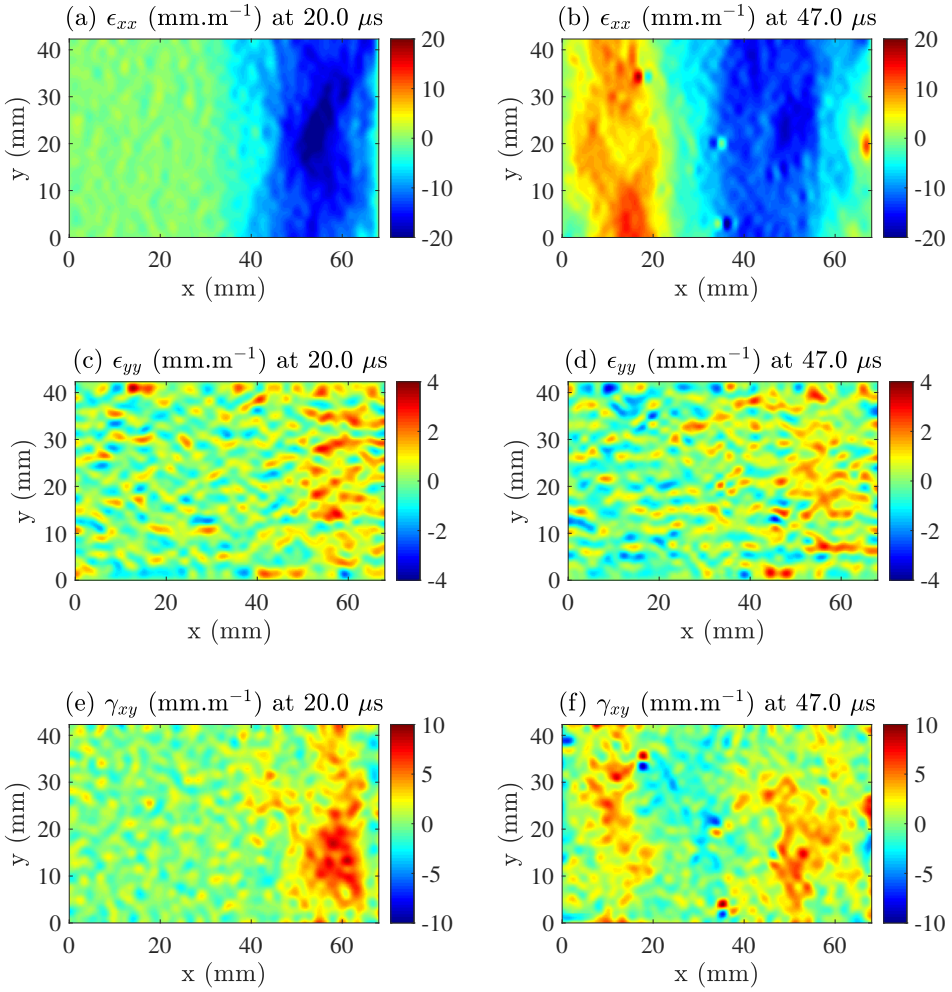

Figure 6.3: Global coordinate system strain fields for UD90-S3: ϵ_{xx} at (a) 20 μs & (b) 47 μs, ϵ_{yy} at (c) 20 μs & (d) 47 μs and γ_{xy} at (e) 20 μs & (f) 47 μs.

Strain-rate fields in global coordinates obtained from the test on UD90-S3 are given in Figure 6.4. Compressive strain rates on the order of $2{\times}10^3$ s^{-1} were present in the $\dot{\epsilon}_{xx}$ fields at 20 μs as seen in Figure 6.4 (a). A region of concentrated high strain rate values evolved at around 15 mm from the free-edge on the lower edge of the specimen, as seen in Figure 6.4 (b). This high strain region was a result of a crack that formed during the test and will be discussed further in Section 7.4. The $\dot{\epsilon}_{yy}$ fields at the two time steps are shown in Figures 6.4 (c) and (d), which reveal lower peak values than the $\dot{\epsilon}_{xx}$ fields, again due to the higher stiffness of the carbon fibres. Figures 6.4 (e) and (f) show peak values for the $\dot{\gamma}_{xy}$ fields on the order of $1{-}2{\times}10^3$ s^{-1}, which was relatively-high considering the UD90° sample configuration.

Acceleration a_x and a_y fields are shown at two time steps in Figure 6.5. In Figure 6.5 (a) at 20 μs, the a_x wave has a width on the order of 25 mm. This pulse width can be explained from the distance-time graph given in Figure 6.6, which provides a simplistic 1D approximation of the longitudinal wave movements in the impact components during an IBII test. After the projectile impacts the wave guide at $t = 0$, a left-moving compressive pulse travelling with a speed of approximately 5.0 mm.μs^{-1} progresses through the wave guide and reaches the specimen at around 10 μs (blue solid line in Figure 6.6). As previously mentioned, the compressive pulse then travels in the specimen at the approximate speed of 2.2 mm.μs^{-1} (green solid line), reaching the centre of the specimen at around 20 μs. Immediately after the initial impact of the projectile on the wave guide, a compressive wave also develops in the projectile, which travels rightward at around 5.0 mm.μs^{-1} toward the back face of the projectile.

After impacting the rear surface it reflects as a tensile wave, which is represented in Figure 6.6 by the dashed red line. This tensile wave travels through the wave guide (represented here by the blue dashed line) where it meets the specimen at about 20 μs. The distance between the solid and dashed green lines gives the approximate compressive wave length of 25 mm, which is similar to that shown in Figure 6.5 (a). The compressive pulse in the specimen (solid green line) reaches the free-edge of the specimen and reflects as a tensile wave. This tensile wave then interacts with the wave generated at the specimen/wave guide interface (dashed green line), creating a highly tensile region at around 45 μs. This location and time corresponds to the formation of the crack in the specimen seen in Figure 6.4 (b). It must be noted that in Figure 6.6 the movement of the interface boundaries and some of the wave reflections are not shown, so that the main wave motions are easier to see. The a_y fields at two time-steps in the loading history are given in Figures 6.5 (c) and (d), where peak accelerations on the order of $6{\times}10^6$ m.s^{-2} were obtained. This was slightly lower than the peak accelerations generated in the a_x fields, which were on the order of $1{\times}10^7$ m.s^{-2} as shown in Figures 6.5 (a) and (b).

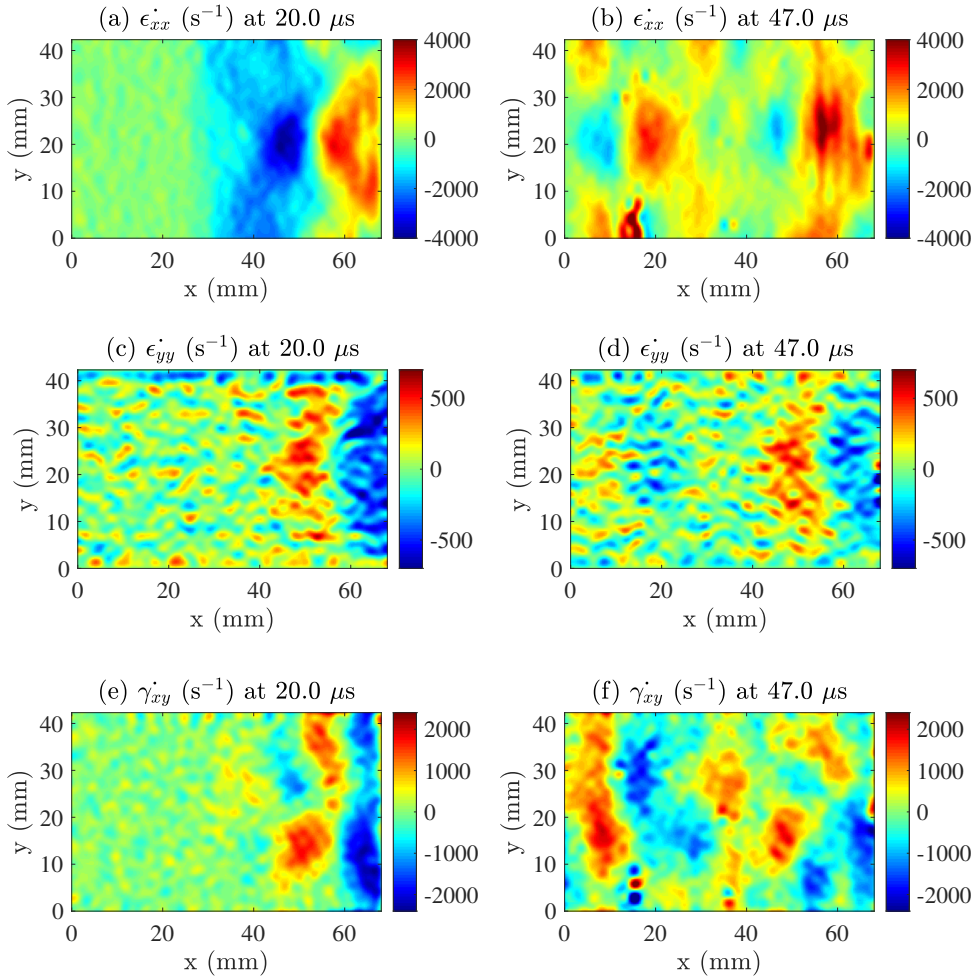

Figure 6.4: Global coordinate system strain rate fields for UD90-S3: $\dot{\epsilon}_{xx}$ at (a) 20 μs & (b) 47 μs, $\dot{\epsilon}_{yy}$ at (c) 20 μs & (d) 47 μs and $\dot{\gamma}_{xy}$ at (e) 20 μs & (f) 47 μs.

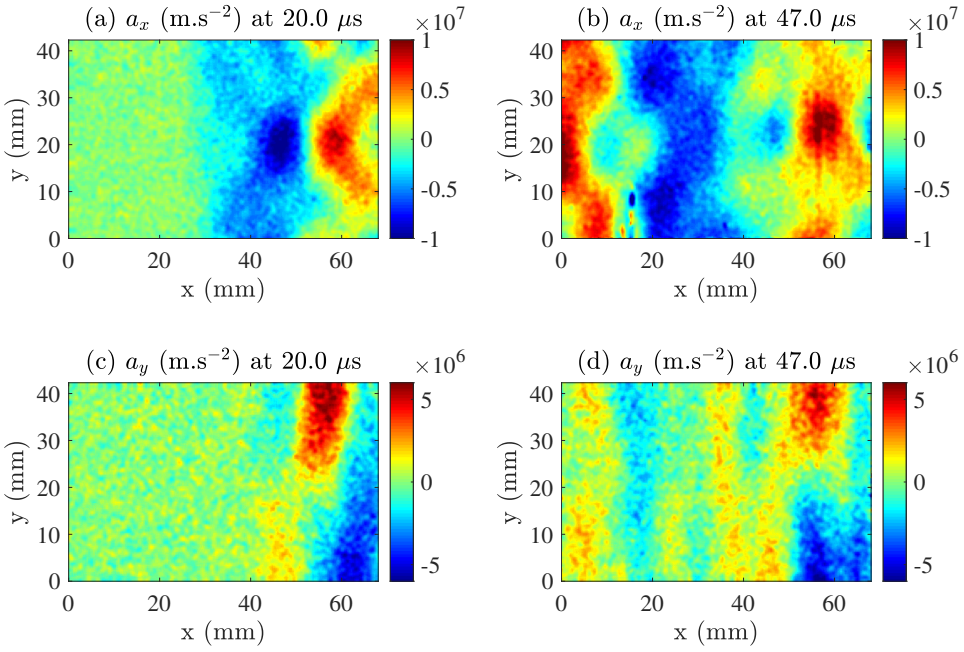

Figure 6.5: Global coordinate system acceleration fields for UD90-S3: a_x at (a) 20 μs & (b) 47 μs and a_y at (c) 20 μs & (d) 47 μs.

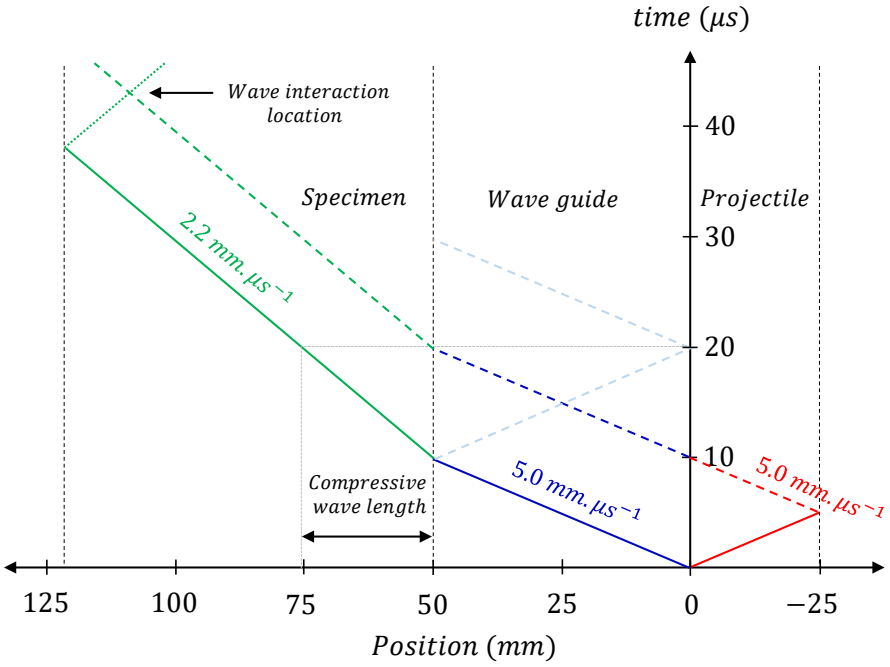

Figure 6.6: Representative distance-time graph of the main longitudinal wave motions within the impact components during an IBII test.

The average force acting on the specimen impact edge in the x-axis direction $\overline{F_x}^y$ was calculated from the specimen mass m_s and the average acceleration over the specimen surface $\overline{a_x}^s$ using the equation $\overline{F_x}^y = m_s \overline{a_x}^s$. At the same time, the average stress acting on the impact edge in the x-axis direction $\overline{\sigma_{xx}}^y$ was obtained by dividing $\overline{F_x}^y$ by the cross sectional area of the specimen. $\overline{F_x}^y$ and $\overline{\sigma_{xx}}^y$ are plotted against time for the IBII test on UD90-S3 in Figure 6.7, where peak values are approximately 22 kN and 170 MPa, respectively. $\overline{F_x}^y$ reaches a first peak of about 22 kN in compression at 14 μs and then starts to unload as the incoming relief wave enters the specimen, which can also be seen as the positive a_x region trailing the negative a_x region in Figure 6.5 (a). At this time, $\overline{F_x}^y$ decreases in

magnitude as the initial loading pulse hits the specimen free-edge and reflects, becoming tensile. The second compressive peak in $\overline{F_x}^y$ at approximately 30 μs corresponds to the arrival of a secondary wave generated at the specimen/wave guide interface, due to the impedance mismatch between the specimen and the wave guide. This wave initially travels rightward, then reflects off the front face of the wave guide and enters the specimen again (dashed light blue line in Figure 6.6). As the main loading pulse reflects off the free-edge of the specimen $\overline{F_x}^y$ becomes less compressive, as seen in Figure 6.7 at 46 μs. Kinematic fields obtained from an IBII test on one of the UD45° specimens are presented in the next section.

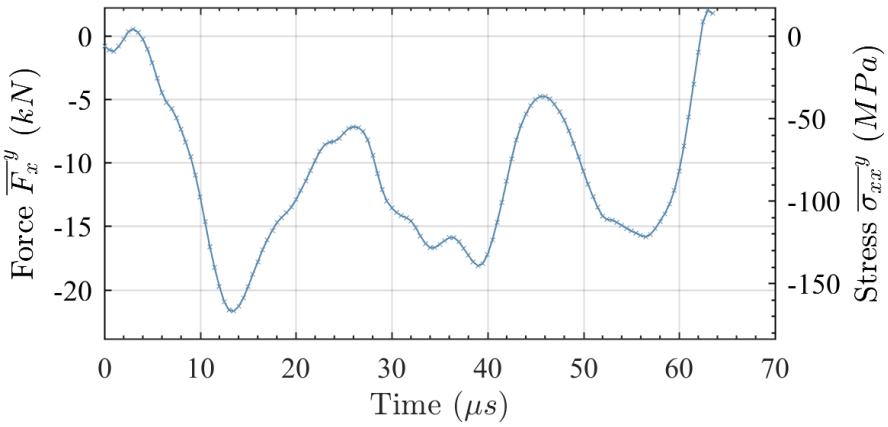

Figure 6.7: Average force acting in the x-axis direction $\overline{F_x}^y$ and the average stress acting on the impact edge in the x-axis direction $\overline{\sigma_{xx}}^y$ obtained from the IBII test on UD90-S3.

6.3.2 UD45° specimen: global coordinates

In this section, kinematic fields from an example UD45° specimen are first presented in global coordinates. Global coordinate system u_x and u_y displacement fields are shown at 20 μs and 50 μs during the IBII test on specimen UD45-S2 in Figure 6.8. As seen in Figure 6.8 (a), the u_x field at 20 μs has developed a curved wave front, which evolved for two reasons. Firstly, the carbon fibres have a higher longitudinal wave speed than the epoxy matrix and therefore, the wave travels faster in the 1-axis than the x-axis. Using the T700GC carbon fibre modulus of $E = 240$ GPa and density $\rho = 1780$ kg.m^{-3} from [139], the longitudinal wave speed is $c = \sqrt{E/\rho} = 11.6$ mm.μs^{-1}, which is considerably faster than the wave speed in the matrix (recalling that this is around 2.2 mm.μs^{-1}). Secondly, the shear-coupling stiffness causes the specimen to rotate (in this case, anti-clockwise) as the specimen is axially loaded, resulting in an angled u_x displacement field. At 20 μs, the curved u_x displacement wave front had just passed the approximate centre on the top edge of the specimen in Figure 6.8 (a). At 50 μs, the u_x field had a complex form due to multiple wave interactions within the specimen, as shown in Figure 6.8 (b). Curvature was also present in the u_y wave front at 20 μs in Figure 6.8 (c). This result was expected because the y-axis displacement u_y is influenced by the faster wave speed in the fibres. After the loading pulse had reflected off the sample's free-edge, it was again difficult to predict the u_y field evolution in Figure 6.8 (d), because of the multiple wave interactions within the sample. For UD45-S7, the peak u_x and u_y displacement component values were similar, which is in contrast to the displacement fields obtained from UD90-S3. This result was also anticipated because the fibres in the UD45° specimen were closer to being axially-aligned with the loading pulse and therefore, deform more significantly compared to the fibres in the transverse specimen, which are aligned at 90° to the loading pulse.

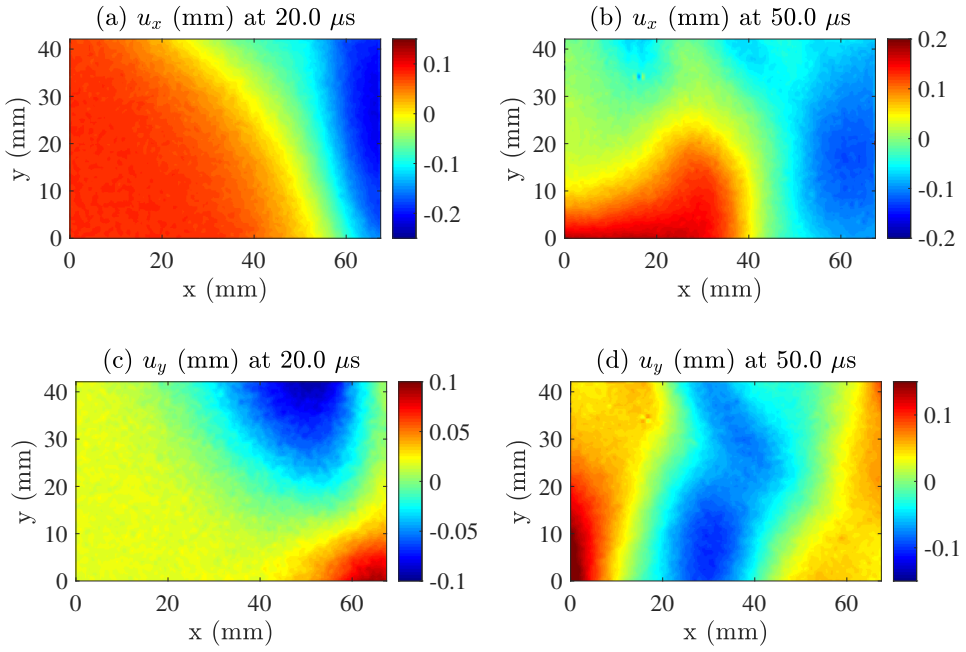

Figure 6.8: Global coordinate system displacement fields for UD45-S2: u_x at (a) 20 μs & (b) 50 μs and u_y at (c) 20 μs & (d) 50 μs.

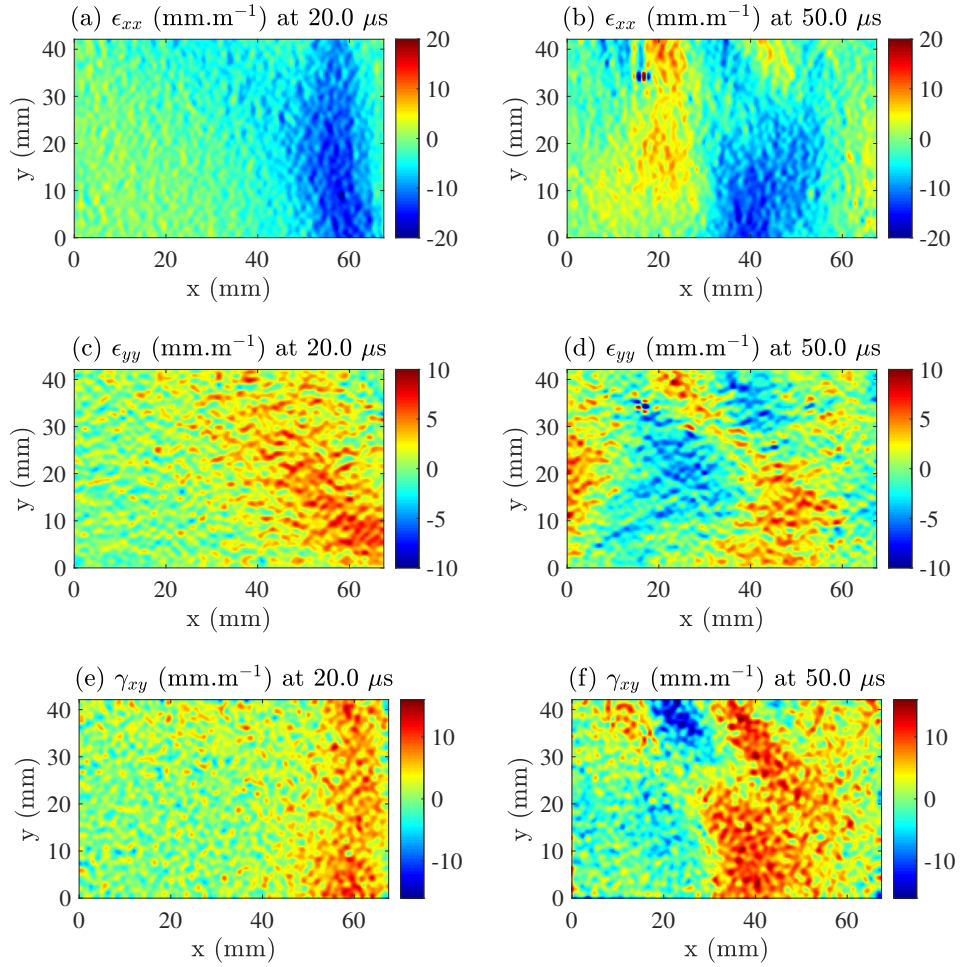

Figure 6.9: Global coordinate system strain fields for UD45-S2: ϵ_{xx} at (a) 20 μs & (b) 50 μs, ϵ_{yy} at (c) 20 μs & (d) 50 μs and γ_{xy} at (e) 20 μs & (f) 50 μs.

Global coordinate system strain fields at two time steps in the loading history for UD45-S2 are given in Figure 6.9. A curved wave front profile was also seen in the ϵ_{xx} field at 20 μs in Figure 6.9 (a), where peak compressive strains were on the order of $10-20$ mm.m^{-1}. The ϵ_{yy} field at 20 μs also had a curved shape, with tensile strains around $5-10$ mm.m^{-1}, as shown in Figure 6.9 (c). Higher ϵ_{yy} peak values for the UD45° off-axis specimens were expected due to the low matrix stiffness in the 2-axis, which was more closely aligned with the y-axis than for the UD90° case. At 20 μs, the γ_{xy} field generated peak strains on the order of $10-15$ mm.m^{-1}, as viewed in Figure 6.9 (e). Similar to the previous fields, the global coordinate strains also had a complex structure following the reflection of the loading pulse (see Figures 6.9 (b), (d) and (f)). Note that the strain rate fields in global coordinates for UD45-S2 are not provided in this report, as they are not used in further analysis.

The global coordinate system acceleration components a_x and a_y at two time steps from the test on UD45-S2 are given in Figure 6.10. Similar to the displacements in Figure 6.8, the acceleration fields had a curved profile, which can be seen in Figures 6.10 (a) and (c). Peak accelerations for the a_x field were on the order of 4×10^6 m.s^{-2}, whereas the a_y peaks were slightly lower, at around 2×10^6 m.s^{-2}. Both the a_x and a_y fields were complex following the reflection of the loading pulse from the free-edge of the specimen (see Figures 6.10 (b) and (d), respectively). In the next section, kinematic fields from the test on UD45-S2 are given in material coordinates.

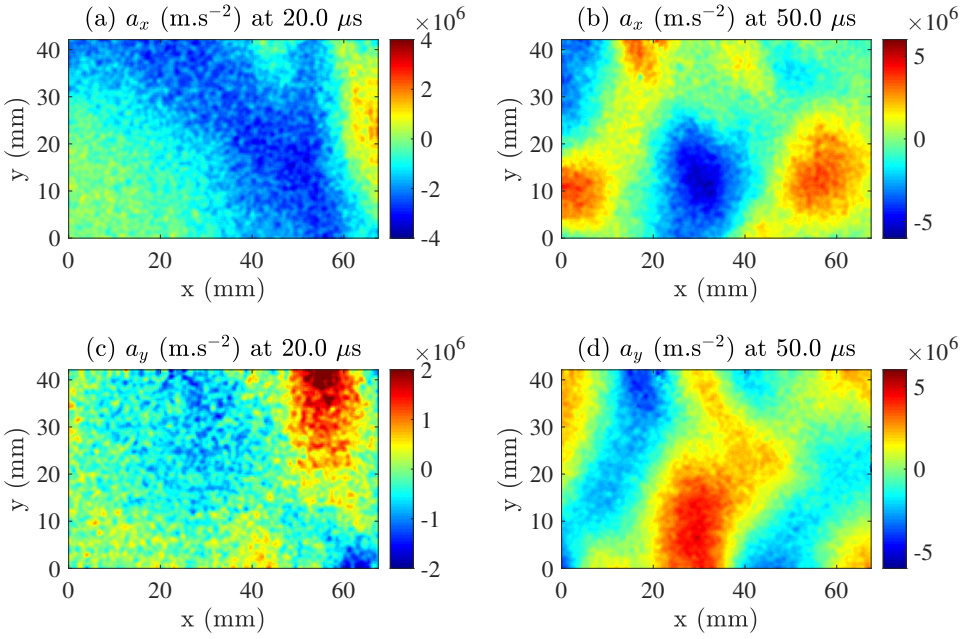

Figure 6.10: Global coordinate system acceleration fields for UD45-S2: a_x at (a) 20 μs & (b) 50 μs and a_y at (c) 20 μs & (d) 50 μs.

6.3.3 UD45° specimen: material coordinates

Material coordinate system strain fields at two time steps from the test on UD45-S2 are given in Figure 6.11. Similar to the UD90° ϵ_{yy} fields in Figures 6.3 (c) and (d), the high fibre stiffness and resulting low signal-to-noise ratio led to noise dominated ϵ_{11} fields, as shown in Figure 6.11 (a) and (b). Given that the strain rate insensitive 1-axis properties of composites (see [54]) were not the focus of this investigation, the ϵ_{11} and $\dot{\epsilon}_{11}$ fields will not be shown further in this thesis. Higher peak compressive ϵ_{22} values resulted because of the relatively low matrix stiffness, where values on the order of 10 mm.m^{-1} can be seen in Figures 6.11 (c) and (d). Out of all the strain components, the γ_{12} fields recorded the highest peak values of about 25 mm.m^{-1}, as shown in Figures 6.11 (e) and (f).

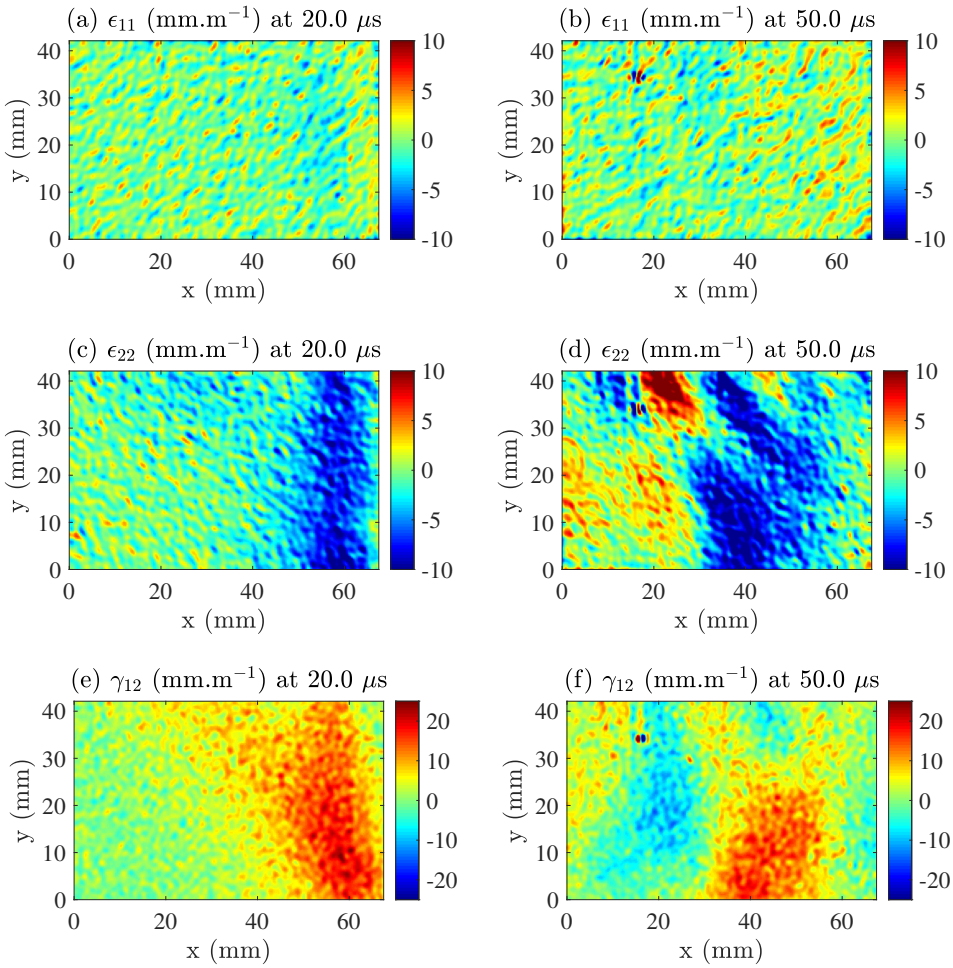

Figure 6.11: Material coordinate system strain fields for UD45-S2: ϵ_{11} at (a) 20 μs & (b) 50 μs, ϵ_{22} at (c) 20 μs & (d) 50 μs and γ_{12} at (e) 20 μs & (f) 50 μs.

Material coordinate system strain rate fields from the test on UD45-S2 are given in Figure 6.12. Figure 6.12 (a) shows a mostly planar wave form in the $\dot{\epsilon}_{11}$ field at 20 μs, whereas the $\dot{\epsilon}_{22}$ and $\dot{\gamma}_{12}$ fields were aligned with the sample fibres, as shown in Figure 6.12 (c) and (e), respectively. Peak strain rates for both the $\dot{\epsilon}_{11}$ and $\dot{\epsilon}_{22}$ were approximately equal at around $1{\times}10^3$ s^{-1} However, the strong shear response from the UD45° sample configuration resulted in higher shear strain rates on the order of $2{-}3{\times}10^3$ s^{-1}. A region of spuriously-high strain rate magnitudes can be seen in the upper left hand corner of Figure 6.12 (d), which was a result of a crack that formed during the test.

The material coordinate a_1 and a_2 fields are given in Figure 6.13. An angled wave profile aligned with the off-axis fibres developed for the a_1 field at 20 μs in Figure 6.13 (a), with peak accelerations on the order of $4{\times}10^6$ m.s^{-2}. The tensile relief wave is also visible in the a_1 field in Figure 6.13 (a), which had a wave front aligned with the specimen fibres. As shown in Figure 6.13 (c), a_2 is positive due to the anti-clockwise rotation of the specimen, which occurred because the sample fibres were orientated at an angle of 45°, clockwise from the x-axis. Both the a_1 and a_2 fields were complex following the reflection of the loading pulse from the free-edge of the specimen (see Figures 6.13 (b) and (d).

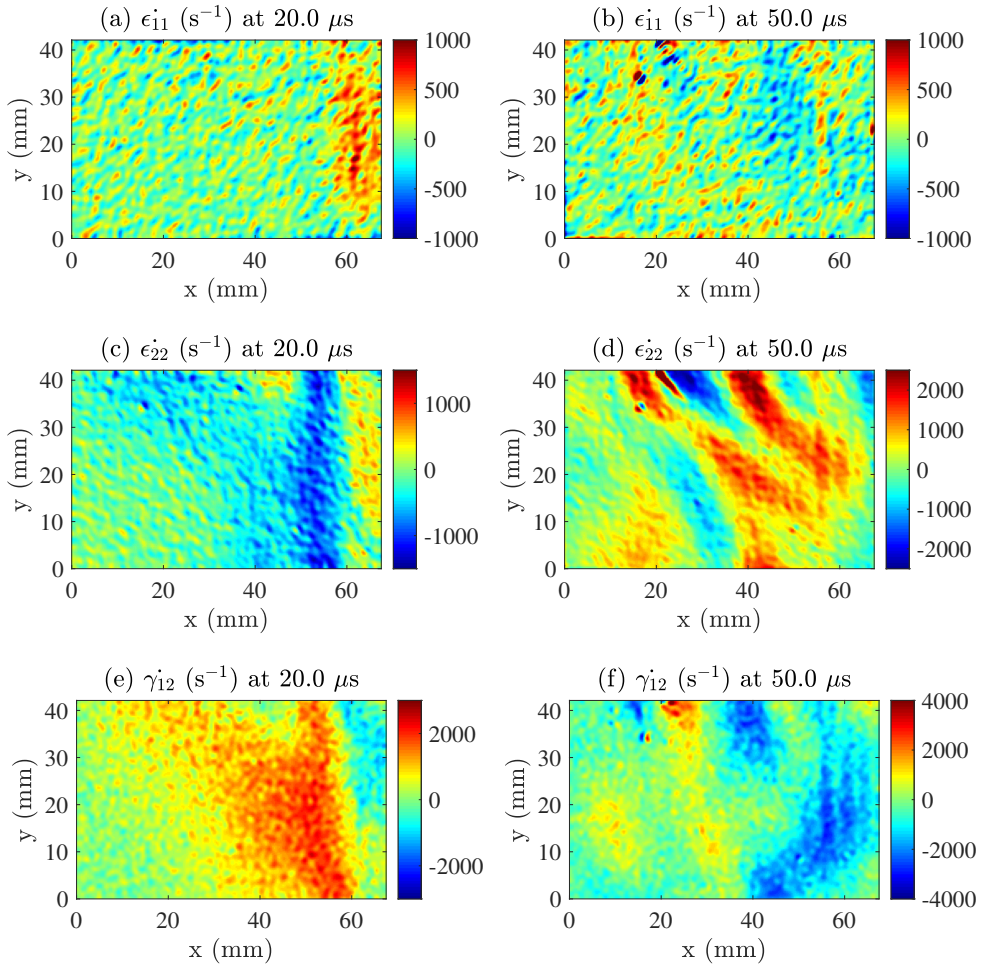

Figure 6.12: Material coordinate system strain rate fields for UD45-S2: $\dot{\epsilon}_{11}$ at (a) 20 μs & (b) 50 μs, $\dot{\epsilon}_{22}$ at (c) 20 μs & (d) 50 μs and $\dot{\gamma}_{12}$ at (e) 20 μs & (f) 50 μs.

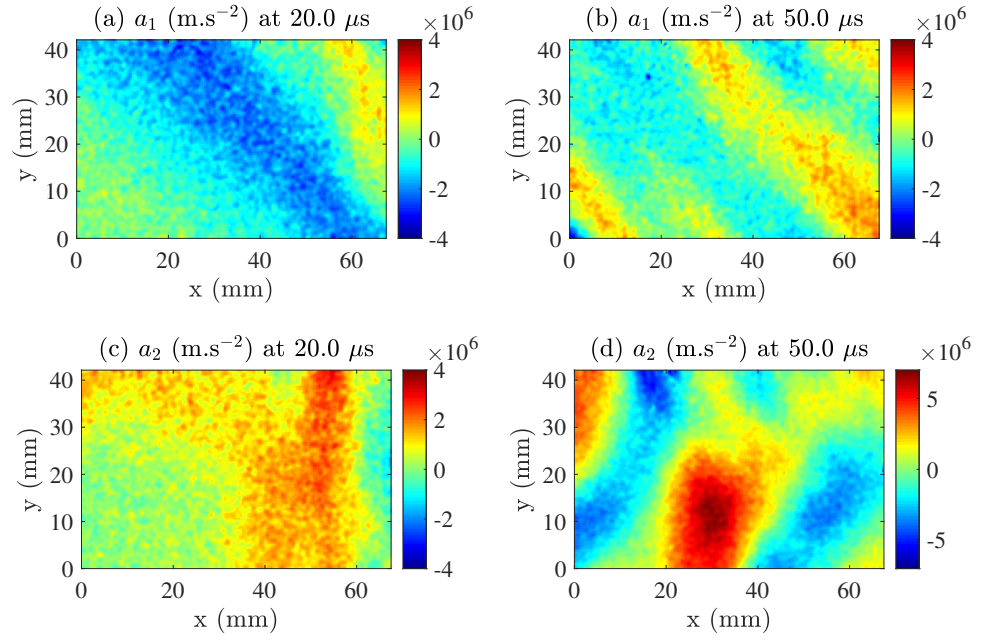

Figure 6.13: Material coordinate system acceleration fields for UD45-S2: a_1 at (a) 20 μs & (b) 50 μs and a_2 at (c) 20 μs & (d) 50 μs.

6.3.4 MD45° specimen: material coordinates

Material properties obtained from the MD45° samples were derived from kinematic fields in material coordinates, so the global coordinate maps are not shown here. Shear strain fields at 20 μs and 50 μs from the test on MD45-S1 are given in Figures 6.14 (a) and (b), respectively. Similar to the UD45° specimens, the γ_{12} field peak strains were on the order of 25 mm.m^{-1} however, the MD45° samples developed 'X-shaped' strain fields in-line with the samples ±45° fibres, as shown in Figure 6.14 (a). The $\dot{\gamma}_{12}$ wave profile had a similar shape to the γ_{12} field, as shown in Figure 6.14 (c). Here, peak $\dot{\gamma}_{12}$ values were on the order of 2−3×10^3 s^{-1}, which was similar to the UD45° values. Acceleration a_1 and a_2 fields in Figures 6.15 (a) and (c) show angled wave fronts aligned with the sample's -45° and +45° fibres, respectively. Peak accelerations for the a_1 and a_2 fields were similar, at around 4×10^6 s^{-1}.

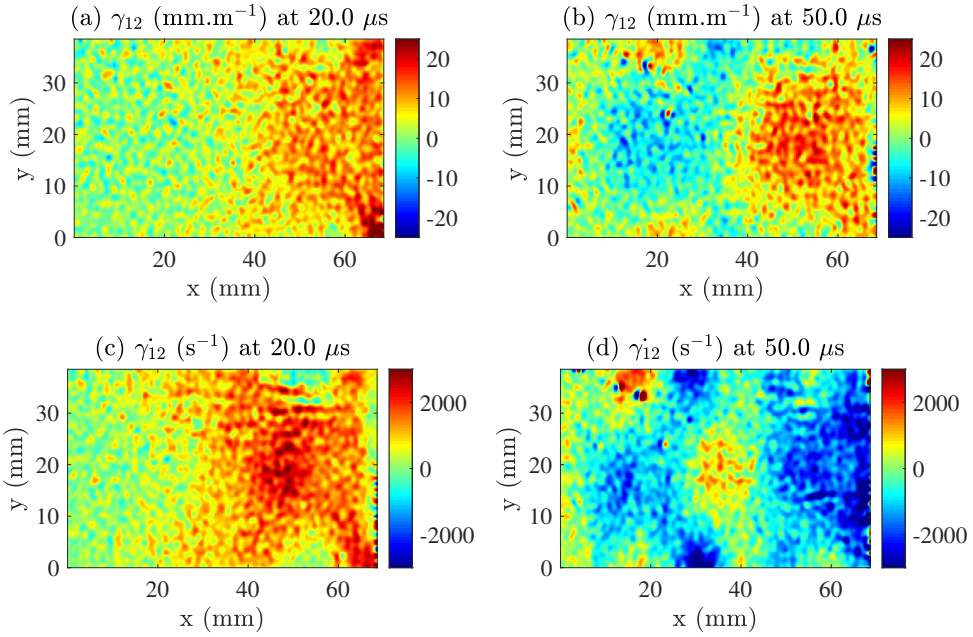

Figure 6.14: Material coordinate system fields for MD45-S1: shear strain γ_{12} at (a) 20 μs & (b) 50 μs together with the shear strain rate $\dot{\gamma}_{12}$ at (c) 20 μs & (d) 50 μs.

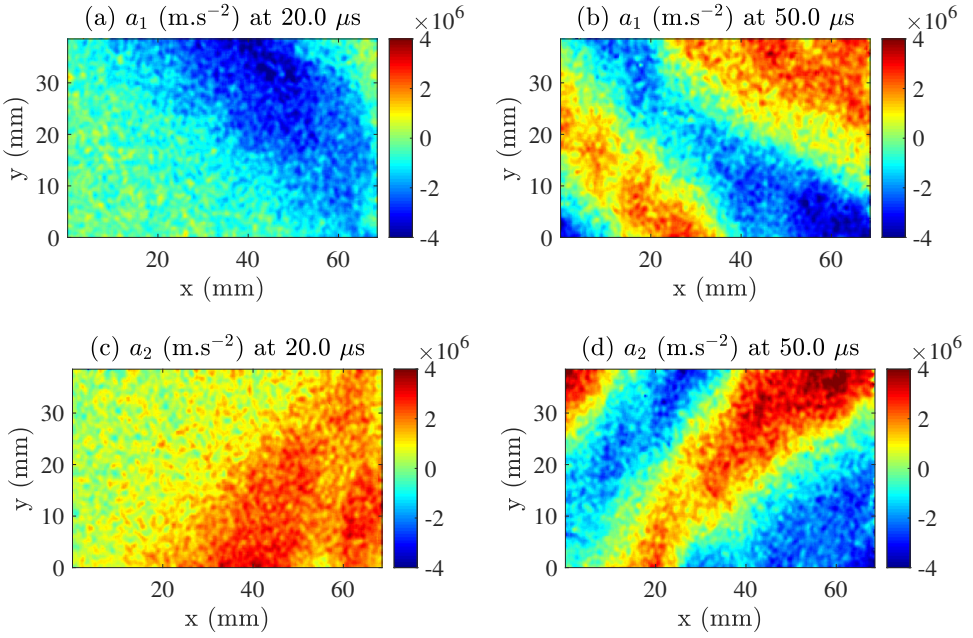

Figure 6.15: Material coordinate system acceleration fields for MD45-S1: a_1 at (a) 20 μs & (b) 50 μs and a_2 at (c) 20 μs & (d) 50 μs.

6.4 Stiffness identification

This section presents the high strain rate stress-strain curves and stiffness data obtained from IBII tests on UD90°, UD45° and MD45° Grid Method samples. The CFRP composite material evaluated here had been previously characterised by ONERA in [20, 140], up to strain rates on the order of $5{\times}10^1$ s^{-1}. Data provided in this section extends the material characterisation to the thousand s^{-1} strain rate regime.

6.4.1 UD90° specimens: transverse component

The transverse stress gauge equation (Equation 3.21 of Chapter 3) was used to calculate the average stress over the specimen height $\overline{\sigma_{22}}^L$ from the a_2 acceleration fields for the UD90° specimens. Next, the average strain over the specimen height $\overline{\epsilon_{22}}^L$ was calculated from the ϵ_{22} fields, and plotted against the transverse stresses at each vertical slice on the sample. Recalling that the UD90° case material 1 and 2-axis are aligned with the global coordinate y and x-axis, the material coordinate strain and acceleration fields can be viewed in Figures 6.3 and 6.5 through the relationships: $\epsilon_{22} = \epsilon_{xx}$, $\epsilon_{11} = \epsilon_{yy}$, $\gamma_{12} = \gamma_{xy}$, $a_2 = a_x$ and $a_1 = a_y$. Stress-strain curves obtained from slices at various x_0 positions (distances from the specimen's free-edge) for UD90-S3 are given in Figure 6.16, where a linear loading in compression and unloading in tension was observed. Some non-linearity was present late in the unloading due to the development of a macro-crack in the specimen. For this particular test, the peak average compressive stress was approximately 160 MPa. Although the quasi-static compressive failure stress of this material is unknown, it is unlikely that the composite specimen experienced damage during the loading portion of the test because the stress-strain response was linear. In addition, compressive failure stress values obtained from quasi-static tests on similar UD90° CFRP composite specimens were reported to be over 200 MPa in [111]. Therefore, the compressive loading portion of the test could be used to obtain the elastic modulus.

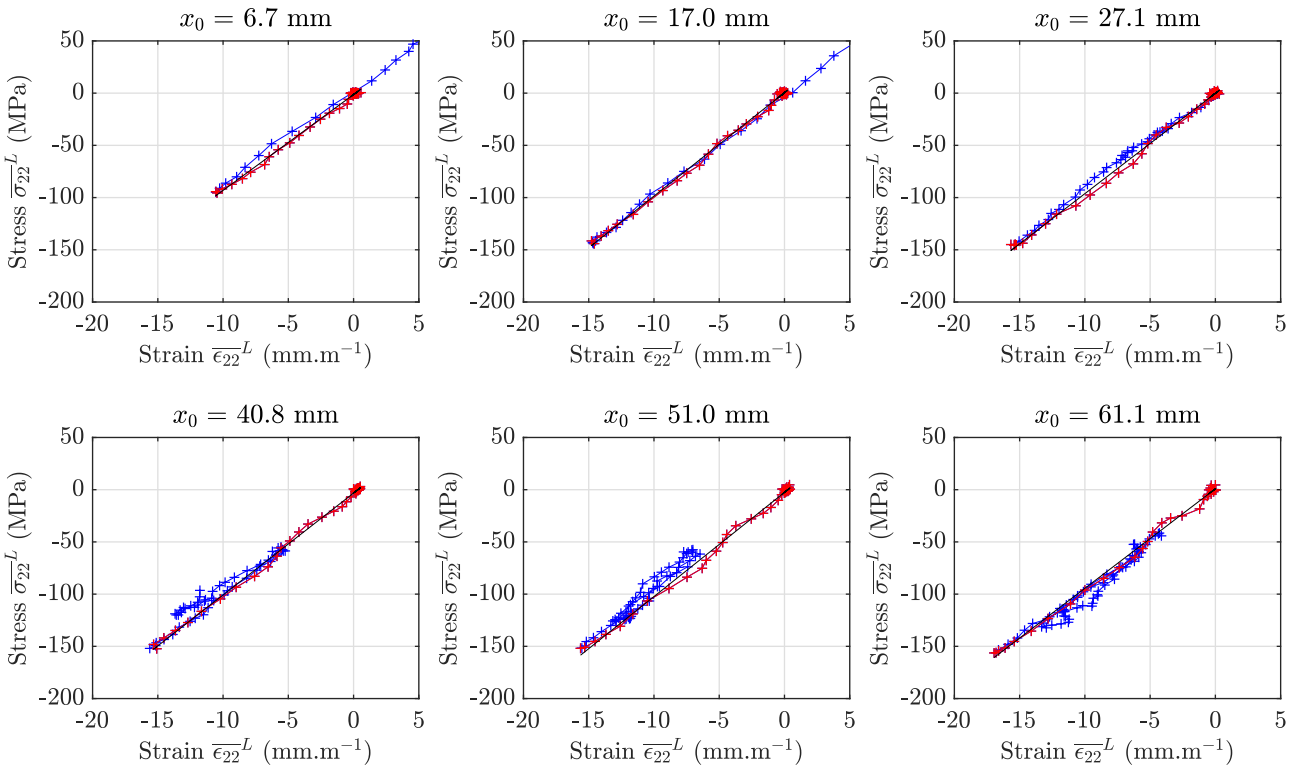

Figure 6.16: Transverse stress-strain curves at various x_0 distances obtained from UD90-S3.

Transverse moduli were obtained by linearly fitting the compressive portion of the transverse stress-strain curve from each slice on the UD90° samples. Figure 6.17 shows the transverse modulus as a function of x_0 position (from the free-edge) results from six IBII tests on UD90° samples. A relatively poor modulus identification was obtained at the sample's impact and free-edges. At these locations, extrapolated data is included in the spatial smoothing kernels that overhang the edges, which consequently induces a bias in the spatially smoothed displacements. As a result of this bias, the modulus values identified at slices within half a spatial smoothing kernel plus one grid pitch from the sample's impact and free edges will be of poor quality. The image deformation study described in Chapter 5 determined an optimised spatial smoothing kernel size of 31 × 31 pixels for the UD90° case samples. Given the 0.18 mm.pixel^{-1} magnification in these tests, approximately 3.8 mm of strain data was affected. Strains closer to the specimen's free-edge are also lower, which results in a low signal-to-noise ratio and subsequently poor modulus identification. In order to avoid the influence of the edge effects, modulus values were identified over the middle 50% of the specimen length, as was done in [29]. Table 6.3 lists the mean transverse modulus identified from the six tests as $E_{22} = 10.2$ GPa, with a SD of 0.154 GPa and a coefficient of variation (COV) of 1.52%, indicating good test-to-test repeatability. Note that Figure 6.17 shows the identified UD90° case transverse modulus E_{22} as the solid purple line. The quasi-static modulus of 8.3 GPa obtained in this work was used to determine the percentage difference to the quasi-static value (% Diff. to QS), which was 22.3%. This result is in-line with the understanding that the transverse properties of composites are dominated by the rate-dependent matrix material response.

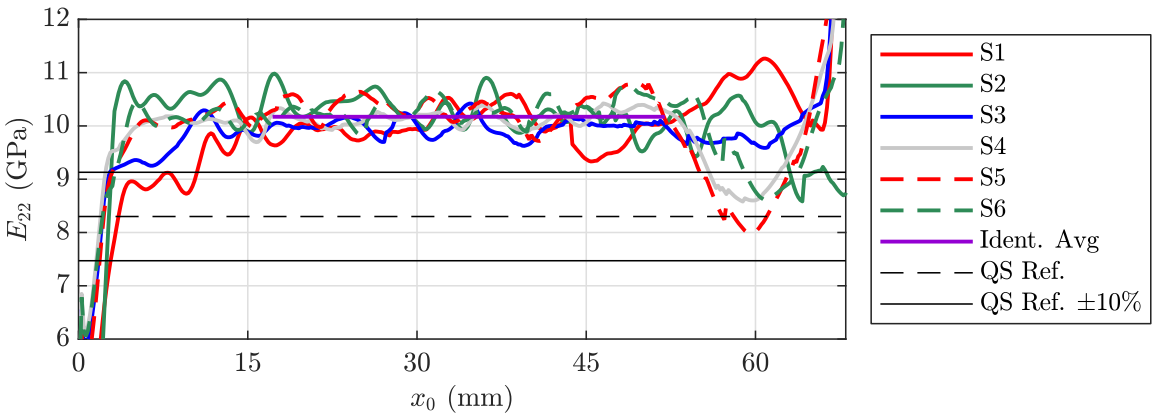

Figure 6.17: Transverse modulus as a function of x_0 distance from the specimen's free edge, identified from the six IBII tests on UD90° grid samples. Also shown is the quasi-static reference value and ±10% of the quasi-static reference value obtained from this work.

Table 6.3 also lists the peak compressive 2−axis strain rate averaged over the vertical slice $\overline{|\dot{\epsilon}_{22}|}^{L}$, which was on the order of $1{-}3{\times}10^3$ s^{-1} for the batch of UD90° samples. Some variation in the peak strain rates was expected because of the heterogeneous strain fields, which can be seen in Figure 6.3. However, the average value for UD90-S1 and UD90-S2 was on the order of $1{\times}10^3$ s^{-1}, which was significantly lower than the peak values obtained for UD90-S3 to UD90-S6, being around $3{\times}10^3$ s^{-1}. The reduced peak strain rates for UD90-S1 and UD90-S2 were a result of an increase in the y-axis displacements, resulting in an increased shear loading of the sample. This finding can be seen in Figure 6.18, which shows the average transverse and shear stresses $\overline{\sigma_{xx}}^{y}$ and $\overline{\sigma_{xy}}^{y}$, respectively, acting on the impact edge in the IBII test on UD90-S2. Here, the red trace shows the shear stress reached around 40−50 MPa over the first 8 μs of the loading history. Over the same duration, the transverse stress peaked at around 90 MPa, which was significantly lower than the value of 160 MPa obtained for UD90-S1, as seen in Figure 6.7. This comparison gives evidence that a portion of the impact energy had been split between a transverse and a shear response and explains why the peak strain rate values in UD90-S1 and UD90-S2 were low.

Table 6.3: The transverse modulus E_{22} and shear modulus G_{12} identified from six IBII tests on UD90° grid specimens, together with the mean, SD, COV, QS value and %Diff. QS value. Peak average and effective transverse and shear strain rates are also listed.

Spec. (#)	$\boldsymbol{E_{22}}$ (GPa)	$\boldsymbol{G_{12}}$ (GPa)	**Peak** $\overline{\lvert\dot{\epsilon}_{22}\rvert}^{L}$ ($\times 10^3$ s^{-1})	**Peak** $\overline{\lvert\dot{\gamma}_{12}\rvert}^{L}$ ($\times 10^3$ s^{-1})	$\hat{\dot{\epsilon}}_{22}$ ($\times 10^3$ s^{-1})	$\hat{\dot{\gamma}}_{12}$ ($\times 10^3$ s^{-1})
UD90-S1	9.97	5.65	1.18	1.38	0.467	0.466
UD90-S2	10.3	5.52	1.18	1.46	0.473	0.555
UD90-S3	10.0	5.34	2.93	1.51	1.18	0.465
UD90-S4	10.1	5.58	3.03	1.18	1.16	0.390
UD90-S5	10.3	5.38	3.19	1.03	1.15	0.277
UD90-S6	10.3	5.61	2.92	1.45	1.17	0.375
Mean	**10.2**	**5.51**	**2.41**	**1.34**	**0.932**	**0.421**
SD	**0.154**	**0.127**				
COV (%)	**1.52**	**2.30**				
QS Value	**8.30**	**4.73**				
%Diff. QS	**22.3**	**16.6**				

The increased average shear stresses obtained from UD90-S1 and UD90-S2 were thought to be generated from a non-planar loading pulse, caused by a pitch-angle misalignment between the projectile and the wave guide during the test. As explained in Chapter 4, at certain test impact velocities, the projectile causes an air loading on the front face of the wave guide. Because the wave guide is anchored at the lower edge (to the foam stand), the air loading causes the wave guide to pitch upward and consequently, the bottom of the wave guide is impacted first by the projectile. This upward pitch is usually accounted for during the side-on alignment procedure, by slightly over-pitching the wave guide. The increased shear response seen in Figure 6.18 indicated that the pre-test alignment routine performed before the tests on UD90-S1 and UD90-S2 still included a slight misalignment and consequently, y-axis displacements were generated. However, the pitch angle from the last side-on alignment test was re-measured and confirmed to be within one pixel. Therefore, it is unknown what caused the pitch angle misalignment in the UD90-S1 and UD90-S2 tests.

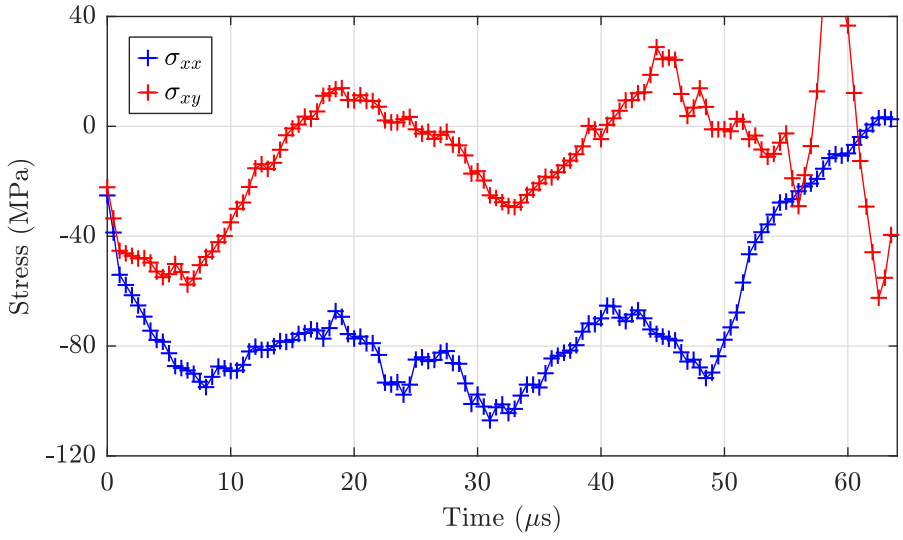

Figure 6.18: Average transverse stress $\overline{\sigma_{xx}}^{y}$ and average shear stress $\overline{\sigma_{xy}}^{y}$ acting on the impact edge as a function of time, obtained from the IBII test on UD90-S2.

Prior to the IBII tests on UD90-S1 to UD90-S2, the projectile/wave guide alignment procedure described in Chapter 4 was followed. However, the step of checking the pitch and yaw angle on the rotary stage dials between specimen tests was not followed because at that time, it was not part of the set-up process. This process was later included in the pre-test alignment procedure, because during testing on one of the UD90° specimens, it was found that the stage had become misaligned. It was likely that the stage misalignment was caused by one of the test components impacting the stage post-impact, *i.e.* the projectile or wave guide rebounding off the catching box located inside the target trap and impacting the stage. For subsequent tests, the 'bumped' stage resulted in a misalignment between the front face of the projectile and the wave guide, leading to 3D loading of the sample and a poor material property identification. Here, the reader is reminded that the theory developed for identifying the material properties (see Chapter 3) assumes that the specimen is loaded under 2D plane stress conditions. In order to check the extent of yaw misalignment, a top-down alignment test was performed, where a misalignment between the front face of the projectile and the wave guide was confirmed. For this reason, the added step of checking the pitch and yaw alignment angles on the rotary stage was included in the test procedure. Tests on specimens UD90-S3 to UD90-S6 presented in Table 6.3 were conducted after the additional pitch and yaw angle checking step was included in the pre-test alignment procedure, where the angles between the projectile and the wave guide were aligned to within the tolerance of 1-pixel. Note that the results for the test with significant projectile/wave guide misalignment were discarded, so they are not included in Table 6.3.

Stress-strain curves obtained from a test with suspected poor projectile/wave guide alignment are given in Figure 6.19. For slices up to 30 mm from the impact edge, a non-linear loading and a 'looping' characteristic in the unloading was thought to be caused by bending waves initiated by the 3D loading of the sample [115]. As the bending wave progresses along the specimen, the surface deformations are no longer wholly in-plane and therefore, the stress and strain quantities are no longer accurate, as they rely on the assumption of 2D deformations. However, the compressive stress-strain behaviour at slices closer to the specimen free-edge was significantly more linear. This transition to a more linear behaviour was possibly due to Saint Venant's effect in dynamics, causing the 3D effects to be reduced further from the point at which the loading is introduced [57].

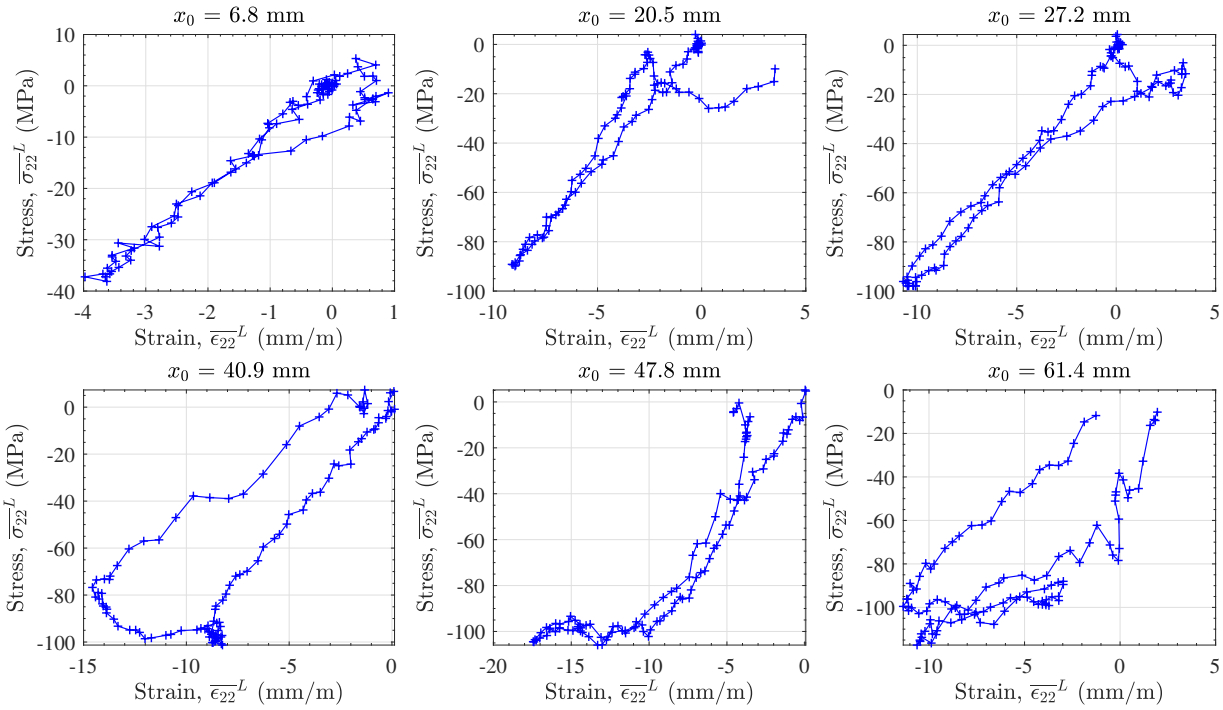

Figure 6.19: Transverse stress-strain curves at various x_0 positions obtained from a UD90° IBII test with suspected poor alignment between the projectile and the wave guide.

The spatial variation in the modulus identified over the specimen surface for the test with poor projectile/wave guide alignment is given in Figure 6.20. Close to the impact edge, poor modulus values were identified from the non-linear (artificial) loading behaviour seen in the stress-strain curves in Figure 6.19. This response was expected because the 3D effects are stronger closer to the impact edge. Moving away from the impact edge, the 3D effects reduce and a linear stress-strain response was obtained. Averaging over the middle 50% of the specimen length, the identified modulus was about 9.8 GPa, which was close to the value identified in the tests where the projectile and wave guide alignment was acceptable. Further, if the stiffness values from the back-half of the specimen were used to determine the average identified stiffness, the value is close to the mean of 10.2 GPa identified for the tests with good alignment. However, as a result of the 3D specimen loading and subsequent non-physical stress-strain response, the results from this test were not used for material property identification in this report.

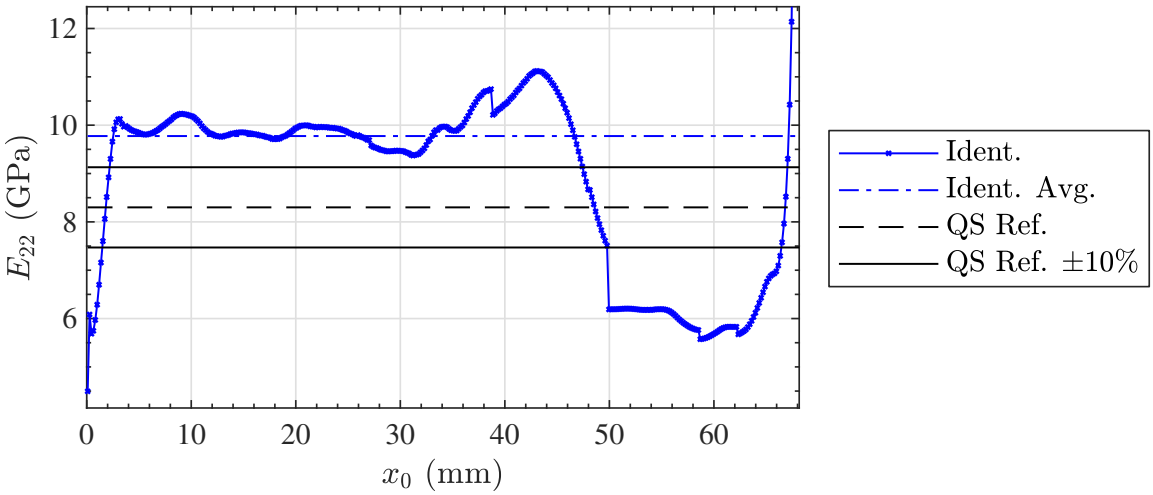

Figure 6.20: Transverse modulus as a function of x_0 position for the UD90° specimen with suspected poor alignment between the projectile and the wave guide.

6.4.2 UD90° specimens: shear component

Shear strain waves seen in the UD90° shear strain maps (*e.g.* in Figure 6.3 (e)) prompted the question of whether shear moduli could be identified from UD90° samples that were impacted with a slight pitch angle misalignment. To investigate the performance of this identification, average shear stress-strain curves were obtained from the UD90° samples, using Equation 3.24 of Chapter 3 to reconstruct the stress averages from the a_1 fields. Figure 6.21 shows the average shear stress-strain curves, which were mostly linear over the loading duration of the test. For these tests, the peak shear stress and strain magnitudes were much lower compared to the transverse response, with values around 20 MPa for the stresses and 2.5−3.5 mm.m^{-1} for the strains. This reduced shear response was expected because here, the induced shear was unintentionally introduced to the sample through the pitch angle misalignment. As a result of the low shear strain magnitudes, it was not possible to measure any non-linearity (or the non-linear onset strain) that was expected from this material [32]. As discussed in Chapter 8, future testing on UD90° samples with more pitch angle misalignment could activate a stronger, non-linear shear response. Note that in Figure 6.21, the red markers show the fitted portion of the loading from which modulus values were obtained, where linear fits to the absolute maximum stress were made.

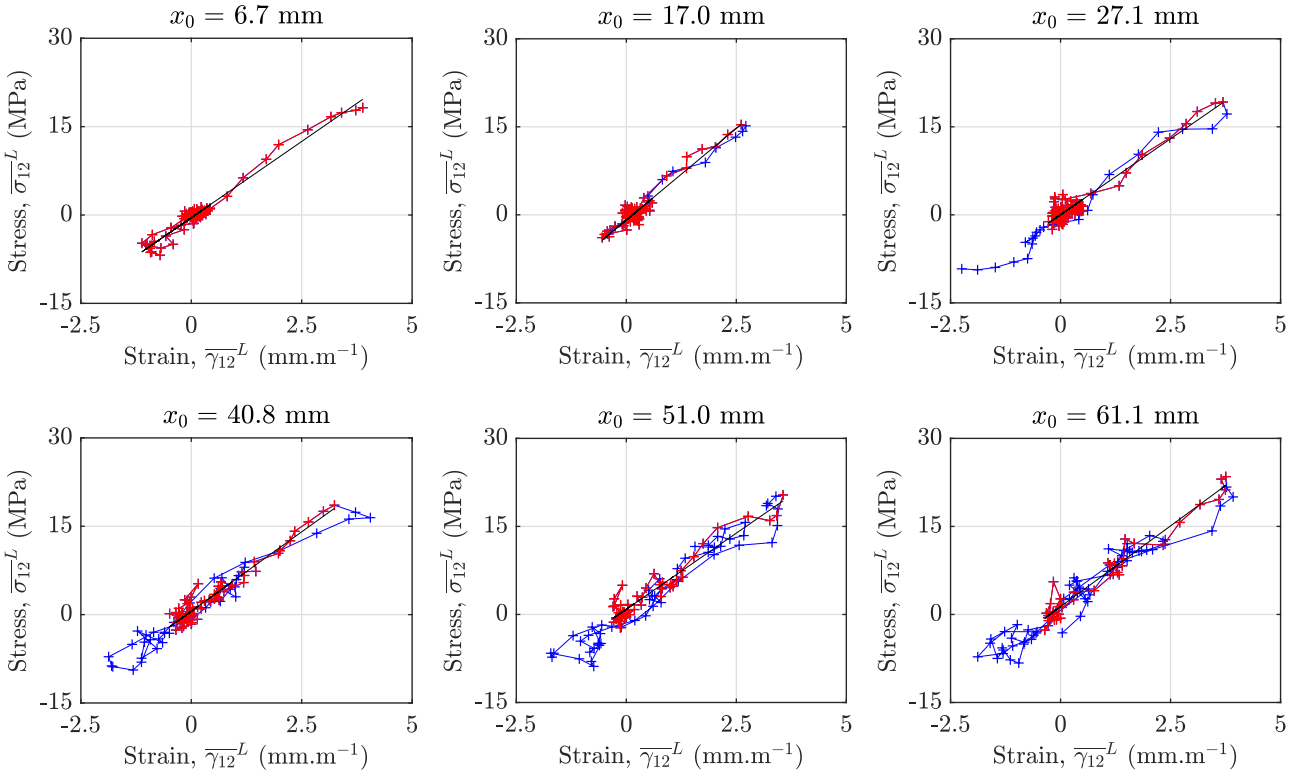

Figure 6.21: Shear stress-strain curves at various x_0 distances obtained from UD90-S3.

The shear modulus G_{12} is plotted against x_0 position for all specimens in Figure 6.22. Similar to the transverse response, a poor modulus identification resulted from the slices close to the impact and free edges. Modulus values from the middle 50% of slices were averaged to identify the G_{12} value for each sample, where the mean from six tests was 5.51 GPa with a SD of 0.127 GPa and a COV of 2.30%, as listed in Table 6.3. These statistics indicated good consistency across the batch of samples, in spite of the low shear-strain magnitudes resulting from the UD90° configuration. Using the quasi-static G_{12} modulus of 4.73 GPa obtained in this work, the %Diff. to QS value was 16.6%. Table 6.3 also lists the mean peak shear strain rate of 1.34×10^3 s^{-1}, which was lower than the mean transverse strain rate of 2.41×10^3 s^{-1} and expected given the low shear strains seen in Figure 6.21. The lower mean strain-normalised shear strain rate of 0.421×10^3 s^{-1} compared to the transverse value of 0.932×10^3 s^{-1} was also consistent with the reduced shear response of the UD90° sample impact conditions in these tests.

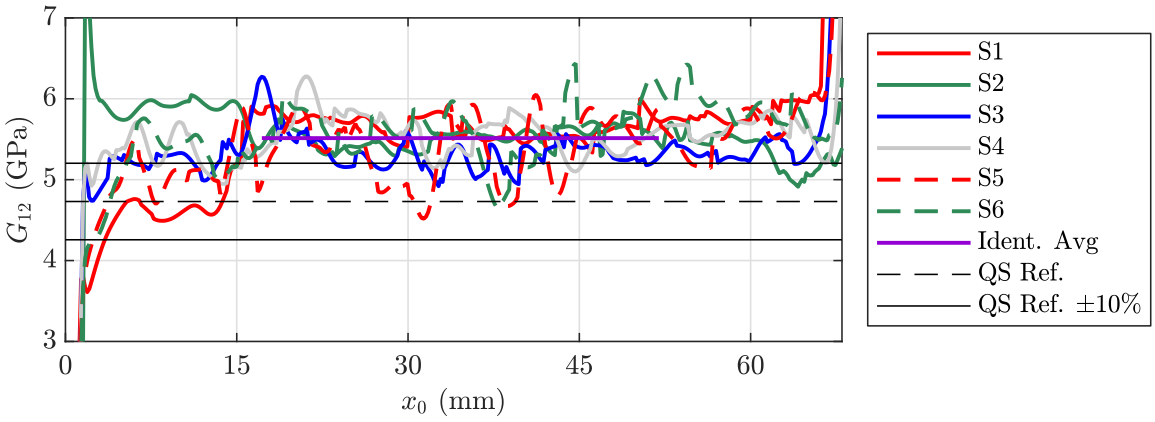

Figure 6.22: G_{12} as a function of x_0 position for the UD90° specimens, the mean identified from six tests, the quasi-static reference value and ±10% of the quasi-static reference value.

6.4.3 UD45° specimens: transverse component

The a_2 acceleration fields obtained from the IBII tests on UD45° samples were used (in Equation 3.30 of Chapter 3) to calculate $\overline{\sigma_{22}}^L$ over each angled slice L transverse to the sample fibres. Average transverse stress-strain curves from selected x_0 distances from UD45-S7 are presented in Figure 6.23. Similar to the transverse material response resulting for UD90-S3 shown in Figure 6.16, the transverse material response for the UD45° specimens was predominantly linear over the compressive loading period of the curve. Peak stresses were around 60 MPa, which was lower than the UD90-S3 result of around 160 MPa (again, see Figure 6.16). When an off-axis sample is impacted axially, the impact energy will be split between a transverse and a shear material response. It is therefore expected that a lower peak average transverse stress would result for the off-axis specimen compared to the transverse specimen, in which the majority of the impact energy invokes a transverse response (for an axially-aligned test). Similar to the UD90° E_{22} identification, linear fits over the compressive loading portion of the transverse stress-strain curves were used to calculate the transverse modulus for each slice. Figure 6.23 indicates the fitted data with red markers, with the fitting range starting at the zero stress condition and ending at the maximum compressive stress.

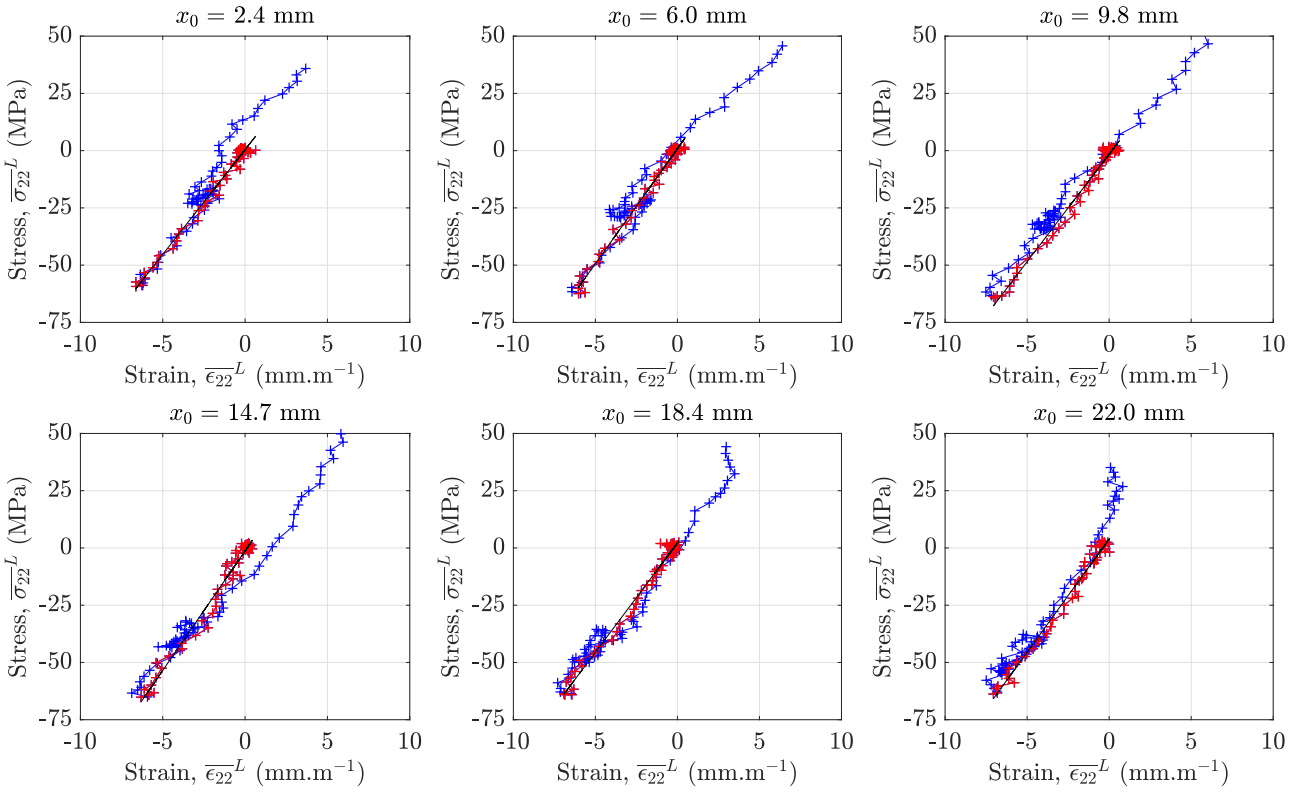

Figure 6.23: UD45-S7 average transverse stress-strain curves at the given x_0 positions. Linear fits to the red data points were used to calculate the transverse compressive modulus.

The average transverse modulus as a function of specimen length calculated over the recorded loading history from seven IBII tests on UD45° samples is given in Figure 6.24. For the UD45° specimens, modulus values were obtained from all angled slices with x_0 positions up to approximately 24 mm, depending on the dimensions of each sample. Table 6.4 gives the mean transverse modulus obtained from seven tests on UD45° specimens as 9.98 GPa, which was 20.2% higher than the quasi-static reference value of 8.30 GPa. Again, the statistics from the batch of seven samples tested indicated

good sample-to-sample consistency, as suggested by the low SD = 0.345 GPa and COV = 3.45% values. The peak and strain-normalised transverse strain rates of 0.795 $\times 10^3$ s^{-1} and 0.513 $\times 10^3$ s^{-1}, respectively, were lower than the UD90° values and expected, given the greater shear response for the UD45° configuration.

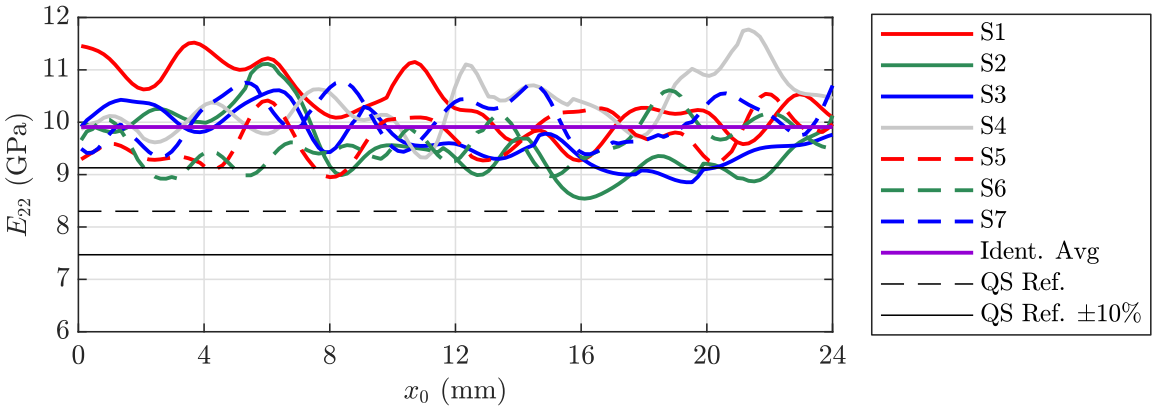

Figure 6.24: Transverse modulus E_{22} as a function of x_0 position identified from the seven IBII tests on UD45° grid samples. Also shown is the quasi-static reference value and ±10% of the quasi-static reference.

Table 6.4: Transverse modulus E_{22} and shear modulus G_{12} identified from seven UD45° grid specimens, together with the mean, SD, COV, QS value and %Diff. to QS value. Peak average and effective transverse and shear strain rates are also given.

Spec. (#)	$\boldsymbol{E_{22}}$ (GPa)	$\boldsymbol{G_{12,Sl.1}}$ (GPa)	$\boldsymbol{G_{12,Sl.2}}$ (GPa)	$\overline{\lvert\dot{\epsilon}_{22}\rvert}^{L}$ ($\times 10^3$ s^{-1})	$\overline{\lvert\dot{\gamma}_{12}\rvert}^{L}_{Sl.1}$ ($\times 10^3$ s^{-1})	$\overline{\lvert\dot{\gamma}_{12}\rvert}^{L}_{Sl.2}$ ($\times 10^3$ s^{-1})	$\hat{\dot{\epsilon}}_{22}$ ($\times 10^3$ s^{-1})	$\hat{\dot{\gamma}}_{12}$ ($\times 10^3$ s^{-1})
UD45-S1	10.6	5.54	5.05	0.513	1.38	0.926	0.316	0.809
UD45-S2	9.65	5.40	5.13	0.585	1.35	0.882	0.417	0.852
UD45-S3	9.79	5.70	5.25	0.913	1.33	1.01	0.672	0.987
UD45-S4	10.2	5.43	5.43	0.814	1.78	1.36	0.490	1.10
UD45-S5	9.81	5.69	5.38	0.968	1.83	1.30	0.591	1.13
UD45-S6	9.65	5.36	5.04	0.952	1.84	1.15	0.596	1.24
UD45-S7	10.1	5.40	5.17	0.819	1.83	1.16	0.509	1.19
Mean	**9.98**	**5.50**	**5.21**	**0.795**	**1.62**	**1.11**	**0.513**	**1.04**
SD	**0.345**	**0.143**	**0.153**					
COV (%)	**3.45**	**2.59**	**2.95**					
QS Value	**8.30**	**4.73**	**4.73**					
%Diff. QS	**20.2**	**16.3**	**10.1**					

6.4.4 UD45° specimens: shear component

Average shear stress values obtained from angled slices parallel to the sample fibres (slices 1) were calculated using Equation 3.36 of Chapter 3. These quantities are plotted against the average shear strains over the slice in Figure 6.25. As explained in Chapter 4, average shear stresses can also be obtained from slices transverse to the fibres (slices 2). In this case, the average shear stress over

the slice is calculated with Equation 3.36, exchanging the a_1 term with a_2. Average shear stresses obtained from slices 2 are plotted against the average shear strains over the slice in Figure 6.26. Comparison of Figure 6.23 with Figures 6.25 and 6.26 shows some distinct differences between the transverse and shear behaviour. Initially the material response over the loading portion of the curve was linear and then turned non-linear. This type of behaviour was expected, as the shear response of fibre composites is generally found to be non-linear, with the non-linearity being attributed to micro-damage formation [32]. As seen in Figure 6.25, the non-linear onset occurred with strain values of around 10−15 mm.m^{-1}. This was consistent with the results obtained in [32], where the non-linear onset strain was around 5 mm.m^{-1} at a strain rate of 5×10^{1} s^{-1}. With increasing strain rate, the non-linear response is delayed [53] and this explains the extended linear response observed in this study.

Figure 6.25 shows peak stresses from slices 1 of around 90 MPa, which were higher than the slice 2 values of about 60 MPa, as shown in Figure 6.26. Here, the lower peak shear stresses resulted because the absolute 2-axis acceleration surface averages $\overline{a_2}^S$ from the transverse slices (slices 2) were lower in magnitude compared to the parallel slices (slices 1), as shown in Figure 6.27. Note that in Figure 6.27, the acceleration surface averages are plotted for the slices with x_0 positions of 12.7 mm. The unloading behaviour was also predominantly linear and appeared to have a reduced stiffness compared to the linear portion of the compressive loading. In addition, there was a residual strain after the specimen had unloaded, which can be seen by comparing the loading and unloading strains at zero average shear stress in Figure 6.25. These residual strains appeared greater at slices closer to the impact edge, where the average stresses were higher compared to the slices near the free-edge. The lower unloading modulus and residual strain may indicate that the material had undergone micro-damage during the loading. As discussed in Chapter 8, physical evidence of damage is required to validate this hypothesis.

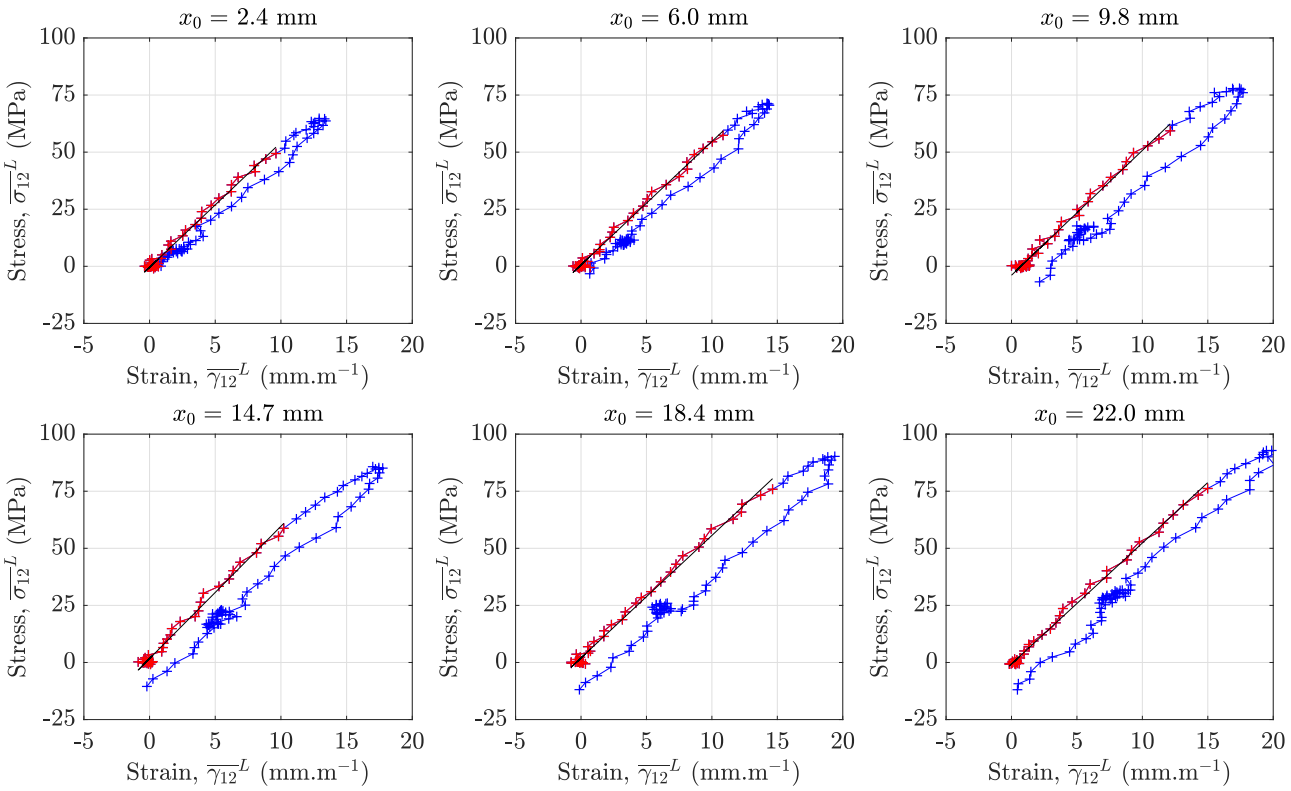

Figure 6.25: UD45-S7 average shear stress-strain curves at the given x_0 positions from slices 1. Red markers indicate the data used for the shear modulus identification.

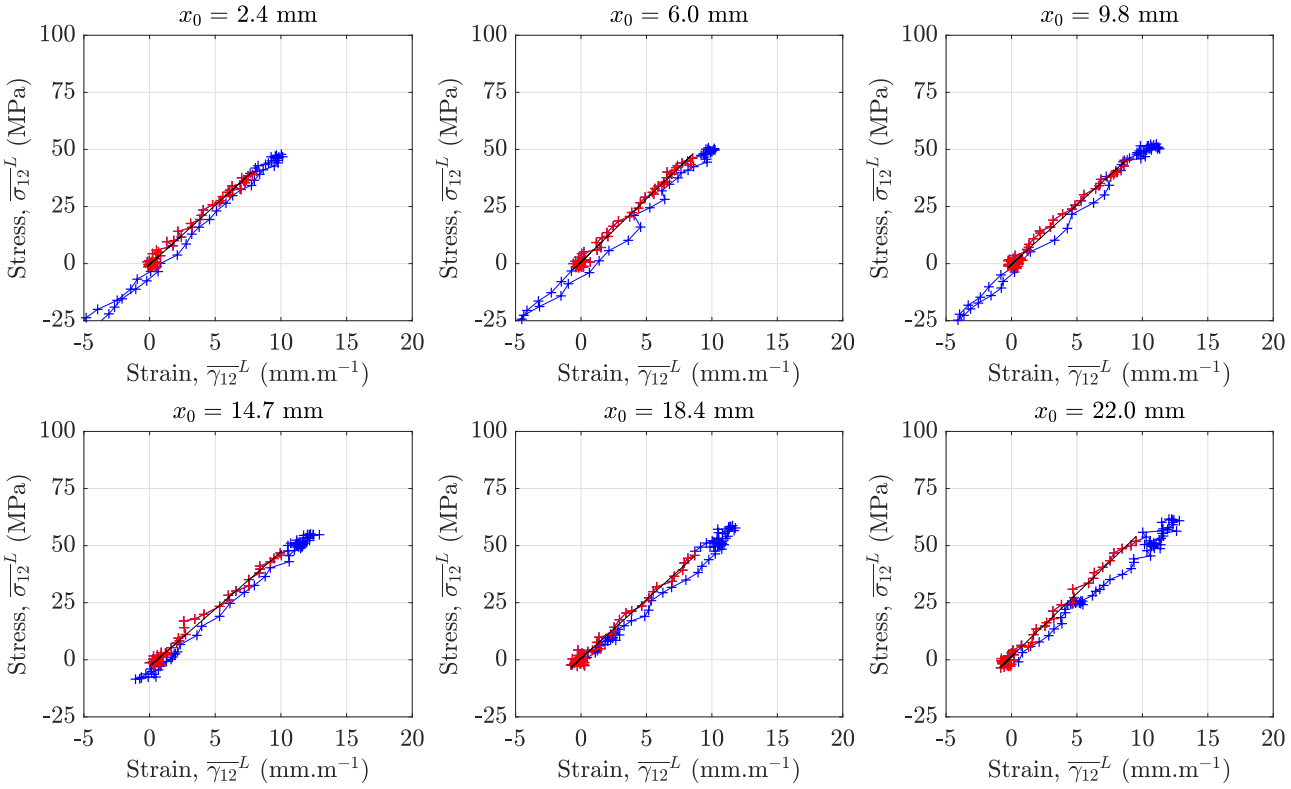

Figure 6.26: UD45-S7 average shear stress-strain curves at the given x_0 positions from slices 2. Red markers indicate the data used for the shear modulus identification.

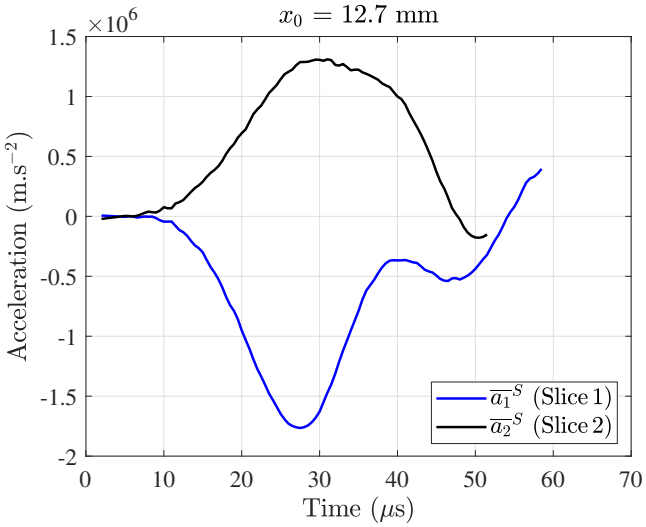

Figure 6.27: Line plots of the 1-axis surface average acceleration $\overline{a_1}^S$ from slices 1 and the 2-axis surface average acceleration $\overline{a_2}^S$ from slices 2 for UD45-S7.

A linear fit to the linear loading portion of the shear stress-strain curve was used to determine the shear modulus, for each x_0 distance on the specimen. The region over which the fits were made are shown as red markers on Figures 6.25 and 6.26. Several approaches are possible to determine the linear fitting range for the shear response. One approach is to observe the stress-strain response and manually select a value corresponding the the onset of non-linearity. However, this method is not systematic and sometimes leads to the inclusion of non-linear response data, because the linear to non-linear

transition strain is different across the range of slices. Therefore, in this report a progressive chord modulus fitting procedure was used to determine the upper limit of the fitting range. Starting at the lower limit strain, chord modulus fits to the stress values were made at progressively increasing strain values over the loading portion of the stress-strain curve, as shown in Figure 6.28. The transition from linear to non-linear behaviour was determined by the point at which the chord modulus fell below the average value, over the compressive loading range.

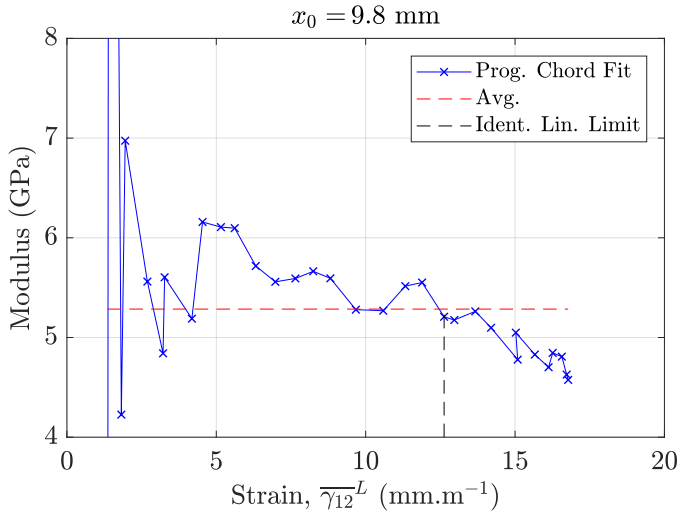

Figure 6.28: Progressive chord modulus against average shear strain for UD45-S7 calculated at $x_0 = 9.8$ mm. The average value over the loading portion of the stress-strain curve is indicated by the dashed red line.

Sometimes the chord modulus fell below the mean before the transition because of noise present in the stress-strain curves, as seen in Figure 6.28. Therefore, data in the range up to twice the strain resolution was excluded from the average chord modulus calculation. With the noisy data excluded, the linear limit was determined as the location where three successive chord moduli fell below the average. Finally, the shear modulus was determined from a linear fit through all data points in the linear range. As seen in Figures 6.25 and 6.26, the method used to determine the linear response fitting range was able to predict the onset of non-linearity in the stress-strain curves. Additional methods including tangent modulus fitting with a sliding window, and image deformation simulations with a non-linear material model are discussed as future work in Chapter 8.

The UD45° case shear modulus as a function of x_0 position plots from slices 1 and 2 are given in Figures 6.29 (a) and (b), respectively. For each test, shear moduli were identified from the average of the modulus values over the range of x_0 positions on the sample. Table 6.4 lists the mean G_{12} results from seven tests for slices 1 and 2 as 5.50 GPa and 5.21 GPa, respectively. Here, the slightly lower slice 2 shear moduli were influenced by the lower (absolute) acceleration surface averages incorporated in the average stress reconstructions (again see Figure 6.27). Statistics from slices 1 (SD = 0.143 GPa, COV = 2.59%) and from slices 2 (SD = 0.153 GPa, COV = 2.95%) were indicative of good consistency across the batch of samples. Using the quasi-static shear modulus of 4.73 GPa, shear strain-rate sensitivities of 16.3% and 10.1% were obtained for slices 1 and 2, respectively.

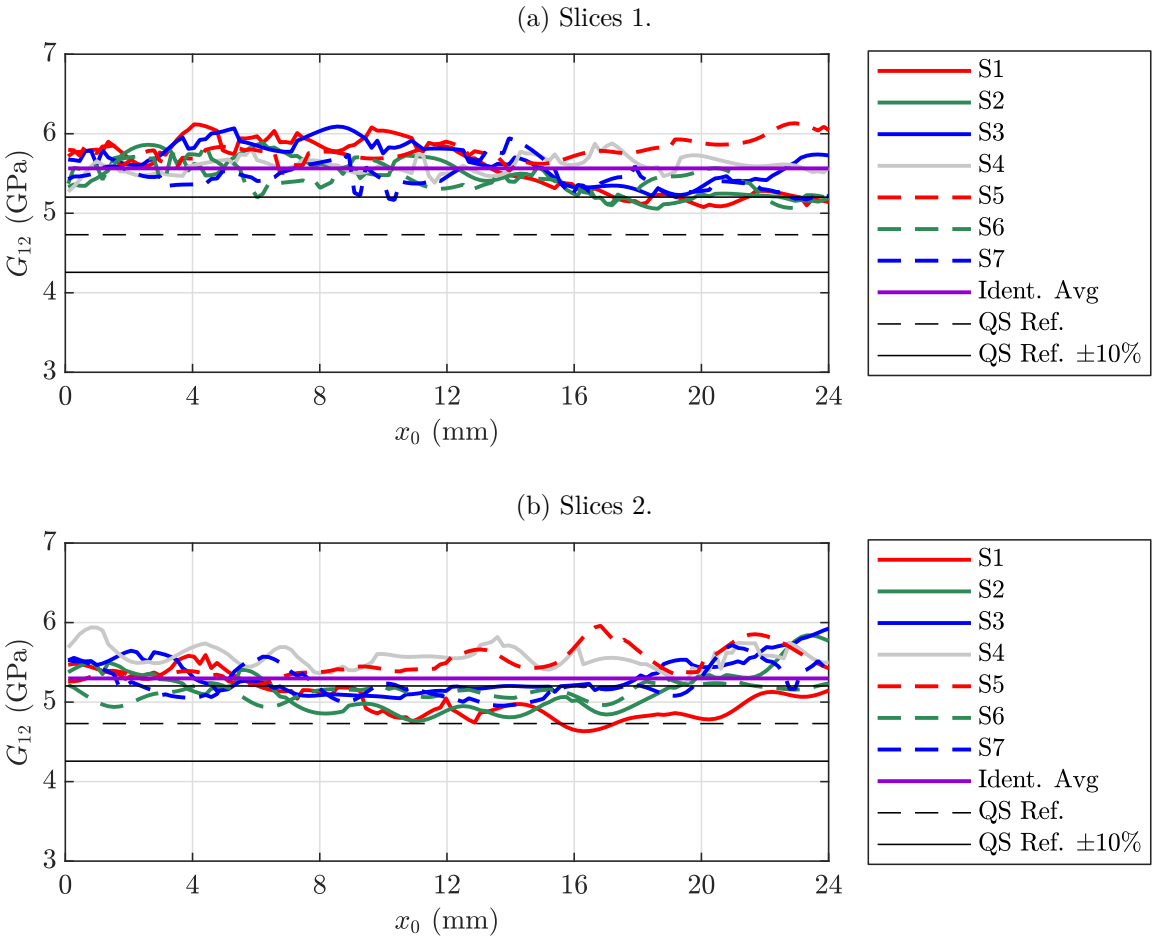

Figure 6.29: G_{12} against x_0 position from seven UD45° grid specimens together with the mean, quasi-static and ±10% of the quasi-static reference value.

Table 6.4 also lists the peak shear strain rates, which were higher than the transverse strain rates due to the increased shear response for the UD45° samples. Similar to the UD45° transverse strain rates, the mean strain-normalised shear strain rate of 1.04×10^3 s^{-1} was lower than the peak values obtained from slices 1 and 2 of 1.62×10^3 s^{-1} and 1.11×10^3 s^{-1}, respectively. Here, the lower peak slices 2 shear strain rates resulted from the lower slices 2 strain gradients, which can be seen in Figure 5.10 of Chapter 5. Given the increased shear strains obtained from the UD45° sample, the higher strain-normalised strain rate value of 1.04×10^3 s^{-1} compared to the UD90° result of 0.421×10^3 s^{-1} was expected.

6.4.5 MD45° specimens: shear component

In addition to the UD45° and UD90° samples, shear moduli were obtained from IBII tests on MD45° specimens. Average shear stress and strain components were obtained from angled slices parallel (slices 1) and transverse (slices 2) to the outer-surface fibres on the sample, as shown in Figure 6.30. Shear stress-strain curves from MD45-S1 at selected x_0 distances from slices 1 and 2 are shown in Figures 6.31 and 6.32, respectively. Overall, the shear response from the MD45° sample was similar to the UD45° samples behaviour shown in Figures 6.25 and 6.26, with a linear region that turned non-linear at around 10−15 mm.m^{-1}. This behaviour was also stronger at slices closer to the sample's impact edge, where the resulting peak shear stresses were higher at around 75−85 MPa. The same shear modulus identification method used for the UD45° samples was applied to the MD45° samples to obtain G_{12} values from both angled slices. Figures 6.33 (a) and (b) give the average shear modulus identified as a function of x_0 position for slices 1 and 2, respectively.

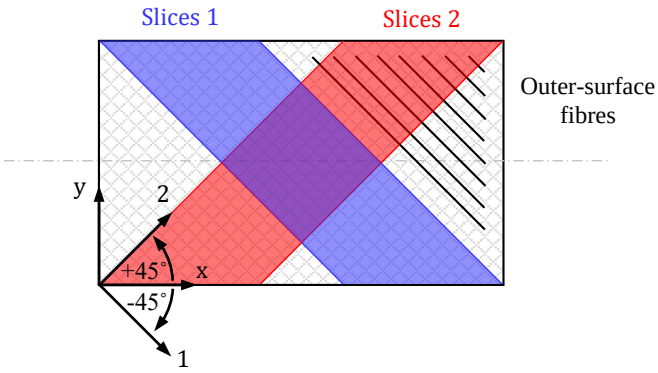

Figure 6.30: Angled slices on the MD±45° specimens.

Results from four IBII tests on MD45° specimens are listed in Table 6.5, which give a mean shear modulus of 5.05 GPa and 5.12 GPa for slices 1 and 2, respectively. These values were slightly lower than the UD45° and UD90° values of 5.51 GPa and 5.36 GPa (average of slice 1 and 2 values), respectively and consistent with the lower density of the MD45° sample density of 1530 ± 41 kg.m^{-3} compared to the UD samples of 1575 ± 17 kg.m^{-3}. The standard deviation and coefficient of variation were slightly higher than the corresponding values for the UD45° specimens. It was thought that the increased variation in the modulus values may have resulted from the sample fibre angles not being exactly ±45°. However, the fibre angle was measured on one side of the specimen surface using ImageJ. Three measurements were made per specimen, where a mean fibre angle of 44.6° ± 1° was obtained. Another reason for the increased variation could have been the larger geometric tolerance variability on the specimens. For some of the MD45° specimens, the edges were found to be not square to each other, which resulted in the specimen sitting slightly angled when adhered to the wave guide. The resulting percentage difference to the quasi-static value of 4.73 GPa obtained in this work was 6.77% and 8.25% for slices 1 and 2, respectively.

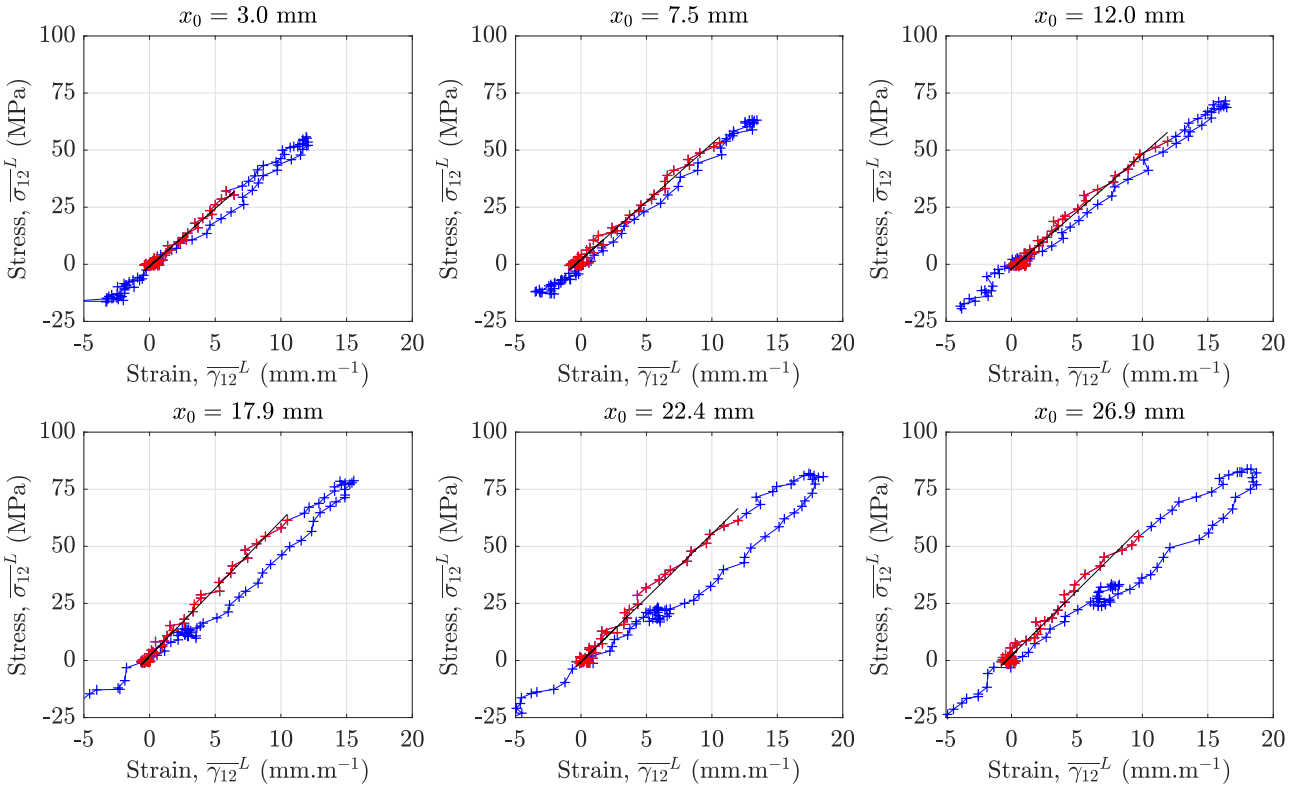

Figure 6.31: MD45-S1 average shear stress-strain curves at the given x_0 positions from slices 1. Red markers indicate the data used for the shear modulus identification.

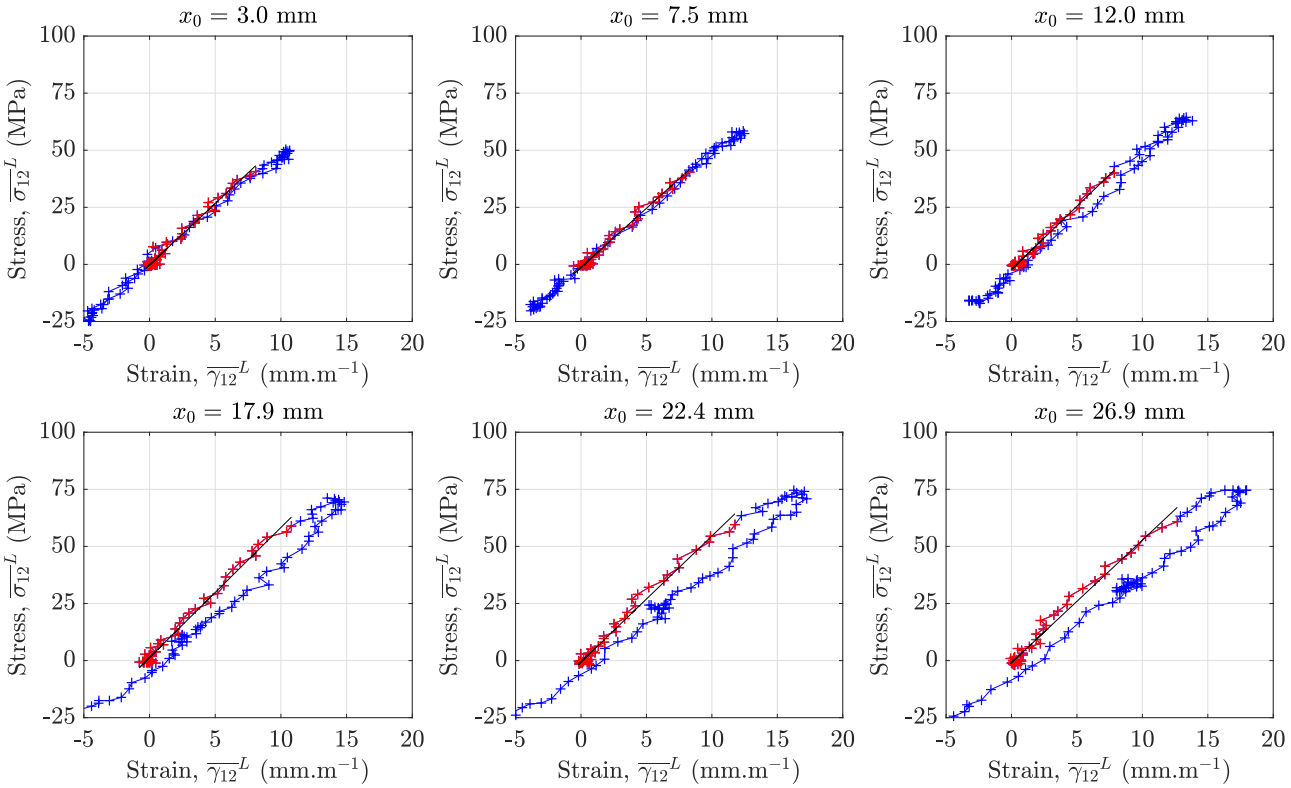

Figure 6.32: MD45-S1 average shear stress-strain curves at the given x_0 positions from slices 2. Red markers indicate the data used for the shear modulus identification.

Strain rate data from the MD45° samples was similar to the UD45° results, with peak shear strain rates of $1.91{\times}10^3$ s^{-1} and $1.60{\times}10^3$ s^{-1} for slices 1 and slices 2, respectively. Similar strain-normalised strain rates were also obtained, with a mean from four tests of $1.22{\times}10^3$ s^{-1}.

Table 6.5: Shear modulus G_{12} identified from four MD45° specimens, together with the mean, SD, COV, QS value and %Diff. to QS value. Peak average and effective shear strain rates are also listed.

Specimen (#)	$\boldsymbol{G_{12,\,Sl.\,1}}$ (GPa)	$\boldsymbol{G_{12,\,Sl.\,2}}$ (GPa)	**Peak** $\overline{\lvert\dot{\gamma}_{12}\rvert}^{L}_{Sl.\,1}$ ($\times 10^3$ s^{-1})	**Peak** $\overline{\lvert\dot{\gamma}_{12}\rvert}^{L}_{Sl.\,2}$ ($\times 10^3$ s^{-1})	$\hat{\dot{\gamma}}_{12}$ ($\times 10^3$ s^{-1})
MD45-S1	5.50	5.52	1.82	1.72	1.05
MD45-S2	4.95	5.04	2.14	1.38	1.20
MD45-S3	4.84	4.89	1.71	1.59	1.20
MD45-S4	4.91	5.03	2.00	1.69	1.46
Mean	**5.05**	**5.12**	**1.91**	**1.60**	**1.22**
SD	**0.305**	**0.275**			
COV (%)	**6.01**	**5.38**			
QS Value	**4.73**	**4.73**			
%Diff. QS	**6.77**	**8.25**			

(a) Slice 1.

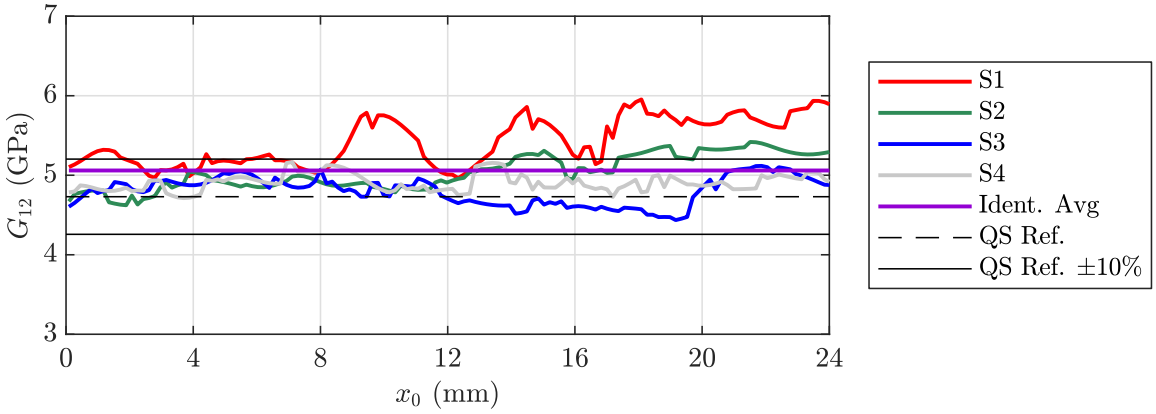

(b) Slice 2.

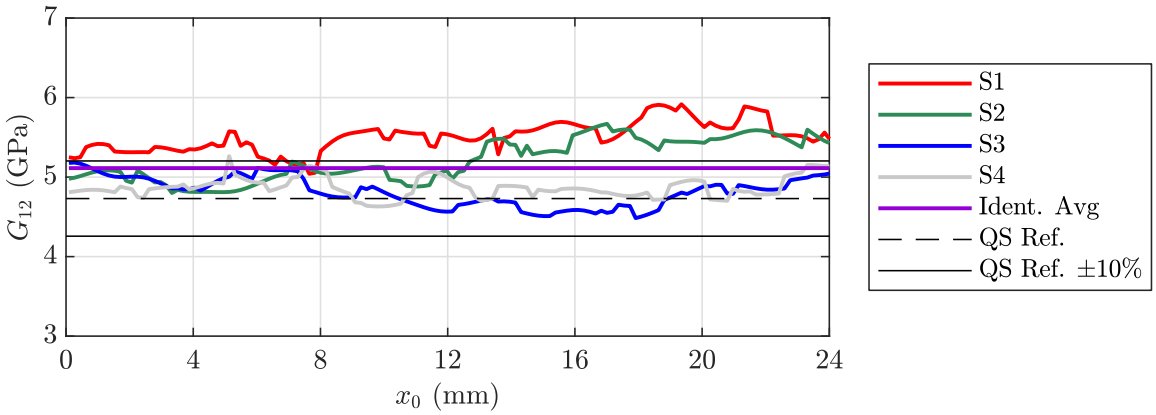

Figure 6.33: G_{12} against x_0 position from four MD±45° specimen tests together with the mean, quasi-static and ±10% of the quasi-static reference value.

6.5 Failure stress identification: UD90° samples

This section describes the tensile failure stress identification of the UD90° samples. Figure 6.34 (a) shows the UD90-S3 stress field calculated from the transverse strains and the constitutive law $\sigma_{xx}(\epsilon)$ at the time of fracture. This field had developed a strong tensile stress region on the left-hand side of the sample, following the reflection of the loading pulse from the free-edge of the sample. Figure 6.34 (b) gives the stress field at the same time step, calculated using the acceleration fields in the linear stress gauge $\sigma_{xx}(LSG)$, as described in Equation 3.38 of Chapter 3. Similar field distributions in Figures 6.34 (a) and (b) illustrate that the linear stress approximation over the specimen height was sufficient to represent the experimentally obtained (smoothed) stress maps. However, the linear approximation may not be sufficient for more complex stress states, where higher order reconstructions would be needed, as described in [141]. Failure stress values were obtained by analysing the stresses over a virtual gauge area, which is overlaid on both fields in Figures 6.34 (a) and (b). The stress calculated from the constitutive law averaged over the virtual gauge area $\overline{\sigma_{xx}}^{A}(\epsilon)$ and the stress calculated from the LSG equation over the virtual gauge area $\overline{\sigma_{xx}}^{A}(LSG)$ are plotted against time in Figure 6.34 (c). At about 45 μs, $\overline{\sigma_{xx}}^{A}(LSG)$ begins to diverge from $\overline{\sigma_{xx}}^{A}(\epsilon)$, indicating the onset of fracture in the specimen. Thereafter, $\overline{\sigma_{xx}}^{A}(\epsilon)$ continues to linearly rise (non-physically), whereas $\overline{\sigma_{xx}}^{A}(LSG)$ reaches a maximum at around 47 μs, which is considered to be the time of fracture initiation. The value of $\sigma_{xx}(LSG)$ at this time is taken as the failure stress, which for UD90-S3 was 93 MPa. $\overline{\sigma_{xx}}^{A}(LSG)$ is plotted against the x-axis strain averaged over the virtual gauge area $\overline{\epsilon_{xx}}^{A}$ in Figure 6.34 (d), where a tensile failure strain around 13.5 mm.m^{-1} resulted. This analysis shows that the stresses in the fracture region at the time of failure were higher than the stress averages presented in the stress-strain plots used for the modulus identification in Figure 6.16. For UD90-S3, taking the mean of the average transverse stress values over the range of slices corresponding to the virtual gauge length resulted in a stress of 60.7 MPa. This is why stress values averaged over the specimen height were not used to determine the failure stress.

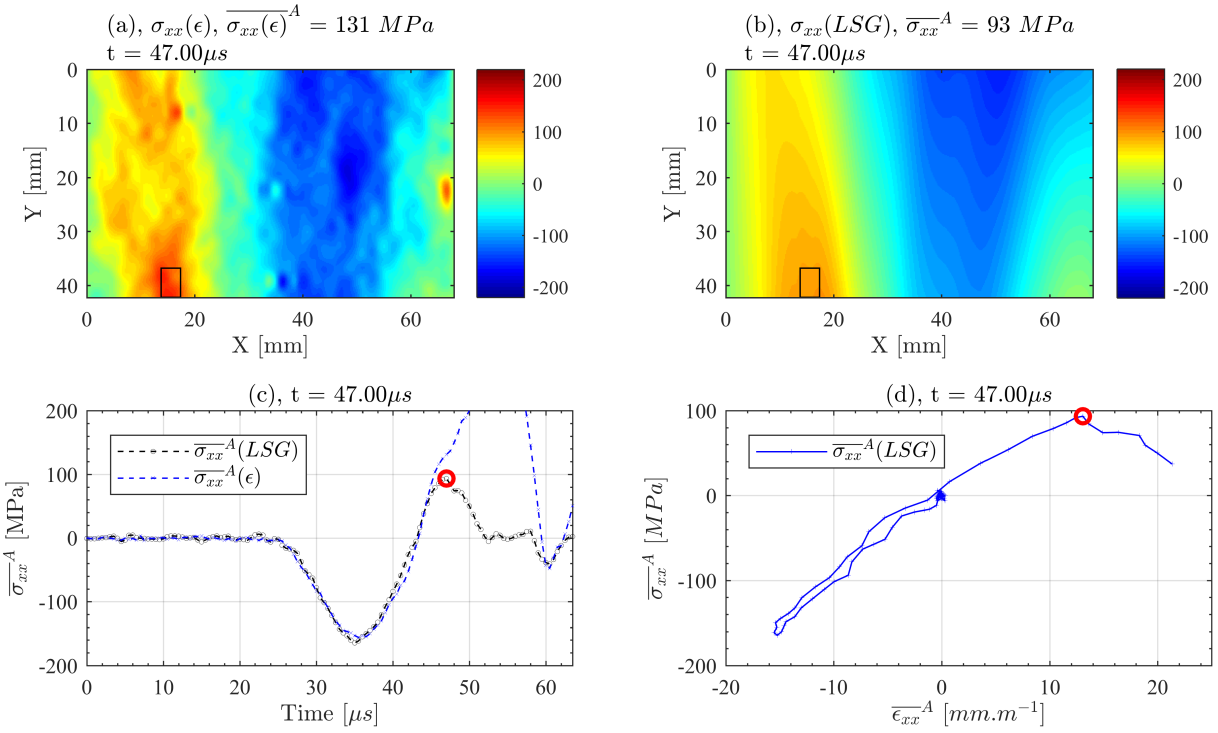

Figure 6.34: UD90-S3 failure stress identification: Stress field calculated from (a) a constitutive law and the strain fields $\sigma_{xx}(\epsilon)$, together with (b) the acceleration fields using the linear stress gauge equation $\sigma_{xx}(LSG)$. Virtual gauge area averages (c) $\overline{\sigma_{xx}}^{A}(\epsilon)$ and $\overline{\sigma_{xx}}^{A}(LSG)$ against time and (d) $\overline{\sigma_{xx}}^{A}(LSG)$ against the average strain over the virtual gauge area $\overline{\epsilon_{xx}}^{A}$.

Table 6.6 lists the mean tensile failure stress obtained from six IBII tests on UD90° grid samples of 89 MPa (SD = 7.1 MPa), which indicated good consistency across the batch of samples. Using the quasi-static data reported in [140], the percentage increase in the transverse tensile failure stress was 18%. Minimum compressive strain rates over the virtual gauge area prior to fracture **Min** $\overline{\dot{\epsilon}_{xx}}^{A}$ are also listed in Table 6.6, which ranged between 1.43×10^3 s^{-1} to 2.18×10^3 s^{-1}. Similar to the E_{22} modulus identification, the increased shear response observed in UD90-S1 and UD90-S2 did not affect the tensile failure stress values away from the mean. The maximum tensile strain rate over the gauge area at the time of failure **Max** $\overline{\dot{\epsilon}_{xx}}^{A}$ is also given in Table 6.6, where values ranged from 1.56×10^3 s^{-1} to 2.40×10^3 s^{-1}.

Table 6.6: Transverse failure stress averaged over the virtual gauge area $\overline{\sigma_{xx}}^{A}$ obtained from six IBII tests on UD90° grid samples, together with the mean, SD, COV, QS value from [140] and the % Diff. to QS value. The minimum compressive $\overline{\dot{\epsilon}_{xx}}^{A}$ (pre-failure) and maximum tensile $\overline{\dot{\epsilon}_{xx}}^{A}$ (at failure) strain rates are listed for each specimen.

Specimen (#)	$\overline{\sigma_{xx}}^{A}$ (LSG) (MPa)	**Min** $\overline{\dot{\epsilon}_{xx}}^{A}$ ($\times10^3$ s^{-1})	**Max** $\overline{\dot{\epsilon}_{xx}}^{A}$ ($\times10^3$ s^{-1})
UD90-S1	92	1.43	2.40
UD90-S2	87	1.45	2.10
UD90-S3	93	2.00	1.90
UD90-S4	98	2.10	1.82
UD90-S5	84	1.85	2.17
UD90-S6	78	2.18	1.56
Mean	**89**		
SD	**7.1**		
COV (%)	**8.1**		
QS Value	**75.4**		
% Diff. to QS	**18**		

Chapter 7

Experimental results 2: DIC

This chapter provides results from IBII tests on UD90°, UD45° and MD45° samples, where DIC was used to calculate the displacement fields. Kinematic fields obtained from DIC and Grid Method displacements are displayed together, so that differences and similarities in the field evolutions can be observed. Stress-strain curves and modulus results are then presented, with the identified material properties listed in summary tables for each laminate configuration. In this chapter, the naming convention: 'UD90-D1' refers to UD90° DIC specimen number one, distinguishing it from the grid samples *e.g.* 'UD90-S1'.

7.1 Kinematic field resolutions

Kinematic field resolutions for each DIC sample are listed in Table 7.1. Prior to the strain and acceleration resolution calculations, the displacement fields were smoothed with the optimised smoothing parameters obtained in Chapter 5. These smoothing parameters are recalled here: $[S_k, T_k] = [31, 5]$ for the UD90° samples and [31, 15] for the UD45° and MD45° samples, with S_k, T_k being the spatial and temporal smoothing kernel sizes in pixels and frames, respectively. Compared to the grids, the DIC samples obtained lower resolutions for all field components. This result was expected due to the additional smoothing of the 13-pixel subsets compared to the 5-pixel sampling used for the grids.

Table 7.1: Kinematic field resolutions for the DIC sample tests.

	Displacement		Strain			Acceleration	
	$\boldsymbol{u_x}$	$\boldsymbol{u_y}$	$\boldsymbol{\epsilon_{xx}}$	$\boldsymbol{\epsilon_{yy}}$	$\boldsymbol{\gamma_{xy}}$	$\boldsymbol{a_x}$	$\boldsymbol{a_y}$
	(μm) [pixels]		(μm.m^{-1})			($\times 10^5$ m.s^{-2})	
UD 90 (5 tests)	0.765 [0.004]	0.735 [0.004]	154	152	217	2.64	2.52
UD 45 (5 tests)	0.688 [0.004]	0.683 [0.004]	469	446	640	1.63	1.57
MD 45 (4 tests)	0.772 [0.004]	0.768 [0.004]	501	492	688	1.78	1.77
Mean	0.742	0.729	375	363	515	2.02	1.95

7.2 Comparison of the DIC and Grid Method kinematic fields

7.2.1 UD90° specimens

Figure 7.1 (a), (b) and (c) gives the ϵ_{22} fields for the DIC sample UD90-D5 at 10 μs, 20 μs and 30 μs, respectively. The same field values obtained from the Grid Method sample UD90-S3 are plotted underneath in Figure 7.1 (d), (e) and (f), at slightly adjusted times so that the wave fronts are aligned. Fields from the DIC tests appeared smoother than their Grid Method counterparts. Given that the same spatial smoothing kernel size of $S_k = 31$ pixels was used to process both the UD90° Grid Method and DIC samples, the 'smoother' appearance of the DIC fields was likely a result of the inherent smoothing from the 13-pixel subsets. The compressive ϵ_{22} magnitudes were similar at around 20 mm.m^{-1} and the ϵ_{22} wave fronts were planar, which indicated that there was a relatively low shear response from the test. This was confirmed by the low magnitudes in the γ_{12} fields shown in Figure 7.2, which were on the order of 5 mm.m^{-1}. Figures 7.2 (a), (b) and (c) obtained from the DIC sample had a slightly weaker shear response compared to the Grid Method fields in Figures 7.2 (d), (e) and (f). This may have resulted from the reduced spatial resolution in the DIC case, or a reduced pitch angle misalignment between the projectile and the wave guide. As this project was focused on strain-rate sensitive material properties, the ϵ_{11} strains are not shown here. For brevity, the strain rate fields are also not presented, but can be found *via* the link to the digital dataset given at the end of this thesis.

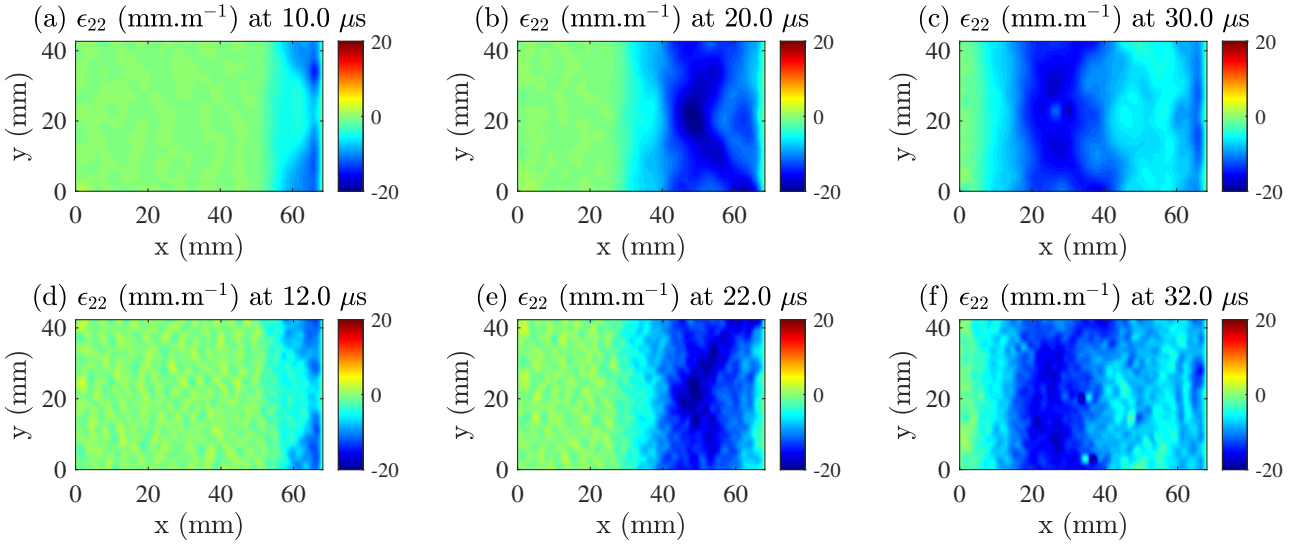

Figure 7.1: Material coordinate system ϵ_{22} strain fields obtained from the DIC sample UD90-D5: at (a) 10 μs, (b) 20 μs and (c) 30 μs, together with the ϵ_{22} fields from the Grid Method sample UD90-S3: at (d) 12 μs, (e) 22 μs and (f) 32 μs.

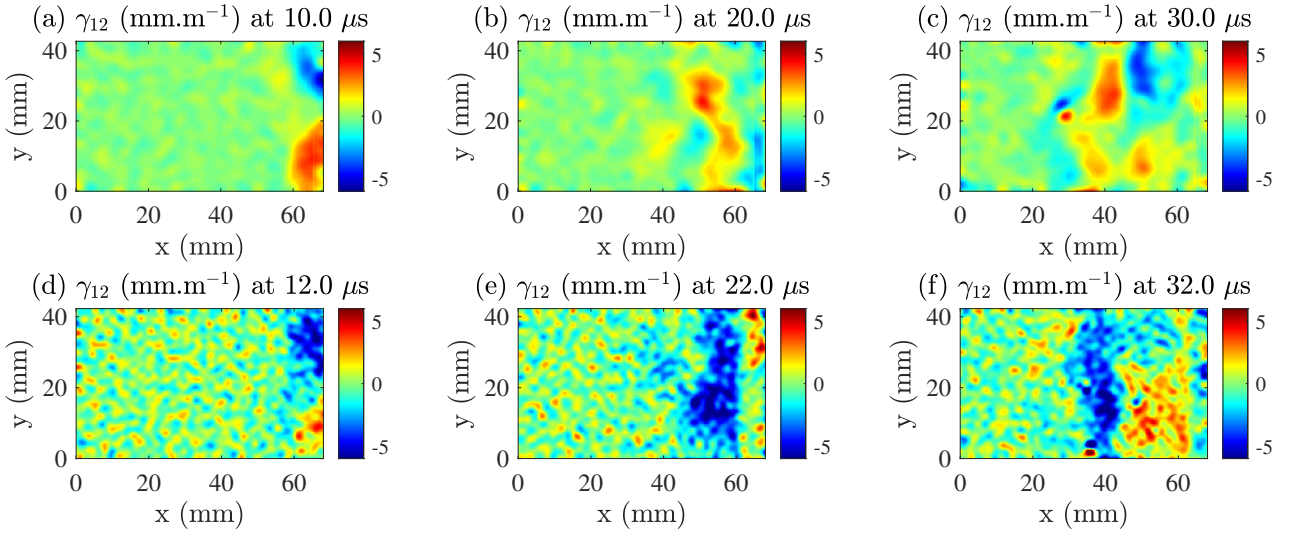

Figure 7.2: Material coordinate system γ_{12} strain fields obtained from the DIC sample UD90-D5: at (a) 10 μs, (b) 20 μs and (c) 30 μs, together with the γ_{12} fields from the Grid Method sample UD90-S3: at (d) 12 μs, (e) 22 μs and (f) 32 μs.

The a_2 acceleration fields from the DIC sample UD90-D5 and the Grid Method sample UD90-S3 are shown in Figures 7.3 (a), (b) and (c) and Figures 7.3 (d), (e) and (f), respectively. No major differences were observed in the fields, with the exception of the additional DIC spatial smoothing that was also visible in the a_1 acceleration fields in Figures 7.4 (a), (b) and (c) compared to the grid results in Figures 7.4 (d), (e) and (f).

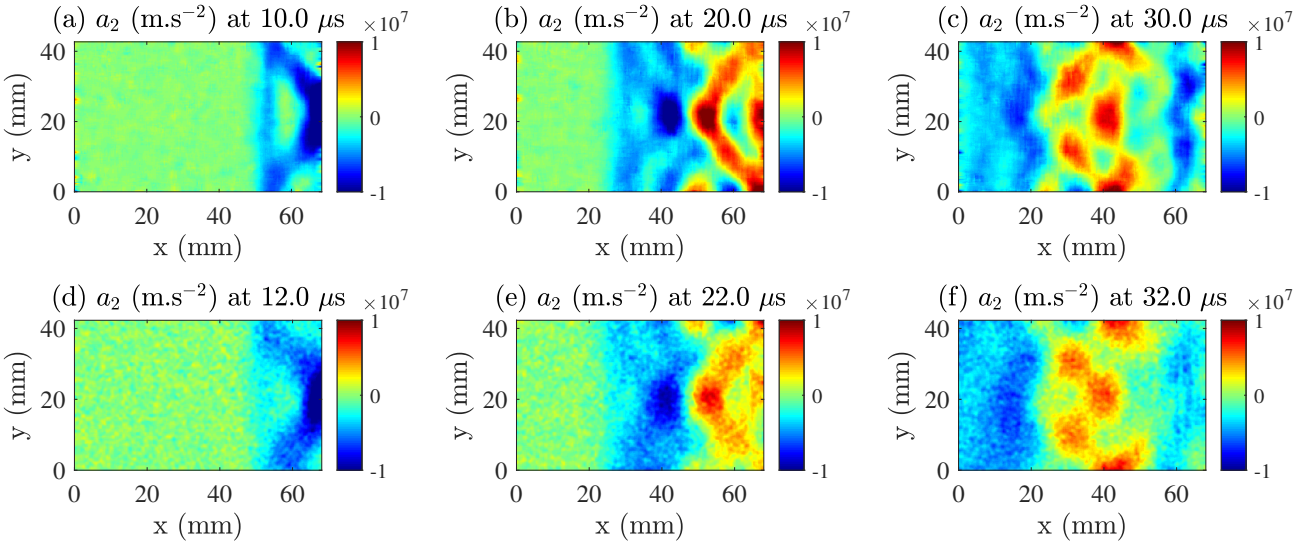

Figure 7.3: a_2 fields from the DIC sample UD90-D5: at (a) 10 μs, (b) 20 μs and (c) 30 μs, together with the a_2 fields from the Grid Method sample UD90-S3: at (d) 12 μs, (e) 22 μs and (f) 32 μs.

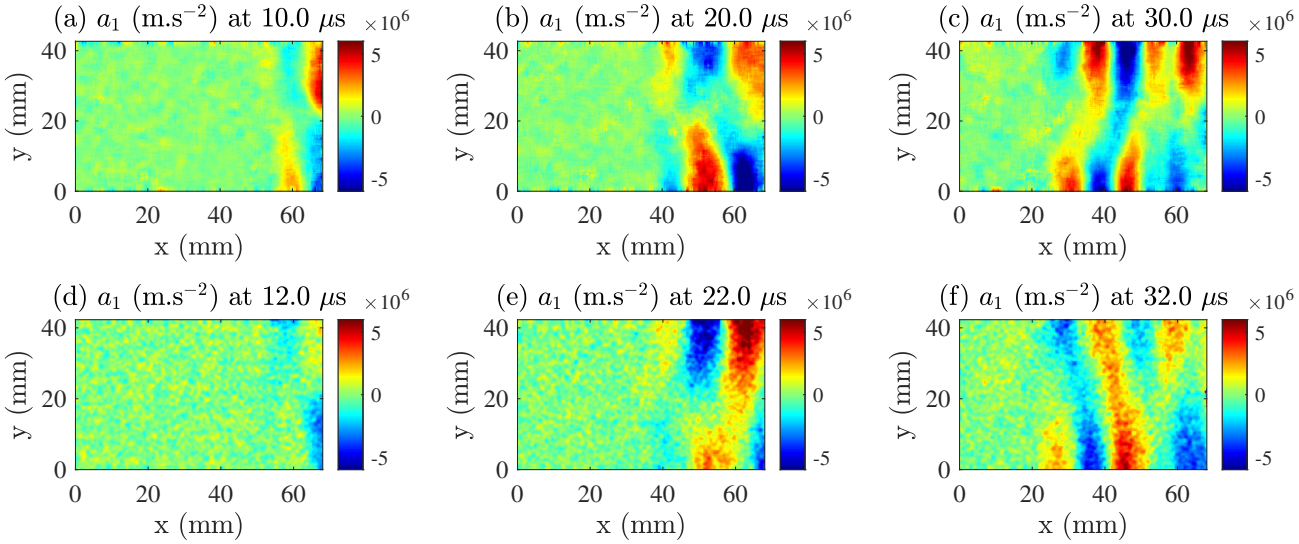

Figure 7.4: a_1 fields from the DIC sample UD90-D5: at (a) 10 μs, (b) 20 μs and (c) 30 μs, together with the a_1 fields from the Grid Method sample UD90-S3: at (d) 12 μs, (e) 22 μs and (f) 32 μs.

7.2.2 UD45° specimens

The ϵ_{22} fields from the DIC sample UD45-D1 are given in Figures 7.5 (a), (b) and (c). Similar to the UD90° results, the UD45° DIC sample ϵ_{22} fields appeared smoother than the Grid Method equivalents, which are shown for UD45-S1 in Figures 7.5 (d), (e) and (f). A portion of this increased smoothing can be attributed to the larger spatial smoothing kernel size used to process the UD45° DIC results of $S_k = 31$ pixels, *vs.* $S_k = 11$ pixels for the grids. But again, some increased smoothing was expected from the 13-pixel subsets in the DIC case. Similar results were obtained for the γ_{12} strain fields from UD45-D1 and UD45-S1, which are given in Figures 7.6 (a), (b) and (c) and Figures 7.6 (d), (e) and (f), respectively. Due to the increased shear response from the UD45° sample, the peak shear strains were on the order of 20 mm.m^{-1} and higher than the transverse strains, which were around 10 mm.m^{-1}.

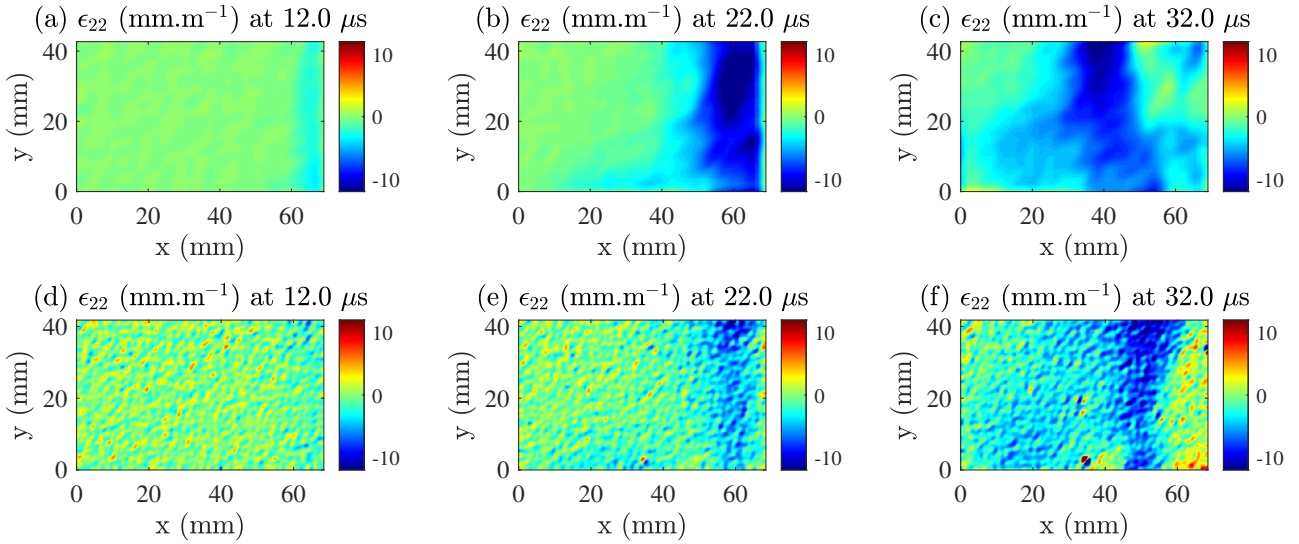

Figure 7.5: Material coordinate system ϵ_{22} strain fields obtained from the DIC sample UD45-D1: at (a) 12 μs, (b) 22 μs and (c) 32 μs, together with the ϵ_{22} fields from the Grid Method sample UD45-S1: at (d) 12 μs, (e) 22 μs and (f) 32 μs.

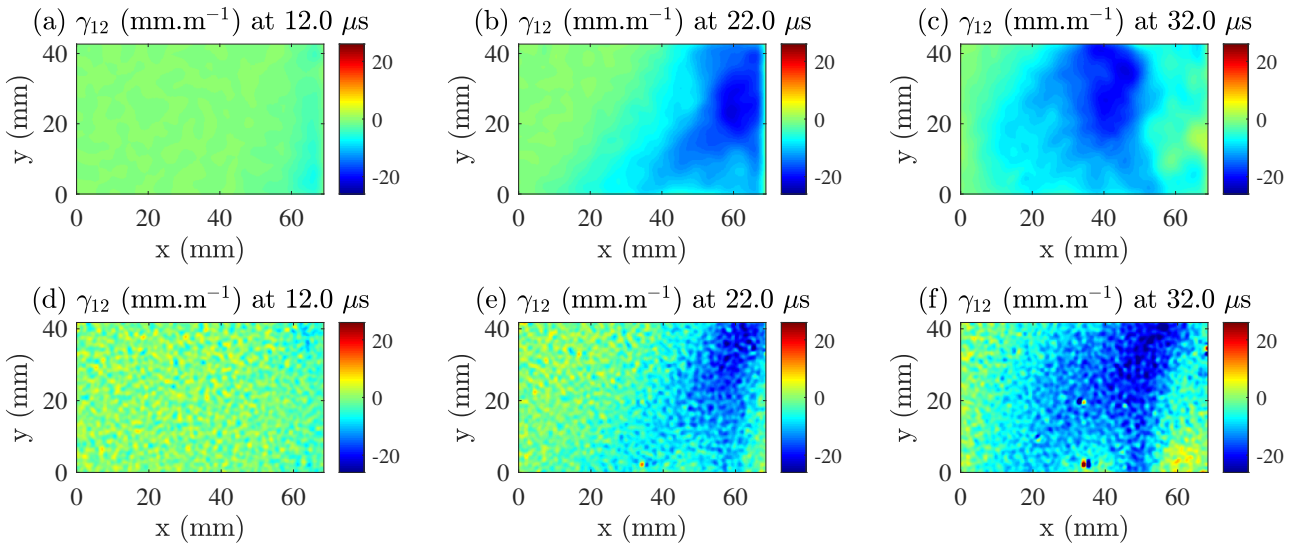

Figure 7.6: Material coordinate system γ_{12} strain fields obtained from the DIC sample UD45-D1: at (a) 12 μs, (b) 22 μs and (c) 32 μs, together with the γ_{12} fields from the Grid Method sample UD45-S1: at (d) 12 μs, (e) 22 μs and (f) 32 μs.

Figures 7.7 and 7.8 give the a_2 and a_1 acceleration fields, respectively. Here, the peak a_2 and a_1 acceleration magnitudes for both sample types were balanced, on the order of 4−6 m.s^{-2}. Gradients can be seen in the DIC case a_1 compressive wave fronts in Figures 7.8 (a) and (b) compared to the Grid Method results in Figures 7.8 (d) and (e). This finding was consistent across the batch of samples tested and may have been caused by the reduced spatial resolution in the DIC case.

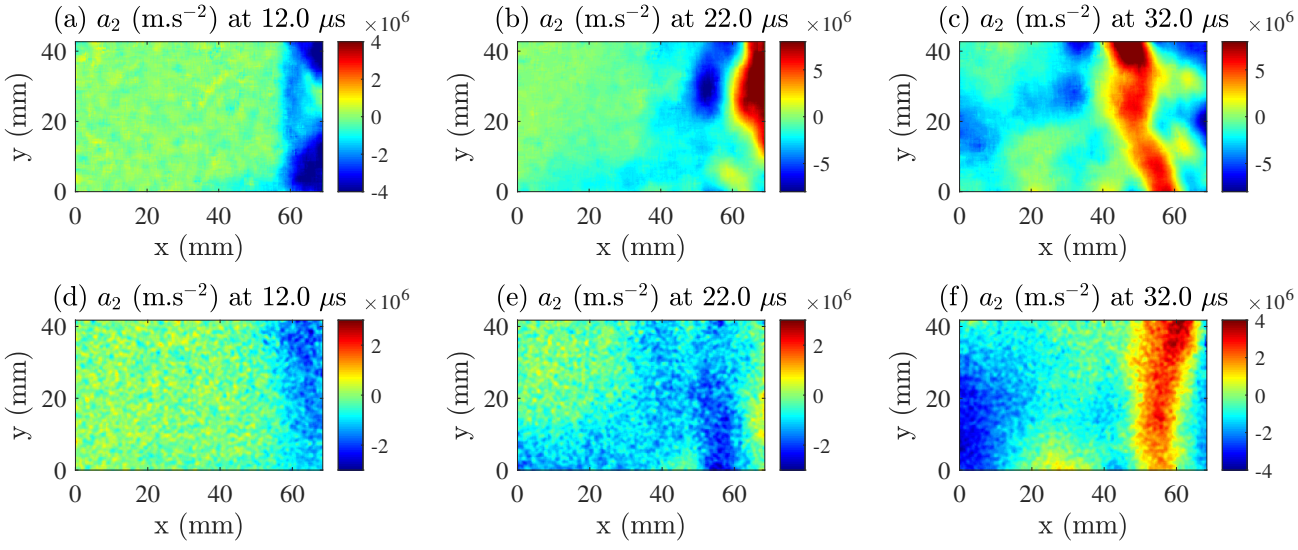

Figure 7.7: a_2 fields from the DIC sample UD45-D1: at (a) 12 μs, (b) 22 μs and (c) 32 μs, together with the a_2 fields from the Grid Method sample UD45-S1: at (d) 12 μs, (e) 22 μs and (f) 32 μs.

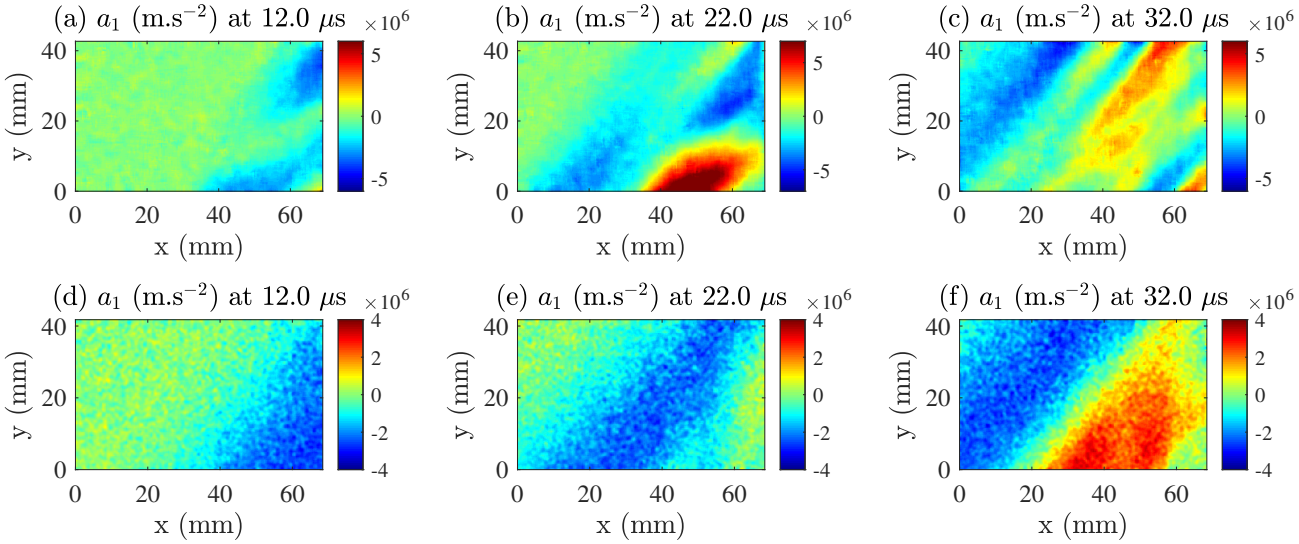

Figure 7.8: a_1 fields from the DIC sample UD45-D1: at (a) 12 μs, (b) 22 μs and (c) 32 μs, together with the a_1 fields from the Grid Method sample UD45-S1: at (d) 12 μs, (e) 22 μs and (f) 32 μs.

7.2.3 MD45° specimens

Similar to the UD samples, the MD45° sample γ_{12} fields shown in Figures 7.9 (a), (b) and (c) were smoother than the Grid Method results shown in Figures 7.9 (d), (e) and (f). In both cases, the peak shear strain magnitudes were close to the UD45° values, at around 20 mm.m^{-1}. Figures 7.10 and 7.11 revealed peak a_2 and a_1 accelerations that were balanced, on the order of 5−10 m.s^{-2}.

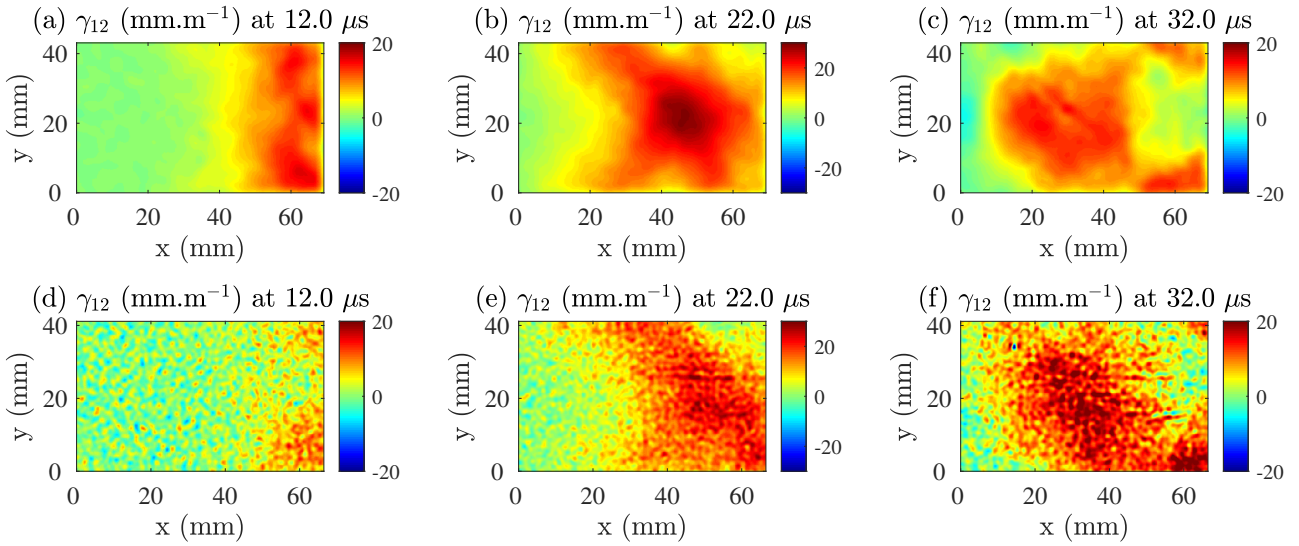

Figure 7.9: Material coordinate system γ_{12} strain fields obtained from the DIC sample MD45-D2: at (a) 12 μs, (b) 22 μs and (c) 32 μs, together with the γ_{12} fields from the Grid Method sample MD45-S2: at (d) 12 μs, (e) 22 μs and (f) 32 μs.

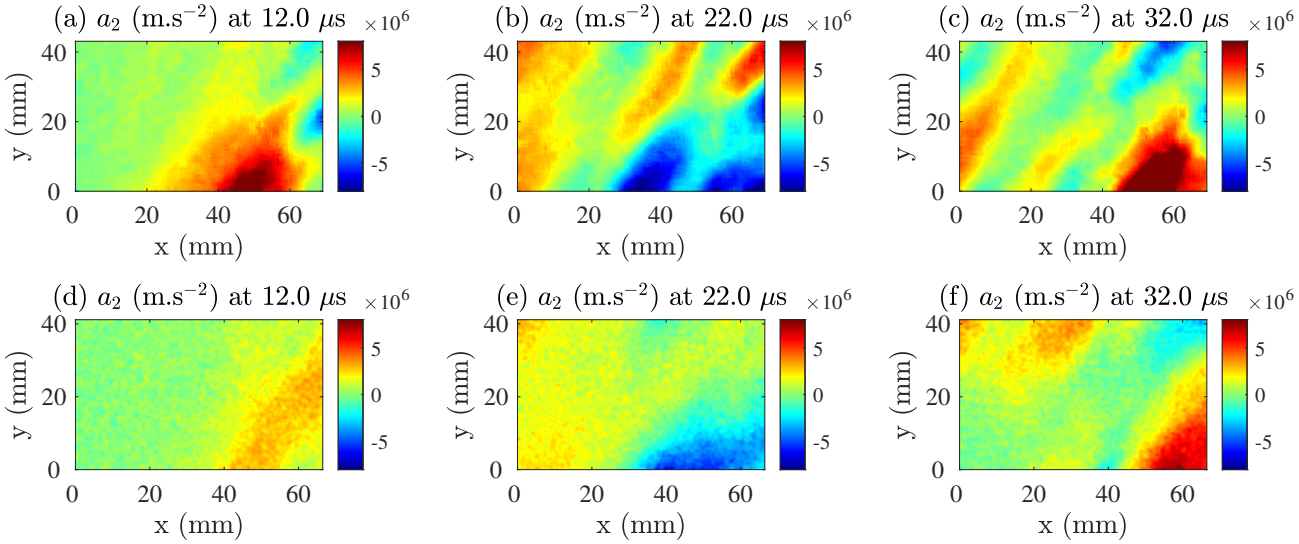

Figure 7.10: a_2 fields from the DIC sample MD45-D2: at (a) 12 μs, (b) 22 μs and (c) 32 μs, together with the a_2 fields from the Grid Method sample MD45-S2: at (d) 12 μs, (e) 22 μs and (f) 32 μs.

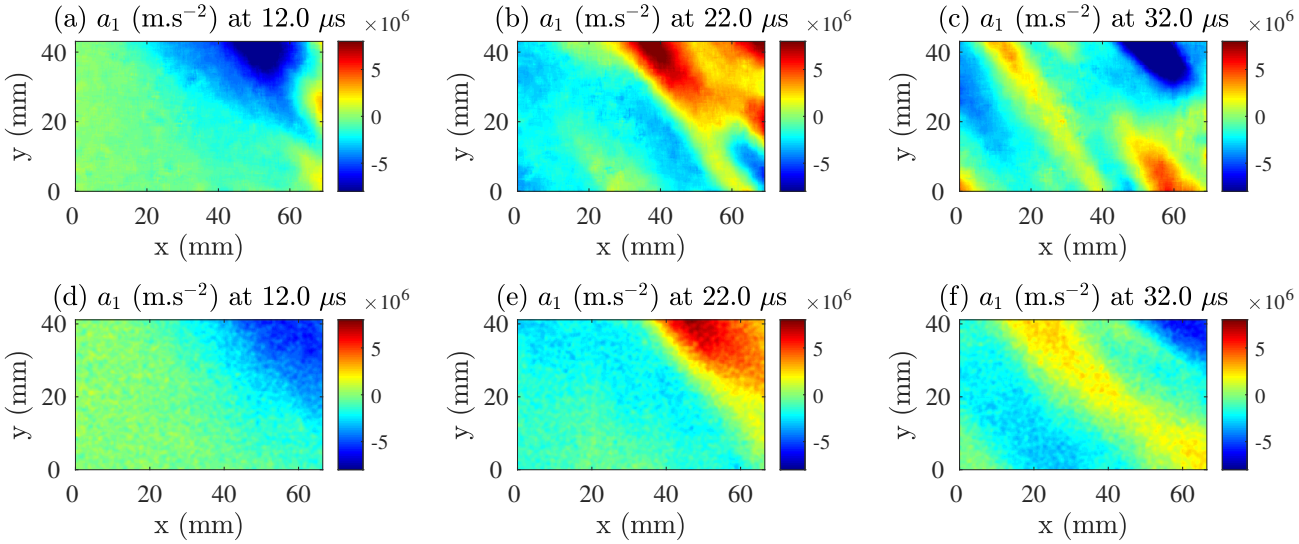

Figure 7.11: a_1 fields from the DIC sample MD45-D2: at (a) 12 μs, (b) 22 μs and (c) 32 μs, together with the a_1 fields from the Grid Method sample MD45-S2: at (d) 12 μs, (e) 22 μs and (f) 32 μs.

7.3 Modulus identification

This section provides stress-strain curves and modulus *vs.* position plots obtained from the DIC samples. Figures showing the DIC derived material properties have the same axis limits as the Grid Method results presented in Chapter 6, so that the results could be easily compared. In-test measurements of the pitch and yaw angles between the projectile and the wave guide are also given for each sample. When combined with the material response data, negligible alignment-induced effects were observed in the identified in-plane transverse and shear moduli.

7.3.1 UD90° specimens: transverse component

Similar to the IBII tests on UD90° Grid Method samples, the average transverse stress over the specimen height $\overline{\sigma_{22}}^L$ was plotted against the average strain over the specimen height $\overline{\epsilon_{22}}^L$ at each vertical slice on the sample. Figure 7.12 shows stress-strain curves at selected x_0 positions for UD90-D2, where a linear response was obtained over the compressive loading. Most of the unloading response was also linear, except for the later stages where a crack formed in the sample. Peak average compressive stresses were on the order of 150 MPa, which was consistent across the batch of tests conducted. Red markers on Figure 7.12 show the linear fitting region that was used to derive transverse moduli from each slice on the UD90° samples.

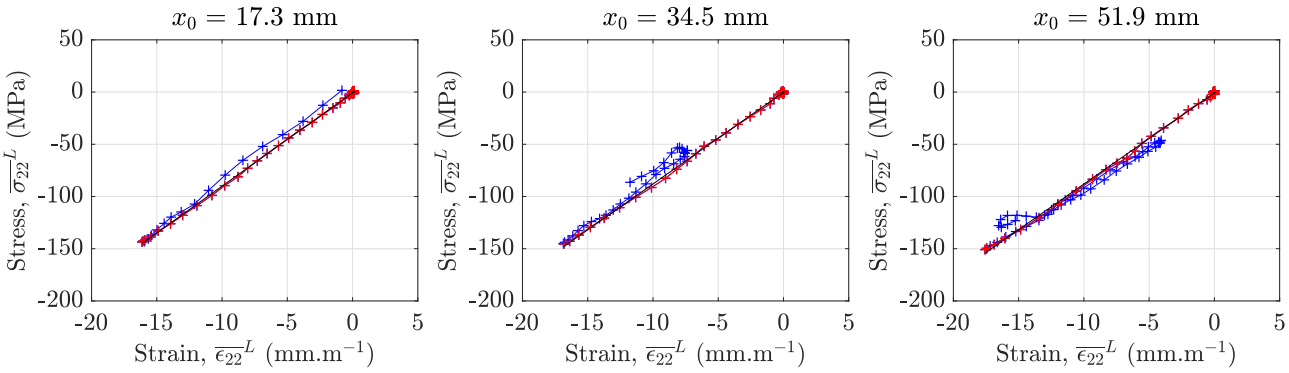

Figure 7.12: Transverse stress-strain curves at various x_0 distances obtained from UD90-D2.

Figure 7.13 shows the transverse modulus as a function of x_0 position (from the free-edge) results from five IBII tests on UD90° DIC samples. As with the UD90° grid samples, E_{22} modulus values were identified by averaging the moduli over the middle 50% of the sample's length. This procedure was undertaken so that spatial smoothing effects at the sample edges and low signal-to-noise strains at the free-edge did not influence the identified moduli [29]. Good repeatability was obtained across the batch of five samples, where the mean transverse modulus was E_{22} = 8.98 GPa (SD = 0.079 GPa), as listed in Table 7.2. Using the quasi-static modulus of 8.3 GPa obtained in this work, the percentage difference to the quasi-static value (% Diff. to QS) was 8.15%. This result was significantly lower than the strain-rate sensitivity obtained from the UD90° grid samples, which was 22.3%. However, lower E_{22} values were expected from these tests because the UD90° DIC samples were cut from a plate that had a lower density compared to the UD90° grid samples. This is further discussed in Chapter 8, where an explanation for the lower laminate density is given. Table 7.2 also lists the peak compressive transverse strain-rate of 3.34×10^3 s^{-1}, which was higher than the strain-normalised transverse strain-rate of 1.50×10^3 s^{-1}.

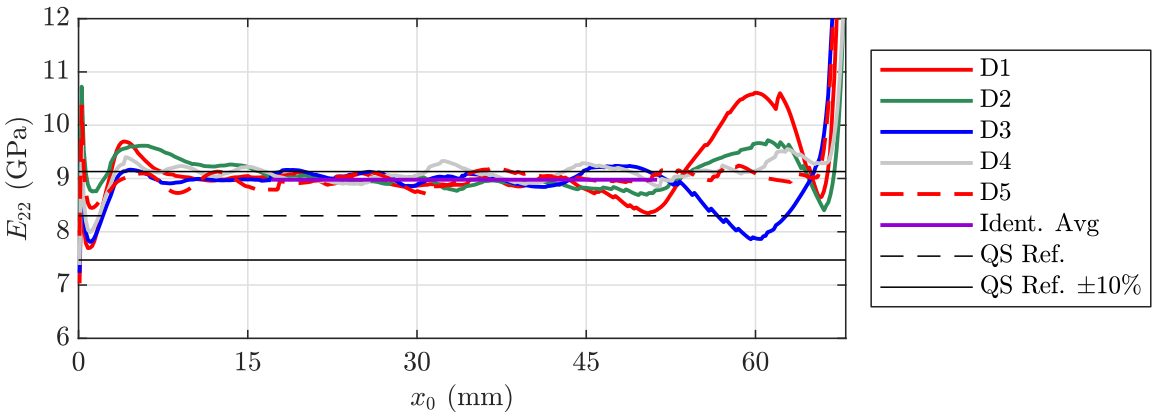

Figure 7.13: Transverse modulus as a function of x_0 distance identified from five IBII tests on UD90° DIC samples. The mean, QS reference and ±10% of the QS reference value are also shown.

Table 7.2: Transverse modulus E_{22} and shear modulus G_{12} identified from five IBII tests on UD90° specimens using DIC displacements, together with the mean, SD, COV, QS and %Diff. QS value. Peak average and effective transverse and shear strain rates are also listed.

Spec. (#)	$\boldsymbol{E_{22}}$ (GPa)	$\boldsymbol{G_{12}}$ (GPa)	**Peak** $\overline{\lvert\dot{\epsilon}_{22}\rvert}^{L}$ ($\times 10^3$ s^{-1})	**Peak** $\overline{\lvert\dot{\gamma}_{12}\rvert}^{L}$ ($\times 10^3$ s^{-1})	$\hat{\dot{\epsilon}}_{22}$ ($\times 10^3$ s^{-1})	$\hat{\dot{\gamma}}_{12}$ ($\times 10^3$ s^{-1})
UD90-D1	8.88	5.22	3.41	1.05	1.38	0.320
UD90-D2	8.90	4.95	3.25	0.671	1.55	0.384
UD90-D3	9.05	5.29	3.07	0.712	1.39	0.324
UD90-D4	9.06	5.25	3.63	0.325	1.64	0.425
UD90-D5	8.99	5.57	3.36	0.810	1.56	0.418
Mean	**8.98**	**5.26**	**3.34**	**0.713**	**1.50**	**0.374**
SD	**0.079**	**0.223**				
COV (%)	**0.885**	**4.24**				
QS Value	**8.30**	**4.73**				
%Diff. QS	**8.15**	**11.1**				

7.3.2 UD90° specimens: shear component

Figure 7.14 shows average shear stress $\overline{\sigma_{12}}^{L}$ against average shear strain $\overline{\gamma_{12}}^{L}$ curves obtained from the IBII test on UD90-D2. These curves reveal low magnitude peak average shear strains of around 1.5−2.0 mm.m^{-1}. With the exception of UD90-D2, peak average shear strains below 1.5 mm.m^{-1} were obtained from all UD90° DIC samples. Therefore, the signal to noise ratio for the UD90° DIC samples was approximately half of the UD90° grid samples, where peak average shear strains around 2.5−4.0 mm.m^{-1} were recorded (see Figure 6.21 of Chapter 6). The low magnitude peak average shear strains resulting from the UD90° DIC samples indicated that the pitch angle misalignments during those tests were minimal. However, the low magnitude average shear strains made it difficult to assess the linearity of the shear response from the UD90° DIC tests. Red markers in Figure 7.14 show the fitted portion of the loading from which shear modulus values were obtained, using linear fits to the absolute maximum stress.

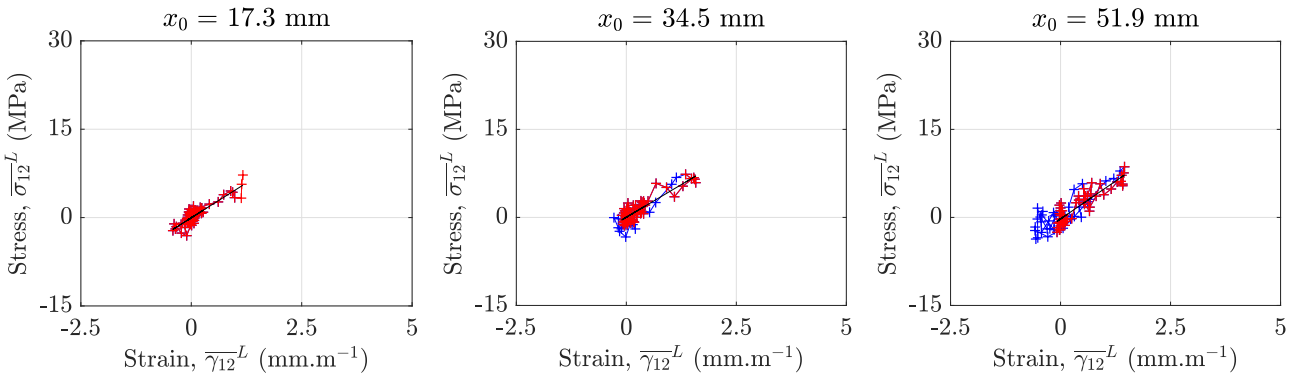

Figure 7.14: Transverse stress-strain curves at various x_0 distances obtained from UD90-D2.

Figure 7.15 shows the G_{12} against x_0 position data from the UD90° DIC tests. This plot shows a greater amount of inter-sample scatter from the DIC tests compared to the grid sample results presented in Figure 6.22 of Chapter 6. Here, the scatter was a result of the low signal to noise ratio induced by the low pitch-angle misalignment present in the tests. This was not ideal for identifying G_{12} values from UD90° samples, where a greater pitch-angle misalignment is required to activate a stronger shear response (increasing the signal to noise ratio). In spite of the low magnitude shear strains, shear moduli were identified from the average of the middle 50% of slices on the sample. From the five tests, the mean identified G_{12} value listed in Table 7.2 was 5.26 GPa (SD = 0.223 GPa), which was close to the UD90° grid sample result of 5.51 GPa (SD = 0.127 GPa). Here, the increased SD from the DIC sample G_{12} values was influenced by the low magnitude shear strains induced by the reduced pitch angle misalignment. The SD was also heavily influenced by the UD90-S2 result, which had the lowest peak average strain from the batch of tests. Using the quasi-static G_{12} modulus value of 4.73 GPa, the %Diff. to QS value was 11.1%. Table 7.2 also lists the mean peak and strain-normalised strain rates of 0.713×10^3 s^{-1} and 0.374×10^3 s^{-1}, respectively. As expected, the shear strain rate metrics were lower than the transverse values for the UD90° configuration.

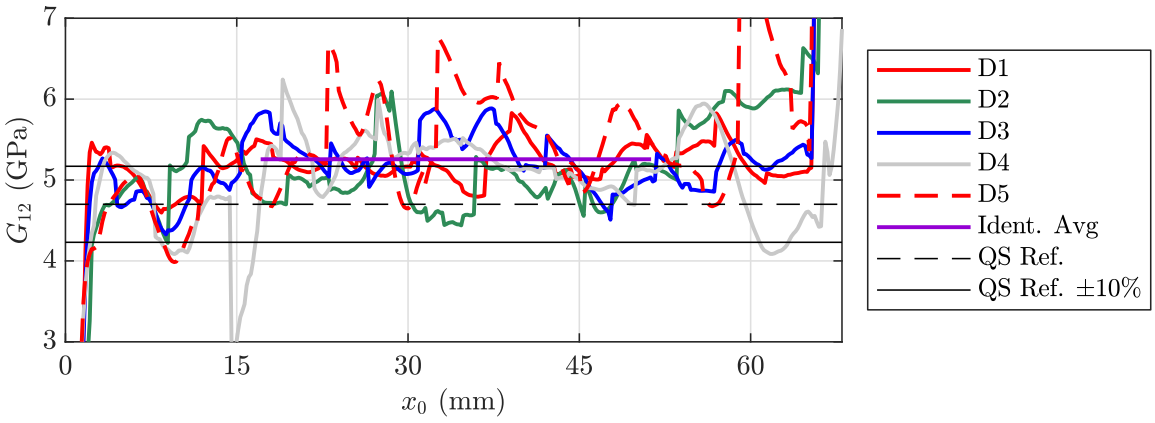

Figure 7.15: G_{12} as a function of x_0 position for the UD90° DIC specimens, the mean identified from five tests, the quasi-static reference value and ±10% of the quasi-static reference value.

7.3.3 UD90° specimens: alignment

Table 7.3 lists the pitch and yaw angles between the projectile and the wave guide for the UD90° DIC samples, which were calculated using the process described in Chapter 4. From the five tests on UD90-D1 to UD90-D5, the mean pitch angle was 0.077° (SD = 0.024°) and the mean yaw angle was 0.149° (SD = 0.111°). These low pitch angle values were likely responsible for the low signal-to-noise ratio in shear stress-strain curves seen in Figure 7.14. When combined with the consistent E_{22} data obtained from the UD90° tests of 8.98 GPa (SD = 0.079 GPa), these results suggest an insignificant

influence on the identified E_{22} modulus over the range of alignment angles obtained in this work. Note that in Table 7.3, the absolute value of the measurements was used to calculate the mean from each batch of samples.

Table 7.3: Angle between the projectile and the wave guide measured from the IBII tests on UD90° DIC samples. Minimum, maximum and the absolute difference between the minimum and maximum pitch and yaw angles are listed, along with the mean and SD of the absolute values.

Specimen (#)	$\boldsymbol{Pitch_{min}}$ (degrees)	$\boldsymbol{Pitch_{max}}$ (degrees)	$\boldsymbol{\lvert\Delta\rvert}$ (degrees)	$\boldsymbol{Yaw_{min}}$ (degrees)	$\boldsymbol{Yaw_{max}}$ (degrees)	$\boldsymbol{\lvert\Delta\rvert}$ (degrees)
UD90-D1	0.077	0.102	0.025	0.272	0.319	0.047
UD90-D2	-0.064	-0.053	0.010	0.154	0.188	0.033
UD90-D3	0.094	0.120	0.026	-0.210	-0.220	0.010
UD90-D4	0.041	0.063	0.021	0.036	0.056	0.020
UD90-D5	0.068	0.092	0.024	-0.025	-0.011	0.014
UD90-D6[1]	-0.197	-0.196	0.001	0.455	0.508	0.053
Mean		**0.077**			**0.149**	
SD		**0.024**			**0.111**	

[1] Not included in mean or SD values

Following the modulus identification tests, one UD90° sample was intentionally impacted with a set amount of yaw misalignment of 0.5°. This test was performed to assess the influence of the yaw angle on the identified modulus value. As explained in Section 4.2.4 of Chapter 4, yaw angle misalignments can induce 3D effects in the sample, leading to a bias in the average stress reconstruction. Table 7.3 gives the pitch and yaw alignment angles of -0.197 to $-0.196°$ and 0.455 to 0.508°, respectively, which were calculated from the test on UD90-D6. Note that the pitch and yaw angles were calculated from the methods explained in Section 4.2.5 of Chapter 4. These impact conditions resulted in a 'positive' zone trailing the compressive ϵ_{22} wave front, which can be seen in Figure 7.16 (a). This artificially-high strain region likely resulted from a 3D bending wave generated from the yaw angle misalignment [115]. For the aligned tests, the region trailing the compressive wave front remained compressive (over the modulus identification duration), as shown in Figure 7.16 (b). In the misaligned case, the 'less-compressive' strains resulted in a different stress-strain response from the slices closer to the impact edge. To demonstrate, Figure 7.16 (c) plots the transverse stress-strain response from all slices on the sample's surface for the misaligned test on UD90-D6. For this analysis, the slice data within half a smoothing kernel size plus one subset size was excluded from both vertical edges. Here, the stress-strain response was less concentrated compared to the aligned test, as shown in Figure 7.16 (d). In addition, the maximum average stress value of around 130 MPa was lower for the misaligned test compared to the aligned test, which recorded values around 150 MPa. Influences on the maximum compressive stress from the projectile impact speed were excluded, as values of 37.9 m.s^{-1} and 38.0 m.s^{-1} were measured for UD90-S5 and UD90-S6, respectively. The yaw alignment induced effects in the stress-strain curves resulted in higher modulus values closer to the impact edge for the misaligned case, as shown in Figure 7.16 (e). However, at $25-20$ mm from the impact edge, the effects dissipated and the modulus value identified over the middle 50% of slices was 8.85 GPa, which was within 1.4% of the mean value obtained from the aligned tests (8.98 GPa). This result demonstrated the robust nature of the test, as reasonable modulus values could be identified with severe yaw misalignment angles.

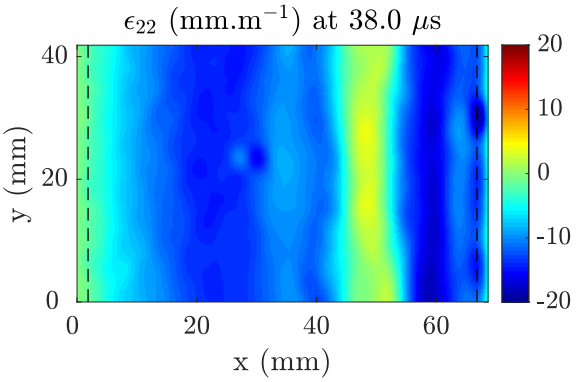

(a) UD90-D6 ϵ_{22} field at 38 μs (misaligned test).

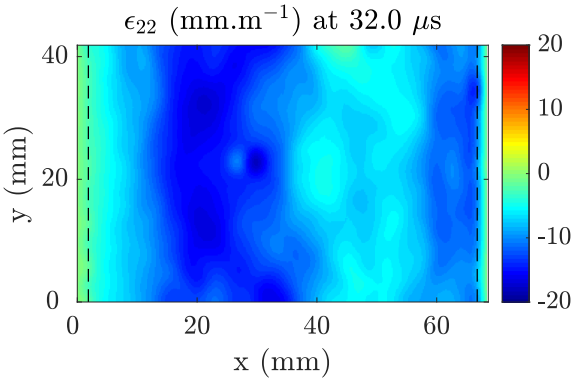

(b) UD90-D5 ϵ_{22} field at 32 μs (aligned test).

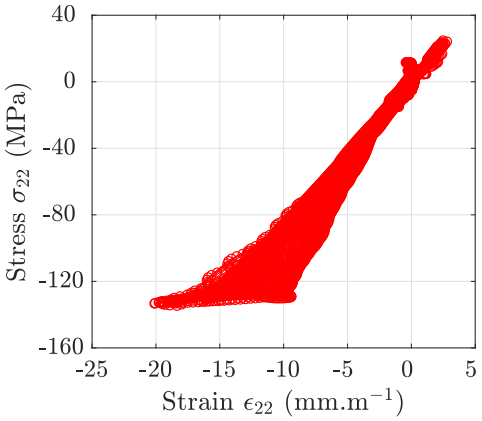

(c) UD90-D6 σ_{22} *vs.* ϵ_{22} curves (misaligned test).

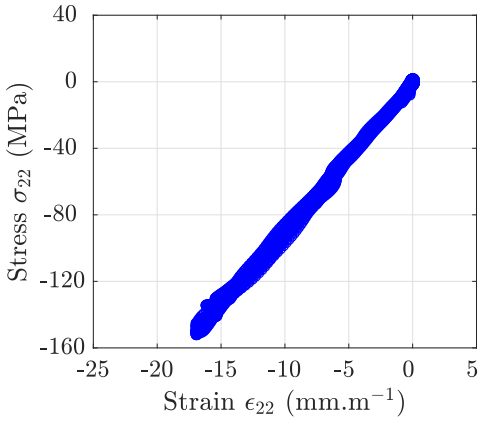

(d) UD90-D5 σ_{22} *vs.* ϵ_{22} curves (aligned test).

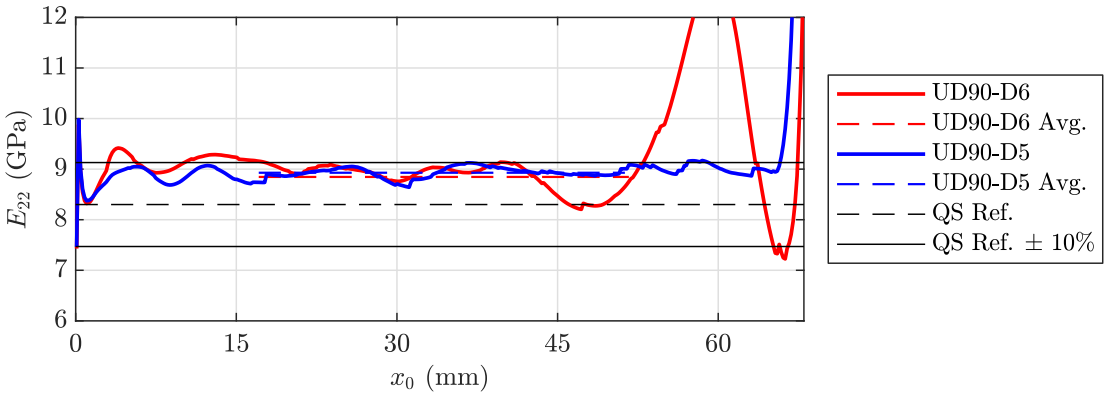

(e) E_{22} against x_0 position from the misaligned and aligned tests.

Figure 7.16: Comparison of the UD90° sample ϵ_{22} strain fields from the (a) misaligned test and (b) aligned test, together with the σ_{22} *vs.* ϵ_{22} curves from the (c) misaligned test and (d) aligned test. Note that the dashed lines on (a) and (b) give the range of slices from which the stress-strain curves in (c) and (d) were plotted. The E_{22} against x_0 position curves from both cases are plotted in (e).

7.3.4 UD45° specimens: transverse component

Average transverse stress-strain curves from selected x_0 positions from UD45-D1 are plotted in Figure 7.17. These curves show a linear response over the compressive loading to a value of around 60 MPa, which was lower than the 150 MPa obtained from the transverse response-dominated UD90° samples. This result was expected because for the UD45° samples, the impact pulse is split between the transverse and shear components of stress. Thereafter, the unloading was also linear until the sample failed later in the test. All of the UD45° DIC samples formed a crack during the test, which was unlike the grid results where only two of the batch of seven samples failed. Note that influences on the maximum compressive stress (and crack formation during a test) from the projectile impact speeds were excluded, as values around 38−40 m.s^{-1} were measured for both the grid and DIC samples. Similar to the UD90° E_{22} identification, linear fits over the compressive loading portion of the transverse stress-strain curves were used to calculate the transverse modulus for each slice.

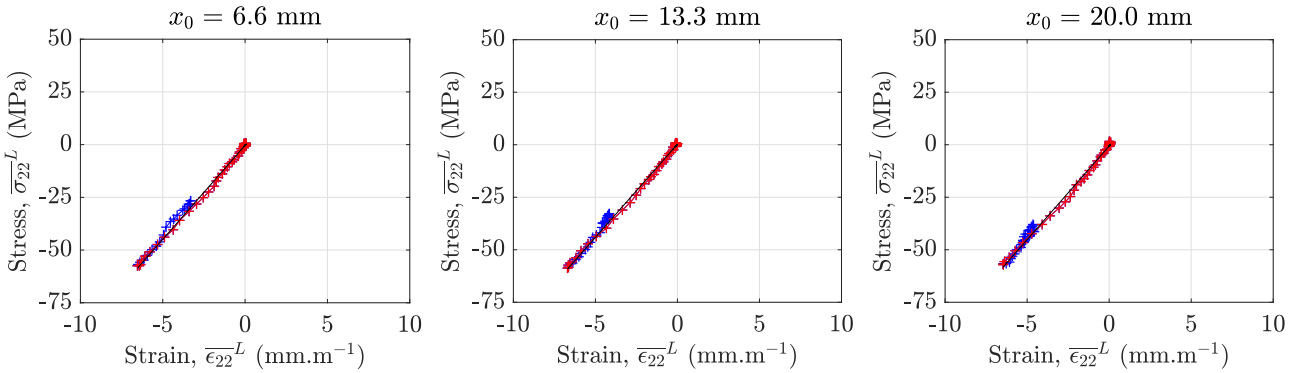

Figure 7.17: UD45-D1 average transverse stress-strain curves at the given x_0 positions. Linear fits to the red data points were used to calculate the transverse compressive modulus.

E_{22} as a function of x_0 position from five IBII tests on UD45° samples is given in Figure 7.18. As explained in Chapter 6, all of the slice data was used to identify the modulus values in the UD45° specimens. Table 7.4 lists the mean E_{22} modulus obtained from five tests on UD45° DIC samples as 9.01 GPa, which was 8.59% higher than the quasi-static reference value of 8.30 GPa. Again, the statistics from the batch of five samples tested indicated good test-to-test consistency, as suggested by the low SD of 0.141 GPa. Table 7.4 also lists the peak average and strain-normalised transverse strain rates of 1.01 $\times 10^3$ s^{-1} and 0.707 $\times 10^3$ s^{-1}, respectively. As expected, the UD45° transverse strain rate values were lower than the UD90° results.

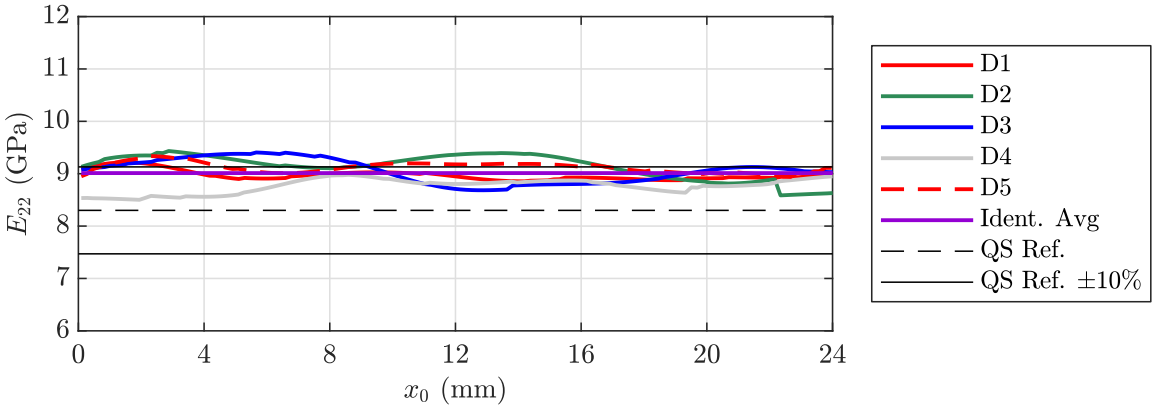

Figure 7.18: E_{22} as a function of x_0 position identified from five IBII tests on UD45° DIC samples. The mean, quasi-static reference and ±10% of the quasi-static reference are also shown.

Table 7.4: Transverse modulus E_{22} and shear modulus G_{12} identified from five UD45° DIC samples, together with the mean, SD, COV, QS value and %Diff. to QS value. Peak average and effective transverse and shear strain rates are also given.

Spec.	$\boldsymbol{E_{22}}$	$\boldsymbol{G_{12,\,Sl.\,1}}$	$\boldsymbol{G_{12,\,Sl.\,2}}$	$\overline{\lvert\dot{\epsilon}_{22}\rvert}^{L}$	$\overline{\lvert\dot{\gamma}_{12}\rvert}^{L}_{Sl.\,1}$	$\overline{\lvert\dot{\gamma}_{12}\rvert}^{L}_{Sl.\,2}$	$\hat{\dot{\epsilon}}_{22}$	$\hat{\dot{\gamma}}_{12}$
(#)	(GPa)	(GPa)	(GPa)	($\times 10^3$ s^{-1})	($\times$ 10^3 s^{-1})	($\times$ 10^3 s^{-1})	($\times$ 10^3 s^{-1})	($\times$ 10^3 s^{-1})
UD45-D1	8.99	5.22	5.11	1.03	1.59	1.22	0.764	1.18
UD45-D2	9.11	5.14	4.96	0.876	1.68	1.19	0.619	1.13
UD45-D3	9.05	5.11	5.01	0.962	1.65	1.90	0.690	1.20
UD45-D4	8.78	5.06	5.01	1.14	1.81	1.98	0.739	1.23
UD45-D5	9.13	5.08	5.11	1.04	1.84	2.15	0.724	1.29
Mean	**9.01**	**5.12**	**5.04**	**1.01**	**1.71**	**1.69**	**0.707**	**1.21**
SD	**0.141**	**0.063**	**0.067**					
COV (%)	**1.56**	**1.22**	**1.33**					
QS Value	**8.30**	**4.73**	**4.73**					
%Diff. QS	**8.59**	**8.29**	**6.55**					

7.3.5 UD45° specimens: shear component

Figure 7.19 (a) gives average shear stress-strain curves obtained from angled slices parallel to the UD45° sample fibres (slices 1) for UD45-D1. These curves show a linear shear response until around 10−15 mm.m^{-1}, which was similar to the results obtained from the UD45° grid samples. At this point, the response turned non-linear to a peak shear stress of around 70 MPa. The unloading behaviour was linear, but slightly less stable than the linear loading response. Some distinct differences were observed in the stress-strain curves obtained from the slices perpendicular to the fibres (slices 2), which are shown in Figure 7.19 (b). Here, the amount of non-linearity proceeding the linear response was reduced and the peak average stresses were lower compared to slices 1. Similar results were obtained from the grid sample average shear stress-strain curves from slices 1 in Figure 6.25 compared to slices 2 in Figure 6.26. These occurrences could be expected given the different strain histories that develop in the orthogonal slices (see Figure 5.10 of Chapter 5). Further to the differences in the loading, the unload response ended earlier for slices 2 than for slices 1, stopping at around 35−40 MPa (compared to 20−25 MPa for slices 1). The reason for the higher unload stresses from slices 2 was that the crack originated close to the top left-hand corner of the sample, covering the slice 2 domain. After the crack formation, the average stresses and strains in this region remained artificially high, which resulted in more compressive average stresses at the end of the unloading. Linear fits to the linear loading portion of the shear stress-strain curves were used to determine the shear modulus for each x_0 position on the samples. Similar to the grid UD45° samples, the progressive chord fitting method determined the linear limit over which shear moduli were derived. Consistent G_{12} *vs.* x_0 position histories were obtained from both slices, as shown in Figure 7.20. This consistency was evidenced by the mean G_{12} values listed in Table 7.4 for slices 1 and 2, which were 5.12 GPa (SD = 0.063 GPa) and 5.04 GPa (SD = 0.067 GPa), respectively. Again, using the quasi-static shear modulus of 4.73 GPa, shear strain-rate sensitivities of 8.29% and 6.55% were obtained for slices 1 and 2, respectively. Table 7.4 also lists the strain-normalised strain rate of 1.21×10^3 s^{-1}, which was expectedly lower than the peak average shear strain rates. Here, the UD45° DIC sample peak average shear strain rates were 1.71×10^3 s^{-1} for slices 1 and 1.69×10^3 s^{-1} for slices 2.

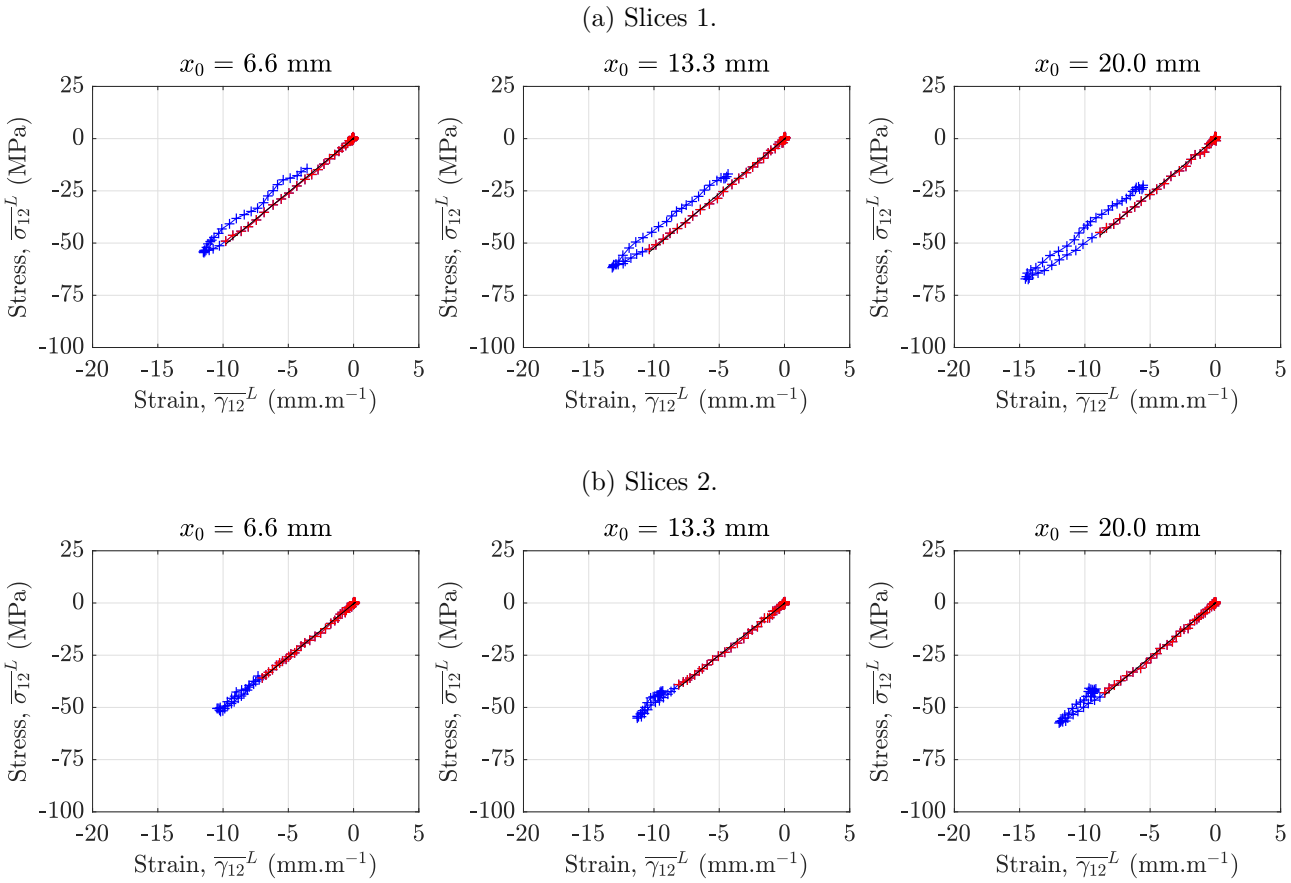

Figure 7.19: UD45-D1 average shear stress-strain curves at the given x_0 positions from (a) slices 1 and (b) slices 2. Red markers indicate the data used for the shear modulus identification.

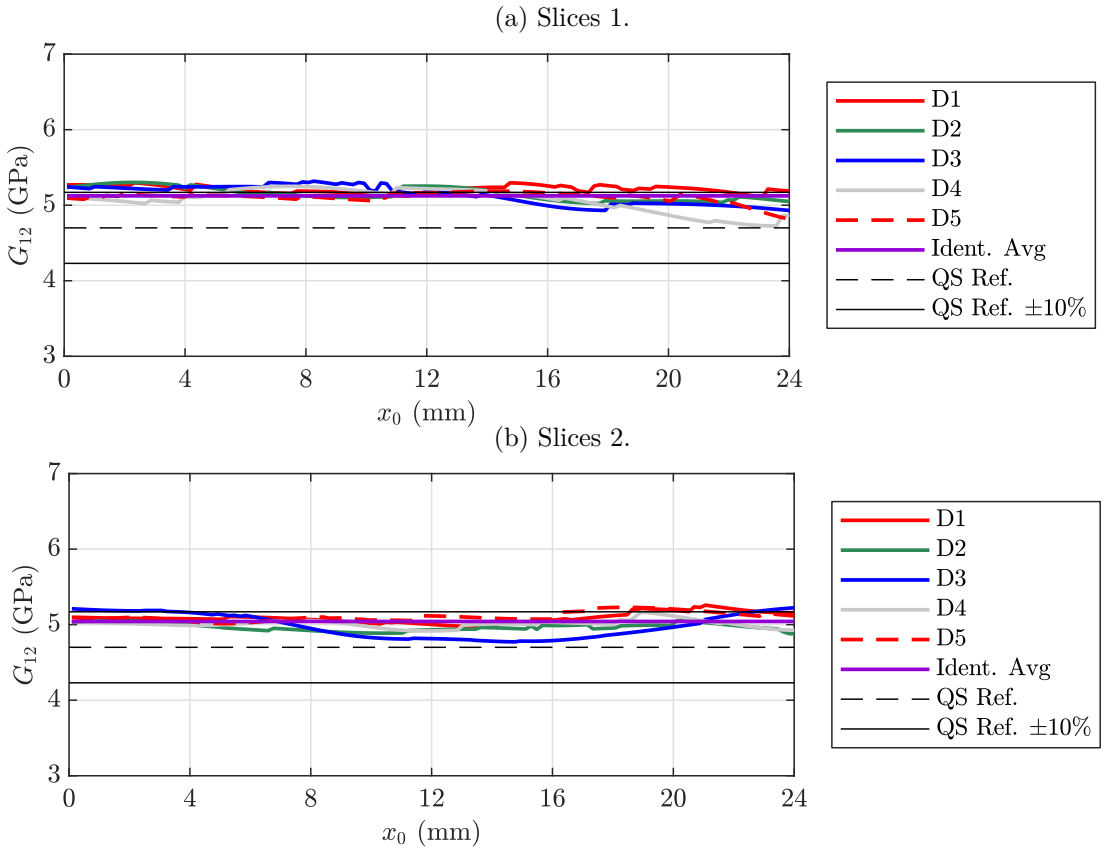

Figure 7.20: G_{12} *vs.* x_0 position for (a) slices 1 and (b) slices 2 obtained from five UD45° DIC tests.

7.3.6 UD45° specimens: alignment

Pitch and yaw angles between the projectile and the wave guide were also calculated for the UD45° DIC sample tests. Table 7.5 lists the results, where the mean pitch angle was 0.220° (SD = 0.010°) and the mean yaw angle was 0.128° (SD = 0.098°). Although the UD45° sample mean pitch angle was greater than the UD90° value, the consistent modulus results in Table 7.4 indicate that there was insignificant influence on the identified E_{22} and G_{12} moduli under the alignment conditions in Table 7.5.

Similar to the UD90° evaluation, one UD45° test was also conducted with intentional yaw-misalignment. However, for this test the rotary stage was set to an offset angle of 1°, which was double the angle set for the UD90° misaligned test of 0.5°. This yaw angle misalignment was detectable 'by eye' and normally would have been removed during the pre-test alignment procedure. However, the test was conducted to evaluate the effects on the identified material properties under severe yaw misalignment conditions, which could occur if the stage was unknowingly knocked during a test campaign. Table 7.3 lists the pitch and yaw angles calculated from the test on UD45-D6, which were -0.046 to -0.033° and 1.124 to 1.249°, respectively. Figure 7.21 (a) shows the ϵ_{22} field obtained from the misaligned test, which revealed lower peak strains compared to the aligned test field showed in Figure 7.21 (b). These lower strains resulted in a steeper stress-strain response compared to the aligned test, clearly seen when comparing the results in Figures 7.21 (c) and 7.21 (d). Lower peak average transverse stresses of around 43 MPa were also obtained from the misaligned test compared to the aligned test, where values around 60 MPa were recorded. The effects seen in the kinematic fields and stress-strain curves translated to increased E_{22} values over a significant portion of the x_0 positions on the sample, as shown in Figure 7.21 (e). As all slices were used to identify the modulus, the misaligned test E_{22} value of 10.0 GPa was 10% higher than the mean value obtained from the aligned UD45° tests of 9.01 GPa. However, it is recalled that this test was not used to identify material properties.

Table 7.5: Angle between the projectile and the wave guide measured from the IBII tests on UD45° DIC samples. Minimum, maximum and the absolute difference between the minimum and maximum pitch and yaw angles are listed, along with the mean and SD of the absolute values.

Specimen (#)	$\boldsymbol{Pitch_{min}}$ (degrees)	$\boldsymbol{Pitch_{max}}$ (degrees)	$\boldsymbol{\lvert\Delta\rvert}$ (degrees)	$\boldsymbol{Yaw_{min}}$ (degrees)	$\boldsymbol{Yaw_{max}}$ (degrees)	$\boldsymbol{\lvert\Delta\rvert}$ (degrees)
UD45-D1	-0.129	-0.125	0.004	0.004	0.021	0.017
UD45-D2	-0.362	-0.384	0.022	0.040	0.061	0.021
UD45-D3	0.161	0.198	0.036	-0.271	-0.280	0.009
UD45-D4	0.254	0.300	0.046	0.121	0.151	0.030
UD45-D5	0.127	0.158	0.032	0.150	0.183	0.033
UD45-D6[1]	-0.046	-0.033	0.012	1.124	1.249	0.126
Mean		**0.220**			**0.128**	
SD		**0.010**			**0.098**	

[1] Not included in mean or SD values

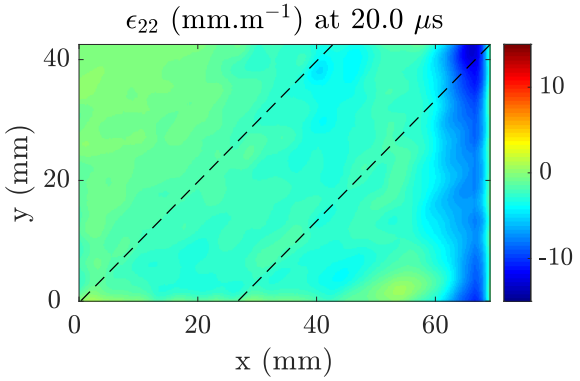

(a) UD45-D6 ϵ_{22} field at 20 μs (misaligned test).

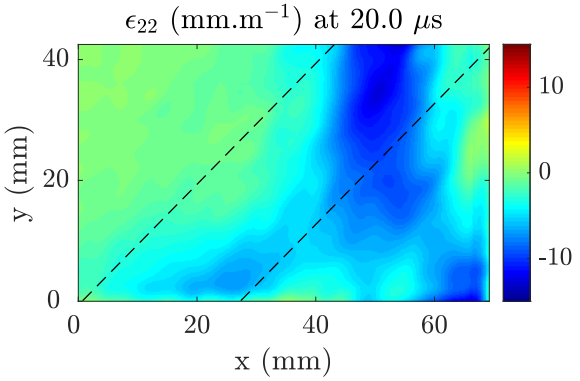

(b) UD45-D5 ϵ_{22} field at 20 μs (aligned test).

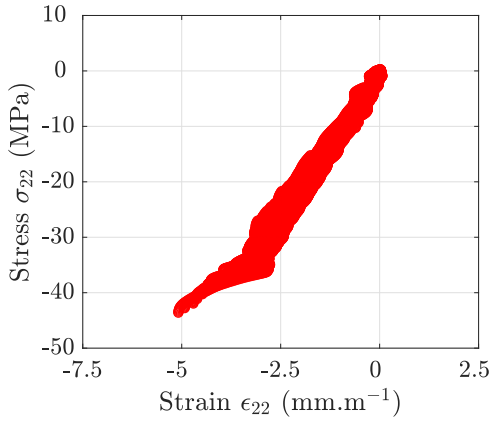

(c) UD45-D6 σ_{22} *vs.* ϵ_{22} curves (misaligned test).

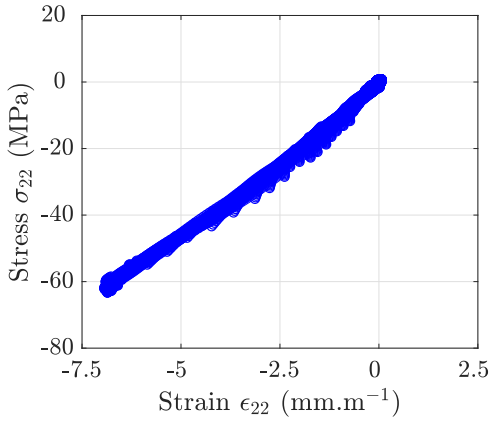

(d) UD45-D5 σ_{22} *vs.* ϵ_{22} curves (aligned test).

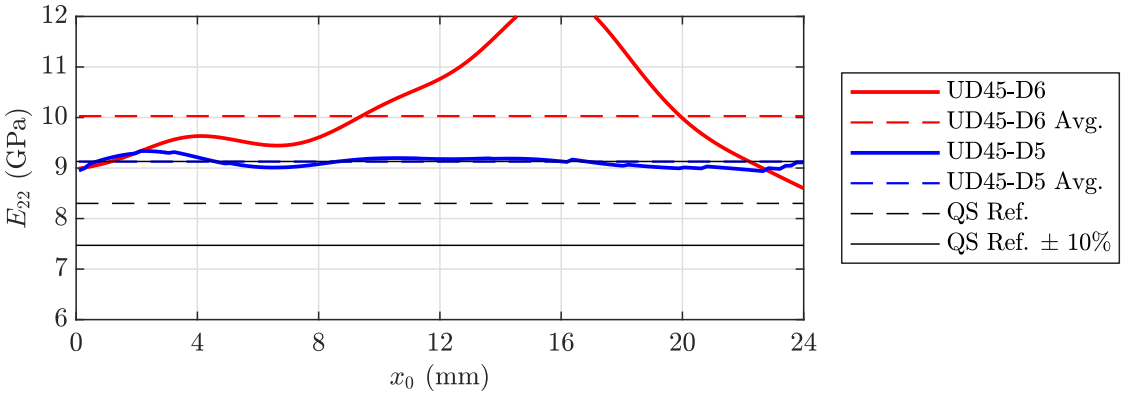

(e) E_{22} against x_0 position from the misaligned and aligned tests.

Figure 7.21: Comparison of the UD45° sample ϵ_{22} strain fields from the (a) misaligned test and (b) aligned test, together with the σ_{22} *vs.* ϵ_{22} curves from the (c) misaligned test and (d) aligned test. Note that the dashed lines on (a) and (b) give the range of slices from which the stress-strain curves in (c) and (d) were plotted. The E_{22} against x_0 position curves from both cases are plotted in (e).

7.3.7 MD45° specimens: shear component

Shear stress-strain curves obtained from MD45-D1 are shown Figures 7.22. Similar to the UD45° samples, the MD45° sample shear response was linear to around 10−15 mm.m^{-1}, over the loading portion of the test. Peak average shear stresses from both slices were around 60−75 MPa, with higher values closer to the impact edge. Unlike the UD90° and UD45° samples, the shear unloading extended past the zero stress condition because the MD45° samples did not form macro-cracks during the test.

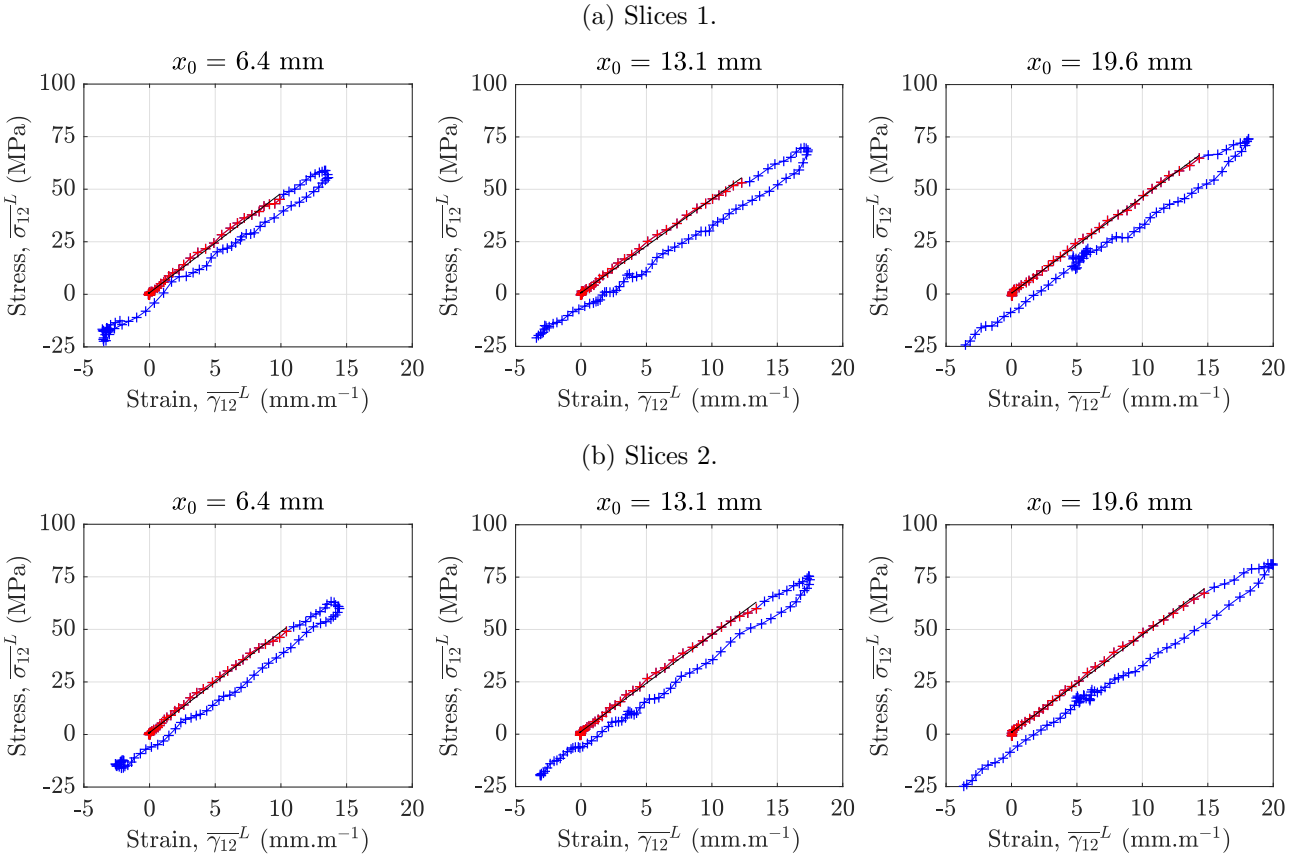

Figure 7.22: MD45-D1 average shear stress-strain curves at the given x_0 positions from (a) slices 1 and (b) slices 2. Red markers indicate the data used for the shear modulus identification.

Shear modulus values were obtained from the angled slices using the same methods applied to the UD45° case. Figure 7.23 shows the G_{12} *vs.* x_0 position plots for both slices, where mean shear moduli of 4.76 GPa (SD = 0.110 GPa) and 4.78 GPa (SD = 0.087 GPa) were identified for slices 1 and 2, respectively. These values were lower than the UD90° and UD45° results of 5.26 GPa and 5.08 GPa (average of slice 1 and 2 values), respectively. The lower G_{12} obtained from the MD45° samples was unexpected for a few reasons. Firstly, the MD45° sample density of 1530 ± 41 kg.m^{-3} was higher than the UD sample density of 1514 ± 17 kg.m^{-3}. This higher density would normally result in an increased modulus for the MD45° sample. Secondly, no effects were expected from differences in the sample tolerances or the impact conditions, as these aspects were similar for both MD45° and UD45° DIC samples. In addition, the shear strain and acceleration field magnitudes obtained from both samples were on a similar order of magnitude. However, as discussed in Chapter 8, the reduced shear modulus may have been influenced by the smoothing parameter selection in the MD45° case. Table 7.6 also lists the MD45° sample G_{12} strain rate sensitivities of 0.581% and 1.11% for slices 1 and 2, respectively. These results indicate negligible strain-rate sensitivity for the MD45° shear modulus, which was contrary to the UD sample data. Lastly, the peak average shear strain rates were 1.85×10^3 s^{-1} for slices 1 and 1.80×10^3 s^{-1} for slices 2, and the strain-normalised strain rate was 1.35×10^3 s^{-1}. Therefore, the strain rate data from the MD45° samples was similar to the UD45° results listed in Table 7.4.

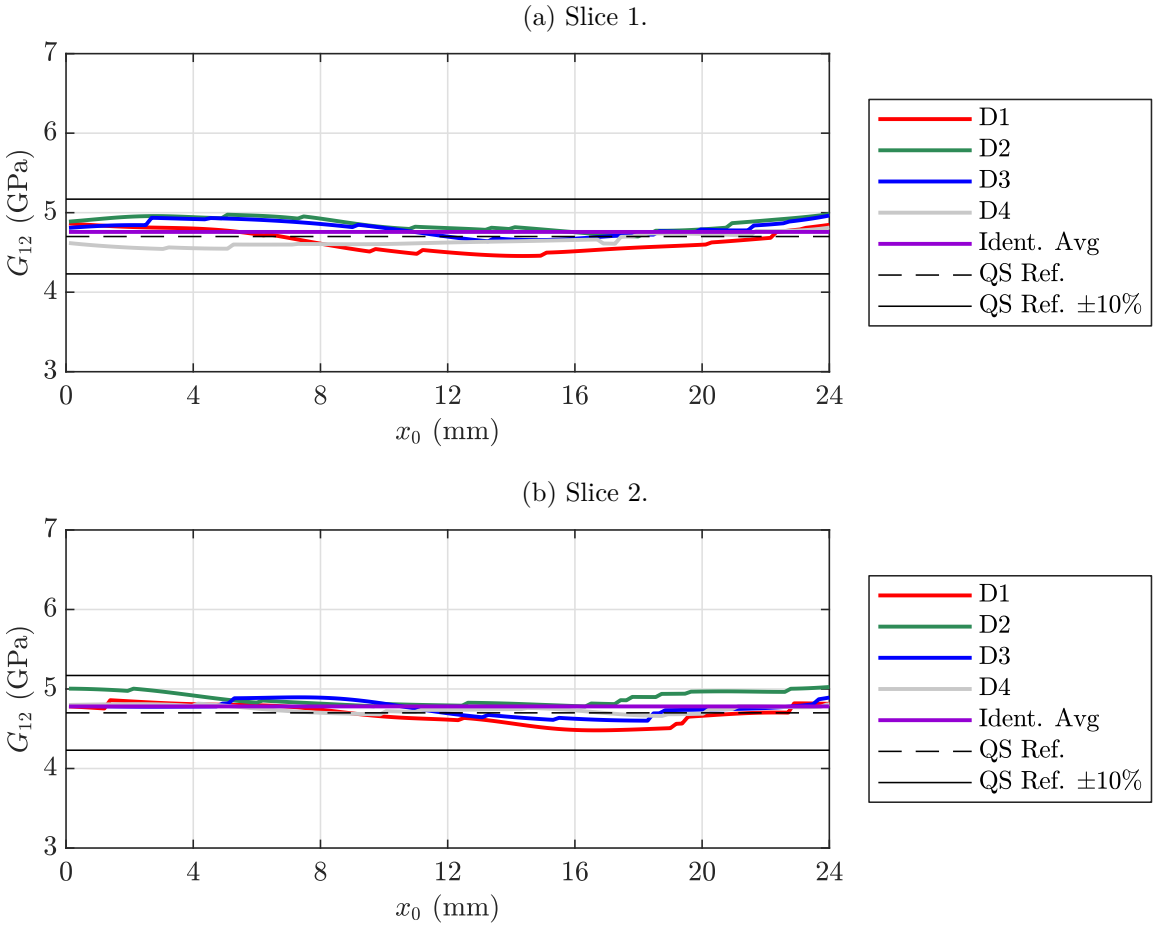

Figure 7.23: G_{12} against x_0 position for (a) slices 1 and (b) slices 2 obtained from four MD±45° DIC tests, along with the mean, quasi-static and ±10% of the quasi-static reference value.

Table 7.6: Shear modulus G_{12} identified from four MD45° DIC specimens, together with the mean, SD, COV, QS value and %Diff. to QS value. Peak average and strain-normalised shear strain rates are also listed.

Specimen (#)	$\boldsymbol{G_{12,\,Sl.\,1}}$ (GPa)	$\boldsymbol{G_{12,\,Sl.\,2}}$ (GPa)	**Peak** $\overline{\lvert\dot{\gamma}_{12}\rvert}^{L}_{Sl.\,1}$ ($\times 10^3$ s^{-1})	**Peak** $\overline{\lvert\dot{\gamma}_{12}\rvert}^{L}_{Sl.\,2}$ ($\times 10^3$ s^{-1})	$\hat{\dot{\gamma}}_{12}$ ($\times 10^3$ s^{-1})
MD45-D1	4.67	4.69	1.66	1.82	1.33
MD45-D2	4.88	4.90	1.90	1.65	1.30
MD45-D3	4.82	4.78	1.94	1.77	1.36
MD45-D4	4.66	4.76	1.88	1.95	1.41
Mean	**4.76**	**4.78**	**1.85**	**1.80**	**1.35**
SD	**0.110**	**0.087**			
COV (%)	**2.30**	**1.83**			
QS Value	**4.73**	**4.73**			
%Diff. QS	**0.581**	**1.11**			

7.3.8 MD45° specimens: alignment

Pitch and yaw angles between the projectile and the wave guide calculated from the four MD45° DIC sample tests are listed in Table 7.7. Here, the mean pitch angle was 0.076° (SD = 0.041°) and the mean yaw angle was 0.179° (SD = 0.111°). Similar to the UD90° and UD45° samples, the consistent shear modulus data obtained from these tests indicated minimal alignment induced effects from the MD45° tests, for the impact angles listed in Table 7.7. Note that no intentionally misaligned tests were conducted using MD45° samples.

Table 7.7: Angle between the projectile and the wave guide measured from the IBII tests on MD45° DIC samples. Minimum, maximum and the absolute difference between the minimum and maximum pitch and yaw angles are listed, along with the mean and SD of the absolute values.

Specimen (#)	$\boldsymbol{Pitch_{min}}$ (degrees)	$\boldsymbol{Pitch_{max}}$ (degrees)	$\boldsymbol{\lvert\Delta\rvert}$ (degrees)	$\boldsymbol{Yaw_{min}}$ (degrees)	$\boldsymbol{Yaw_{max}}$ (degrees)	$\boldsymbol{\lvert\Delta\rvert}$ (degrees)
MD45-D1	0.110	0.119	0.009	0.256	0.277	0.021
MD45-D2	0.096	0.122	0.025	-0.238	-0.243	0.005
MD45-D3	0.082	0.106	0.024	-0.255	-0.264	0.008
MD45-D4	-0.033	-0.019	0.014	-0.042	-0.030	0.013
Mean		**0.076**			**0.179**	
SD		**0.041**			**0.111**	

7.4 Failure stress identification: UD90° samples

Transverse failure stress values were also identified from the UD90° DIC samples. Diagnostic figures from the test on UD90-S2 are shown in Figure 7.24. Figure 7.24 (a) shows the stress field calculated from the transverse strains and the constitutive law $\sigma_{xx}(\epsilon)$ at the time of fracture. During the test, multiple cracks originated in a region of high tensile stress, which formed as the compressive loading pulse reflected off the sample's free edge. This resulted in a curved tensile stress distribution over the sample height, which can be seen in Figure 7.24 (a). As shown in Figure 7.24 (b), this feature was not well represented by the LSG equation due to its linear approximation of the stress field (over the sample height). Although the LSG equation was not sufficient to represent the experimentally obtained (smoothed) stress maps, the peak average stresses in the virtual gauge area ($\overline{\sigma_{xx}}^{A}(LSG)$ and $\overline{\sigma_{xx}}^{A}(\epsilon)$) were similar in magnitude. Figure 7.24 (c) plots the two stresses over the virtual gauge area, where good agreement can be seen until the fracture time of 45.5 μs. At this time, $\overline{\sigma_{xx}}^{A}(LSG)$ diverged from $\overline{\sigma_{xx}}^{A}(\epsilon)$, which indicated that the sample had fractured with a (LSG) failure stress of 66 MPa. $\overline{\sigma_{xx}}^{A}(LSG)$ is plotted against the x-axis strain averaged over the virtual gauge area $\overline{\epsilon_{xx}}^{A}$ in Figure 7.24 (d), where a tensile failure strain around 8.5 mm.m^{-1} resulted.

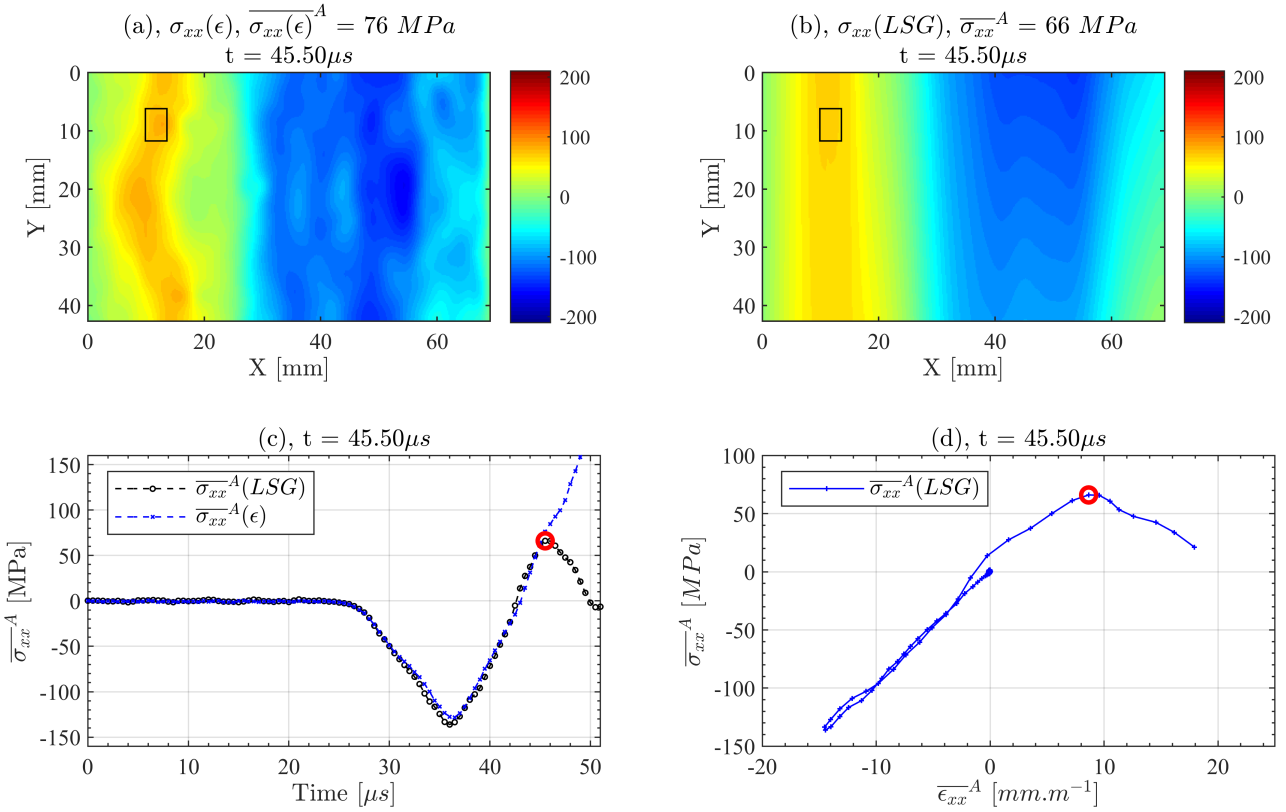

Figure 7.24: UD90-D1 failure stress identification: Stress field calculated from (a) a constitutive law and the strain fields $\sigma_{xx}(\epsilon)$, together with (b) the acceleration fields using the linear stress gauge equation $\sigma_{xx}(LSG)$. Virtual gauge area averages (c) $\overline{\sigma_{xx}}^{A}(\epsilon)$ and $\overline{\sigma_{xx}}^{A}(LSG)$ against time and (d) $\overline{\sigma_{xx}}^{A}(LSG)$ against the average strain over the virtual gauge area $\overline{\epsilon_{xx}}^{A}$.

Table 7.8 gives the mean tensile failure stress obtained from five IBII tests on UD90° DIC samples of 66 MPa (SD = 2.9 MPa), indicating good inter-sample consistency. Using the quasi-static failure stress value of 75.4 MPa reported in [140], the difference in the transverse tensile failure stress was -13%. This result was unexpected because composite failure stresses are generally thought to increase with increasing strain rate [103]. However, these samples were cut from a laminate that contained voids, which would have reduced the identified failure stress (this is further discussed in Chapter 8).

The failure stress resulting from the IBII test that had a set amount of yaw misalignment (UD90-D6) was 69 MPa. This result was only 4.5% lower than the mean of 66 MPa, and unexpected given the modest 0.5° yaw misalignment. However, the failure location was close to the free-edge, where the 3D effects induced from the misalignment should be reduced compared to the impact-edge. Results from [115] showed a more significant error of around 30% on the identified failure stress compared to the test on UD90-D6. However, in [115] the sample length and length to thickness ratios were reduced compared to the samples tested here, so the 3D effects may still have been strong when (and where) the samples failed. Although only one sample was tested here, this result suggested that for long, thin samples, 3D effects induced from misalignment could be mitigated if the failure occurs close to the free-edge. However, further testing is required for confirmation of these effects and should include testing at higher framing rates to reduce any temporal bias. Table 7.8 also gives the mean minimum compressive and maximum tensile strain rates over the virtual gauge area prior to fracture, which were on the order of 1.88×10^3 s^{-1} to 2.38×10^3 s^{-1}.

Table 7.8: Transverse failure stress averaged over the virtual gauge area $\overline{\sigma_{xx}}^A$ obtained from five IBII tests on UD90° DIC samples, together with the mean, SD, COV, QS value from [140] and the % Diff. to QS value. The minimum compressive $\overline{\dot{\epsilon}_{xx}}^A$ (pre-failure) and maximum tensile $\overline{\dot{\epsilon}_{xx}}^A$ (at failure) strain rates are listed for each specimen. The test with 0.5° of yaw misalignment (UD90-D6) is also listed in the table, but not included in the statistics.

Specimen (#)	$\overline{\boldsymbol{\sigma_{xx}}}^{\boldsymbol{A}}$ (LSG) (MPa)	**Min** $\overline{\boldsymbol{\dot{\epsilon}_{xx}}}^{\boldsymbol{A}}$ ($\times10^3$ s^{-1})	**Max** $\overline{\boldsymbol{\dot{\epsilon}_{xx}}}^{\boldsymbol{A}}$ ($\times10^3$ s^{-1})
UD90-D1	71	1.94	2.38
UD90-D2	66	1.88	2.28
UD90-D3	65	1.94	1.94
UD90-D4	64	2.12	2.06
UD90-D5	64	2.01	1.95
UD90-D6[1]	69	1.40	0.825
Mean	**66**		
SD	**2.9**		
COV (%)	**4.4**		
QS Value	**75.4**		
% Diff. to QS	**-13**		

[1] Not included in mean or SD values

Chapter 8

Discussion

This chapter provides a discussion on the experimental results presented in Chapters 6 and 7. Results from the Grid Method IBII tests are presented first, where the modulus identification methods are validated by comparing the moduli obtained from each sample configuration. Differences in the high strain rate material properties identified from Grid Method and DIC displacements are then evaluated, where influences from the spatial resolution, laminate configuration and integrity of the laminates are considered. All of the material data is then compared to values in the literature and reasons for the excessive scatter seen in the previously published data are given.

8.1 Validation of the modulus identification methods

The purpose of this section is to validate the IBII test methods used to identify the high-strain rate moduli from the Grid Method samples. This task was complicated by the fact that there are currently no reasonable datasets for comparison, as most data found in-literature was obtained with the split-Hopkinson bar. Here, it is recalled that identifying composite material properties with the split-Hopkinson bar can be easily corrupted by inertial effects, when the evaluated strain rates are above a few hundred inverse seconds. Therefore, the validation process was completed by comparing the identified moduli obtained from different laminate configurations. This provides a reasonable comparison for the identification methods because each of the sample configurations had unique features that could potentially affect the results. For example, the UD90° and UD45° samples were expected to have better matrix consolidation compared to the MD45° samples, due to the ±45° layup. Additionally, the UD90° samples had a much lower y-axis strain resolution compared to the UD45° samples, and a different surface area over which the acceleration averages are obtained in the stress gauge equations. In [127], the transverse stress gauge approach used to obtain the transverse modulus from UD45° CFRP specimens was validated. However, that evaluation was performed on a single sample, so this study extends the assessment to include a larger sample size. Note that the transverse stress gauge methodology used to identify UD90° E_{22} values had already been experimentally validated in [29].

8.1.1 Transverse modulus from UD45° samples

Figure 8.1 plots the mean E_{22} value of 10.2 GPa (SD = 0.154 GPa) obtained from the batch of six UD90° grid samples. As previously stated in Chapter 6, the statistical data from this batch of samples indicated excellent shot-to-shot consistency. Although, this could be expected given the strong transverse response from the UD90° configuration. Also plotted in Figure 8.1 is the mean E_{22} value of 9.98 GPa (SD = 0.345 GPa) obtained from the batch of seven UD45° grid samples. Comparing the results variance from the two sample batches, the increased SD from the UD45° samples may have resulted from the slightly lower signal to noise ratio in the transverse strains. However, the UD45° E_{22} value was within one SD of the UD90° result, when the SD of the UD45° samples is considered. Given the consistent results between the two sample laminate configurations, the transverse stress gauge method used to obtain the transverse modulus from UD45° samples was considered validated.

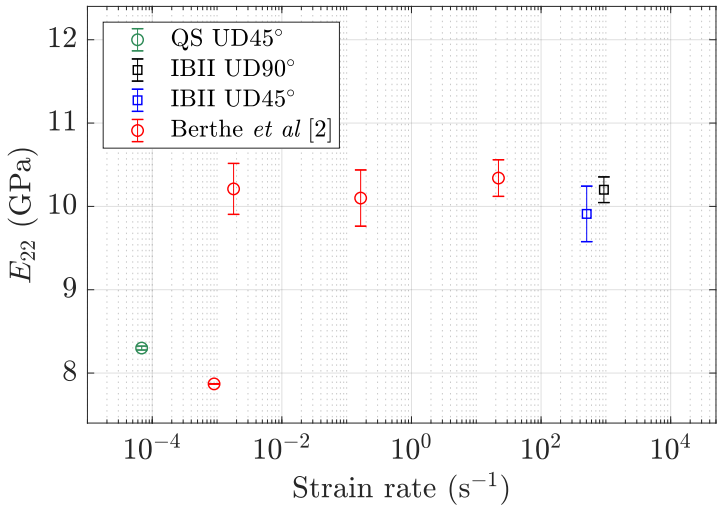

Figure 8.1: Comparison of the transverse modulus E_{22} results from this study with data from [20].

8.1.2 Shear modulus from UD90° samples

In-plane shear moduli of composites are often identified with off-axis configurations (*e.g* UD45° or MD45°), as the angled fibres can induce a strong shear response in the sample. However, in this work G_{12} values were also identified from UD90° specimens. As explained in Chapter 6, the shear modulus identification from the transverse samples was unintended, and resulted from a slight pitch-angle misalignment between the projectile and the wave guide. However, this discovery unexpectedly added to the versatile nature of the IBII test because 1) it proved that shear moduli could be identified from more basic sample configurations and 2) it provided another data point to evaluate the UD45° and MD45° sample shear modulus identification methods. Averaging the slice 1 and 2 values, the mean G_{12} obtained from the UD45° samples was 5.36 GPa (SD = 0.148 GPa), which is plotted against the UD90° result of 5.51 GPa (SD = 0.127 GPa) in Figure 8.2. Both of these datasets indicate excellent consistency between tests, particularly for the UD90° case because of the low signal to noise ratio of the y-axis strains. As the UD90° G_{12} was within one SD of the UD45° result, the method of obtaining the shear modulus from UD90° samples was experimentally validated.

8.1.3 Shear modulus from MD45° samples

The mean MD45° G_{12} values identified from slices 1 and 2 were 5.05 GPa (SD = 0.305 GPa) and 5.12 GPa (SD = 0.275 GPa), respectively. Figure 8.2 plots the average of the two slices, giving a mean MD45° sample shear modulus of 5.09 GPa (SD = 0.290 GPa). In comparison to the UD sample results, the MD45° G_{12} value was 5.0% and 7.6% lower than the UD45° and UD90° sample results, respectively. It was suspected that the reduced MD45° modulus may have resulted from a lower fibre volume fraction of the MD laminate. When the laminates are manufactured, the alternating -45° and +45° laminae can lead to regions of trapped resin at the ply interfaces as the matrix consolidates. This hypothesis was supported by the MD laminate's reduced density value of 1530 kg.m^{-3}, which was 2.9% lower than the UD laminate density of 1575 kg.m^{-3}. Therefore, the lower MD45° shear modulus is consistent with the lower fibre volume fraction resulting from its layup configuration.

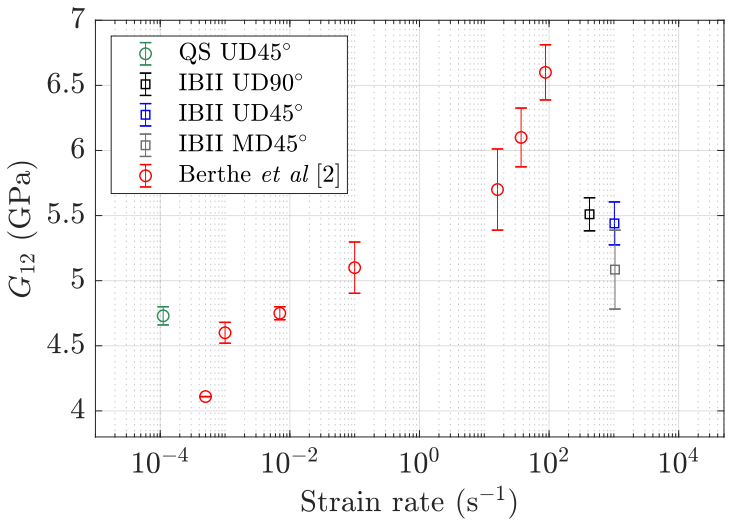

Figure 8.2: Comparison of the shear modulus G_{12} results from this study with data from [20].

8.2 Comparison of the DIC and Grid Method results

8.2.1 Transverse modulus from UD90° samples

The mean transverse modulus obtained from the UD90° DIC samples was 8.98 GPa (SD = 0.079 GPa), which was 12.0% lower than the grid specimen results of 10.2 GPa (SD = 0.154 GPa). Here, a difference in the results could have been expected because of the lower spatial resolution resulting from the 13-pixel subsets chosen to process the DIC images. However, this amount of disparity was thought to be excessive, as the errors in the identified Q_{22} values obtained from the image deformation study were under 1% for both image types. Given that optimised smoothing parameters were selected to process the experimental images, it was unlikely that the lower DIC E_{22} value was entirely due to a lower spatial resolution. Some variation was expected from the different densities of the plates that the samples were cut from, with the UD90° DIC samples having a density of 1514 ± 20 kg.m^{-3}, which was 3.9% lower than the UD90° grid sample density of 1575 ± 20 kg.m^{-3}.

Differences in the calculated sample densities were unexpected, as both plates had the same material specification and were manufactured at the same facility. Therefore, optical inspection techniques were used to investigate the cause of the reduced density. Micrographic images of the IBII test sample laminates are given in Figure 8.3. These images provide a view that is parallel to the sample fibres from the in-plane perspective. All images were obtained using an Olympus BX41M−LED microscope and the samples were cold-mounted using Struers Epofix epoxy resin. Micrographs of the UD0° (Plate 1) laminate that the UD90° and UD45° Grid Method samples were cut from are shown in Figures 8.3 (a) and 8.3 (b). In these images, the absence of voids indicate that this laminate had good bonds between the fibres and the matrix. However, the microscope images of the plate that the UD90° and UD45° DIC samples were manufactured from were quite different. Figures 8.3 (c) and 8.3 (d) show micrographs of the UD0° (Plate 2) laminate, where multiple inter and intra-laminar voids can be seen. This finding indicated that poor consolidation of the matrix had occurred during the laminate curing. Computed Tomography (CT) scans conducted at the University of Southampton's μ-vis imaging centre confirmed that voids on the order of 2−5 μm in length were present in the UD0° (Plate 2) laminate. The detection of voids from the micrographs of Plate 2 was consistent with its lower calculated density, and also explained why lower E_{22} values were obtained from the UD90° DIC samples. This also meant that it was difficult to undertake a fair comparison between the Grid Method and DIC derived E_{22} values, as the manufactured quality of both samples was not the same. Here it is recalled that the QS data was obtained from the plate containing voids (Plate 2).

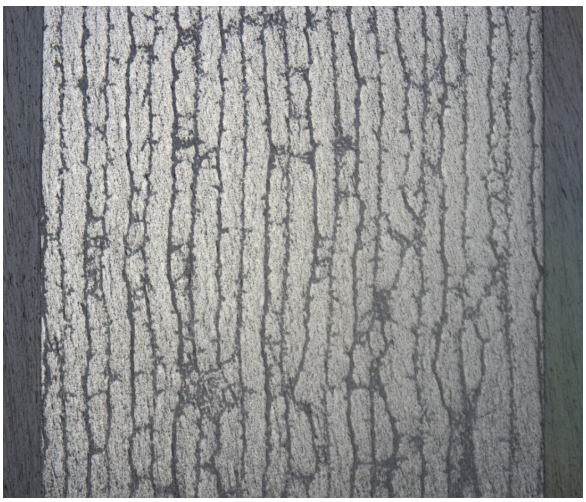

(a) UD0° Plate 1 at 5× resolution.

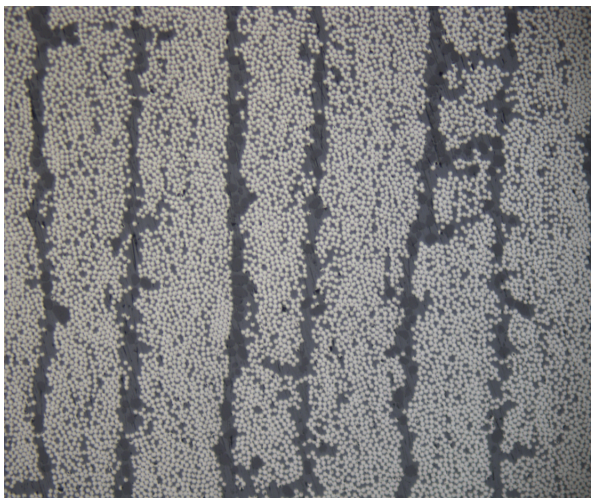

(b) UD0° Plate 1 at 20× resolution.

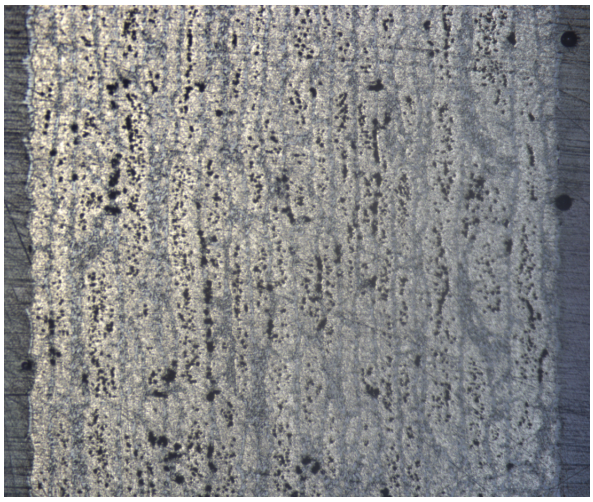

(c) UD0° Plate 2 at 5× resolution.

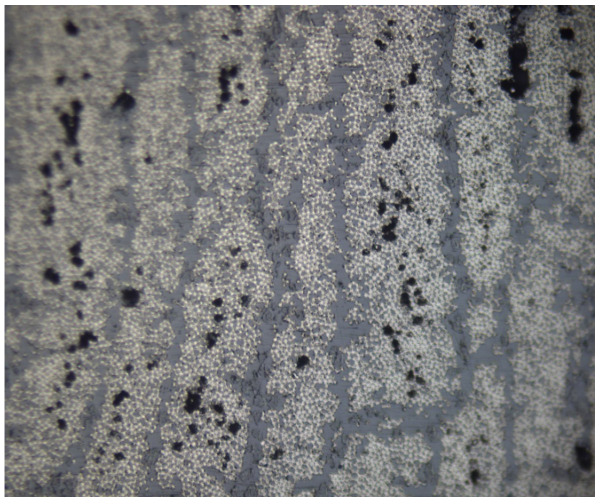

(d) UD0° Plate 2 at 20× resolution.

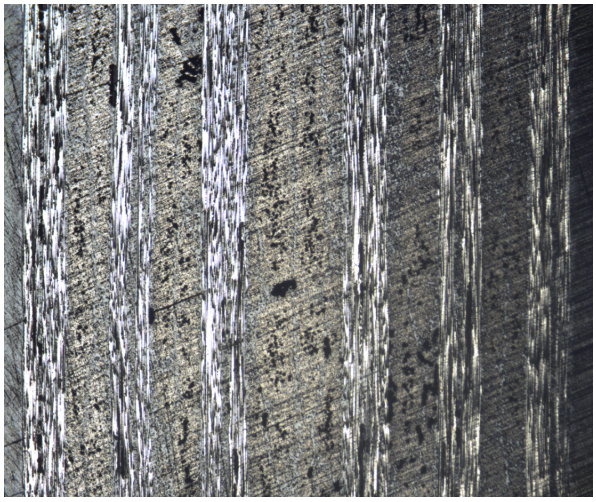

(e) UD0°/90° Plate 1 at 5× resolution.

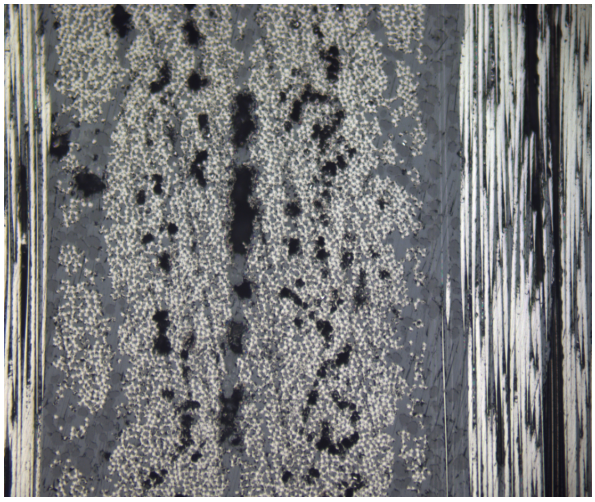

(f) UD0°/90° Plate 1 at 20× resolution.

Figure 8.3: Through-thickness micrographs of UD0° Plate 1 in (a) and (b), UD0° Plate 2 in (c) and (d) and UD0°/90° Plate 1 in (e) and (f).

8.2.2 Transverse modulus from UD45° samples

The mean transverse modulus identified from five UD45° DIC tests was 9.01 GPa (SD = 0.141 GPa), which was 9.7% lower than mean of 9.98 GPa (SD = 0.345 GPa) obtained from the Grid Method tests. This difference in the E_{22} values identified from the Grid Method and DIC tests on UD45° samples was close to the UD90° result of 12%. These differences were not expected to be identical because the optimised smoothing parameters used to process the UD90° and UD45° samples had slightly different predicted error magnitudes of 0.54% and 0.14%, respectively (see Chapter 5). Although, this would only account for a small portion of the difference between the Grid Method and DIC results from the UD90° and UD45° samples *i.e.* 12% - 9.7% = 2.3%. Comparison of the E_{22} values obtained from the Grid Method and DIC UD45° samples was difficult, because the UD45° DIC samples were cut from the same UD0° (Plate 2) laminate as the UD90° DIC samples. Therefore, it was likely that a significant portion of the 9.7% difference in the identified E_{22} value was due to the voids and lower measured density in the UD45° DIC samples. Using a simple rule of mixtures analysis, the reduction in density between the Plate 1 and Plate 2 laminates corresponds to a reduction in the matrix volume fraction of around 10%. When this was applied to the mean transverse modulus of 9.98 GPa obtained from the Plate 1 laminate (grid tests), a value of 9.0 GPa resulted from the rule of mixtures analysis. Therefore, when the difference in matrix volume fraction was accounted for in the rule of mixtures, the E_{22} results from the DIC and grid tests were similar.

8.2.3 Shear modulus from UD90° and UD45° samples

From the five UD90° DIC samples, the mean identified shear modulus of 5.26 GPa (SD = 0.223 GPa) was 4.5% lower than the Grid Method result of 5.51 GPa (SD = 0.127 GPa). As explained in Chapter 7, the lower signal to noise levels in these tests resulted in low magnitude shear strains, which were likely responsible for the relatively large SD in the G_{12} values. In spite of this, when the DIC case SD is added to the mean, the result is less than 1% from the Grid Method value, *i.e* variance in the results from both sample types overlap. Comparison of the G_{12} values derived from Grid Method and DIC displacements is also complicated by the defects detected in the Plate 2 laminates that the UD90° DIC samples were manufactured from. In consideration of the reduced density of the DIC samples of 3.9%, the 4.5% lower UD90° DIC sample G_{12} was similar to the Grid Method result. Averaging the results from the five UD45° DIC samples, the mean G_{12} value of 5.08 GPa (SD = 0.065 GPa) was 5.2% lower than the Grid Method value of 5.36 GPa (SD = 0.148 GPa). Using the same rule of mixtures analysis that was applied to the transverse modulus, a 10% reduction in the matrix volume fraction (from the voids) results in a reduction of the shear modulus of around 10%. This reduction was greater than the 4.5% and 5.2% reductions observed from the UD90° and UD45° DIC tests, respectively. However, the shear response could include some bias from the determination of the non-linear shear strains (further discussed in Section 8.4.2), so the comparison may not be as straightforward as the transverse response.

8.2.4 Shear modulus from MD45° samples

The detection of voids in the UD90° and UD45° DIC samples made it difficult to directly compare the transverse and shear moduli from the Grid Method and DIC tests. However, both Grid Method and DIC MD45° samples were cut from the same plate, so a direct comparison between the identified shear moduli was possible. Micrographs of the 0°/90° (Plate 1) laminate that the MD45° samples were cut from are shown in Figures 8.3 (e) and 8.3 (f). Similar to the UD0° (Plate 2) laminates, the MD45° samples also contained voids. Averaging the results from both slices, the mean identified shear modulus from the four MD45° DIC samples was 4.77 GPa (SD = 0.099 GPa). This result was 6.3% lower than the Grid Method result of 5.09 GPa (SD = 0.290 GPa). The image deformation study in Chapter 5 did not consider the MD45° sample configuration, so it is likely that some of this difference was a result of processing with non-optimal smoothing parameters. However, because the samples

were cut from the same laminate, this comparison provides a clearer understanding of the differences in the G_{12} identification from the Grid Method and DIC. Variances in the results obtained from both datasets overlapped and therefore, it was difficult to detect any differences in the MD45° G_{12} values identified with DIC and the Grid Method.

8.2.5 UD90° sample failure stress

The mean transverse failure stress identified from the UD90° DIC samples was 66 MPa (SD = 2.9 MPa), which was 26% lower than the grid method result of 89 MPa (SD = 7.1 MPa). This result was similar to the 30% reduction in tensile failure stress obtained from a UD CFRP composite tested at quasi-static strain rates in [142]. The lower failure stress values obtained from the DIC samples were due to the presence of voids, which act as stress concentration points that can initiate fracture at lower stresses compared to laminates without voids. Therefore, the failure stress values obtained from the DIC samples did not represent the 'true' failure stress of the composite system. Lower failure strains were also measured from the DIC tests compared to the grid tests. This can be seen in Figure 7.24 (d) of Chapter 7 where a tensile failure strain of around 8.5 mm.m^{-1} resulted for UD90-D1, compared to the 12.0 mm.m^{-1} value obtained from UD90-S3 in Figure 6.34 (d) of Chapter 6. These lower failure strains could be expected given the voids detected in the DIC sample laminates [143, 144]. Unfortunately, the presence of voids in the DIC samples meant that the transverse failure stresses obtained from the DIC and Grid Method samples were not directly comparable.

8.3 Comparison with literature

8.3.1 Transverse modulus

The quasi-static and high strain rate moduli identified in this work are now compared to results for the same composite material system reported in [20]. Comparison of the high strain rate data will only consider the IBII test results on the Grid Method samples, due to the detection of voids in the laminates that the DIC samples were manufactured from. In [20], the mean transverse modulus obtained from two tests on UD90° samples was 7.98 GPa. This value is plotted against the evaluated quasi-static strain rate of 9×10^{-4} s^{-1} in Figure 8.1. The E_{22} value of 8.30 GPa obtained from the quasi-static tests conducted here is also plotted in Figure 8.1, which was 4.0% higher than the result in [20]. One possible reason for the different results was that in this study, the moduli were calculated using the average of the strains measured on the front and the back of the specimen. Conversely, the moduli in [20] were derived from strains on one side of the specimen. In quasi-static tensile tests, some bending of the sample can be expected due to the alignment of the test machine grips, and the positioning of the sample in the grips. Depending on what side of the sample the strain gauge is located on, the bending can induce a decrease or an increase in the measured strains. Therefore, it is possible that a bias due to specimen bending could be included in the results from [20]. A second reason for the variation in the quasi-static E_{22} values could be related to the reduced density of 1514 kg.m^{-3} calculated for the tensile test samples. As previously discussed, this reduced density was thought to be resulting from voids formed during manufacture, as shown in Figure 8.3, which may account for some of the variation seen in Figures 8.1 and 8.2. Although, it is unknown whether the samples evaluated in [20] were cut from plates that contained voids or not.

Following the quasi-static result of 7.98 GPa from [20], the transverse modulus obtained at 1.8×10^{-3} s^{-1} increased to around 10.2 GPa. At this point there was a step change in the E_{22} value, which also corresponded to a change in test method used to obtain the results (from a standard tensile test machine to a high-speed hydraulic test machine). Thereafter, similar values were recorded at the strain rates of 1.1×10^{-1} s^{-1} and 2.1×10^{1} s^{-1}, indicating that the E_{22} modulus was (approximately) strain

rate insensitive. Transverse moduli obtained from the UD90° and UD45° IBII tests are also plotted in Figure 8.1. When combined with the quasi-static values, these results showed an increasing strain rate sensitivity of the E_{22} modulus, which agreed with the understanding that the matrix-dominant properties of composites are generally considered to be strain rate sensitive [103]. This finding was contrary to the results from [20] however, the strain rate insensitivity was largely influenced by the increased E_{22} obtained when changing the test method. At this stage, it is difficult to directly compare the strain rate sensitivities in the intermediate strain rate range, as this data was not obtained in this work. However, intermediate strain rate tests on the same material using an ultrasonic rig similar to that in [145] are currently being obtained in a separate study.

Positive E_{22} strain rate sensitivities of 22.3% and 19.4% above quasi-static values were obtained for the UD90° and UD45° samples, respectively. IBII tests on UD90° CFRP composite specimens in [29] resulted in a E_{22} value of 7.9 GPa with strain rates around $2{\times}10^3$ s^{-1} (8% increase over the quasi static value). The same material was evaluated in the UD45° configuration in [127], where the same E_{22} = 7.9 GPa value was obtained. In [29, 127], the composites utilised a low-temperature out-of-autoclave epoxy matrix, which may have behaved differently to the autoclave cured matrix used in samples evaluated here. Therefore, E_{22} values obtained in this work are reasonably consistent with the results from [29, 127].

8.3.2 Shear modulus

Quasi-static G_{12} data obtained from standard test machine tests on three specimens in [20] were averaged to a value of 4.11 GPa and plotted in Figure 8.2. This result was 13.1% lower than the 4.73 GPa value obtained in this work. The elastic limit strains used to determine the modulus values in both studies were similar at around 2.5 mm.m^{-1}. Therefore, any variation in the modulus values due to the fitting ranges was assumed to be negligible. Similar to the transverse modulus, differences between the shear modulus results from this work and in [20] may have been influenced by the single-sided strain measurements. In addition, the quasi-static results from [20] were derived from MD45° specimens and therefore, some differences from the different laminate configurations could be expected.

Figure 8.2 also plots the G_{12} result of 4.6 GPa obtained at the higher strain rate of $1.0{\times}10^{-3}$ s^{-1}, which also corresponded to a change from a standard test machine to a high-speed hydraulic test machine. Thereafter, the shear modulus increased to a value of around 6.6 GPa at a strain rate of $8.8{\times}10^1$ s^{-1}. Shear modulus results from all three IBII sample configurations are also shown in Figure 8.2. When combined with the quasi-static data, the results from this study also show a positive G_{12} strain rate sensitivity, but at a lower rate compared to that in [20]. Again, it is difficult to assess the different strain rate sensitivities without intermediate data. However, one possible explanation for the difference in the results obtained here and in [20] could be due to load cell ringing. Recalling that in [24], finite element simulations of a high-speed hydraulic test machine test showed load cell ringing at speeds as low as 5 m.s^{-1}. Because the materials, testing apparatus and testing speeds in [20] were similar, it is possible that the higher strain rate data may have been affected by load cell ringing.

Acknowledging differences in fibre and resin systems, transverse and shear moduli values obtained during this evaluation generally conform to published data from [59], where maximum strain rates were around a few hundred s^{-1}. At this 'lower end' of the high strain rate regime, inertial effects are lower and the quasi-static equilibrium assumption used in the split-Hopkinson bar test may be more admissible. Further, strains reported in [59] were obtained from 'on-sample' full-field measurements using the DIC technique, which may have produced more realistic results compared to traditional split-Hopkinson bar analysis [146]. As seen in Figures 2.13 (a) and 2.14 (a) of Chapter 2, there was significant scatter in the published results, particularly at strain rates of 10^2 s^{-1} and above. In this strain-rate regime, inertial effects are stronger and the quasi-static equilibrium assumption can be

violated. Therefore, it is difficult to make meaningful comparison with split-Hopkinson bar data obtained at strain rates higher than a few hundred s^{-1}, because it is possible that inertial effects have influenced the result away from the 'true' material response.

8.3.3 UD90° sample failure stress

The mean tensile failure stress obtained from six UD90° grid specimens was 89 MPa (SD = 7.1 MPa). These results were good, considering that values obtained from split-Hopkinson bar tests on a similar material at strain rates an order of magnitude lower had a larger variance (Hexply IM7-8552 UD90° specimens mean failure stress = 79.0 MPa, SD = 11.9 MPa and COV = 15.1% obtained at $\dot{\epsilon} = 2.71\times10^{2}$ s^{-1} in [102]. However, failure stress is highly dependent on material defects and considering that the sample material is a composite, variance in the obtained values was expected. One source of error could be due to the use of a linear approximation of the stress using the LSG, which may have over or under-predicted the maximum average stresses in the vicinity of the crack. For example, consider a convex loading pulse shape in the specimen. Here, the LSG will not be able to accurately reconstruct the stress profile and therefore the calculated failure stress will be incorrect. This would be particularly important for failure stress predictions in off-axis specimens, which develop angled acceleration profiles across the specimen height. Therefore in future work, higher order approximations of the stress should be assessed. Recalling that when the quasi-static data reported in [140] was considered, the percentage increase in the UD90° sample tensile failure stress was 18%. Figure 8.4 plots the mean tensile failure stress value obtained from the IBII tests compared to the results reported in literature (previously shown in Figure 2.13 (b) of Chapter 2). On the whole, this plot shows how the results from this work predict a much lower strain rate sensitivity compared to the in-literature values at strain rates above a few hundred s^{-1}. As most of the datasets came from split-Hopkinson bar tests, the results obtained at the higher strain rates may have been over-predicted, due to violation of the quasi-static equilibrium assumption in the tests. Below a few hundred s^{-1}, the results were consistent with that of [19, 102], which both used full-field measurements in their analysis. Therefore, using full-field measurements to identify failure stress properties may give more accurate results, as effects such as stress concentrations at the sample−bar interfaces can be measured and accounted for during the identification process.

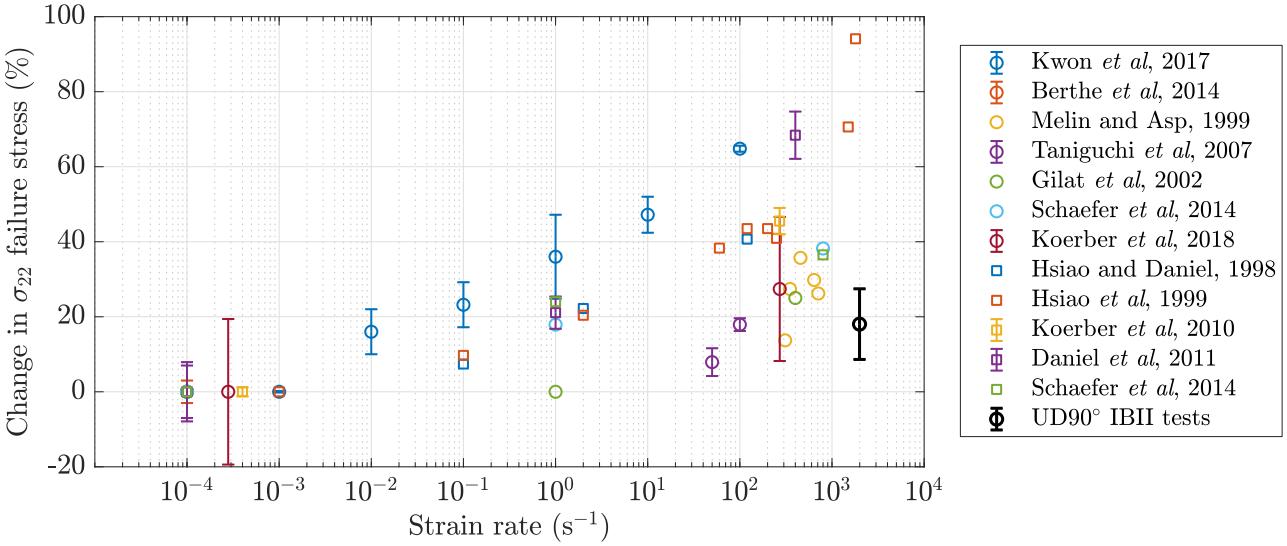

Figure 8.4: Comparison of the percentage change in failure stress relative to quasi-static value from the UD90° IBII tests compared with data from [16–20, 53, 54, 59, 95, 101, 102].

8.4 Limitations and future work

This section discusses the limitations of the IBII test method and their effect on the resulting modulus and failure stress values. Future research activities aiming to further understand the effects of these limitations and extend the versatile nature of the technique are also discussed.

8.4.1 2D plane stress assumption

A key assumption of the IBII test method applied here is that the samples are loaded under 2D plane stress conditions. The validity of this assumption was investigated in [115], where modulus and failure stress properties were identified on both sides of a sample using back-to-back cameras. The results of this study showed that the unintentionally induced, out-of-plane loading due to projectile misalignment caused only a small bias on the identified elastic modulus. Results from this work agree well with [115], where in-test projectile misalignment measurements confirmed that when the pre-test alignment procedure was followed, there was insignificant influence on the identified elastic moduli. When coupled with the linear transverse response observed in all tests in this work, the impact of 3D effects on the results are considered negligible. Similar to the finite element simulation results, the off-axis sample E_{22} and G_{12} responses were very stable over the range of x_0 positions, indicating that the sample was loaded under 2D plane stress conditions.

8.4.2 Determination of the linear shear strain region

In this work, a non-linear shear response was obtained from the UD45° IBII tests. The range over which linear fits to the shear stress-strain curves were made influenced the shear modulus value. Because the linear limit strain varied in space and time, chord moduli were progressively fitted to the shear stress-strain curves and the linear limit was determined when the value fell below the average modulus. This method was affected by noise induced oscillations in the shear response, which made the linear limit identification troublesome because the oscillations were often of similar magnitude to the non-linear onset strains. There is currently no efficient method to check every slice and time step to evaluate the linear elastic limit determined from the chord fitting method. Future work could therefore include image deformation studies, including a non-linear material model in the finite element simulations, which can be used to determine the linear fitting range for experimental results processing.

A major limitation of the method used to obtain the non-linear onset strain was that it was affected by the non-linear shear response in the sample. When the strains are uniformly distributed along the slice, averaging the strains over the slice gives a good approximation of the material response. Here, the stress-strain curves are 'smeared' as points of different stress/strain are averaged to produce the response, but the smeared curve will still be a straight line of the correct slope. However, when the material behaviour is non-linear, the strains may not be uniformly distributed along the slice. This could be particularly relevant for the UD45° samples, where the kinetic fields were more complex compared to the UD90° samples. When non-linear behaviour is present, some of the linear points are averaged with the non-linear data and therefore, the obtained modulus will be biased. In this case, a more accurate method to detect the non-linear onset would be to utilise a shear damage model, which is discussed in Section 8.4.7.

8.4.3 Optimised smoothing parameters for the MD45° samples

The MD45° sample IBII tests were processed using the optimised smoothing parameters obtained from the UD45° case image deformation study. However, the symmetric ±45° nature of the MD45°

samples generated different kinematic field shapes compared to the UD45° specimens. This may require different smoothing kernels to minimise errors on the MD45° G_{12} moduli. Therefore, optimised smoothing parameters for the MD45° samples should also be obtained using image deformation. Here, the reference moduli specified in the finite element simulation material model could be calculated with Classical Lamination Theory (CLT) and the optimised smoothing parameters could then be compared to the UD45° and UD90° results. Due to the symmetric nature of the fields, it is expected that the optimised smoothing parameters for the MD45° case could be similar to the UD90° sample values.

8.4.4 Optimisation of the shear response from UD90° samples

The shear modulus identification from UD90° specimens was obtained from shear stresses and strains, generated from a pitch angle misalignment between the projectile and the wave guide during the tests. Here, the pitch angle misalignment was not intentional, so the resulting shear stress and strain magnitudes were low. In the future, it should be possible to design the test to intentionally use this misalignment to more strongly activate the shear response. This could be achieved using an appropriate finite element model to predict the loading from a misaligned projectile. Results from the misaligned finite element simulation could then be used to deform synthetic grid or DIC images in an image deformation study. Initially, this study would determine whether there was a strong enough shear response resulting from the particular misalignment set in the finite element model. This would be confirmed by a low systematic error on the identified shear modulus, excluding effects from noise. Simulated noise could then be included in the analysis to obtain optimised smoothing parameters, which provide the best compromise between systematic and random errors. IBII tests could then be conducted using the in-test alignment procedure, to confirm the angle set on the rotary stage (and in the simulation). Printed contacts or alternative sensors such as polyvinylidene di-fluoride (PVDF) gauges [147] could be trialled to achieve an improved accuracy on the angle calculations. However, a more straightforward option of inducing a stronger shear response could be to impact the sample over half its height. This could be achieved by aligning the horizontal centreline of the sample with the top of the wave guide.

8.4.5 Failure stress identification from UD90° samples

In this work, image deformation studies were undertaken to obtain optimised smoothing parameters for identifying modulus properties from IBII tests. These same smoothing parameters were also applied in the identification of failure stress values from the UD90° samples. Therefore, errors due to non-optimal smoothing parameter selection are expected from the failure stress values, which could be more significant because of their localised nature. Because the stresses are calculated from the accelerations, temporal smoothing can mask the failure location determined from the departure of the LSG stress from the stress calculated from the strains and the constitutive model (see Section 4.2.11 of Chapter 4). Future image deformation studies could be undertaken to reveal the extent of the systematic, random and total errors on the transverse failure stress. Displacement fields from a finite element model with a cohesive zone in the crack location could be imposed on synthetically generated images. Full-field techniques could then be used to generate kinematic fields from which stress maps are derived. The stresses can then be analysed over a 'virtual gauge area' on the synthetic images, which is positioned in the same location as the fracture zone observed in the experiments. Errors could then be calculated by comparing the identified failure stresses to quasi-static or high strain rate values as the reference.

8.4.6 Failure stress envelope

The first aim of this thesis was to develop and validate transverse and shear modulus identification methods for off-axis composites with the IBII technique. A further aim was to obtain an accurate transverse failure stress dataset from UD90° samples. The next research task is to extend these methods to obtain the dynamic failure stress under a combined tension/shear or compression/shear loading, using off-axis composite samples. Mechanical properties associated with failure often require a more localised approach, because the stress state at the exact point of failure is required. As a first step, the Linear Stress Gauge (LSG) approach described in [29] can be applied to off-axis specimens in global coordinates, using the free-edge boundary conditions to populate the stress tensor. The stress tensor is then rotated into material coordinates to obtain the transverse and shear failure stresses. However, this is only valid when failure occurs at the specimen edges, where shear and y-axis stresses are zero and the full stress tensor can be obtained. A preliminary failure stress identification using UD45° samples was undertaken as part of this research project. However, the results were unexpectedly low, with values around 20 MPa for both the transverse and shear failure stresses. These low failure stress values were thought to be resulting from the linear stress reconstruction over the sample height. With this method, the stresses resulting from the off-axis sample's angled wave kinetics were not well-approximated. In addition, the presence of voids in the UD45° sample laminates may have resulted in lower identified failure stresses. For these reasons, the UD45° sample failure stress values are not presented here, but will be investigated in future work.

Alternative methods are possible for instances where the failure does not occur at the specimen edge. One option is to utilise angled slice boundary condition information together with rigid body virtual fields, to construct higher order (quadratic or cubic) approximations of the transverse and shear stress in the material coordinate system. Another option is to use the full-field accelerations to approximate the local equilibrium equation as described in [141]. Once the failure stress reconstruction methodology is determined, a range of off-axis specimens could be evaluated in IBII tests to populate a high strain rate failure envelope under combined tension/shear and compression/shear states of stress. Comparisons between the failure stresses identified using DIC and Grid Method displacements could also be undertaken.

8.4.7 Shear damage model

Shear stress-strain curves obtained in this work revealed different load and unload moduli together with a residual shear strain upon return to the zero stress condition. These observations may have indicated that damage had occurred, in the form of plastic deformation of the matrix or the formation of micro-voids or cracks within the sample. Therefore, a shear damage model such as that reported in [72] could be adapted for this high strain rate application. Micrography of recovered specimens could then facilitate an experimental validation of the damage model, comparing the reduction in modulus with the percentage void increase in recovered samples. Following the tests on samples that did not form cracks, no changes to the recovered sample length or height measurements were recorded. This indicated that the loading conditions had not initiated plastic deformation of the matrix, but rather a viscoelastic response. However, these measurements were obtained using callipers with a resolution of ± 0.005 mm, so more accurate methods could be used to detect permanent strains. Preliminary x-ray CT scans of the recovered samples also revealed no damage in the samples however, it is possible that cracks formed during the loading had closed following the test. Further scans using a small loading fixture to lightly load the samples and re-open the cracks could therefore be investigated. Results from the preliminary scans also indicate that the samples should be impacted at greater speeds, to initiate a stronger non-linear shear response. This may lead to damage in the recovered samples, which can be detected using optical inspection methods. Lastly, the progressive chord modulus fitting technique applied in this work was affected by noise. Therefore, noise-optimised virtual fields could be used in the VFM to extract modulus data as in [65].

Chapter 9

Conclusions

This chapter lists the conclusions from the two main research activities in this project. The first aim was to generate an accurate high strain rate material property dataset for off-axis CFRP composites. This required the application of VFM techniques within the IBII test methodology, which were tailored to match the different laminate configurations of the evaluated samples. Validation of these methods was achieved by comparing the results from each of the laminate configurations. The outcome of this process was an experimentally validated method to identify the in-plane transverse and shear moduli of orthotropic composites in the $0.5 - 2{\times}10^3$ s^{-1} strain rate regime. Conclusions from this evaluation are listed below:

- The mean transverse modulus obtained from seven tests on UD45° specimens was $E_{22} = 9.98$ GPa (SD = 0.345 GPa), indicating good repeatability between specimens. This was similar to the mean UD90° result of $E_{22} = 10.2$ GPa (SD = 0.154 GPa). These results demonstrated how consistent in-plane transverse moduli could be identified from different sample configurations with the IBII test.

- Shear moduli were also identified from the UD90° samples, where the mean G_{12} value was 5.51 GPa (SD = 0.127 GPa), which was again indicative of low inter-sample variation. The UD90° result was consistent with the mean shear modulus obtained from the UD45° samples of 5.36 GPa (SD = 0.148 GPa), which was calculated from the average of slices 1 and 2. The outcome of this evaluation was proof that accurate shear moduli could be identified from IBII tests on relatively easy to manufacture UD90° specimens, provided that enough in-plane misalignment was present to generate the shear wave.

- Four tests were performed on MD45° specimens, where the resulting shear modulus was 5.09 GPa (average of slices 1 and 2). This was 5.0% lower than the UD45° value and consistent with the reduced fibre volume fraction of the MD laminate, as evidenced by its lower density.

- The mean transverse failure stress obtained from six tests on UD90° specimens was 89 MPa (SD = 7.1 MPa). Good repeatability was obtained from the tests, considering the additional variation that could be expected from localised failure stress measurements. This result represented an 18% increase over the quasi-static value, with peak transverse tensile strain-rates on the order of $2{\times}10^3$ s^{-1}.

The second aim of this project was to evaluate the off-axis properties identified using DIC displacements, and compare them to the Grid Method results. Voids detected in the laminates that the DIC samples were cut from resulted in a reduced sample density compared to the grid samples. This made the comparison of moduli identified from the grid and DIC tests difficult, because the specific mass and structural integrity of the samples differed. However, when a simple rule of mixtures was applied, the moduli obtained from the DIC samples were comparable to the grid results. The MD45° samples were cut from the same composite plate, so a direct comparison was possible. The main conclusions from this evaluation were:

- The mean transverse modulus obtained from five tests on UD45° DIC specimens was 9.01 GPa (SD = 0.141 GPa). This result was was 9.7% lower than the Grid Method result of 9.98 GPa (SD = 0.345 GPa). A mean E_{22} value of 8.98 GPa (SD = 0.079 GPa) was obtained from the UD90° DIC samples, which was 12.0% lower than the Grid Method result of 10.2 GPa (SD = 0.154 GPa). These values were consistent with the 3.9% reduction in density of the UD DIC samples. When the reduced matrix volume fraction (due to voids) was accounted for in a rule of mixtures analysis, there was an insignificant difference in the E_{22} value obtained from the Grid Method and DIC tests.

- Shear moduli were also identified from the UD90° DIC samples, where the mean G_{12} value was 5.26 GPa (SD = 0.223 GPa), which was 4.5% lower than the Grid Method result of 5.51 GPa (SD = 0.127 GPa). This result was consistent with the mean shear modulus obtained from the UD45° DIC samples of 5.08 GPa (SD = 0.065 GPa), which was 5.2% lower than the Grid Method result of 5.36 GPa (SD = 0.148 GPa). Similar to the transverse modulus comparison, the results were consistent with the 3.9% reduced laminate density of the UD DIC samples.

- Four tests were performed on MD45° DIC specimens, where the resulting shear modulus was 4.77 GPa (SD = 0.099). This result was 6.3% lower than the MD45° Grid Method value of 5.09 GPa (SD = 0.290), calculated from the average of the slice 1 and 2 results. As the samples were cut from the same plate, the results were directly comparable. When the results variance is considered, the DIC and Grid Method results were similar.

- The mean transverse failure stress obtained from the five IBII tests on UD90° DIC samples was 66 MPa (SD = 2.9 MPa). This was 26% lower than the mean failure stress of 89 MPa (SD = 7.1 MPa) resulting from tests on the grid samples, which were cut from a pristine laminate. The reduced failure stress value was consistent with the presence of voids detected in the DIC samples.

In consideration of the consistent results and experimental validation in this study, the IBII technique represents an excellent test method to use in pursuit of high strain-rate modulus property identification for composites. The good consistency was evidenced by the coefficients of variation between dynamic tests, which were better than many quasi-static tests reported in the literature. Because of this consistency, it was possible to detect a reduction in moduli of 10% between pristine and porous composite panels. Results from this project have also demonstrated the versatile nature of the test, given that systematic errors on the identified moduli were less than 1% when different full-field measurement techniques were used in conjunction with the IBII methodology. These attributes suggest that the IBII test is an obvious candidate for a new standard high strain-rate test for modulus identification. Undoubtedly, as camera technology improves the efficacy of the IBII method will also improve.

Appendices

A Density calculations

Density values were calculated from small samples cut from the same laminate that the IBII and quasi-static specimens were manufactured from. Surfaces of the density samples were first sanded to the same amount as the quasi-static and IBII test specimens. Each density sample mass was measured using a mass balance with a resolution of 1×10^{-4} grams. Six measurements of each specimen dimension were taken with a digital calliper, which had a length measurement resolution of ± 0.005 mm. The lower and upper geometric measurements were used to calculate the specimen's (approximate) minimum and maximum volume. Maximum and minimum density values were calculated by dividing the specimen mass by the minimum and maximum volumes, respectively. Tables A1, A2 and A3 list the mean density value and standard deviation for each laminate.

Table A1: Measurements from five samples cut from the UD0° laminate (Plate 1) used to calculate the density for the UD90° and UD45° IBII specimens.

Spec.	**Length**	**Height**	**Thickness**	**Vol.**$_{min}$	**Vol.**$_{max}$	**Mass**	$\boldsymbol{\rho}_{min}$	$\boldsymbol{\rho}_{max}$
(#)	(mm)	(mm)	(mm)	($\times 10^{-6}$ m^3)		($\times 10^{-3}$ kg)	(kg.m^{-3})	
1	23.83 ± 0.02	18.15 ± 0.06	3.05 ± 0.02	1.301	1.331	2.0732	1558	1593
2	18.07 ± 0.12	19.18 ± 0.04	3.06 ± 0.01	1.050	1.075	1.6682	1552	1589
3	23.84 ± 0.03	23.83 ± 0.03	3.05 ± 0.02	1.717	1.750	2.7239	1557	1586
4	23.84 ± 0.04	23.83 ± 0.02	3.05 ± 0.01	1.718	1.738	2.7352	1574	1592
5	23.82 ± 0.01	17.95 ± 0.08	3.05 ± 0.02	1.291	1.316	2.0550	1562	1592
						Mean	1575	
						SD	17	

Table A2: Measurements from four samples cut from the MD0°/90° laminate used to calculate the density for the MD±45° IBII specimens.

Spec.	**Length**	**Height**	**Thickness**	**Vol.**$_{min}$	**Vol.**$_{max}$	**Mass**	$\boldsymbol{\rho}_{min}$	$\boldsymbol{\rho}_{max}$
(#)	(mm)	(mm)	(mm)	($\times 10^{-6}$ m^3)		($\times 10^{-3}$ kg)	(kg.m^{-3})	
1	31.14 ± 0.03	12.29 ± 0.05	3.07 ± 0.04	1.155	1.199	1.8038	1504	1561
2	35.27 ± 0.04	10.34 ± 0.07	3.10 ± 0.07	1.098	1.167	1.7265	1479	1573
3	35.48 ± 0.04	11.56 ± 0.06	3.10 ± 0.07	1.234	1.308	1.9446	1486	1576
4	30.88 ± 0.04	28.14 ± 0.04	3.09 ± 0.05	2.635	2.738	4.1094	1501	1560
						Mean	1530	
						SD	41	

Table A3: Measurements from five samples cut from the UD0° laminate (Plate 2) used to calculate the density for the quasi-static tensile test samples, along with the UD90° and UD45° IBII samples evaluated with DIC.

Spec.	**Length**	**Height**	**Thickness**	**Vol.**$_{min}$	**Vol.**$_{max}$	**Mass**	ρ_{min}	ρ_{max}
(#)	(mm)	(mm)	(mm)	($\times 10^{-6}$ m^3)		($\times 10^{-3}$ kg)	(kg.m^{-3})	
1	28.55 ± 0.03	10.26 ± 0.02	3.14 ± 0.03	0.908	0.929	1.3925	1498	1534
2	26.99 ± 0.04	9.33 ± 0.04	3.13 ± 0.02	0.778	0.799	1.1928	1493	1533
3	29.56 ± 0.03	8.26 ± 0.04	3.13 ± 0.02	0.756	0.773	1.1532	1492	1526
4	25.29 ± 0.03	13.01 ± 0.04	3.13 ± 0.03	1.015	1.044	1.5657	1499	1542
5	31.84 ± 0.09	39.03 ± 0.04	3.13 ± 0.02	3.852	3.933	5.8863	1497	1528
						Mean	1514	
						SD	20	

B Sample edge angle measurements

Top-down and Bottom-up macroscopic images of the vertical edges of six UD45° samples were taken with a WILD M420 macroscope. The images were captured with the measured edge located in the centre of the field of view. Front and back face angles were measured from each edge using ImageJ, as shown in Figure 1. When taking the measurements, each arm of the angle measurement tool was as long as the sample thickness. The accuracy of the measurements was determined by shifting the endpoint of each arm of the angle measurement tool by one pixel (increasing the angle). This angle measurement was subtracted from the actual measured value to determine the angle measurement resolution, which was ±0.17°. Table B1 lists the measured angles.

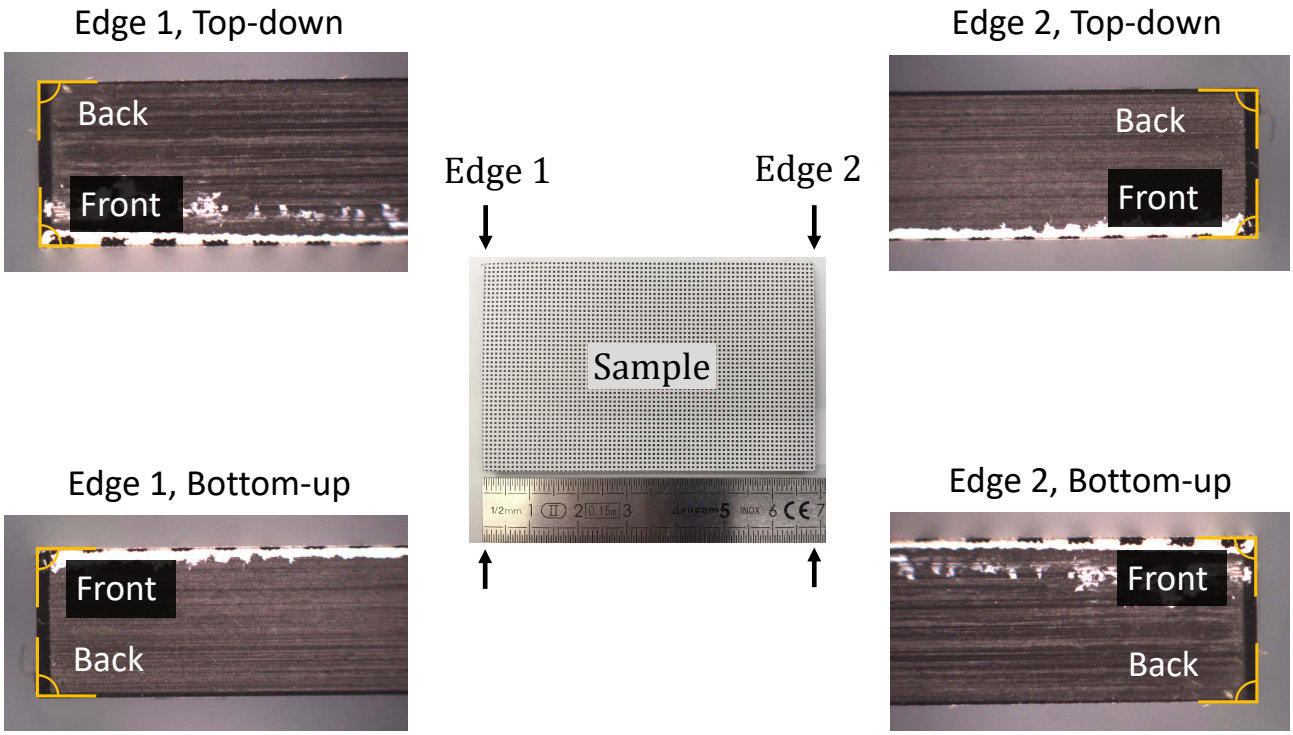

Figure 1: Diagram showing the perspective and location from which the macroscopic images were taken to measure the sample edge angles.

Table B1: Edge angle measurements from six UD45 samples, where the location of the measured angle is shown in Figure 1.

		Edge 1		**Edge 2**	
Sample	**Face**	**Top-down**	**Bottom-up**	**Top-down**	**Bottom-up**
(#)	(Front/Back)	(degrees)	(degrees)	(degrees)	(degrees)
1	Front	89.99	90.16	89.77	90.43
	Back	89.94	90.56	90.45	89.60
2	Front	90.25	89.76	89.79	90.10
	Back	90.18	90.72	90.71	90.64
3	Front	90.63	89.64	90.25	89.87
	Back	89.86	90.26	90.28	90.20
4	Front	90.26	90.06	90.27	90.11
	Back	90.24	90.35	88.95	90.09
5	Front	90.37	89.85	89.60	90.44
	Back	90.19	90.14	90.52	89.51
6	Front	90.44	90.33	89.65	90.42
	Back	89.55	90.65	89.99	90.17
	Mean		**90.13**		
	SD		**0.37**		

C Wave guide assembly procedure

Select a wave guide and measure the diameter at four equidistant positions at both ends. Then measure the length at four locations. Average both sets of measurements and ensure that they are within the measurement resolution of the callipers used to make the measurements (here, 0.005 mm). Place the wave guide on an aluminium 'V-block' and using an engineering square and pencil, rule two orthogonal lines on one of the end surfaces as shown in Figure 2. Notice that both lines intersect at the approximate centre of the wave guide.

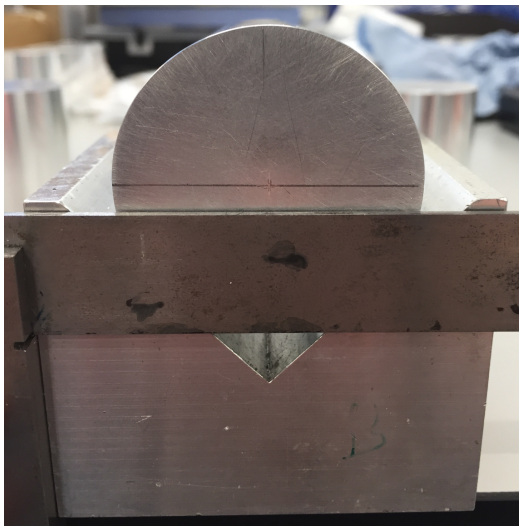

Figure 2: Marking orthogonal lines on the wave guide.

Cut three strips of double-sided tape and position them over the marked lines as shown in Figure 3. Ensure that the edges of the tape touch one another, but do not overlap.

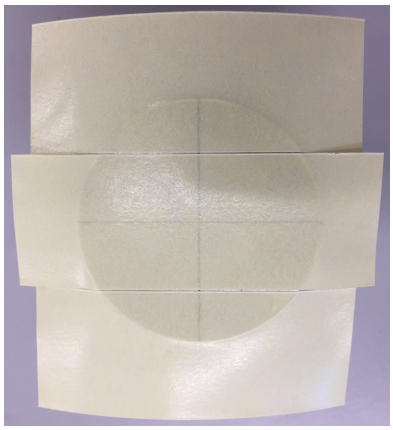

Figure 3: Three strips of double-sided tape positioned on the wave guide.

Place the wave guide tape-side down on a flat wooden board. Use a sharp blade to cut around the wave guide diameter, leaving square tabs at the end of each line as shown in Figure 4. Fold the tabs back along the wave guide's central axis. The double sided tape provides electrical insulation for the contact circuits, which give the projectile impact times at four locations on the wave guide.

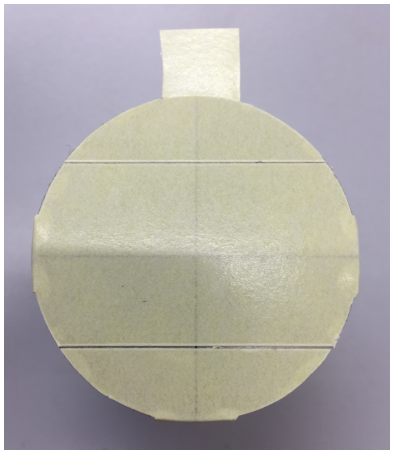

Figure 4: Trimmed double-sided tape and the location of an insulating tab.

After removing the double sided tape, cut small strips of adhesive copper tape approximately 2×10 mm in size. Position two tabs at the end of each line ruled on the wave guide, ensuring that 2-3 mm of the tab is located on the impact face as shown in Figure 5. Place the double-sided tape backing sheet back onto the impact face and using another wave guide, press down on the copper tabs using firm body weight. Measure the length of the wave guide plus the double-sided tape and the copper tabs to ensure that the height of the tabs is within the tolerance of the callipers used to make the measurement.

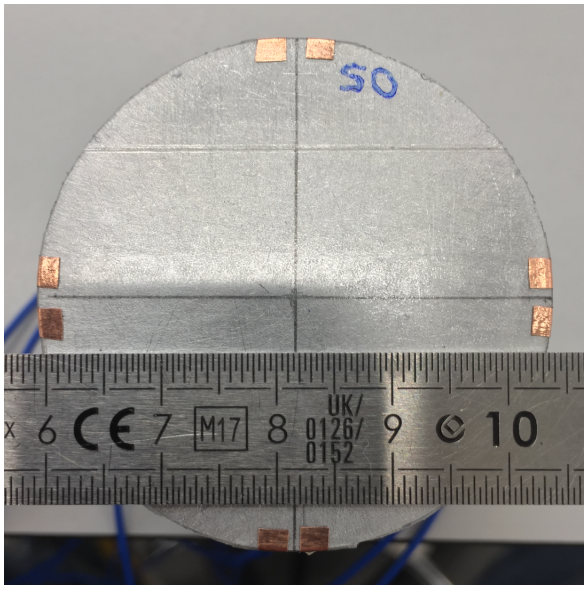

Figure 5: Positioning of the copper tabs.

Cut eight lengths of insulated wire and solder them to each tab. Label four wire pairs according the location of their tabs, e.g. 'Top', 'Bottom', 'Left' and 'Right'. Cut two strips of double-sided tape and position them on the foam stand as shown in Figure 6.

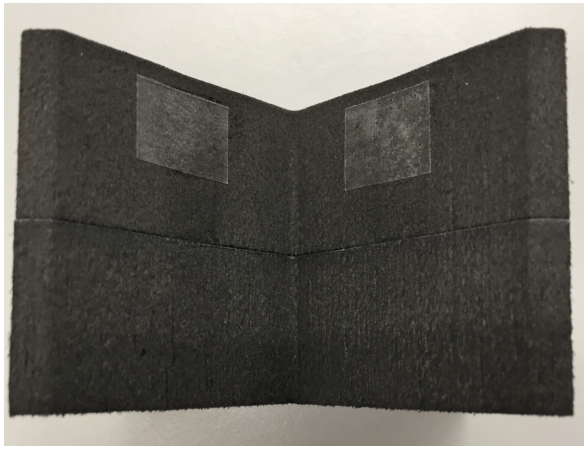

Figure 6: Positioning of the double-sided tape on the foam stand.

Place the wave guide 'impact-end upwards' on a flat surface that contains a slot (or hole), and thread the 'Bottom' position wires through the slot, as shown in Figure 7. Position a piece of 0.2 mm PTFE sheet underneath the wave guide. This will ensure that the front face of the wave guide is slightly forward of the foam stand during a test. Place the foam stand on the flat surface and gently bring it towards the wave guide, aligning the centres of both items 'by-eye'.

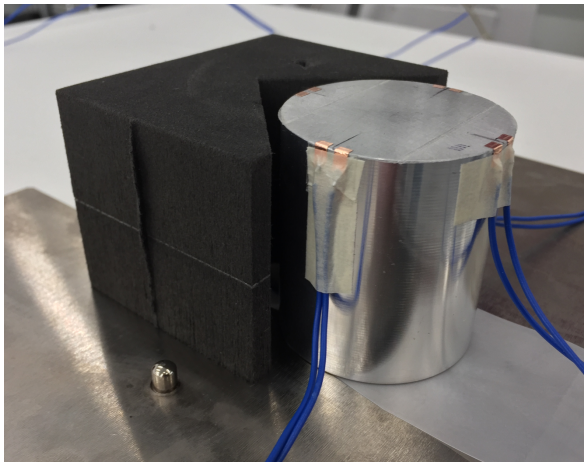

Figure 7: Positioning of the wave guide on the foam stand.

Check that the front face of the wave guide is square with the bottom surface of the foam stand. This can be done by placing the wave guide and foam stand on a flat surface (*e.g.* a laboratory workbench) and taking an image of an engineering square resting on the work bench, close to the impact face, as shown in Figure 8.

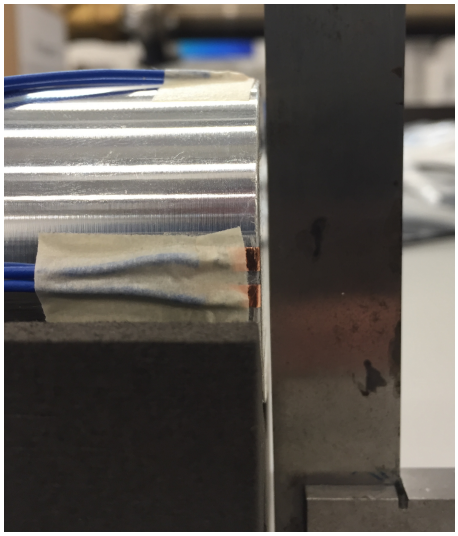

Figure 8: Check that the wave guide is positioned square to the bottom of the foam stand.

The next step is to position the sample on the wave guide and foam stand assembly. It is important that the long-edge, central axis of the sample is axially-aligned with the central axis of the wave guide. Firstly, mark the centre of the foam stand with a felt-tipped pen and re-position on the workbench. Using the engineering square, rule a vertical line on the back face of the wave guide as shown in Figure 9.

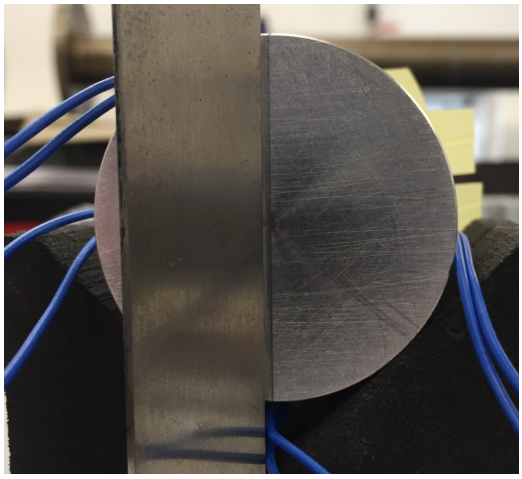

Figure 9: Marking a centreline on the wave guide.

Using a ruler, draw a line parallel to the centreline, offset by half the sample width (approximately 1.5 mm) from the centreline. Position a flat, square object on the wave guide, such as the mechanical test machine fitting (referred to here as a 'square block') shown in Figure 10 (a). Position a ruler underneath and place strips of masking tape over the edges of the square block to permit easy removal after the sample is adhered to the wave guide. Align the vertical edge of the square block with the offset line and position a sample against it to ensure that the sample edge is aligned with the centreline, as shown in Figure 10 (b). If the sample is not axially aligned with the centreline, the centre and offset lines must be redrawn.

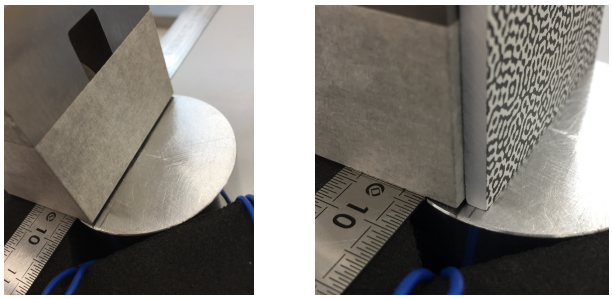

(a) (b)

Figure 10: Positioning the square block on the offset line in (a) and checking the sample is axially-aligned on the wave guide in (b).

Use a wooden applicator to spread a thin coat of instant adhesive on the impact edge of the sample. Run the applicator along the centre of the sample, forming an even, convex section of adhesive with a height of approximately 0.5 mm. Take care to ensure that the glue does not extend to the edges of the sample, as shown in Figure 11.

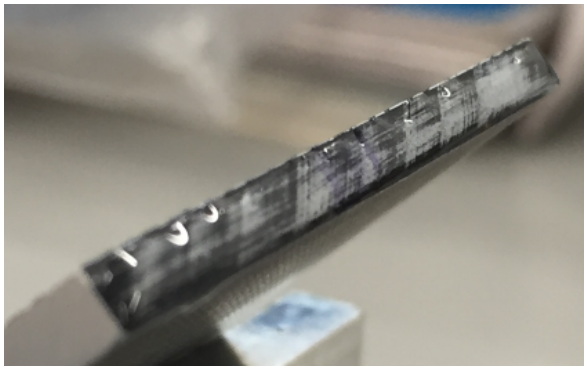

Figure 11: Application of adhesive on the sample's impact edge.

Holding the flat edge firmly on the wave guide, position the sample 'impact-edge down' on the wave guide, aligning the sample with the square block's vertical edge, then press downwards with firm hand pressure for 20 seconds. Ensure to remove the excess glue from the sample/wave guide edge, particularly on the imaged side of the sample, as this may enter the field of view during a test. Remove the square block and position a piece of masking tape on the rear surface of the wave guide, cutting it to the wave guide diameter as shown in Figure 12.

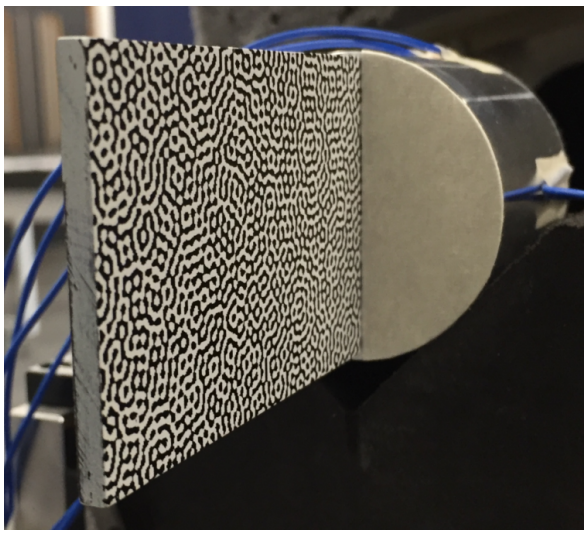

Figure 12: Masking tape on the rear face of the wave guide (imaged side).

Place the wave guide, foam stand and sample assembly on the workbench. Position an engineering square at the end of the sample as shown in Figure 13 and capture a still image. Measure the vertical angle of the sample (Angle 1 in Table C1) using Image processing software such as ImageJ. Ensure that the angle is less than 0.5°, meaning that the impact edge is perpendicular to the base of the foam stand within this tolerance. This measurement collectively accounts for the edge squareness of each component following assembly. It is also important for achieving consistent pitch angles when using the vernier scale on the 5-axis stage. If the angle here is greater than 0.5°, it may be an indication that the sample was positioned incorrectly on the wave guide or that the foam stand may need to be replaced.

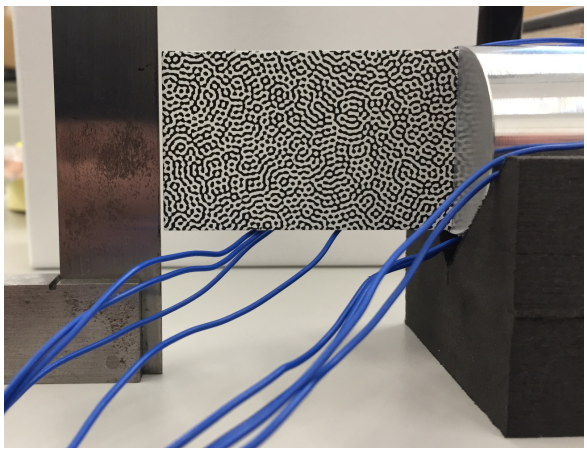

Figure 13: Check that the sample edge is perpendicular to the bottom of the foam stand after assembly.

Looking at the sample's free-edge, position the engineering square perpendicular to the wave guide's centre axis at the end of the sample, as shown in Figure 14. Again, using image processing software measure the angle between the vertical centre-axis of the sample relative the the straight edge of the engineering square (Angle 2 in Table C1). Assuming that the workbench has an angular tolerance of less than 0.1°, this angle will provide an indication of the angle between the vertical centre-axis of the sample and the wave guide/foam stand assembly. When the angle is less than 0.5°, the sample has been positioned well on the wave guide. If the angle is greater than this, the sample may need to be re-positioned because the kinematic field calculations above the sample centre-line may be affected differently to those below.

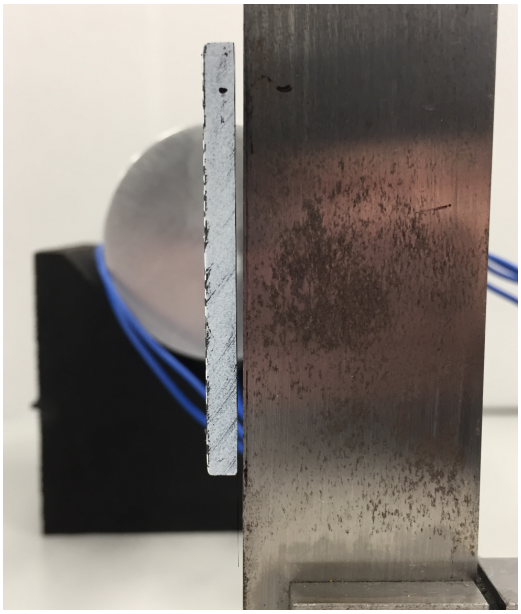

Figure 14: Image used to measure the angle between the vertical centre-axis of the sample and the wave guide/foam stand assembly.

Take a top-down image of the sample on the wave guide, ensuring that the vertical centre axis of the sample and the back face of the wave guide are in the centre of the image (see Figure 15). Using image processing software, measure the angle between the sample's long edge and the back face of the wave guide (Angle 3 in Table C1). This measurement will provide an indication of how perpendicular the sample's long-edge centre-axis is relative to the rear face of the wave guide.

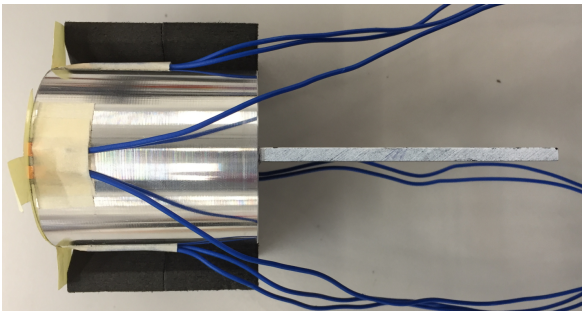

Figure 15: Image used to measure the perpendicularity of the sample's long edge centre axis to the rear face of the wave guide.

Position the assembly on the 5-axis stage and secure the wires to the bottom of the target trap with masking tape, so that the wires do not interfere with the stage during a test. Supporting the aluminium guide, press the assembly down. Use a spirit level to ensure the top of the wave guide is approximately horizontal to the aluminium guide. Figure 16 gives an image of the sample, wave guide and foam stand assembly in position on the 5-axis stage.

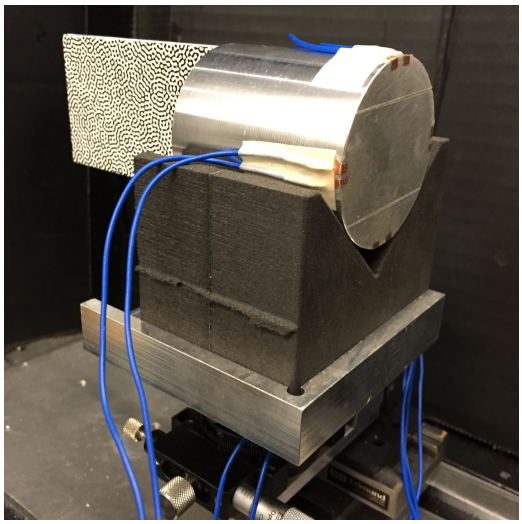

Figure 16: Sample, wave guide and foam stand assembly in position on the 5-axis stage.

Record the pitch angle on the vernier printed on the Edmunds Optics TechSpec series Goniometer, which facilitates the pitch angle adjustment on the 5-axis stage. The smallest increment on the vernier is 5 minutes or 0.083°, however the manufacturer's specified resolution is 0.1°. Figure 17 (a) gives an image of the vernier printed on the Goniometer. The vernier scale is quite small, so the reading is obtained by taking a 'zoomed-in' image of the vernier using a smart phone camera. The pitch angle vernier is additionally difficult to read, because it is positioned in front of the vertical translation post on the 5-axis stage. Therefore, the pitch angle vernier was read by pointing the smart phone camera lens trough a small hole in the stage's vertical post, as shown in Figure 17 (b). In the future, the hole in the post could be made wider so that the image easier to obtain.

(a) (b)

Figure 17: Goniometer vernier with a pitch angle resolution of 0.1° in (a) and an image of the vernier used to record the angle during a test in (b).

Yaw angle adjustment is facilitated by a rotary stage, which is part of the 5-axis stage assembly. Record the yaw angle on the vernier scale printed on the rotary stage (see Figure 18). Like the pitch angle reading, this was done by taking a 'zoomed-in' image of the vernier with a smart phone camera. Note that the smallest increment on the rotary stage vernier is 10 minutes or or 0.17°.

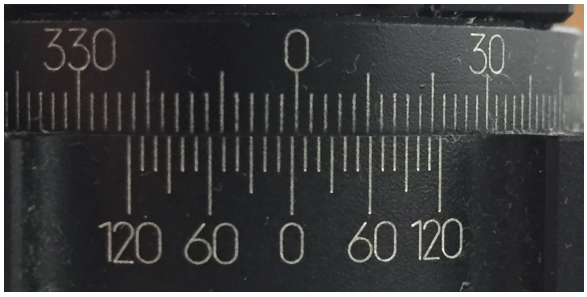

Figure 18: Rotary stage vernier with a yaw angle resolution of 0.17°.

Each pair of wires soldered to the tabs on the wave guide formed part of a circuit that generated an electrical current when shorted by the projectile. For the 'Right', 'Bottom' and 'Left' positions, the ends of the wires were connected to one side of an electronics box *via* a cable with alligator clips on one end and a BNC fitting on the other. The other side of the electronics box was connected to a PicoScope 4244 series PC oscilloscope with double-ended BNC cables, as shown in Figure 19. The 'Top' wires were connected to the trigger input on the HSV camera, and the 'Aux1' output was connected to the Oscilloscope. This 'Top' or 'Aux1' signal was used to trigger both the camera and the oscilloscope, while giving the projectile impact time for the 'Top' position on the wave guide.

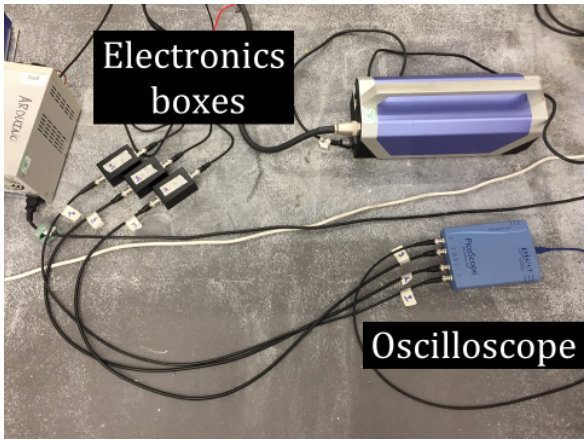

Figure 19: Experimental setup for the impact timing circuit.

Table C1: Measurements of the DIC samples on the wave guide once assembled, with Angle 1 calculated from an image similar to Figure 13, Angle 2 from Figure 14 and Angle 3 from Figure 15.

Sample (#)	**Angle 1** (degrees)	**Angle 2** (degrees)	**Angle 3** (degrees)
UD90-D1	0.20	0.40	89.3
UD90-D2	0.15	0.29	90.3
UD90-D3	0.30	0.20	90.2
UD90-D4	0.15	0.32	89.7
UD90-D5	0.20	0.33	90.6
UD90-D6	0.04	0.30	90.0
UD45-D1	0.24	0.08	90.0
UD45-D2	0.07	0.28	90.0
UD45-D3	0.25	0.11	89.8
UD45-D4	0.14	0.32	90.4
UD45-D5	0.21	-0.33	90.2
UD45-D6	0.05	-0.25	89.9
MD45-D1	0.50	0.34	89.4
MD45-D2	0.03	0.48	90.3
MD45-D3	0.07	0.05	90.6
MD45-D4	0.18	0.07	90.5
Mean	**0.17**	**0.26**	**90.1**
SD	**0.12**	**0.12**	**0.39**

D Modulus *vs.* position plots from the different image types with no applied noise or smoothing

(a) UD90° case E_{22} *vs.* x_0 position.

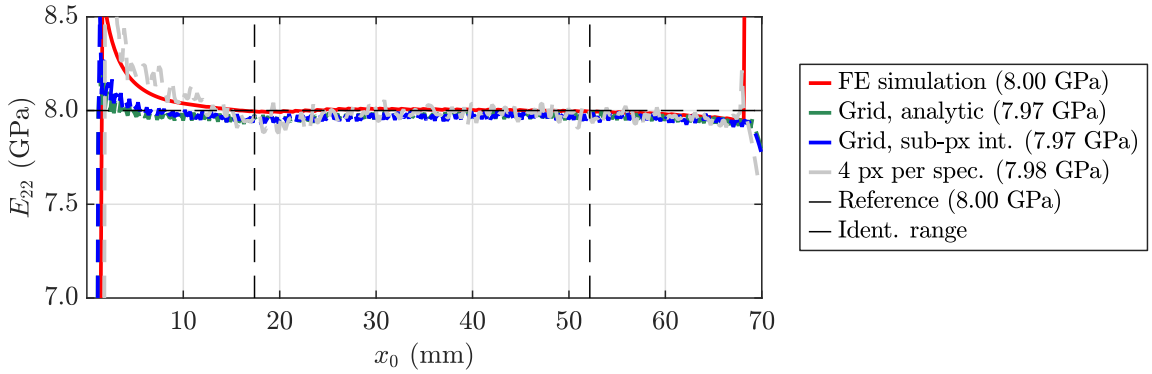

(b) UD45° case $G_{12\,Sl.\,1}$ *vs.* x_0 position.

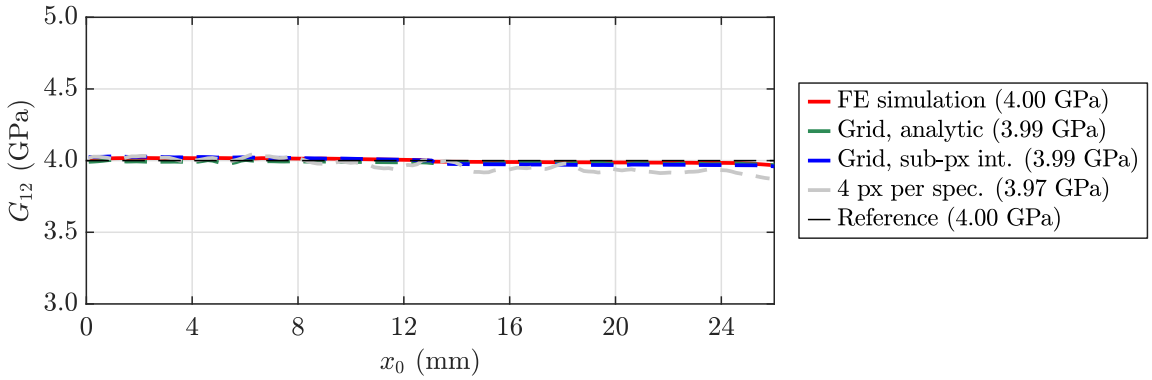

(c) UD45° case $G_{12\,Sl.\,2}$ *vs.* x_0 position.

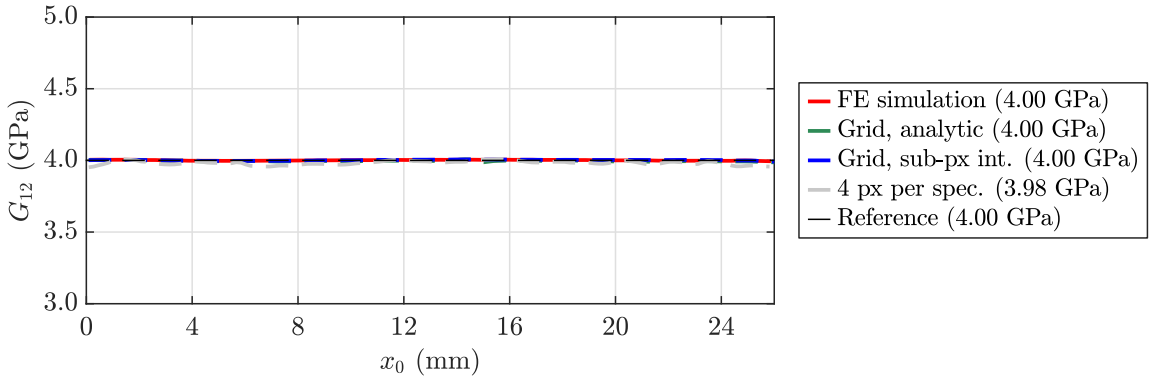

Figure 20: Modulus against position for the three image types, where no noise fields or smoothing was applied in the identification of the UD90° E_{22} (a), UD45° $G_{12\,Sl.\,1}$ (b) and UD45° $G_{12\,Sl.\,2}$ (c) case moduli.

E Noiseless and noisy systematic error heat maps

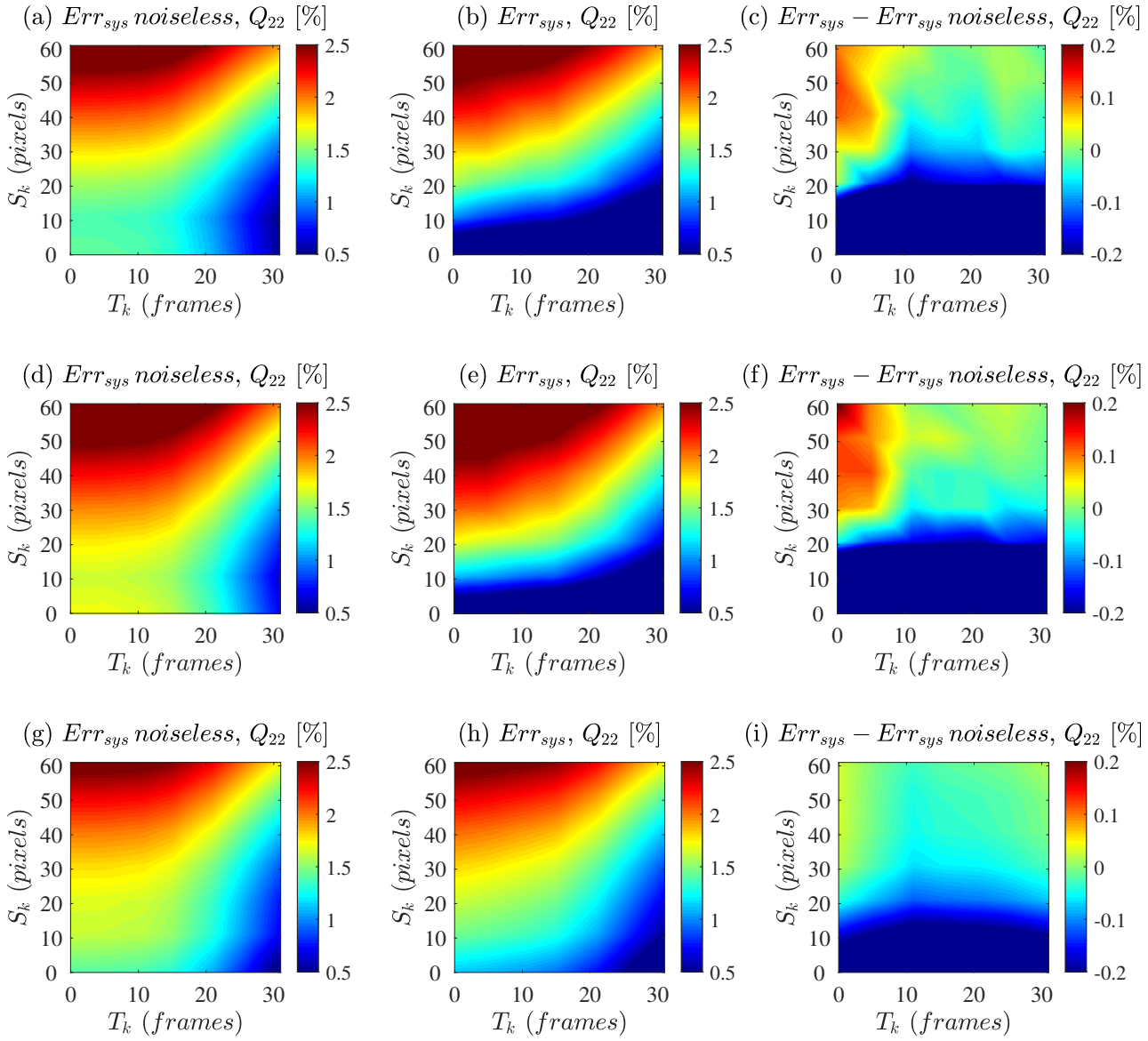

Figure 21: Systematic error maps from the noiseless sweep, the noise sweep and the difference between the noise and noiseless sweeps for the analytic grids (a)−(c), sub-pixel interpolation grids (d)−(f) and sub-pixel interpolation speckles (g)−(i) for the UD45° case Q_{22} identification.

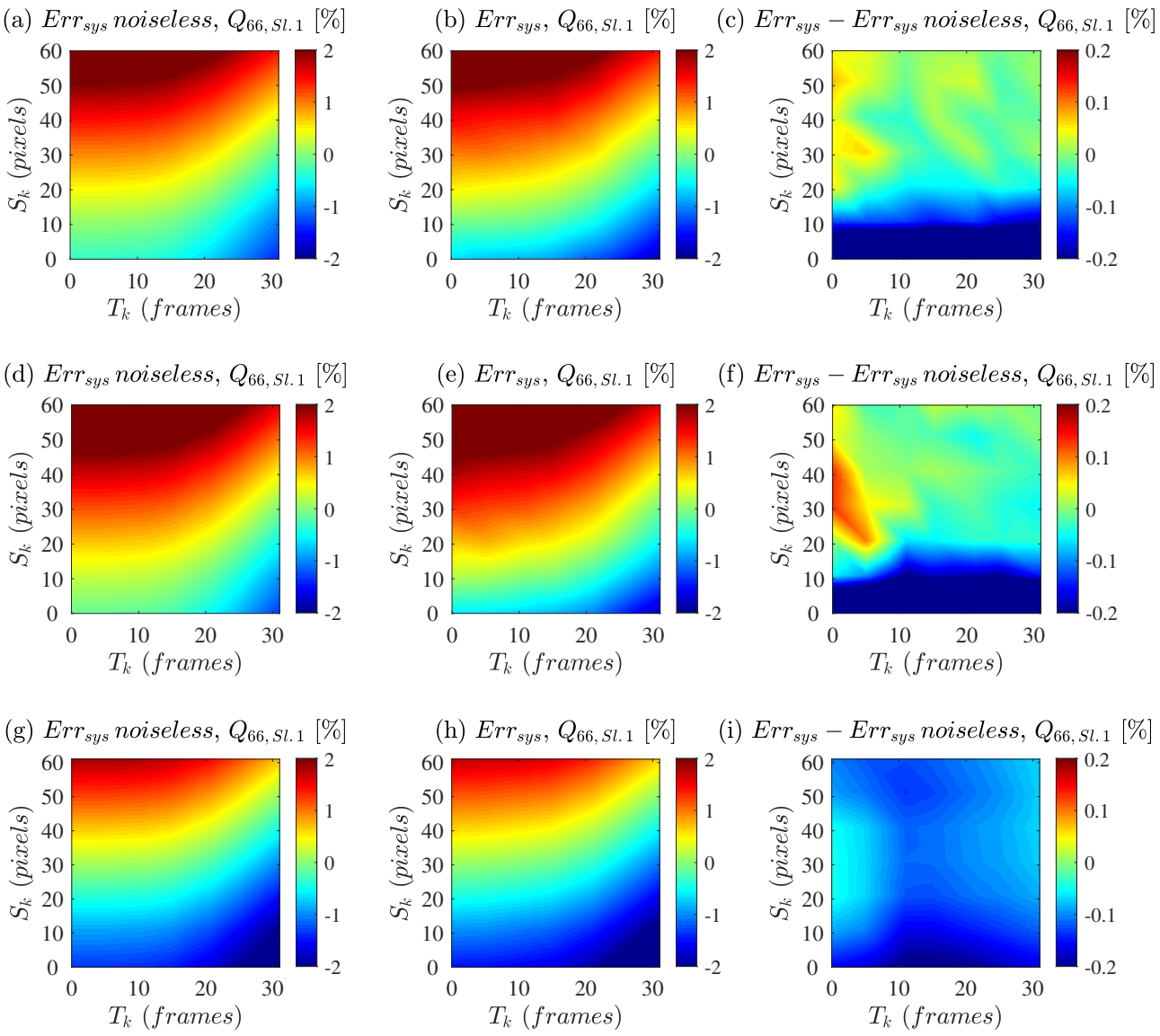

Figure 22: Systematic error maps from the noiseless sweep, the noise sweep and the difference between the noise and noiseless sweeps for the analytic grids (a)−(c), sub-pixel interpolation grids (d)−(f) and sub-pixel interpolation speckles (g)−(i) for the UD45° case $Q_{66,Sl.1}$ identification.

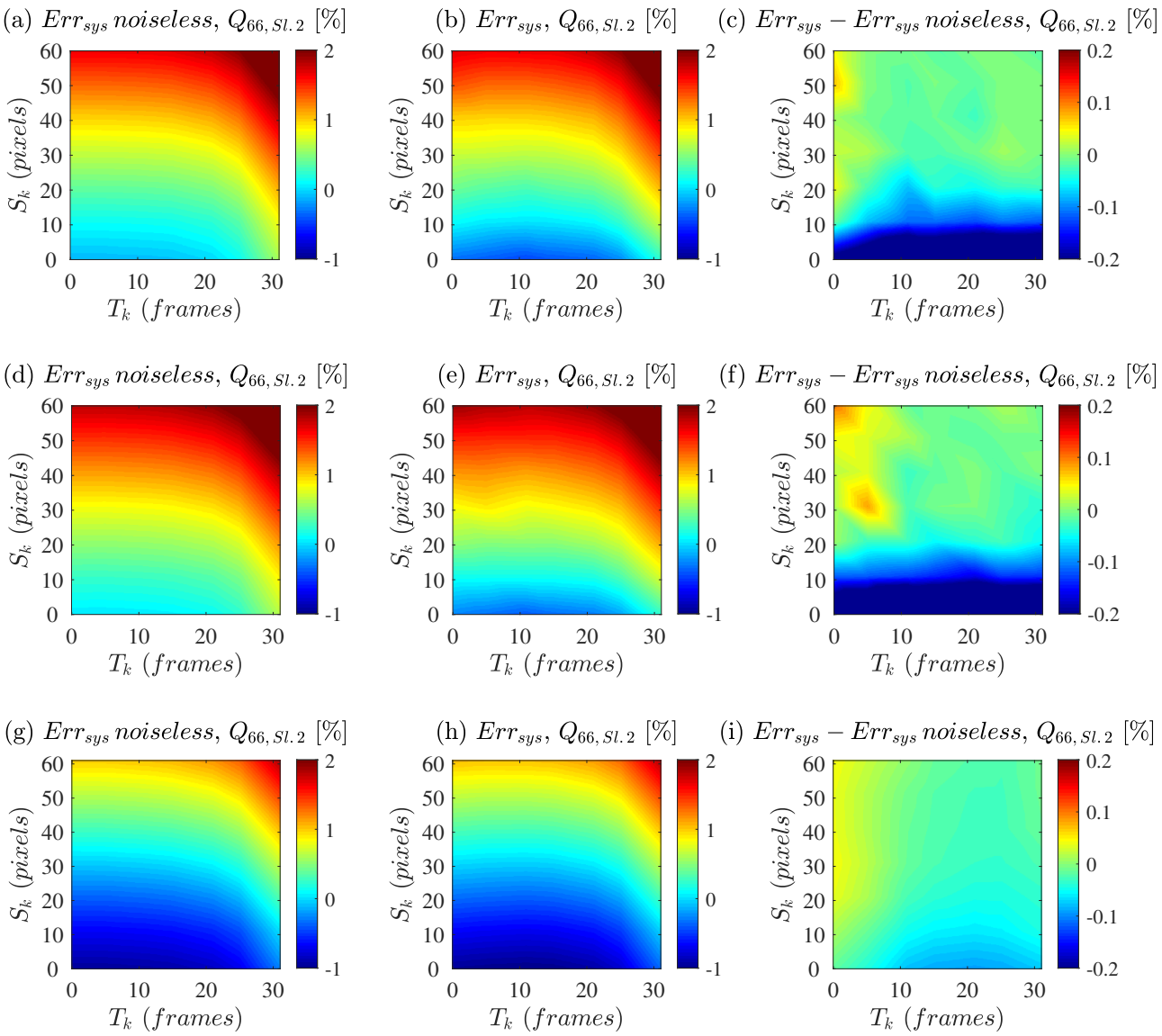

Figure 23: Systematic error maps from the noiseless sweep, the noise sweep and the difference between the noise and noiseless sweeps for the analytic grids (a)−(c), sub-pixel interpolation grids (d)−(f) and sub-pixel interpolation speckles (g)−(i) for the UD45° case $Q_{66,Sl.2}$ identification.

References

[1] F. Campbell. "Introduction to composite materials". *Structural Composite Materials*. Ohio, USA: ASM International, 2010.

[2] R. Bardenheier and G. Rogers. "Dynamic impact testing with servohydraulic testing machines". *Journal de Physique IV* 134, 2006, pp. 693–699.

[3] A. Uenishi, Y. Kuriyama, H. Yoshida, and M. Takahashi. *Material characterisation at high strain rates for optimising car body structures for crash events*. Nippon Steel Technical Report 88. Japan, 2003.

[4] Z. J. Goraj and K. Kustron. "Review of current research trends in bird strike and hail impact simulations on wing leading edge". *Aircraft Engineering and Aerospace Technology* 90(4), 2018, pp. 602–612.

[5] I. C. Metz, J. Ellerbroek, T. Mühlhausen, D. Kügler, and J. M. Hoekstra. "The bird strike challenge". *Aerospace* 7(3), 2020.

[6] J. Liu, Y. Li, X. Yu, X. Gao, and Z. Liu. "Design of aircraft structures against threat of bird strikes". *Chinese Journal of Aeronautics* 31(7), 2018, pp. 1535–1558.

[7] T. Casillas Gil. "Impact simulation of bird strike on semi-spherical transparencies. Application to observation bubbles in the C-295 aircraft". PhD thesis. Spain: University Carlos III de Madrid, 2015.

[8] P. J. Hogg. "Composites in armor". *Science* 314(5802), 2006, pp. 1100–1101.

[9] W. Caywood, R. Rivello, and L. Weckesser. "Tactical missile structures and materials technology". *Johns Hopkins APL Technical Digest* 4(3), 1983, pp. 166–174.

[10] S. Tenden and K. Fossumstuen. *IM improvement of rocket motor by composite motor case*. Tech. rep. RTO-MP-091. Norway: Nammo, 2002.

[11] B. Gama, J. Gillespie, H. Mahfuz, R. Raines, A. Haque, S. Jeelani, T. Bogetti, and B. Fink. "High strain-rate behavior of plain-weave S2 glass/vinyl ester composites". *Journal of Composite Materials* 35(13), 2001, pp. 1201–1228.

[12] K. Akella and N. Naik. "Composite armour: a review". *Journal of the Indian Institute of Science* 95(3), 2015, pp. 297–312.

[13] C. Anderson and J. Walker. "An examination of long-rod penetration". *International Journal of Impact Engineering* 11(4), 1991, pp. 481–501.

[14] B. Terranova, A. Whittaker, and L. Schwer. "Analysis of wind-borne missile impact of reinforced concrete panels using three concrete materials models". *Proceedings of the 17th International Symposium on Interaction of the Effects of Munitions with Structures (ISIEMS).* Bad Neuenahr, Germany, 2017.

[15] S. Heimbs. "Bird strike simulations on composite aircraft structures". *Conference proceedings of the 2011 Simulia customer conference*. Barcelona, Spain, 2011.

[16] A. Gilat, R. Goldberg, and G. Roberts. "Experimental study of strain-rate-dependent behavior of carbon/epoxy composite". *Composites Science and Technology* 62, 2002, pp. 1469–1476.

[17] N. Taniguchi, T. Nishiwaki, and H. Kawada. "Tensile strength of unidirectional CFRP laminate under high strain rate". *Advanced Composite Materials* 16(2), 2007, pp. 167–180.

[18] J. Kwon, J. Choi, H. Huh, and J. Lee. “Evaluation of the effect of the strain rate on the tensile properties of carbon–epoxy composite laminates”. *Journal of Composite Materials* 51(22), 2017, pp. 3197–3210.

[19] L. Melin and L. Asp. “Effects of strain rate on transverse tension properties of a carbon/epoxy composite: studied by moiré photography”. *Composites Part A: Applied Science and Manufacturing* 30(3), 1999, pp. 305–316.

[20] J. Berthe, M. Brieu, E. Deletombe, G. Portemont, P. Lecomte-Grosbras, and A. Deudon. “Consistent identification of CFRP viscoelastic models from creep to dynamic loadings”. *Strain* 49(3), 2013, pp. 257–266.

[21] S. Barré, T. Chotard, and M. Benzeggagh. “Comparative study of strain rate effects on mechanical properties of glass fibre-reinforced thermoset matrix composites”. *Composites Part A: Applied Science and Manufacturing* 27(12), 1996, pp. 1169–1181.

[22] B. Gama, S. Lopatnikov, and J. Gillespie. “Hopkinson bar experimental technique: A critical review”. *Applied Mechanics Reviews* 57(4), 2004, p. 223.

[23] N. Dioh, A. Ivankovic, P. Leevers, and J. Williams. “Stress wave propagation effects in split Hopkinson pressure bar tests”. *Proceedings of the Royal Society A: Mathematical, Physical and Engineering Sciences* 449(1936), 1995, pp. 187–204.

[24] S. Spronk, E. Verboven, F. Gilabert, R. Sevenois, D. Garoz, M. Kersemans, and W. Van Paepegem. “Dynamic tensile testing of brittle composites using a hydraulic pulse machine: stress-strain synchronization and strain rate limits”. *Proceedings*. Brussels, Belgium, 2018.

[25] J. Field, S. Walley, W. Proud, H. Goldrein, and C. Siviour. “Review of experimental techniques for high rate deformation and shock studies”. *International Journal of Impact Engineering* 30(7), 2004, pp. 725–775.

[26] R. Moulart, F. Pierron, S. R. Hallett, and M. R. Wisnom. “Full-field strain measurement and identification of composites moduli at high strain rate with the virtual fields method”. *Experimental Mechanics* 51(4), 2011, pp. 509–536.

[27] F. Pierron, H. Zhu, and C. Siviour. “Beyond Hopkinson’s bar”. *Philosophical Transactions of the Royal Society A: Mathematical, Physical and Engineering Sciences* 372, 2014.

[28] L. Fletcher and F. Pierron. “An image-based inertial impact (IBII) test for tungsten carbide cermets”. *Journal of Dynamic Behavior of Materials* 4(4), 2018, pp. 481–504.

[29] L. Fletcher, J. Van-Blitterswyk, and F. Pierron. “A novel image-based inertial impact (IBII) test for the transverse properties of composites at high strain rates”. *Journal of Dynamic Behavior of Materials* 5(1), 2019, pp. 65–92.

[30] L. Fletcher, J. Van-Blitterswyk, and F. Pierron. “Combined shear/tension testing of fibre composites at high strain rates using an image-based inertial impact test”. *EPJ Web of Conferences* 183, 2018.

[31] M. Grédiac, F. Sur, and B. Blaysat. “The grid method for in-plane displacement and strain measurement: a review and analysis”. *Strain* 52(3), 2016, pp. 205–243.

[32] M. Castres, J. Berthe, E. Deletombe, and M. Brieu. “Experimental evaluation of the elastic limit of carbon-fibre reinforced epoxy composites under a large range of strain rate and temperature conditions”. *Strain* 53(6), 2017, pp. 1–10.

[33] W. Chen and B. Song. *Split Hopkinson (Kolsky) bar design, testing and applications*. New York, USA: Springer, 2011.

[34] J. Chen, B. Guo, H. B. Liu, H. Liu, and P. Chen. “Dynamic brazilian test of brittle materials using the split Hopkinson pressure bar and digital image correlation”. *Strain* 50(6), 2014, pp. 563–570.

[35] P. Church, R. Cornish, I. Cullis, P. Gould, and I. Lewtas. “Using the split Hopkinson pressure bar to validate material models”. *Philosophical Transactions of the Royal Society A: Mathematical, Physical and Engineering Sciences* 372(2023), 2014.

[36] N. Bourne. *Materials in mechanical extremes*. New York, USA: Cambridge University Press, 2013.

[37] L. Yang and V. Shim. "An analysis of stress uniformity in split Hopkinson bar test specimens". *International Journal of Impact Engineering* 31(2), 2005, pp. 129–150.

[38] D. Parry, P. Dixon, S. Hodson, and N. Al-Maliky. "Stress equilibrium effects within Hopkinson bar specimens". *Journal de Physique IV* 4, 1994.

[39] B. Song, W. Chen, and T. Weerasooriya. "Quasi-static and dynamic compressive behaviors of a S-2 glass/SC15 composite". *Journal of Composite Materials* 37(19), 2003.

[40] M. S. Chaudhry and A. Czekanski. "FE analysis of critical testing parameters in kolsky bar experiments for elastomers at high strain rate". *Materials* 12(23), 2019.

[41] A. T. Owens and H. Tippur. "A tensile split Hopkinson bar for testing particulate polymer composites under elevated rates of loading". *Experimental Mechanics* 49(6), 2009.

[42] G. T. Gray III. "Classic split-Hopkinson pressure bar testing". *ASM Handbook Volume 8 Mechanical Testing and Evaluation*. ASM International, 2000, pp. 462–476.

[43] F. Richter, E. Köppe, and W. Daum. "Tracking deformation history in split Hopkinson pressure bar testing". *Materials Today: Proceedings* 3(4), 2016, pp. 1139–1143.

[44] S. Rigby, A. Barr, and M. Clayton. "A review of Pochhammer–Chree dispersion in the Hopkinson bar". *Proceedings of the Institution of Civil Engineers - Engineering and Computational Mechanics* 171(1), 2018, pp. 3–13.

[45] Z. Li and J. Lambros. "Determination of the dynamic response of brittle composites by the use of the split Hopkinson pressure bar". *Composites Science and Technology* 59(7), 1999, pp. 1097–1107.

[46] J. Wang and J. Zhang. "Research on high-power and high-speed hydraulic impact testing machine for mine anti-impact support equipment". *Shock and Vibration* 2019, 2019, pp. 1–12.

[47] D. Zhu, S. Rajan, B. Mobasher, A. Peled, and M. Mignolet. "Modal analysis of a servo-hydraulic high speed machine and its application to dynamic tensile testing at an intermediate strain rate". *Experimental Mechanics* 51(8), 2010, pp. 1347–1363.

[48] M. Shokrieh and M. Omidi. "Tension behavior of unidirectional glass/epoxy composites under different strain rates". *Composite Structures* 88(4), 2009, pp. 595–601.

[49] J. Berthe, E. Deletombe, M. Brieu, G. Portemont, and P. Paulmier. "Dynamic characterization of CFRP composite materials – Toward a pre-normative testing protocol – Application to T700GC/M21 material". *Procedia Engineering* 80, 2014, pp. 165–182.

[50] S. Spronk, E. Verboven, F. Gilabert, R. Sevenois, D. Garoz, M. Kersemans, and W. Van Paepegem. "Stress-strain synchronization for high strain rate tests on brittle composites". *Polymer Testing* 67, 2018, pp. 477–486.

[51] S. Yoo, D. Schueler, M. Brodbeck, N. Toso, G. Catalanotti, and H. Voggenreiter. "An improved load introduction technique for dynamic material characterisation at intermediate strain rate". *Proceedings*. Vol. 2. Brussels, Belgium, 2018, p. 381.

[52] K. Naresh, K. Shankar, B. Rao, and R. Velmurugan. "Effect of high strain rate on glass / carbon / hybrid fiber reinforced epoxy laminated composites". *Composites Part B: Engineering* 100, 2016, pp. 125–135.

[53] H. Hsiao, I. Daniel, and R. Cordes. "Strain rate effects on the transverse compressive and shear behavior of unidirectional composites". *Journal of Composite Materials* 33(17), 1999, pp. 1620–1642.

[54] H. Hsiao and I. Daniel. "Strain rate behavior of composite materials". *Composites Part B: Engineering* 29(5), 1998, pp. 521–533.

[55] M. Sutton, J.-J. Orteu, and H. Schreier. *Image correlation for shape, motion and deformation measurements*. USA: Springer, 2009.

[56] B. Pan, K. Qian, H. Xie, and A. Asundi. "Two-dimensional digital image correlation for in-plane displacement and strain measurement: a review". *Measurement Science and Technology* 20(6), 2009.

[57] H. Zhu and F. Pierron. "Exploration of Saint-Venant's principle in inertial high strain rate testing of materials". *Experimental Mechanics* 56(1), 2016, pp. 3–23.

[58] F. Pierron, M. Sutton, and V. Tiwari. "Ultra high speed DIC and virtual fields method analysis of a three point bending impact test on an aluminium bar". *Experimental Mechanics* 51(4), 2011, pp. 537–563.

[59] H. Koerber, J. Xavier, and P. Camanho. "High strain rate characterisation of unidirectional carbon-epoxy IM7-8552 in transverse compression and in-plane shear using digital image correlation". *Mechanics of Materials* 42(11), 2010, pp. 1004–1019.

[60] A. Gilat and J. Seidt. "Compression, tension and shear testing of fibrous composite with the split Hopkinson bar technique". *EPJ Web of Conferences* 183, 2018.

[61] P. L. Reu, W. Sweatt, T. Miller, and D. Fleming. "Camera system resolution and its influence on digital image correlation". *Experimental Mechanics* 55(1), 2015, pp. 9–25.

[62] J.-L. Piro and M. Grédiac. "Producing and transferring low-spatial-frequency grids for measuring displacement fields with moiré and grid methods". *Experimental Techniques* 28(4), 2004, pp. 23–26.

[63] Y. Surrel. *Printing grids at the university of Southampton printing centre*. 2017.

[64] Y. Surrel. *Printing grids at the university of Southampton print centre - using the 'high quality' mode*. 2017.

[65] J. Van Blitterswyk, L. Fletcher, and F. Pierron. "Image-based inertial impact test for composite interlaminar tensile properties". *Journal of Dynamic Behavior of Materials* 4(4), 2018, pp. 543–572.

[66] S. Avril, M. Bonnet, A.-S. Bretelle, M. Grédiac, F. Hild, P. Ienny, F. Latourte, D. Lemosse, S. Pagano, E. Pagnacco, and F. Pierron. "Overview of identification methods of mechanical parameters based on full-field measurements". *Experimental Mechanics* 48(4), 2008, pp. 381–402.

[67] E. Markiewicz and B. Langrand. "Characterisation and parameters identification of materials constitutive and damage models: from normalised direct approach to most advanced inverse problem resolution". *Procedia Engineering* 173, 2017, pp. 33–40.

[68] M. Grédiac and F. Pierron. "Identifying constitutive parameters from heterogeneous strain fields using the virtual fields method". *Procedia IUTAM* 4, 2012, pp. 48–53.

[69] S. Cooreman, D. Lecompte, H. Sol, J. Vantomme, and D. Debruyne. "Elasto-plastic material parameter identification by inverse methods: calculation of the sensitivity matrix". *International Journal of Solids and Structures* 44(13), 2007, pp. 4329–4341.

[70] L. Zhang, S. Thakku, M. Beotra, M. Baskaran, T. Aung, J. C. H. Goh, N. G. Strouthidis, and M. J. A. Girard. "Verification of a virtual fields method to extract the mechanical properties of human optic nerve head tissues in vivo". *Biomechanics and Modeling in Mechanobiology* 16(3), 2017, pp. 871–887.

[71] F. Pierron and M. Grédiac. *The virtual fields method*. New York, USA: Springer, 2012.

[72] H. Chalal, S. Avril, F. Pierron, and F. Meraghni. "Experimental identification of a nonlinear model for composites using the grid technique coupled to the virtual fields method". *Composites Part A: Applied Science and Manufacturing* 37(2), 2006, pp. 315–325.

[73] F. Pierron and P. Forquin. "Ultra-high-speed full-field deformation measurements on concrete spalling specimens and stiffness identification with the virtual fields method". *Strain* 48(5), 2012, pp. 388–405.

[74] B. Lukić, D. Saletti, and P. Forquin. "On the processing of spalling experiments. Part II: Identification of concrete fracture energy in dynamic tension". *Journal of Dynamic Behavior of Materials* 4(1), 2018, pp. 56–73.

[75] H. Schuler, C. Mayrhofer, and K. Thoma. "Spall experiments for the measurement of the tensile strength and fracture energy of concrete at high strain rates". *International Journal of Impact Engineering* 32(10), 2006, pp. 1635–1650.

[76] S.-h. Yoon, I. Giannakopoulos, and C. Siviour. "Application of the virtual fields method to the uniaxial behavior of rubbers at medium strain rates". *International Journal of Solids and Structures* 69-70, 2015, pp. 553–568.

[77] A. Marek, F. Davis, and F. Pierron. "Sensitivity-based virtual fields for the non-linear virtual fields method". *Computational Mechanics* 60(3), 2017, pp. 409–431.

[78] B. Koohbor, S. Mallon, A. Kidane, and W.-Y. Lu. "The deformation and failure response of closed-cell PMDI foams subjected to dynamic impact loading". *Polymer Testing* 44, 2015, pp. 112–124.

[79] R. Othman, S. Aloui, and A. Poitou. "Identification of non-homogeneous stress fields in dynamic experiments with a non-parametric method". *Polymer Testing* 29(5), 2010, pp. 616–623.

[80] P. Reu and T. Miller. "The application of high-speed digital image correlation". *The Journal of Strain Analysis for Engineering Design* 43(8), 2008, pp. 673–688.

[81] D. Saletti and P. Forquin. "A comparison of DIC and grid measurements for processing spalling tests with the VFM and an 80-kpixel ultra-high speed camera". *The European Physical Journal Special Topics* 225(2), 2016, pp. 311–323.

[82] S. Pinho, C. Davilia, P. Camanho, L. Iannucci, and P. Robinson. *Failure models and criteria for FRP under in-plane or three-dimensional stress states including shear non-linearity*. Tech. rep. NASA / TM-2005-213530. Hampton, U.S.A.: NASA Langley Research Center, 2005.

[83] N. Chen and C. Soares. "Ultimate strength and reliability of composite material structures". *Marine Technology and Engineering*, 2011, pp. 817–840.

[84] E. Barbero. *Finite element analysis of composite materials using Abaqus*. 1st ed. Boca Raton, USA: CRC Press, 2013.

[85] S. W. Tsai and E. M. Wu. "A general theory of strength for anisotropic materials". *Journal of Composite Materials* 5, 1971, pp. 58–80.

[86] Y. Zhou, Y. Wang, Y. Xia, and S. Jeelani. "Tensile behavior of carbon fiber bundles at different strain rates". *Materials Letters* 64(3), 2010, pp. 246–248.

[87] Y. Ou, D. Zhu, H. Zhang, L. Huang, Y. Yao, G. Li, and B. Mobasher. "Mechanical characterization of the tensile properties of glass fiber and its reinforced polymer (GFRP) composite under varying strain rates and temperatures". *Polymers* 8(5), 2016, p. 196.

[88] C. Siviour and J. Jordan. "High strain rate mechanics of polymers: a review". *Journal of Dynamic Behavior of Materials* 2(1), 2016, pp. 15–32.

[89] J. L. Jordan, J. R. Foley, and C. R. Siviour. "Mechanical properties of Epon 826/DEA epoxy". *Mechanics of Time-Dependent Materials* 12(3), 2008, pp. 249–272.

[90] C. Buckley, J. Harding, J. Hou, C. Ruiz, and A. Trojanowski. "Deformation of thermosetting resins at impact rates of strain. Part I: Experimental study". *Journal of the Mechanics and Physics of Solids* 49(7), 2000, pp. 1517–1538.

[91] J. Hou, C. Ruiz, and A. Trojanowski. "Torsion tests of thermosetting resins at impact strain rate and under quasi-static loading". *Materials Science and Engineering: A* 283(1-2), 2000, pp. 181–188.

[92] A. Gilat, R. Goldberg, and G. Roberts. "Strain rate sensitivity of epoxy resin in tensile and shear loading". *Journal of Aerospace Engineering* 20(2), 2007, pp. 75–89.

[93] J. Harding and L. M. Welsh. "A tensile testing technique for fibre-reinforced composites at impact rates of strain". *Journal of Materials Science* 18(6), 1983, pp. 1810–1826.

[94] H. Koerber and P. Camanho. "Characterisation of unidirectional carbon-epoxy IM7-8552 in longitudinal compression under high strain rates". *DYMAT 2009 - 9th International Conferences on the Mechanical and Physical Behaviour of Materials under Dynamic Loading*. Vol. 1. Brussels, Belgium: EDP Sciences, 2009, pp. 185–191.

[95] J. Schaefer, B. Werner, and I. Daniel. "Strain-rate-dependent failure of a toughened matrix composite". *Experimental Mechanics* 54(6), 2014, pp. 1111–1120.

[96] S. Pardo, D. Baptiste, F. Decobert, J. Fitoussi, and R. Joannic. "Tensile dynamic behaviour of a quasi-unidirectonal E-glass/polyester composite". *Composites Science and Technology* 62(4), 2002, pp. 579–584.

[97] G. Makarov, W. Wang, and R. A. Shenoi. "Deformation and fracture of unidirectional GFRP composites at high strain rate tension". *Proceedings of the 2nd International Conference on Composites Testing and Model Identification*. Bristol, U.K., 2004, p. 10.

[98] P. Kumar, A. Garg, and B. Agarwal. "Dynamic compressive behaviour of unidirectional GFRP for various fibre orientations". *Materials Letters* 4(2), 1986, pp. 111–116.

[99] I. Daniel and T. Liber. *Strain rate effects on mechanical properties of fiber composites*. Tech. rep. NASA CR-135087. Cleveland, USA: NASA Lewis Research Centre, 1976.

[100] D. Asprone, E. Cadoni, A. Prota, and G. Manfredi. "Strain-rate sensitivity of a pultruded E-Glass/Polyester composite". *Journal of Composites for Construction* 13(6), 2009, pp. 558–564.

[101] I. Daniel, B. Werner, and J. Fenner. "Strain-rate-dependent failure criteria for composites". *Composites Science and Technology* 71(3), 2011, pp. 357–364.

[102] H. Koerber, P. Kuhn, M. Ploeckl, F. Otero, P.-W. Gerbaud, R. Rolfes, and P. Camanho. "Experimental characterization and constitutive modeling of the non-linear stress–strain behavior of unidirectional carbon–epoxy under high strain rate loading". *Advanced Modeling and Simulation in Engineering Sciences* 5(1), 2018.

[103] A. Kidane, H. Gowtham, and N. Naik. "Strain rate effects in polymer matrix composites under shear loading: a critical review". *Journal of Dynamic Behavior of Materials* 3(1), 2017, pp. 110–132.

[104] A. Gilat and C. Cheng. "Torsional split Hopkinson bar tests at strain rates above 10000 inverse seconds". *Experimental Mechanics* 40(1), 2000, pp. 54–59.

[105] H. Koerber. "Mechanical response of advanced composites under high strain rates". PhD thesis. Portugal: University of Porto, 2010.

[106] H. Cui, D. Thomson, A. Pellegrino, J. Wiegand, and N. Petrinic. "Effect of strain rate and fibre rotation on the in-plane shear response of $\pm 45°$ laminates in tension and compression tests". *Composites Science and Technology* 135, 2016, pp. 106–115.

[107] J. Tsai and C. Sun. "Dynamic compressive strengths of polymeric composites". *International Journal of Solids and Structures* 41(11 - 12), 2004, pp. 3211–3224.

[108] J.-L. Tsai and C. Sun. "Strain rate effect on in-plane shear strength of unidirectional polymeric composites". *Composites Science and Technology* 65(13), 2005, pp. 1941–1947.

[109] Y. Tao, H. Chen, K. Yao, H. Lei, Y. Pei, and D. Fang. "Experimental and theoretical studies on inter-fiber failure of unidirectional polymer-matrix composites under different strain rates". *International Journal of Solids and Structures* 113 - 114, 2017, pp. 37–46.

[110] M. Shokrieh and M. Omidi. "Investigation of strain rate effects on in-plane shear properties of glass/epoxy composites". *Composite Structures* 91(1), 2009, pp. 95–102.

[111] J. Schaefer, B. Werner, and I. Daniel. *Strain-rate-dependent failure criteria for composite laminates: application of the northwestern failure theory to multiple material systems*. Tech. rep. SAND2017-3082C. California, USA: Sandia National Laboratories, 2017, pp. 187–196.

[112] P. Soden, A. Kaddour, and M. Hinton. "Recommendations for designers and researchers resulting from the world-wide failure exercise". *Composites Science and Technology* 64, 2004, pp. 589–604.

[113] M. Hinton and A. Kaddour. "The background to the second world-wide failure exercise". *Journal of Composite Materials* 46(19 - 20), 2012, pp. 2283–2294.

[114] M. H. Sadd. *Elasticity: Theory, Applications and Numerics*. Massachusetts, USA: Elsevier, 2005.

[115] J. Van Blitterswyk, L. Fletcher, and F. Pierron. "Investigation of the 2D assumption in the image-based inertial impact (IBII) test". *Strain* 57(6), 2020.

[116] B. Koohbor, A. Kidane, and W.-Y. Lu. "Characterizing the constitutive response and energy absorption of rigid polymeric foams subjected to intermediate-velocity impact". *Polymer Testing* 54, 2016, pp. 48–58.

[117] L. Fletcher, J. Van Blitterswyk, and F. Pierron. *A manual for conducting image-based inertial impact (IBII) tests*. Faculty of Engineering and Physical Sciences, University of Southampton, UK, 2019.

[118] H. Zhu. "A novel methodology for high strain rate testing using full-field measurements and the virtual fields method". PhD thesis. France: University of Technology of Troyes, 2015.

[119] A. Resnyansky, S. Parry, and S. Weckert. "Gas gun ballistic testing of moving pre-stressed targets". *Proceedings of the Conference of the American Physical Society Topical Group on Shock Compression of Condensed Matter*. St. Louis, MO, USA, 2018.

[120] R. Whelchel, G. Kennedy, S. Dwivedi, T. Sanders, and N. Thadhani. "Spall behavior of rolled aluminum 5083-H116 plate". *J. Appl. Phys.* 113(233506), 2013.

[121] M. Grédiac, B. Blaysat, and F. Sur. "A critical comparison of some metrological parameters characterizing local digital image correlation and grid method". *Experimental Mechanics* 57(6), 2017, pp. 871–903.

[122] F. Sur and M. Grédiac. "Influence of the analysis window on the metrological performance of the grid method". *Journal of Mathematical Imaging and Vision* 56(3), 2016, pp. 472–498.

[123] F. Pierron, R. Cheriguene, P. Forquin, R. Moulart, M. Rossi, and M. Sutton. "Performances and limitations of three ultra high-speed imaging cameras for full-field deformation measurements". *Applied Mechanics and Materials* 70, 2011, pp. 81–86.

[124] M. Rossi and F. Pierron. "On the use of simulated experiments in designing tests for material characterization from full-field measurements". *International Journal of Solids and Structures* 49(3 - 4), 2012, pp. 420–435.

[125] P. Reu. "All about speckles: Aliasing". *Experimental Techniques* 38(5), 2014, pp. 1–3.

[126] M. Rossi, P. Lava, F. Pierron, D. Debruyne, and M. Sasso. "Effect of DIC spatial resolution, noise and interpolation error on identification results with the VFM". *Strain* 51(3), 2015, pp. 206–222.

[127] F. Pierron and L. Fletcher. "Generalized stress–strain curves for IBII tests on isotropic and orthotropic materials". *Journal of Dynamic Behavior of Materials* 5(2), 2019, pp. 180–193.

[128] P. Lava, S. Cooreman, S. Coppieters, M. De Strycker, and D. Debruyne. "Assessment of measuring errors in DIC using deformation fields generated by plastic FEA". *Optics and Lasers in Engineering* 47(7-8), 2009, pp. 747–753.

[129] P. Lava, S. Cooreman, and D. Debruyne. "Study of systematic errors in strain fields obtained via DIC using heterogeneous deformation generated by plastic FEA". *Optics and Lasers in Engineering* 48(4), 2010, pp. 457–468.

[130] X. Gu and F. Pierron. "Towards the design of a new standard for composite stiffness identification". *Composites Part A: Applied Science and Manufacturing* 91, 2016, pp. 448–460.

[131] P. Wang, F. Pierron, M. Rossi, P. Lava, and O. T. Thomsen. "Optimised experimental characterisation of polymeric foam material using DIC and the Virtual Fields Method". *Strain* 52(1), 2016, pp. 59–79.

[132] B. Lukić, D. Saletti, and P. Forquin. "Use of simulated experiments for material characterization of brittle materials subjected to high strain rate dynamic tension". *Philosophical Transactions of the Royal Society A: Mathematical, Physical and Engineering Sciences* 375(2085), 2017, p. 20160168.

[133] P. Lava, E. M. C. Jones, L. Wittevrongel, and F. Pierron. "Validation of finite-element models using full-field experimental data: Levelling finite-element analysis data through a digital image correlation engine". *Strain* 56(4), 2020.

[134] M. Dokainish and K. Subbaraj. "A survey of direct time-integration methods in computational structural dynamics—I. Explicit methods". *Computers & Structures* 32(6), 1989, pp. 1371–1386.

[135] G. Stoilov, V. Kavardzhikov, and D. Pashkouleva. "Multiscale monitoring of deformation fields by digital image correlation method". *Journal of Theoretical and Applied Mechanics* 48(3), 2018, pp. 23–40.

[136] S. Bossuyt. "Optimized patterns for digital image correlation". *Imaging Methods for Novel Materials and Challenging Applications*. Vol. 3. Series Title: Conference Proceedings of the Society for Experimental Mechanics Series. USA, 2012.

[137] G. Stoilov, V. Kavardzhikov, and D. Pashkouleva. "A comparative study of random patterns for digital image correlation". *Journal of Theoretical and Applied Mechanics* 42(2), 2012, pp. 55–66.

[138] J. Millett, N. Bourne, and D. Deas. "The equation of state of two alumina-filled epoxy resins". *Journal of Physics D: Applied Physics* 38(6), 2005, pp. 930–934.

[139] J. Zhang. "Different surface treatments of carbon fibres and their influence on the interfacial properties of carbon fibre/epoxy composites". PhD thesis. France: École Centrale Paris, 2012.

[140] J. Berthe. "Comportement thermo-visco-élastique des composites CMO – De la statique à la dynamique grande vitesse". PhD thesis. France: University of Lille, 2013.

[141] R. Seghir, F. Pierron, and L. Fletcher. "Image-based stress field reconstruction in complex media". *Conference Proceedings of the Society for Experimental Mechanics Series*. Greenville, USA, 2019.

[142] P. Olivier, J. P. Cottu, and B. Ferret. "Effects of cure cycle pressure and voids on some mechanical properties of carbon/epoxy laminates". *Composites* 26(7), 1995, pp. 509–515.

[143] S. Aratama, R. Hashizume, K. Takenaka, K. Koga, Y. Tsumura, T. Miyake, M. Nishikawa, and M. Hojo. "Microscopic observation of voids and transverse crack initiation in CFRP laminates". *Advanced Composite Materials* 25, 2016, pp. 115–130.

[144] M. Mehdikhani, E. Steensels, A. Standaert, K. A. M. Vallons, L. Gorbatikh, and S. V. Lomov. "Multi-scale digital image correlation for detection and quantification of matrix cracks in carbon fiber composite laminates in the absence and presence of voids controlled by the cure cycle". *Composites Part B: Engineering* 154, 2018, pp. 138–147.

[145] R. Seghir and F. Pierron. "A novel image-based ultrasonic test to map material mechanical properties at high strain-rates". *Experimental Mechanics* 58(2), 2018.

[146] J. Neumayer, P. Kuhn, H. Koerber, and R. Hinterhölzl. "Experimental determination of the tensile and shear behaviour of adhesives under impact loading". *The Journal of Adhesion* 92(7-9), 2016.

[147] D. G. Tasker, P. K. Gustavson, and W. H. Wilson. *A PVDF trigger and tilt detector for projectile impact experiments*. Tech. rep. NAVSWC TR 91-640. USA: Naval Surface Warfare Center, 1991.